UNIVERSIDAD AUTONOMA
DE MADRID

FACULTAD DE CIENCIAS
DEPARTAMENTO DE FÍSICA DE MATERIALES

The Effect of Crystal Growth Conditions and Surface Treatment on CdZnTe Bulk Single Crystal

PhD Dissertation

Hakima Bensalah

Supervisor

Prof. Ernesto Diéguez

Prof. José Luis Plaza

Madrid, June 2013

Dedicated to my parents

Acknowledgements

First and foremost, I would like to thank my supervisor Prof. Ernesto Diéguez who continually supported and pushed me educationally forward through research work. I am thankful to my Co-Director Prof. Jose Luis Plaza for ample advice whenever it was needed.

I wish to express my deepest gratitude to Prof. Jan Franc for giving me the opportunity of three months internship in his group at Charles University in Prague, and I'm very grateful to him for his valuable advices, help and fruitful discussions. I would like to thank also Eduard Belas, Pavel Hlidek, Vaclav Dedic and Hassan Elhadidy.

I would like to acknowledge the collaboration of several Institutes and scientists who have also aided me in making various measurements for the scientific investigations which have been carried out. Prof. Leonardo Soriano from Universidad Autónoma de Madrid for XPS measurments. Dr. Oscar Martínez from Universidad de Valladolid for PL, CL and Raman spectroscopy measurements. Prof. Artur Medvid from Riga Technical University for Laser irradiation. Dr. José Manuel Pérez and Oscar Vela from Centro de Investigation Energéticas Medioambientales y Tecnológicas (CIEMAT) in Madrid for gamma ray measurements.

I am deeply grateful to European Synchrotron Radiation Facility (ESRF) for giving me the opportunity of 3 days research stay in Grenoble for EXAFS measurements. Many thanks to all the members for their help especially Miquel Luis Corro Moya.

I sincerely would like to thank Ralph James Michael Fiederle for the financial support to attend the RTSD conference 2012 in California.

I must also acknowledge SEGAINVEX group for their technical support, especially, Juan Antonio Higuera and José Rízquez López.

I would like to thank the people from el Servicio Interdepartamental de Investigación (SIDI) in UAM for the scientific investigations. Especially thanks to the people from SEM, FTIR, ICP-MS, HRXRD teams.

I extend my sincere thanks to all the members of the Department of Física de Materiales in UAM, and all those who contributed directly or indirectly to my work thesis.

Special thanks to all of the past and present members of crystal growth laboratory, my colleagues and friends for providing a great atmosphere in which to work and for many valuable discussions and ideas: Dr. Fabrice Dierre, Dr. Veronica Carcelen, Dr. Jerome Crocco, Dr. Qian Zheng, Andres Black, Juan Medina, Sandra Rubio and Axa Piñeiro.

I would like to thank my parents, sisters: Lamia and her husband Moncef, Sara, Oulaya, Kawthar y Rim, and brother: Hamza, for all of their help and support which has allowed me to realize this ambition. I would like to thank them for their encouragement through this time and their help with the production of this thesis. Thanks to Bouchra, my grandparents, my uncles, aunts and cousins for their support.

This thesis is also dedicated to Masood Kader, for encouraging and helping me to reach the goal of completing this task.

I would like to give special thanks to my best friend Naima Ezzirari. Thanks to my friends Salama Seleima and Mounia Albahri.

Finally I express my thanks, and I apologize, to anybody that provided any help to me and I could not remember at this moment.

General introduction

The ability to detect high energy X-rays and gamma rays radiation has shown an effective improvement in recent years. Radiation detectors have become increasingly more important for different applications such as homeland security and medical imaging. In general, there are three types of detectors: i) Gas filled detectors ii) scintillation detectors and iii) semiconductors detectors. In fact, solid state semiconductor detectors are commonly used because of their excellent energy resolution, better efficiency and also the smaller energy required for creating an electron hole pair. The most commonly used semiconductor detectors are silicon and germanium single crystals, but the use of these detectors is still limited by the requirement of liquid nitrogen cooling in order to reduce their noise levels. Consequently, room temperature semiconductor detectors such as cadmium zinc telluride (CZT), gallium arsenide (GaAs), indium phosphide (InP) are available.

CdTe and CdZnTe have long been known to have great potential in room-temperature X-ray and gamma ray semiconductor detector applications, mainly due to their attractive material properties. The high atomic number and density of these compounds provide strong absorption and high detection efficiency of high energy photons. The wide band gap of the materials allows the fabrication of highly resistive devices enabling large depletion depths and low leakage currents. A good CdTe/CdZnTe detector must have high resistivity ($> 10^9 \Omega.cm$), which decreases dark current and device noise, and large mobility-lifetime product $\mu\tau$, which ensures that carriers can travel through a large volume of the detector material to be collected by electrodes. Indeed, the combination of these attractive properties also makes CZT an excellent detector for medical, security, and astrophysics applications.

Despite these inherent advantages, the use of CZT material is still limited by some deleterious problems such as the presence of secondary phases, impurities, low resistivity, and surface quality. Each of these factors causes degradation of the detector performance. Another limiting factor of CdZnTe for the use as detectors is its charge transport properties. Electron mobility lifetime products for holes and electrons are low compared to Si and Ge, limiting the spatial range of carriers. Indeed, apart from the limiting properties of CdZnTe material, the experimental processes utilized for detector fabrication present an obstacle for achieving an appropriate material for radiation

applications. The methods used for surface preparation and contact deposition play a critical and sensitive role in determining the performance of the radiation detector.

There exist a wide range of methods used for the growth of CdZnTe including vapor phase growth, solution growth, and melt growth. Growth from the melt seems to be the most often used method due to its effectiveness at growing large single crystals. Within the melt growth methods, Vertical Gradient Freeze (VGF), Vertical Bridgman, High Pressure Bridgman, and Travelling Heater Method (THM) have been used for fabricating bulk CdTe/CdZnTe. The proper control of growth process parameters such as feedstock starting material, growth rate, and cooling rates are essential issues in determining the final properties and quality of CdZnTe crystals.

The growth of CdTe/CdZnTe without pressure control leads to the evaporation and loss of Cd, due to its high vapor pressure, resulting in a Te-rich melt and bulk material, even if the starting material is stoichiometric. Undoped CdTe crystals are usually low resistivity *p*-type material, mainly due to the presence of uncompensated shallow acceptor impurities. In order to grow high resistivity CdTe and CZT, one usually needs to dope with shallow donors such as Cl, and In.

The purpose of this thesis has been focused on the development of high performance CdZnTe gamma ray detectors. This work consists of five chapters, organized as follows:

The first chapter discusses the most important parameters of crystal growth from the melt and the most commonly used methods to grow CdZnTe bulk crystal. The properties and defects formed during crystal growth and also introduced after surface preparation will be discussed. In the last part of this chapter, the applications of CdZnTe will be detailed.

The second chapter describes the experimental methods and processes which have been used during this investigation. This includes (i) the preparation of starting material and conditions used for crystal growth, (ii) a complete process of surface preparation including lapping, polishing and etching, (iii) methods used for detector preparation, and finally (iv) the most important techniques used for sample characterization.

In the third chapter, different characterization techniques were used to investigate samples harvested from ingots grown using different growth parameters, including superheating, cooling and annealing. This investigation will be mainly focused on the

influence of these parameters on the size and distribution of Te inclusions, deep defects, optical and electrical properties of CdZnTe detectors.

In the fourth chapter, the effect of surface preparation has been studied. The influence of polishing, etching and passivation was characterized in terms of surface roughness, surface composition and leakage current. The best process for improving the performance of radiation detectors will be described.

Chapter five is dedicated to the influence of argon ion beam and Nd:YAG laser irradiation on Te inclusions. The optical and electrical properties were studied using different techniques. In fact, the possibility to improve CdZnTe after irradiation has been demonstrated.

Introducción general

La capacidad tecnológica para la detección de radiación de alta energía, como los rayos-X o gamma, ha conocido una enorme mejora en los últimos años. Los detectores de radiación se han ido convirtiendo paulatinamente en dispositivos de enorme importancia en sectores como la defensa o la instrumentación médica. In general, hay tres tipos de detectores: i) Detectores en base a gas; ii) Detectores de centelleo y iii) Detectores basados en semiconductores. Los detectores de estado sólido basados en semiconductores se emplean de manera muy común dada su buena resolución en energías, mejor eficiencia y menor energía necesaria para la creación de un par electrón-hueco. De esta clase de detectores, los más usados son los basados en silicio y germanio, a pesar de la limitación que supone la necesidad de refrigeración por nitrógeno líquido con el fin de reducir los niveles de ruido. Es por ello el interés creciente en detectores que puedan operar a temperatura ambiente como los fabricados a partir de cadmio zinc teluro (CZT) arseniuro de galio (GaAs) o fosfuro de indio (InP).

Tanto el CdTe como el CdZnTe son materiales de los que hace tiempo se conoce su gran potencial como componentes para detectores a temperatura ambiente de radiación X o gamma dadas sus propiedades optoelectrónicas. Su número atómico y elevada densidad les confiere una alta absorción y alta eficiencia a la hora de detectar fotones de alta energía. El elevado valor de su zanja de energía prohibida permite la fabricación de detectores con alta resistividad, una zona de carga espacial ancha y corrientes de fuga pequeñas. Un buen detector de CdTe/CdZnTe debe tener una alta resistividad ($>10^9$ Ω.cm) que reduce la corriente oscura y el nivel de ruido, y un mayor producto movilidad-tiempo de vida μτ, lo que asegura que los portadores pueden atravesar una mayor proporción de volumen y llegar a los electrodos. La combinación de estas propiedades convierte al CZT en un buen material para detectores de aplicación médica, de seguridad o astrofísica.

A pesar de sus bondades inherentes, el uso de materiales CZT viene limitado por algunos problemas importantes como la presencia de fases secundarias, impurezas, baja resistividad y calidad de la superficie. Cada uno de estos factores supone una reducción en el rendimiento del detector. Otro aspecto limitador del CdZnTe para su uso en detectores son las propiedades de los portadores de carga. El producto movilidad-tiempo de vida tanto para electrones como para huecos es bajo comparado con aquel del

Si y el Ge, limitando el rango espacial de movilidad de los portadores. En efecto, aparte de las propiedades limitadoras del CdZnTe, los procesos experimentales empleados en la fabricación de detectores suponen un obstáculo para la consecución de un material apropiado para aplicaciones de detección de radiación. Los métodos utilizados en la preparación superficial y la deposición de los contactos eléctricos juegan un papel crítico en la determinación de las propiedades de un detector de radiación.

Existen diversos métodos para el crecimiento de CdZnTe incluyendo el crecimiento en fase de vapor, a partir de disolución y a partir del fundido. Este último suele ser el más empleado dado su buen rendimiento a la hora de crecer cristales monocristalinos de gran tamaño. Dentro de estas técnicas de crecimiento a partir de fundido podemos distinguir: Vertical Gradient Freeze (VGF), Vertical Bridgman, Bridgman de alta presión y Travelling Heat Method (THM) como aquellas que se han empleado para la obtención de lingotes de CdTe/CdZnTe. Un adecuado control de los distintos parámetros involucrados en el crecimiento, como el material de partida, el ritmo de crecimiento y de enfriamiento es un aspecto fundamental a la hora de determinar la calidad final y las propiedades de los lingotes de CdZnTe.

El crecimiento de CdTe/CdZnTe en ausencia de un control de la presión conduce a la evaporación y consecuente pérdida de Cd, dado su alto valor de presión de vapor, resultando en un lingote rico en Te a pesar de que se partiera de una mezcla estequiometria. Los cristales no dopados de CdTe suelen ser de tipo p y baja resistividad, debido principalmente a la presencia de impurezas aceptoras no compensadas poco profundas. Para obtener cristales de CdTe/CZT de alta resistividad es necesario dopar al material con donores poco profundos como el Cl o el In.

El objetivo de esta tesis se ha centrado en el desarrollo de detectores de radiación gamma de alta eficiencia, basados en CdZnTe. El trabajo se estructura en cinco capítulos diferentes organizados de la siguiente manera:

El primer capítulo aborda los principios del crecimiento de cristales a partir de fundido y los procedimientos más comunes para el crecimiento de lingotes de CdZnTe. Las propiedades, defectos y aplicaciones del CdZnTe también aparecen detalladas.

El segundo capítulo describe los procedimientos y métodos experimentales utilizados en la presente tesis. Esto incluye i) la preparación del material de partida y las condiciones empleadas en el crecimiento de los cristales ii) el proceso completo de preparación

superficial incluyendo lapping, pulido mecánico y ataque químico, iii) métodos empleados en la preparación de los detectores y finalmente iv) las técnicas de caracterización más importantes de las que se ha hecho uso.

En el tercer capítulo se detallan las diferentes técnicas empleadas para caracterizar las muestras obtenidas a partir de los lingotes, cada uno de los cuales fue crecido a partir de diferentes condiciones, incluyendo superheating, enfriamiento y recocido. Esta investigación se centrará especialmente en la influencia de estos parámetros sobre el tamaño y distribución de las inclusiones de Te, defectos profundos y la homogeneidad de las propiedades ópticas y eléctricas de los detectores de CdZnTe.

En el cuarto capítulo se desarrolla el estudio sobre las condiciones de preparación de la superficie. La influencia del pulido, ataque químico y pasivación de bordes viene caracterizada en términos de rugosidad superficial, composición y corrientes de fuga. En este capítulo se detallan las mejores condiciones para el tratamiento superficial con el objetivo de mejorar la eficiencia de los detectores.

El quinto capítulo se centra en el efecto de la irradiación por haz de iones de argón y fuente láser Nd:YAG sobre las inclusiones de Te. Se presentan resultados del estudio de las propiedades ópticas y eléctricas mediante diferentes técnicas. De hecho, la posibilidad de mejorar el material de CdZnTe después de la irradiación ha quedado demostrada.

Table of contents

Chapter I: General aspects and applications of CdZnTe

Table of Contents

I.1. Introduction

CdTe and CdZnTe have long been known to have great potential in room-temperature X-ray and gamma ray semiconductor detector applications, mainly due to its attractive material properties. The crystal growth process plays an important role in determining the properties of a device. In fact, obtaining high quality single crystal materials requires control over a number of crystal growth parameters.

The use of CZT material is still limited by some deleterious defects such as the presence of secondary phases, Cd vacancies, dislocations, and trapping. Each of these factors causes degradation of detector performance.

This chapter concentrates on theories of crystal growth, properties and defects of CdZnTe semiconductors. To develop a deeper understanding of crystal growth, a description of phase diagram, parameters, methods of growth and principles will be presented in the first part. The focus of the second part will be on the properties of CdTe/CdZnTe, these properties are essential to be known for the fabrication of high quality detectors. In addition, the intrinsic and extrinsic defects associated with crystal growth will be discussed in the third section of this chapter. The chapter ends with a description of the most important applications of CdZnTe.

I.2. Properties of CdZnTe

In the following section, the crystallographic, electrical, thermal and mechanical properties of CdZnTe will be developed. The purpose of this section is to introduce the properties of CdZnTe which make this material suitable as a room temperature gamma ray detector.

I.2.1. Crystal structure

CdZnTe has Zinc-blende structure which can be regarded as CdTe lattice with a fraction of Cd substituted by Zn. This structure is considered as two interpenatring FCC sub-lattices, which one is occupied by Cd or Zn and the other by Te, as presented in **Figure 1**. In the lattice, every atom is surrounded by four hetero atoms and held by covalent bonds. This covalent nature of the bond between Cd and Te plays an important role in the properties of CdZnTe. The Cd-Te chemical bond shows a pretty high ionicity of 0.55 and is one of the highest in II-VI family of semiconductors (1).

CZT shows crystallographic polarity along the (111) direction. There are two types of (111) alternate planes, one formed by randomly distributed Cd and Zn atoms and the

other formed by Te atoms (2). The control of Zn concentration, *x* is crucial for obtaining a CZT alloy with the required lattice parameter. The Zn concentration *x* is governed by Vegards law which follows the lattice parameter and vary linearly. The concentration of zinc *x* can be calculated from the lattice constant relation given by (3)

Equation 1 $$a(x) = a_1(1 - x) + a_2 \cdot x$$

where a is the lattice constant. a_1=6.481Å and a_2=6.104Å are the lattice parameter for CdTe and ZnTe respectively (4).

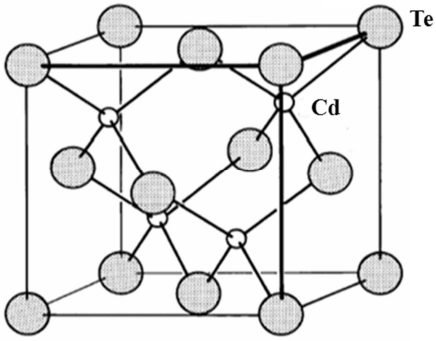

Figure 1: Zinc Blende Structure of CdZnTe

The zinc blende structure of CdZnTe is shared by other semiconductors including group (IV) Si, Ge, (III-VI) GaAs, GaP, and (II-VI) InP, HgCdTe. As we observe in **Figure 2** CdTe is a direct gap semiconductor and has the largest lattice parameter. Indead, introducing Zn in the lattice of CdTe increases the band gap and decreases the lattice.

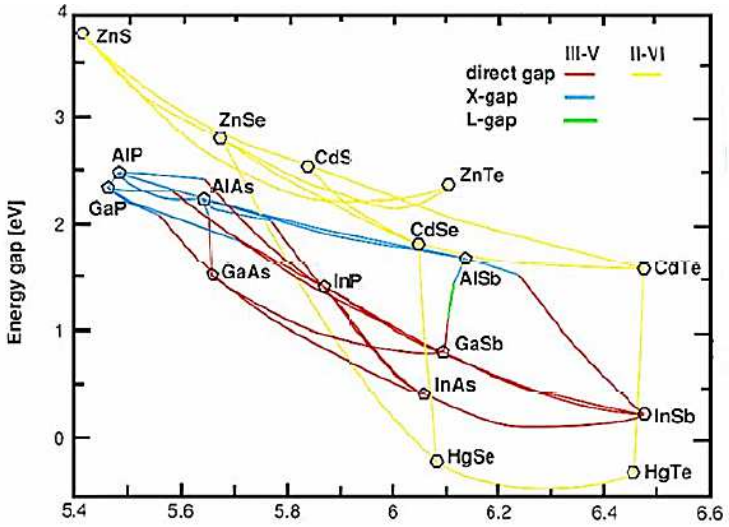

Figure 2: lattice parameter and band gap energy of semiconductors compounds

Some lattice constants of CZT with different zinc concentrations are shown in **Table 1** .

Table 1: Lattice constants of $Cd_{1-x}Zn_xTe$

Compound	Lattice Parameter(Å)
$Cd_{0.95}Zn_{0.05}Te$	6.462
$Cd_{0.9}Zn_{0.1}Te$	6.443
$Cd_{0.7}Zn_{0.3}Te$	6.364
$Cd_{0.5}Zn_{0.5}Te$	6.289

I.2.2. Crystallographic polarity

In CdZnTe, we must take into account the effects of crystallographic polarity. Crystallographic polarity is known to determining significant differences in the chemical behaviors of facets of many semiconductors. CZT has two types of (111) surface polarities, (111)A or (111)Cd and (111)B or (111)Te as shown in **Figure 3**, and hence there will be an electrostatic attraction between these different planes (5).

It has been demonstrated that the work function of CdZnTe (111)A is higher than that of (111)B surface, which should be ascribed to the polarity of CdZnTe (111) surface and the difference of the electronegativity between Cd and Te (6).

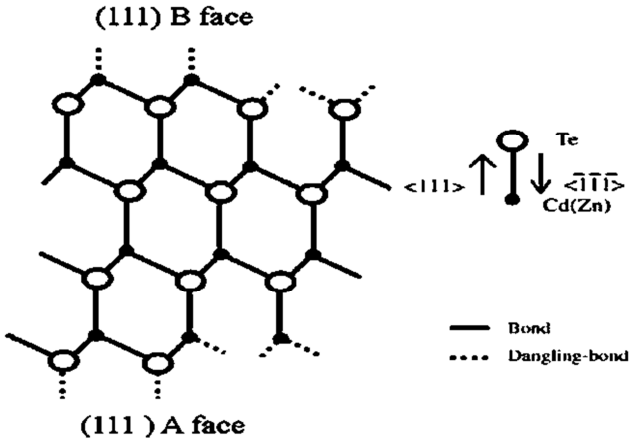

Figure 3: Atomic structure of CZT

Surface polarity of CZT could be determined using etching after lapping the surface of the samples**.** After etching we can observe a ´bright´ face which is related to the Te-face while the ´dark´ face is the Cd-face. Different etching solutions have been used to identify the crystallographic polarities (111)A and (111)B surfaces. G. Zha et al. (7) have chosen HNO_3 (10ml), H_2O (20ml), and $K_2Cr_2O_2$ (4g), while, P. Capper et al. have used $HF:HNO_3:CH_3COOH$ (1:1:1). W. Xiaoqin et al. (8) have identified the polarity with HNO_3:HF (1:1‑3:1). In **Figure 4** is presented a CZT sample after etching using $HF:HNO_3$ (1:1).

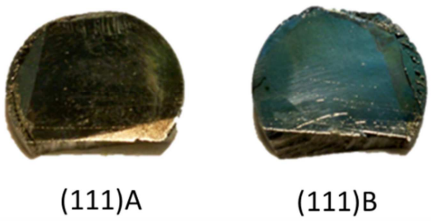

Figure 4: CZT sample after etching to determine the surface polarity

I.2.3. Role of zinc in CdZnTe

CdTe is now replaced by CdZnTe for most applications. The substitution of the element Zn in lattice locations of Cd results in the compound semiconductor $Cd_{1-x}Zn_xTe$, where *x* is the fraction of Zn. Zinc in CdTe increases the band gap, and thus resistivity, facilitating the fabrication of nuclear detectors with improved performance. Recently it was also shown that the addition of Zn increases the maximum solid solubility of Te and hence it is expected to increase the concentration of native defects (9). Zn also strengthens the lattice and leads to solution hardening that reduces the dislocation density in the crystals.

It is well known that the electron–hole pair creation energy increases by 2% by adding 10% Zn in CdTe, which clearly show the fact that any variation of Zn composition in the sample can affect the detector performance (10)

Due to the increased demand for large and thick detectors for homeland security applications, it is thus necessary to produce large CZT crystals with minimum compositional variation (10). In addition, the presence of Zinc makes the crystal growth more complex due to the shape of the ternary phase diagram (11).

I.2.4. Electrical properties

I.2.4.1. Band structure

The property which distinguishes semiconductors from other materials concerns the behaviour of their electrons, in particular the existence of gaps in their electronic excitation spectra, where electrons are forbidden to have a certain range of energies.

The properties of electrons inside semiconductors are described by the solution of Schrödinger equation under periodic potentials due to crystal periodicity. There are various approaches to solving this equation such as linear combination of atomic orbitals, pseudopotential method, k.p perturbation method and the orthogonalized plane wave method (12) (13).

Equation 2

$$\left[\frac{-h^2}{2m_0}\nabla^2 + U(r^2)\right]\Psi(r) = E\Psi(r)$$

Compound semiconductors are categorized to two types as direct and indirect transition materials. In direct transition materials, as shown in **Figure 5** electrons can be excited from the valence band to the conduction band without any phonon generation, while in indirect transition materials, electrons are recombined via holes with phonons interactions.

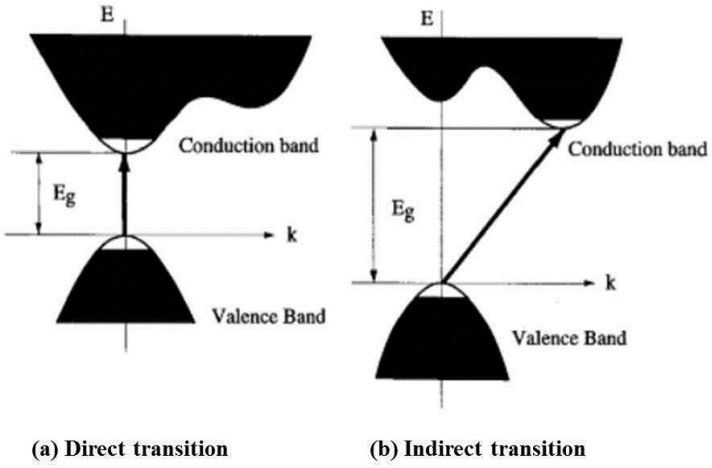

Figure 5: Direct and indirect transitions

I.2.4.2. Resistivity

The materials properties required for a good room temperature nuclear detector include high resistivity and long lifetime of charge carriers. ZnTe has a higher bandgap than CdTe so that alloying CdTe with Zn increases the bandgap and intrinsic resistivity of CZT from $10^{10}\Omega$.cm to over $10^{16}\Omega$.cm (14). By increasing the fraction of *x* from 0 to 0.2, there is an increase of almost two orders of magnitude in the resistivity as shown in **Table 2**. In fact, electrical resistivity is classically described using **Equation 3**.From this simple equation it may be observed how reducing the concentration of carriers has the effect of increasing the resistivity of the material.

Equation 3

$$\rho = \frac{1}{q(n\mu_n + p\mu_p)}$$

where q is the electric charge (1.6×10^{-19}C), n and p the carriers concentrations, and μ_n and μ_p are the electron and hole mobilities respectively.

Table 2: Resistivity of $Cd_{1-x}Zn_xTe$

Composition	Resistivity (Ω.cm)
CdTe	3.0×10^{9}
$Cd_{0.96}Zn_{0.04}Te$	2.5×10^{10}
$Cd_{0.8}Zn_{0.2}Te$	2.5×10^{11}

I.2.4.3. Charge transport properties

The charge transport properties determine the collection efficiency of free carriers induced by the incident high energy photons and the various sources of noise in the crystals. There are two aspects of the charge transport properties that are extremely important for room temperature semiconductor detector devices. The materials have to be semi-insulating and the concentration of residual electrically active defects has to be low to provide sufficiently high carrier mobility and lifetime.

The carrier mobility influences the device performance through frequency response in two ways. Firstly, at low electric fields the carrier velocity is proportional to the mobility such that higher mobility material produces higher frequency response as carriers take less time to travel through the device. Secondly, higher mobility devices have higher currents that charge capacitances more rapidly to produce a higher frequency response. The mobility-lifetime product is often used as a simple parameter to determine material quality. Mobility-lifetime ($\mu\tau$) values of charge carriers have traditionally been determined using the 'Hecht' method. For CZT, typical lifetimes might be 10^{-6}s for electrons and 0.5×10^{-7}s for holes. For CdTe, the hole lifetime is typically 2×10^{-6}s which is an order of magnitude larger than in CZT.

In fact, research considering the charge collection efficiency is necessary in order to properly analyze the characteristics of CZT detectors. The charge collection efficiency (CCE) is the ratio of the charge induced at the sensitive electrode (Q) and the charge produced due to the radiation interaction (Q_0). For a detector of thickness L in planar configuration, an approximated expression for CCE can be described by the Hecht equation (14):

Equation 4
$$CCE = \frac{Q(x)}{Q_0} = \frac{\lambda_e}{L}\left[1 - exp\left(\frac{L-x}{\lambda_e}\right)\right] + \frac{\lambda_h}{L}\left[1 - exp\left(\frac{x}{\lambda_h}\right)\right]$$

where x is the interaction depth, L is the thickness of the detector, λ_e and λ_h are the mean drift lengths for electrons and holes, respectively.

The factors which can affect the CCE of a radiation detector can be attributed to structural defects (grain boundaries, dislocations), point defects (vacancies or interstitials), second phase inclusions, or deep levels introduced by impurities in the crystal.

I.2.5. Thermal properties

Thermal properties play an important role and are useful for a better understanding of the crystal growth from the melt. It has been shown that thermal properties of the charge also will have a major influence on the interface shape and position (15).

The most important thermal properties are presented in **Table 3** (16) (17).

Table 3: Thermal properties of CdTe

Thermal properties	CdTe
Melting temperature (T_m) K	1365
Solid thermal conductivity (k) W/m K	1.5
Melt thermal conductivity (k) W/m K	3.0
Solid Specific heat (C_p) J/g K	0.16
Melt Specific heat (C_p) J/g K	0.187
Thermal expansivity (β_T) K^{-1}	5×10^{-4}
Melt kinematic viscosity (ν) m^2/s	4.16×10^{-7}
Heat of fusion (H) J/g	209.2

The exothermic behavior of CdTe synthesis is due to its heat of fusion, this value has been reported to be 209.2J/g and must be taken into account for a properly controlled and safe crystal growth process. The heat capacity or specific heat of CdTe plays an important role in the thermodynamics of the crystal growth process. The heat capacity for CdTe in a molten state is reported to be 0.187J/g.K while for the solid state the heat capacity is 0.16J/g.K, which means that heat capacity for the solid is nearly 20% lower than for the melt.

Another important parameter is the thermal conductivity, we observe from the table a difference value of thermal conductivity between the solid crystal and the melt, which can lead to unfavorable interface shape (15).

The melting temperature of CdTe is also fundamental for crystal growth process and it has been estimated to be 1092°C. It plays an important role to establish appropriate growth conditions such as crystal growth rate and thermal gradient.

In fact, the Prandtl number which is the ratio of the kinematic viscosity and thermal diffusivity should be taken into account in case of CdTe melt, and can be expressed as:

Equation 5

$$P_r = \frac{v}{\alpha}$$

where, v is the kinematic viscosity and α is the thermal diffusivity. Considering that the thermal diffusivity is thermal conductivity (k) divided by density (ρ) and specific heat capacity (C_p), the Prandtl number can alternatively be expressed as:

Equation 6

$$P_r = \frac{\rho C_p v}{k}$$

The consequence of low thermal conductivity and a high melt viscosity lead to a Prandtl number of approximately 0.4 for the CZT melt which is high with respect to other semiconductors such as Si (0.023), InP (0.015) and GaAs (0.068) (18). This behavior results from a liquid phase that is semiconducting, rather than metallic, as are the melts of more common electronic materials (19). This means that the heat flow in the melt is more dependent on convection rather than conduction, so the conditions affecting interface shape are a balance among latent heat, conduction in the solid, and convection in the melt (20).

I.2.6. Mechanical properties

Thermal and mechanical stresses play an important role in the formation of dislocations during the directional solidification of CdTe. To avoid the formation of these defects and improve the crystalline quality, it is necessary to know the mechanical properties of CdTe.

The elastic constants are important parameters that describe the response to an applied macroscopic stress. In **Table 4** are summarized Elastic constants, bulk modulus, and shear modulus for CdTe, $Cd_{1-x}Zn_xTe$, and $Cd_{0.9}Zn_{0.1}Te$ (21). The residual stresses in the crystals are closely related to their microstructure and seriously influence the physical properties of CdZnTe single crystals (22). D. Zeng et al. have applied X-ray diffraction to measure the stress and strain in single crystal near the surface.

The residual stresses in CdZnTe single crystal were determined to be σ_1=30MPa, σ_2=14MPa, and τ_{12}=-4MPa, respectively, where σ_1 and σ_2 are axial stresses and τ_{12} is the shearing stress. The act of incorporating zinc into the CdTe structure strengthens the crystal lattice; this effect is due to the Zn-Te ionicity being lower than the Cd-Te ionicity, which increase the stability of the material and consequently increase the shear

modulus. In addition, the Zn-Te bond length is shorter than the Cd-Te, which leads to increase the hardness.

Z. Zhang et al. (23) have demonstrated that (111) $Cd_{0.96}Zn_{0.04}Te$ has higher hardness than (100), which is attributed to the fact of that (111) face has more atoms than the (110) face.

Table 4: Elastic constants (C_{11}, C_{12} and C_{44}), bulk modulus (Bs) and shear modulus (Cs) for CdTe, $Cd_{1-x}Zn_xTe$, and $Cd_{0.9}Zn_{0.1}Te$

Mechanical properties (10^{10} N m^{-2})	**CdTe**	**$Cd_{0.9}Zn_{0.1}Te$**
Elastic constant C_{11}	7.34	7.5589
Elastic constant C_{12}	3.68	3.2322
Elastic constant C_{44}	2.74	3.058
bulk modulus Bs	4.9	4.6732
shear modulus Cs	1.83	2.1514

I.3. Important parameters of crystal growth

Crystal growth is an interdisciplinary subject covering physics, chemistry, material science, chemical engineering, metallurgy, crystallography, mineralogy, etc. There has been an interest on crystal growth processes, particularly in view of the increasing demand of high quality semiconductors for technological applications.

Fundamental aspects of crystal growth had been established from early crystallization experiments by Elwell and Scheel in the 18th and the 19th century. Theoretical understanding started with the development of thermodynamics in the late 19th century by Gibbs, Arrhenius and Van't Hoff, and with the development of nucleation and crystal growth theories and the increasing understanding of the role of transport phenomena in the 20th century (24).

Growth is treated both under thermodynamic and kinetic control. Thermodynamics is a basic practical knowledge for the crystal grower. It helps to determine the most effective phase transitions, growth method, and the driving force of crystallization. The nucleation and existence conditions of a given crystalline phase and the optimization of the crystal composition during growth could be estimated by the principles of thermodynamics (24). Kinetics are of practical importance because they govern the change in growth rate which occurs when the growth conditions change, and because they affect the manner in which impurities are incorporated (25).

I.3.1. Phase diagram

The phase diagram of a given semiconductor, and in this case the phase diagram of CdZnTe, is a representation of the chemical equilibrium between the components in the system. More specifically, the phase diagram describes the interdependence of the composition (x), pressure (P) and temperature (T) for any ´x´, ´P´ and ´T´ of a system. It is necessary to have precise knowledge of the solid, liquid and gas existence regions with respect to temperature ´T´, pressure ´P´ and composition ´x´ to work with this material, especially to understand crystal growth. The work carried out by J.H .Greenberg gives accurate data for such stoichiometric calculations (26) (27) (28). Below are summarized some of the more interesting results from this study.

From the T-x projection shown in **Figure 6**, for $Cd_{0.9}Zn_{0.1}Te$ alloys, also adapted from (28), it can be observed that CdZnTe melt-solidification does not occur under congruent conditions. In fact, the liquidus line displays a hyperbolic shape near the congruent melting point. Some useful information obtained from this T-x diagram is that the maximum deviation from stoichiometry occurs on the Te-rich side of the solidus liquidus, with a maximum solid solubility of Tellurium at $4\times10^{18}cm^{-3}$ (0.04-0.05 at % Te) at approximately 860ºC.

A very important consequence of this retrograde solubility is that Te precipitation (to be discussed later) occurs at temperatures below the melting point of CZT, and therefore must be taken into consideration for a well-controlled crystal growth process.

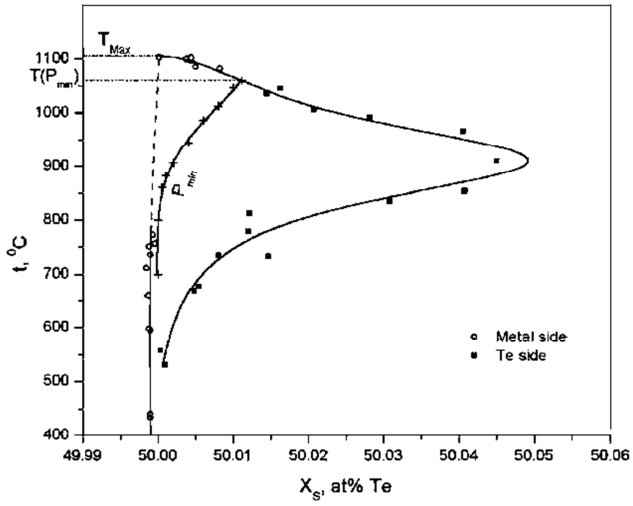

Figure 6: T-x phase diagram for $Cd_{0.9}Zn_{0.1}Te$

From the P-T projection shown in **Figure 7**, it can be seen that with increasing the Te content, the Cd overpressure decreases by approximately one order of magnitude, while the Te_2 overpressure increases by nearly double. Solid solution is in equilibrium with a

predominantly Te vapour, important information concerning the temperature dependence of the partial pressure for a given composition of the melt is presented. This information is useful not only for improving crystal growth technologies and methodologies (Crystal composition can be preserved during the cooling stage by means of a programmed control of the vapour pressure), but from these results evaporation thermodynamics for a given melt composition can be predicted.

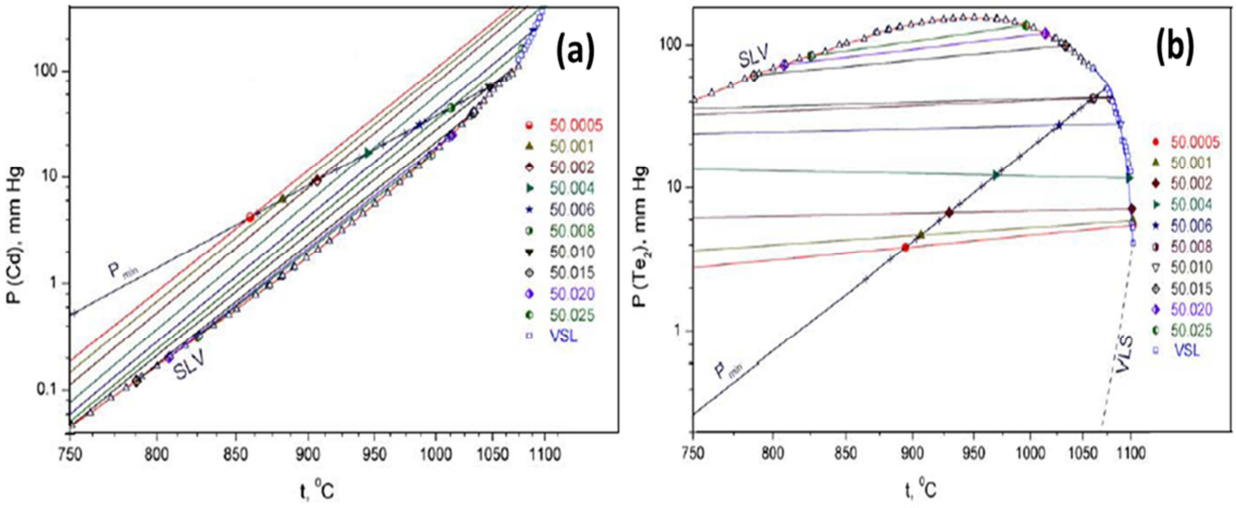

Figure 7: P-T phase diagram of $Cd_{0.9}Zn_{0.1}Te$ for (a) Cd and (b) Te_2 species (29)

Finally, from the P-x phase diagram shown in **Figure 8**, the vapour pressure of the elements for the ternary Cd-Zn-Te alloy is presented at fixed temperatures. These results provide important information regarding the relationship between Cd, Zn, and Te vapours in equilibrium for a given temperature. It is important to note that for Te-rich melts, the vapor pressure is dominated by Te-species, while under Cd-rich melts, the vapor pressure is dominated by Cd species. The minimum system pressure is realized under slightly Te-rich conditions.

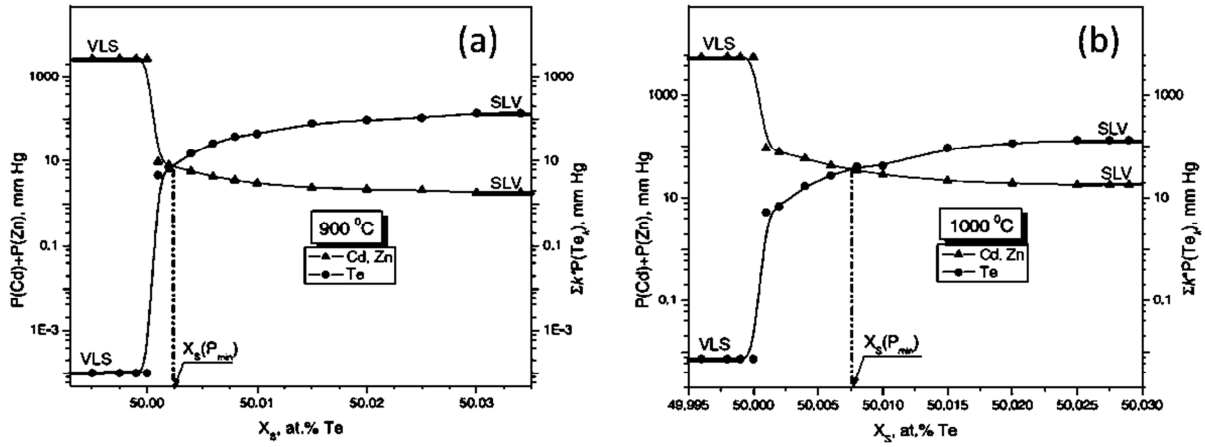

Figure 8: The P-x diagram for $Cd_{0.9}Zn_{0.1}Te$ at (a) 900ºC and (b) 1000ºC

In summary, the phase diagrams for $Cd_{0.9}Zn_{0.1}Te$ provides very important information not only for understanding the crystal growth and the defect formation, but also for establishing safe experimental conditions for a successful and reproducible crystal growth process.

I.3.2. Axial temperature gradient

The axial temperature gradient must be controlled with precision in the case of CdTe/CdZnTe, due to its low thermal conductivity (1.5-3W/m K) and generally, the semiconductor crystal growth from the melt is performed under conditions of low temperature gradients with the goal of minimizing the mechanical stress and the generation of macroscopic defects such as cracks and dislocations.

In fact, there have been shown considerable improvements in structural perfection of the CdTe crystals with densities of dislocations of the order of $10^4 cm^{-2}$, using low temperature gradients (30).

Before the selection of the axial temperature gradient for growth of CdTe/CdZnTe crystals, the following considerations should be taken into account:

- A superheating of the melt by more than 10K is recommended for a controlled growth (see section **I.3.4**).
- Due to the higher thermal conductivity of liquid phase (3W/m.K) than that of the solid phase (1.5W/m.K), the temperature gradient in the melt should be lower in order to maintain a steady state heat flow through the crystallization front. Therefore, lower is the gradient temperature, more stable will be the heat balance during growth. It has shown that the optimum ratio G_L/G_S of temperature gradients in liquid G_L and solid G_s, for maintaining a flat crystallization front in CdTe this ratio is about 0.3 (31). In this case, if we use a temperature gradient of 10K/cm during crystallization, a temperature gradient of 3K/cm will be required in the liquid phase.
- To reduce the thermo-mechanical stress, it is better to choose a temperature gradient approximately constant after growth.

In the case of CdTe where the thermal conductivity in the melt phase is clearly higher than that in the solid phase, a lower temperature gradient in the liquid will lead in a temperature distribution as shown in **Equation 7** (31):

Equation 7
$$\boldsymbol{T(z) = T_c + 0.5(T_h - T_c)\left[tanh\left(\frac{G_t}{0.5(T_h - T_c)}\right) z_t + 1\right]}$$

Where, T_c is the temperature of the cold zone, T_h is the temperature of the hot zone, z is the axial position, G_t is the value gradient in the point z_t. The distribution of the axial temperature gradient can be obtained by differentiation of **Equation 7**, and it will be equivalent to:

Equation 8
$$\frac{dT}{dz}(z) = G_t cosh^2\left[\frac{2G_t}{(T_h - T_c)}(z - z_t)\right]$$

The second differentiation is essential to evaluate the thermo-mechanical stress and is presented as:

Equation 9
$$\frac{d^2T}{dz^2}(z) = -4\frac{G_t^2}{(T_h - T_c)} tanh\left[\frac{2G_t}{(T_h - T_c)}(z - z_t)\right] cosh^{-2}\left[\frac{2G_t}{(T_h - T_c)}(z - z_t)\right]$$

I.3.3. Growth rate

The growth velocity is a basic parameter to take into account during crystal growth of CdZnTe crystals. The value of growth rate is determined by the heat and mass balance at the solid-liquid interface, as well as by the kinetics of growth. The progress of the solidification is the function of the heat flow at the solid-liquid interface and defined as:

Equation 10
$$\rho_s \Delta H \nu = \Phi_s - \Phi_l$$

where Φ_s and Φ_l are the heat flux in the solid and the liquid, ρ_s is the density of the solid phse, ΔH is the latent heat and ν is the growth rate. In the approximation that heat is primarily transported by thermal conduction at the solid-liquid interface, the heat balance equation simplifies to:

Equation 11
$$\rho_s \Delta H \nu = \lambda_s G_s - \lambda_l G_l$$

where λ_s and λ_l are the thermal conductivity and G_s and G_l are the temperature gradients of the solid and liquid phases, respectively. The above equation shows that the solid has to transport the heat from the melt and the heat released during solidification (the solidification of CdZnTe being an exothermic reaction).

Considering that $G_{s,l} = (dT/dz)^{s,l}$ the approximation of the growth rate is given as:

Equation 12
$$\nu \leq \frac{1}{\rho_s \Delta H}\left(\lambda_s \frac{dT^s}{dz} - \lambda_l \frac{dT^l}{dz}\right)$$

One can observe that the growth rate is a very sensitive function of G_l, since from the relation λ_s / λ_l, is less than unity (0.5) for CdTe. The growth rate decreases with increasing G_l. For a G_s value of about 10 K/cm, a value of G_l of 3K/cm is required in order to achieve a growth rate of about 1 mm/h.

I.3.4. Superheating of CdZnTe

The ionic character of the Cd-Te chemical bond makes CdTe melts highly associated close to the melting point as shown in **Table 5**, resulting in the presence of extremely organized particles affecting nucleation process, growth kinetics and also favourable to the formation of Te clusters (24). Therefore large superheating ΔT^{+} (ΔT^{+}= $T-T_m$) is necessary to destroy this associated melt complexes (32) (33), where T is the maximum melt temperature before the crystal growth and T_m is the melting point.

Table 5: Selected material properties of CdTe in comparison with GaAs and Si

Parameter (Units)	CdTe	GaAs	Si
Melting point (°C)	1092	1238	1410
Ionicity f_i (%)	70	25-30	0
Degree of dissociation β (%)	5	90	-

The quality of the as grown CZT crystal is related to the temperature of the mother phase before the growth process start (34). In fact, P. Rudolph et al demonstrated that slight superheating temperature affect the crystal growth by generating subgrains and twins, while after marked superheating temperature these defects disappear. Therefore, the crystal growth process could be improved by using a defined superheating and holding time before the crystallization. **Figure 9** shows some results adapted by P. Rudolph illustrating experimental results for the effect of superheating and supercooling of the melt of CdTe. As shown in this figure, for small values of superheating (< 9K) no supercooling can be observed in a stoichiometric CdTe melt, while for values higher than about 9-l0K cause a distinct supercooling of up to 30K. The high degree of association resulting at small superheating temperatures (< 9K) is assumed to reduce the nucleation energy and the result is a reduced supercooling.

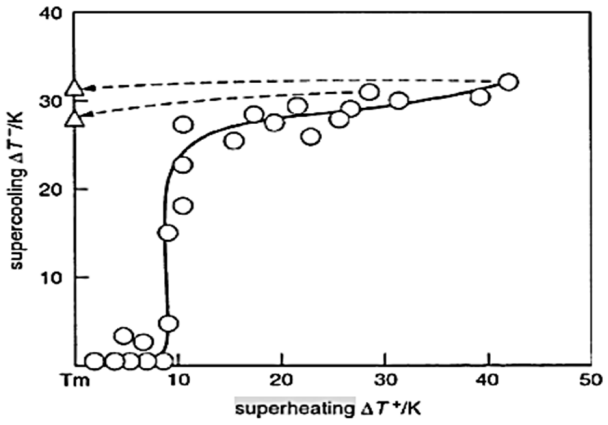

Figure 9: The effect of superheating and supercooling of the melt of CdTe (31)

The influence on the crystalline quality of the tip region is shown in **Figure 10**. Taking a stoichiometric composition, a large extended polycrystalline region can be observed if a superheating of > 9-10K is used. After this breakdown, a single crystal or a crystal with only 1 or 2 grain boundaries is normally grown. Contrary to this situation, in the case of a small superheating of about < 9-10K, initial monocrystalline growth is very often observed. However, a higher number of grain boundaries and twins originate during the further part of the growth.

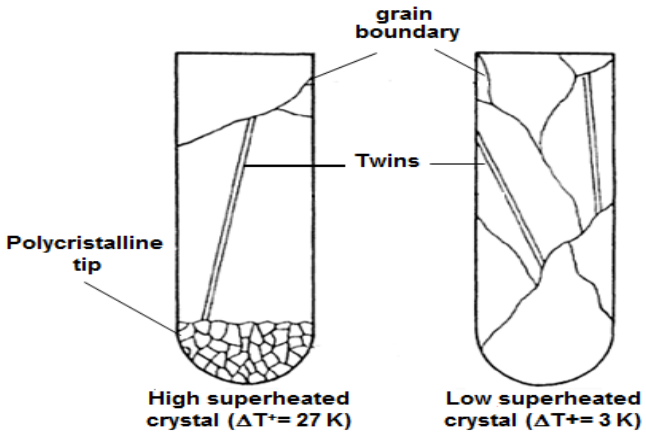

Figure 10: Structural consequences of the superheating on the structural quality in first-to-freeze regions of CdTe crystals

I.3.5. Constitutional supercooling

The growth at the solid-liquid interface is not only determined by the heat balance and kinetic processes but it is also necessary to consider the transport of matter in the case of non-stoichiometric, doped melts and also alloy systems (31). The transport of these components in the front of crystallization leads to the destabilization of the growth interface with increasing the growth rate or decreasing the temperature gradient in the melt. Morphological stability and its relationship to constitutional supercooling was studied by Tiller et al. and they deduced theoretically the condition for the prevention of constitutional supercooling as:

Equation 13

$$\frac{G}{v} \geq \frac{mC_0(1-k)}{Dk}$$

where *G* is the temperature gradient in the melt at the interface, *v* is the solidification front velocity, m is the slope of the liquidus line from the T-x phase diagram projection, C_0 is the initial concentration of excess (mixing or doping) component, D is the overall diffusion coefficient in the melt and k is the segregation coefficient.

The general compositional supercooling criterion shows that the ratio of temperature gradient on the liquid phase to the interface velocity, *G/v*, must be larger than a critical value in order to maintain a stable plane front.

The constitutional supercooling can occur when a gradient of chemical composition exceeds a critical value at the solid-liquid interface during solidification of a compound, and is increased by conditions of low thermal gradient and high growth rate.

The constitutional supercooling can influence the growth and causes the instability of the growth interface which is the leading hypothesis to explain the formation of Te inclusions. It has been found that the quality of the grown material could be improved via mixing processes which can delay the onset of the constitutional supercooling (35).

Cockayne at al. attributed the formation of voids and bubbles to the constitutional supercooling combined with the segregation of dopant impurities and basic constituents (36). In fact, careful control of the interface shape, low-temperature gradients, and suppression of constitutional supercooling can lead to subgrain-free material (35).

I.3.6. Control of stoichiometry

The control of stoichiometry is the prime criterion for managing the development of defect formation during crystallization. In order to achieve a stoichiometric CZT crystal, a control of the starting charge is paramount.

Due to the difficulties with weighing Cd, this material was weighed first with some idea of the approximate quantity necessary for a boule with a given mass. In addition to the stoichiometric quantity required, an excess of cadmium was used to compensate for material loss arising from its equilibrium overpressure of Cd at high temperature. This excess was calculated using **Equation 14**, where *P* is the system pressure measured in Pascals, *V* is the volume of the ampoule measured in m^3, $n_{Cd,gp}$ is the number of moles of Cd in the gas phase, *R* is the ideal gas constant, and *T* is the system temperature measured in Kelvin. The total system pressure was approximated by using experimental data at 1273K reported in (28). The ampoule volume could be calculated from its geometry.

Equation 14
$$P_{Cd} \cdot V_{ampoule} = n_{Cd,gp} \cdot R \cdot T$$

From this equation, the quantity of material that will exist in the vapor phase can be calculated. This weight is then subtracted from the total weight of Cd which has been measured. This subtraction is a result of the Cd existing in the gas phase, and therefore is not a component of the melt. In order to calculate the required quantity of tellurium, this new quantity is used to obtain a perfectly stoichiometric charge, described by **Equation 15**, where n_{Te} represents the moles of Tellurium required for a perfectly stoichiometric charge.

Equation 15 $$(\boldsymbol{n_{Cd\,total} - n_{Cd,gp}}) + \boldsymbol{n_{Zn}} = \boldsymbol{n_{Te}}$$

The stoichiometry of the CdZnTe charge was chosen to be slightly tellurium rich in order to minimize system pressure, following experimental results produced by Greenberg (28). The stoichiometry which minimized pressure within the ampoule at high temperature (1273K) was Te:50.007. Therefore, from the stoichiometric point, the required quantity of Te could be calculated using **Equation 16**.

Equation 16 $$\boldsymbol{n_{Te}} = (\boldsymbol{n_{Cd}} + \boldsymbol{n_{Zn}}) \cdot \frac{\mathbf{50.007}}{\mathbf{50}}$$

I.3.7. Segregation and non-uniformity in CZT ingots

In addition to the CdZnTe growth problems, the segregation of Zn and dopants during the growth process is another issue. Because of the inherent nature of the growth process and non-unity segregation coefficient of Zn (k=1.35) (37), it is difficult to produce CdZnTe crystals with compositional homogeneity.

The segregation coefficient of Zn during the crystal growth of the CZT ingots can be extracted using the following Pfann equation (38):

Equation 17 $$\boldsymbol{C_s = C_0 . k(1-g)^{k-1}}$$

where *k* is the segregation coefficient, *g* is the solidified fraction of the ingot, C_0 is the initial Zn concentration, and C_s is the Zn concentration at the solid/liquid interface during growth, which is approximately equivalent to the Zn concentration in the as-grown ingot. **Figure 11** shows the axial Zn distribution profile of a CdZnTe crystal grown using VGF method. The zinc concentrations were determined by ICP technique. The Zn segregation coefficient has been calculated to be k=1.37 using **Equation 17**.

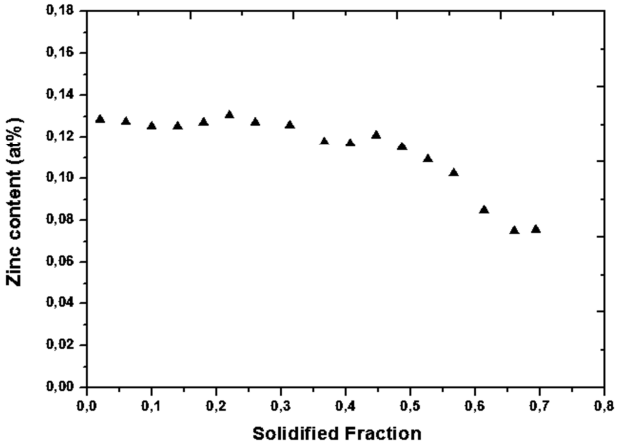

Figure 11: Axial Zinc distribution in CdZnTe ingot

Some success in reducing zinc segregation along the growth axis has been achieved by controlling the partial pressures of Cd and Zn in the growth atmosphere (37) or by placing a solid source in contact with the melt (39).

In crystal growth, it is necessary to dope with impurities to control the conductivity type and the resistivity of the crystals growth. When impurities are doped in the melt and crystal is grown, the segregation occurs. For example, the segregation coefficient can be either smaller than one (In=0.07, Cu=0.05, Ag=0.05, Bi=0.02 and Na=0.001) or larger than one (Al= 3.6) depending on the chemical species (40). Most of the impurities tend to segregate toward the heel, causing the impurity content to be relatively high in the last-to-freeze position of the ingot as shown in **Figure 12**, in the case of CdZnTe ingot doped with 3ppm indium.

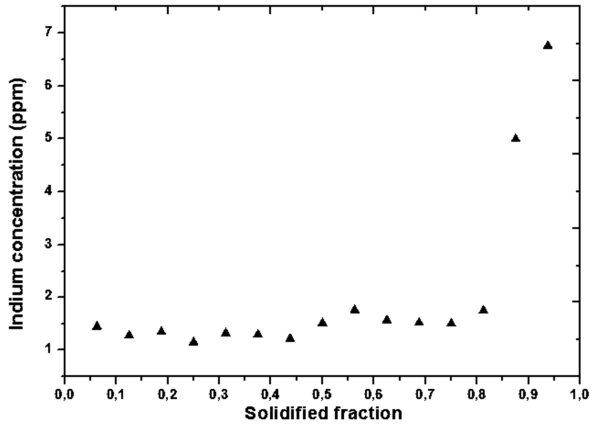

Figure 12: Indium distribution in CdZnTe ingot

In consequence, the production of uniform materials along the whole ingot is difficult and only a limited portion of the ingot can be used as a radiation detector.

The non-uniformity has been demonstrated by preparing samples from different positions (Bottom, middle and top) of a CZT ingot. These samples have been characterized with PL at 4K in order to compare the uniformity and distribution of defects and impurities along the ingot. **Figure 13** exhibits the PL spectra of the bottom, middle and top of the ingot. For all positions, we observe a donor-bound (D^0,X) and an acceptor-bound-exciton (A^0,X) around 1.657 and 1.646eV respectively. Also, a donor–acceptor pair (DAP) recombination band is apparent at 1.603eV followed by two distinct LO phonon (21 meV separation) replicas. The A-center peak reflecting the complex of Cd vacancies and compensating dopant is visible at 1.469eV.

As can be seen, the intensity of (D^0,X) and (A^0,X) in the bottom and middle of the ingot is higher, indicating more compensation and recombination between Cd vacancies and donors. The intensity of A-center peak in the top of the ingot is distinctly stronger that the others positions, which indicates that the Cd vacancies (V_{Cd}) are not compensated by metal donors (In) which could be related to the high content of indium in the top of the ingot as shown in **Figure 12**. The donor-acceptor pair (DAP) of the top is stronger than that of the bottom and middle of the ingot. It seems that the donor impurity concentrations are increased from bottom to top by segregation phenomenon (41).

We also observe the free-exciton (FX) peak for the bottom and middle positions at 1.662eV. The existence of FX peak indicates crystallinity improvement in CZT crystal.

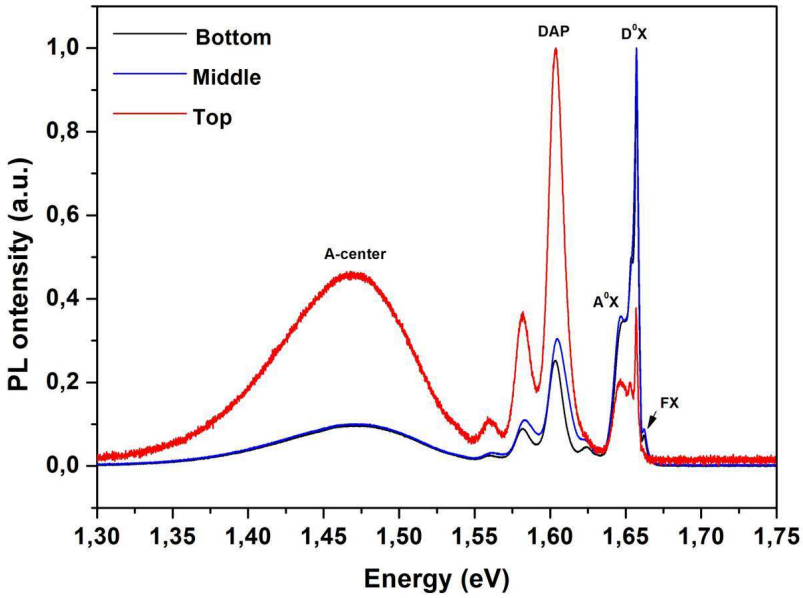

Figure 13: PL spectra from the bottom, middle and top of CZT ingot at 4K

From these results we conclude that the top part of CZT ingot contain more defects and impurities such as Cd vacancies which can increase the leakage current and then affect the detector performance.

The radioactive source ^{133}Ba has been used for comparing the performance of the detectors achieved from two different positions (Bottom and top) of the same ingot. **Figure 14** exhibits the gamma spectroscopy of these two samples. By comparison, we can observe that the performance of the detector obtained from the bottom part of the ingot is better than the one obtained from the top part of the ingot, the FWHM values are 10.1 and 20.8% respectively.

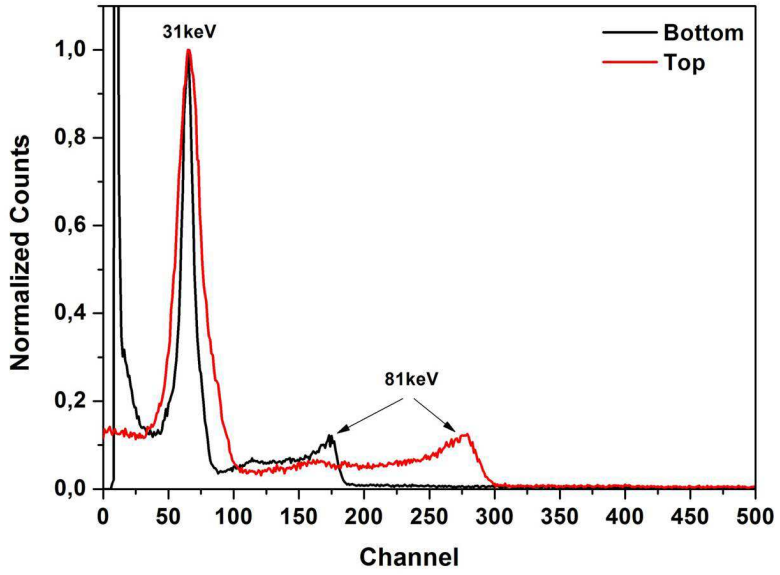

Figure 14: Gamma response with ^{133}Ba source of the detectors harvested from the bottom and top part of the ingot

We can conclude that the results of the gamma spectroscopy measurements are consistent with PL results. In fact, we observe that the ingot produce non-uniform samples, the first-to-freeze region acquire the best detectors, the performance of the detectors gradually deteriorate from bottom to the top of the ingot.

I.4. Crystal growth methods

For CdZnTe, melt growth methods are the main methods of industrial manufacture. This is because they are appropriate to grow large single crystals quickly compared to solution and vapour growth methods.

CdTe and CdZnTe have been successfully grown using a variety of methods, including Traveling Heater method (THM), Vertical Bridgman (VB), Vertical Gradient Freeze (VGF). Numerous variations of each method have been reported.

I.4.1. Vertical Bridgman (VB)

The Bridgman technique is a method of growing single crystal ingots. It is a popular method of producing certain semiconductor crystals, such as gallium arsenide, and II-V Crystals (ZnSe, CdS, CdTe) and BGO, where the Czochralski process is more difficult.

Bridgman growth has been used since the earliest days of CdTe development and still used by the major world suppliers of substrate quality material.

In Bridgman growth technique, an ampoule containing a polycrystalline material is introduced into a gradient furnace. After the melting, growth is initiated by an imposed displacement of the crucible**.** During the Bridgman process, the ampoule is moved from an isothermal hot zone where the molten semiconductor is melted, through an adiabatic or thermal-gradient zone where the molten semiconductor solidifies, and then into a cold zone where the crystal is cooled. The process can be carried out in a horizontal or vertical geometry.

The orientation of the crystal during Bridgman growth can be selected by using a seed crystal with the desired orientation at the cold end of the crucible. During the initial melting of the charge material, a small portion of the seed is also melted to allow for better adhesion between the seed and the melt.

Bridgman furnaces with different configurations have been reported. High pressure Bridgman is the most commonly used method for commercial production of CZT, where the material is typically grown under Te-rich conditions (45). This method employs an Ar over-pressure between 100-120atm (46) (47) (48) or higher. Accelerated crucible rotation technique (ACRT) facilities are also used in order to homogenize the melt composition (49) (50) (51) (52).

I.4.2. Vertical Gradient Freeze (VGF)

The Vertical Gradient Freeze method (VGF) was first applied for the growth of GaAs by Chang et al. in a pyrolytic boron nitride crucible without seed crystals (42).

The VGF method is analogous to the Bridgman method except for the fact that the temperature gradient is translated along the melt to implement directional solidification.

In the BR method, it is difficult to achieve long term stability at the growth interface due to the fact that the charge and the furnace move relatively to each other. As a result, the radiative heat transport is continuously modified for the same thermal gradient, leading to process non-uniformities. This effect is eliminated in VGF where the heat

transport can be stabilized, and the translation of temperature is done by temperature programming in a multizone furnace (43).

In the VGF method, several heaters are used to create a temperature profile across the ampoule. While the ampoule and the heaters are fixed, the temperature profile is gradually lowered, moving the Solid Liquid Interface (SLI) upwards across the charge (44). As we observe in **Equation 18,** thermal stresses can be generated due to temperature gradients and can introduce some defects in CZT such as cracks.

Equation 18 $$\sigma = E\alpha L^2\left(\frac{d^2T}{dz^2}\right)$$

Where, α is the coefficient of thermal expansion, E is the Young's modulus, L is the characteristic length, T is the temperature and z is the position.

For this reason, to minimize thermal stress, very small axial temperature gradients are needed.

The process can be carried out in a horizontal or vertical geometry. The source material is at the fixed position without movement, while the temperature is gradually lowered so that the growth rate changes as a function of temperature. Generally, the growth rate becomes faster when the temperature becomes lower. Therefore, stable crystal growth becomes difficult as the crystal growth proceeds. In order to prevent this growth rate change, the temperature distribution in the furnace must be precisely controlled.

VGF involves the progressive freezing of the lower end of a melt upwards. This freezing process can be controlled by moving the temperature gradient in a furnace with several independently controlled zones. Low temperature gradients are normally obtained, leading to reduced dislocations densities, and the crystal is of a defined shape and size. Difficulties include furnace design, the choice of boat material, and the issue of seeding.

I.4.3. Traveling Heater method (THM)

The THM technique was developed for II-VI and III-V compounds, which cannot be grown adequately by standard melt growth technique.

The THM approach translates the applied thermal profile by moving the heater relative to the growth ampoule. The displacement of the liquid zone leads to the dissolution of the charge at the top liquid to solid interface, while simultaneously leading to the deposition of CdTe compound at the bottom interface.

The advantage of the THM is to grow at low temperature compared with Bridgman and VGF method which result in low contamination and vapour pressure (53).The melting temperature can be decreased drastically by increasing the Te fraction, and with 80% Te, melting occurs at 800°C (54). The same thing can be done for Cd but with more technical difficulties such as pressure and solubility. Tellurium as a solvent is a better choice and the Te molten zone crosses trough a CdTe ingot. THM has been known to grow uniform CdTe single crystals. It had been thought that large single crystals suitable for commercial applications could not be grown by THM, while ACRORAD was manufacturing 50mm diameter CdTe single crystals in 1999 and creating radiation detectors which were commercially available. The effect of the THM growth rate on the crystalline quality and the detector performance has been investigated by H.Shiraki et al. (55).

I.5. Defects in CdZnTe

The spectroscopic performance of cadmium zinc telluride (CZT) room temperature radiation detectors is currently limited by both bulk and surface imperfections introduced during the growth, harvesting and fabrication of these devices. Bulk imperfections including impurities, vacancies, interstitials, grain boundaries and dislocations have been relatively well studied and are known to trap charge and reduce detector performance. However, the effect of specific traps on the electronic decay process has been difficult to quantify. Surface imperfections including mechanical damage or adsorbed chemical species are also known to trap charge and increase leakage current.

Strong knowledge about the origin and formation of these defects is required in order to improve crystal growth and the quality of CZT detectors.

A summary of the most common defects associated with the growth process, cutting and surface treatment will be detailed in this chapter.

Crystal lattice defects are usually classified according to their dimension as follows:

- Zero-dimensional defects are point defects, which include vacancies, interstitials, antisites, and impurities.
- One-dimensional defects include all types of dislocations such as screw and edge dislocations.
- Two-dimensional defects are grain boundaries, stacking faults, and twins.
- Three-dimensional defects include secondary phases and voids.

I.5.1. Point defects

Point defects have always been of principal significance materials research and technology. The understanding of native defects and their complexes is essential to the successful application of semiconductors. They are responsible for compensation, doping, minority carrier lifetimes, luminescence efficiency, and a number of other properties. The defects assist the diffusion mechanism, which affect crystal growth, and then degrade the detectors performance. Point defects can be grouped in:

- Intrinsic point defects which include vacancies, interstitials and antisites.
- Extrinsic point defects or impurities which do not belong to the lattice, they usually act as dopants.

Vacancies are point defects due to the absence of atoms at the lattice site, while interstitials are atoms which are located at the interstitial site deviated from the proper lattice site. Antisite defects are atoms which are located at the lattice site for another constituent atom. Because CdTe is a binary compound, two versions of each vacancy, interstitial, and antisite defects are possible, one involving the Cd atom and one involving the Te atom. In total, there are six elemental intrinsic point defects as shown in **Figure 15**.

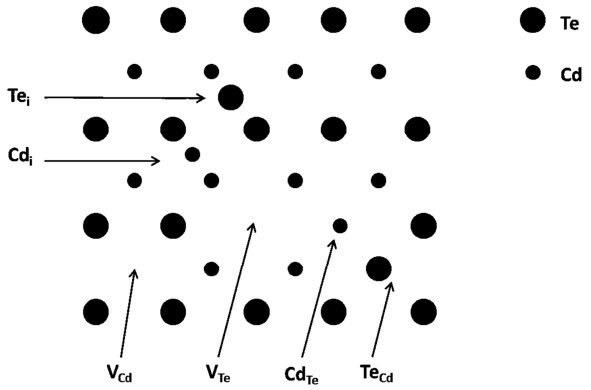

Figure 15: Schematic diagram for various point defects in CdZnTe

Table 6: Native defects and nomenclature

Native defects	Nomenclature
Vacancy of Cd	V_{Cd}
Vacancy of Te	V_{Te}
Cd interstitial	Cd_i
Te interstitial	Te_i
Cd Antisite	Cd_{Te}
Te Antisite	Te_{Cd}

Point defects increase the configurational entropy, leading to a decrease in free energy. Thus, such native point defects are always presented in as-grown crystals and their concentration can be influenced by the growth conditions (56). **Table 7** shows an approximate values of the first ionization energy, Second ionization energy, and formation energy of native point defects in CdZnTe (57) (58) (56) (59).

Table 7: First ionization energy, Second ionization energy, reaction energy, entropy, and formation energy of native point defects in CdZnTe

Defects	Cd_i	V_{Cd}	V_{Te}	Te_{Cd}	Te_i
First ionisation energy (eV)	0	0.38	0.4	0	0.1
Second ionization energy (eV)	0.54	0.76	0.5	0.4	0.6/0.7
Formation energy E_f (eV)	0.96	3.55	-	2.29	1.97

In real crystal, some point defects are predominant over others depending on the difference of the formation energies of these point defects.

V_{Cd} are one of the most important point defects in CdZnTe which can give two acceptors levels, V_{Cd}^{-} and V_{Cd}^{2-}, localized in the forbidden gap, following the reactions:

$$\mathbf{V_{Cd} + e^- \rightarrow V_{Cd}^-}$$

$$\mathbf{V_{Cd}^- + e^- \rightarrow V_{Cd}^{2-}}$$

The vacancy concentration must be low enough that deep level defects successfully compensate the material to yield a resistivity $>10^9 \Omega$.cm. In a like manner, Cd interstitial creates two donors levels:

$$\mathbf{Cd_i \rightarrow Cd_i^+ + e^-}$$

$$\mathbf{Cd_i^+ \rightarrow Cd_i^{2+} + e^-}$$

Te antisite defects are formed by Te occupying a Cd position in the lattice. This defect influences strongly the electrical properties of CdZnTe, acting as a trap. Te_{Cd} is commonly assumed to be the reason of the high resistivity of CZT (60).

Complexes of native defects are formed due to the native acceptors (V_{Cd}) and native donors (Te_{Cd}). In addition, when a V_{Cd} is paired with shallow donors such as In_{Cd}, they form a complex named ″A-center″.

M. A. Berding found that under Te rich conditions, CdTe at high temperatures is a highly compensated p-type with cadmium vacancy, V_{Cd}, as the dominant acceptor and

tellurium antisite, Te_{Cd}, as the compensating donor, while Under Cd rich conditions, interstitial Cd_i is expected to dominate and make the material n-type (61).

Several experimental studies directed toward native point defects have been performed using various methods, such as Thermoelectric Effect Spectroscopy (TEES), Deep Level Transient Spectroscopy (DLTS), and Photo Induced Current Transient spectroscopy (PICTS) (62) (63) (64).

In addition to these native defects, intentionally added dopants also cause some single or complex defects. Furthermore, other types of defects might be present, related to elemental impurities such as Ag, Al, Cl, Cu, Li, Na, P, Ga, I, Sn, Pb, Sc, Mn, Fe, Co, and Ni (65). There are several potential sources of these impurities in CdZnTe ingots, some of the most notable being components of the quartz ampoules, carbon coating, and especially from the Cd, Zn, and Te source materials (66).

Doping with transition metal elements such as V, Cu, and Co is promising for the material photorefractive effect and applications in optoelectronics. Such dopants, normally occupy the Cd site, act as deep donors and form near midgap levels.

K. Allachen et al. found that doping with Vanadium in the range of 10^{18}-$10^{19}cm^{-3}$ can make CdZnTe semi-insulating with resistivity in the 10^{8}-10^{10} Ω.cm range (67).

Due to the small ionization energy (<0.2eV) of the elements from groups I, III, V and Vll, their doping can be referred to as shallow doping. Group I elements, like Li and Na act as acceptors (A) when occupying the Cd sites, but, on interstitial sites, they act as donors. Group III elements, like In, Ga and Al, on the Cd sites and VII elements like Cl, Br and I, on the Te sites are donor states (D). Group V elements, like P, Sb, and Bi, on Te sites are acceptor states. In **Table 8** is shown a summary the behavior of dopants for CdZnTe. The number between the brackets represents the number of levels generated for every dopant.

The most important feature of the shallow donor doping in CdTe and CdZnTe is the formation of the A center, and the self-compensation process (68) (69).

Table 8: Behavior of dopants in CdZnTe

Substituted atom	**Group of dopants**						
	I	II	III	IV	V	VI	VII
Cd (II)	A(1)		D(1)	D(2)			
Te (VI)				A(2)	A(1)		D(1)

I.5.2. Trapping

Traps are formed by deep defects in the lattice which can create energy levels near the middle of the bandgap. They are traps because if an electron or hole is captured, it will be immobilized for a relatively long period of time. Theory predicts that the lifetime of charge carriers could be as high as a second, but in reality lifetimes are several orders of magnitude below this value. In fact, lifetimes for carriers in CZT detectors have been reported as 100ns to several microseconds for electrons and 50-300ns for holes (70).

Some types of deep defects act as recombination centers where both holes and electrons can be captured, causing them to annihilate. They could, for example, capture an electron from the conduction band and then a hole from the valence band causing the electron to fill the hole. It would then be in its original state and recombination could take place again. Both trapping and recombination lead to shorter lifetimes for charge carriers. For a detector to work efficiently it needs to collect a large fraction (ideally 100%) of the charge carriers, and so having a collection time much shorter than the charge carrier lifetime is a desirable characteristic.

Without trapping, holes and electrons are completely collected regardless of position at which they are created in the detector, therefore the gamma spectrum can be illustrated by a sharp line or peak at full collection. However, when the trapping phenomenon occurs, the entire electrons (holes) cloud does not reach the positive (negative) electrode.

I.5.3. Cracks

Cracks represent one of the major macroscopic structural defects in CdZnTe. Cracks could be formed in a bulk CdZnTe crystal upon incorporation of residual and thermal stress during cooling of the material from growth temperature. Cracks are also results of the low rupture modulus of CdZnTe and stress during the slicing and cutting of the material. In fact, the free surface areas associated with the cracks can act as nucleation sites for secondary phases such as Te precipitates and impurities. Chemical analysis of the cracks using X-ray energy dispersive showed high amount of carbon and zinc, which can influence the electrical properties and destroy the performance near the region of accumulation (71).

Usually, cracks propagate through grains and twins and travel towards the center of the ingot as shown in **Figure 16**. Choosing adequate thermal profiles and crucible materials can lead to suppress the formation of these macro defects in CdZnTe ingots.

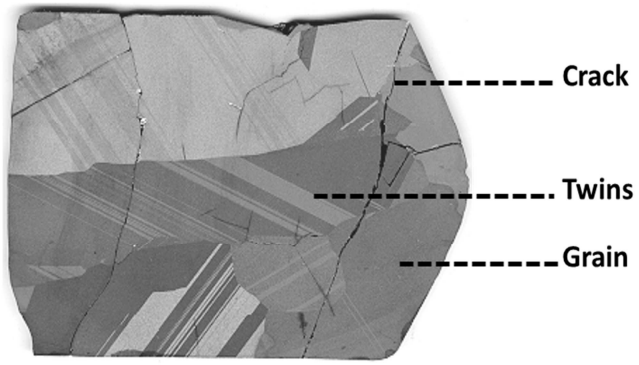

Figure 16: Axial slice of CdZnTe ingot **(72)**

I.5.4. Grain boundaries

Grain boundary in a solid crystalline material is a region separating two crystals (grains) of the same phase. Such defects are a serious problem which can influence the thermal conductivity and electrical properties. They act as barriers for transport, nucleation centers for impurities, second phase inclusions, and dislocations and carrier trapping which degrade the detector performance.

For CdZnTe, these grain boundaries may be formed at the very early stages of growth wherein nucleation of several grains occurs, or later due to instabilities at the growth interface. Nucleation of more than a single grain may occur if the crystal is grown using high growth velocities, under high temperature gradients, or may also be a result of the melt convection and latent heat extraction properties (73) .

The consequences for the single carrier sensitive radiation detectors are serious performance degradation. Degradation can range from catastrophic degrading (loss of signal) to a spectrometric degrading (double peak or peak broadening) for a single carrier sensitive device (74).

I.5.5. Twinning

Twins are another type of macroscopic defects that are usually occurring in CZT, and which can induce disorientation in the crystal. G.Li et al demonstrated that twins in CZT are habitually grouped in 3-6 microtwins parallel to each other. For the zinc-blende crystalline structure, (111) planes are the densest planes and share the largest interplane spacing which make weak interactional force between (111) planes. Therefore, this is a chance for twinning to locate there (75).

Growth conditions such as temperature instabilities, presence of impurities, and morphological instability of the crystallization front could be the most responsible for enhancing twinning formation (56). In addition, with low stacking fault energy of

$11\times10^{-7}J/cm^2$ (56) twinning can form easily due to the temperature fluctuation during crystal growth (41). For this reason, a careful control of the growth condition is necessary to reduce the twin density.

I.5.6. Dislocations

Dislocations are linear crystallographic defects within a crystal structure. These kinds of defects produce imperfection in crystalline structure and plastic deformation which affect the mechanical properties of the material.

There are two basic types of dislocations, the edge dislocation and the screw dislocation as shown in **Figure 17**. The screw dislocation is slightly more difficult to visualize and it is parallel to the direction in which the crystal is being displaced (Burgers vector is parallel to the dislocation line), while for the edge dislocation the burger vector and the dislocation line are perpendicular.

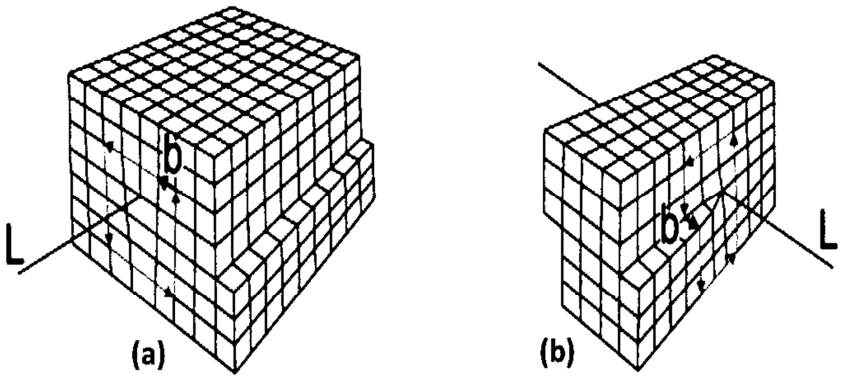

Figure 17: Model of (a) an edge and (b) a screw dislocation. The Burger's vector b and dislocation line L are indicated

In CZT, these defects can have different origins. They can be generated at the ampoule wall due to thermally induced stress; dislocations can also be induced by excess of strain during solidification and cooling process (41) and can be formed when crystallization occurs under uncontrolled conditions such as high thermal gradient (76).

Dislocations could be also associated to the structural changes induced by secondary phases such Te inclusions and precipitates.

The density of dislocations is revealed by surface chemical etching and subsequent measurements of the corresponding etch pit density (EPD) (77). Inoue suggested the E1-Ag and E2-Ag etch solutions to reveal dislocations in CdTe, but it was found that it cannot reveal all the dislocations. Nakagawa solution is the most applied method for revealing dislocations; however it has a limit to use. It only can be used to reveal

dislocations on (1 1 1)A surfaces (78). In fact, for a good quality sample, the EPD value is normally in the range of 10^3-10^4cm^{-2} (32) (79).

I.5.7. Pipes and voids

Voids and pipes are macroscopic three-dimensional defects which can be seen upon visible inspection. Voids have a lenticular and oval shape, while pipes have tubular hollow shape but some were suggested to be filled with carbon (80). The size of these pipes is usually from 500μm to a few of mm long, and about 20-50μm wide (81).

These defects could be the consequence of trapping Cd gas bubbles, which are related to the fluctuation in the growth conditions such as temperature, pressure and growth rate.

Pipes usually cause high leakage currents, distorted electric fields, and generally render the crystals useless in most the detector applications.

These defects could be suppressed by choosing the correct thermal profiles, crucible materials, and growth rates (82).

I.5.8. Inclusions and precipitates

It has been demonstrated that the presence of second phase (SP) particles markedly affects the electronic, crystalline, thermal and optical bulk quality of CdZnTe crystals (83). Second phases are the most studied defect in as grown CdZnTe crystals. It is also important to note that even randomly distributed inclusions can also influence the performance of detectors (84).

Due to the narrow band gap of Te which is about 0.3eV, Te precipitates have higher electrical conductivity, which may affect the detector leakage current and distort the electric field distribution and carrier transport in CZT devices (85).

One explanation for the formation of Te-rich SP has been attributed to the excess of Te in the melt of CZT and CdTe phases. Such Te-rich phases may form during crystal growth or post growth annealing due to the retrograde solubility within the phase diagram.

In CdTe or CdZnTe compound semiconductor crystals, one of the most important and complicated parameter to be controlled is the stoichiometry. This control will be complicated by the incongruent vaporization of CdTe melts. Even if the starting boule charge is stoichiometric or slightly Cd-rich, the most volatile element in the melt (Cd) will preferentially evaporate into the free space of the ampoule and leave behind a Te-rich melt. This melt composition causes the formation of Te inclusions and precipitates

(86). Considering that inclusions and precipitates have spherical geometry, the total Te excess in the crystal can be calculated as:

Equation 19

$$N_{Te} = \frac{4\pi\rho_{Te}N_A}{3A_{Te}} \sum_{i=1}^{n} r_i^3 \rho_i$$

With r_i the radius and ρ_i the density of precipitates or inclusions, A_{Te} the relative atom mass of Te and ρ_{Te} the density the mass density of Te, and *i* is the index for each class of particle.

The melt composition could be influenced by two parameters. Firstly, corresponding to the formula $Cd_{0.5-\delta y}Te_{0.5+\delta y}$ a deviation δy may occur because of weighing errors. Therefore, the Te or Cd excess N_w (cm^{-3}) is expressed as follow:

Equation 20

$$N_w \approx 2\delta y N_0$$

With $N_0=1.47\times10^{22}cm^{-3}$ is the number of Te or Cd atoms in stoichiometric CdTe. Secondly, the formation of Cd gas over the melt. The different vapour pressures of Cd and Te_2 indicate that the vapour phase established over the Cd-Te melts consists to about 96% of Cd atoms. The number of Cd atoms evaporating which is equal to the number of excess Te atoms in the melt can be calculated using the Perfect-Gas Law (87). Then, the concentration of excess Te atoms becomes:

Equation 21

$$N_e = \frac{P_{Cd}N_A}{RT}\frac{h_v}{h_l}$$

where P_{Cd} is the Cd partial pressure, N_A is the Avogadro's number, R is the universal gas constant, and h_v and h_l the length of the gaseous phase and the melt respectively. For the growth conditions, at 1100°C the partial pressure is approximately 10^5Pa (88). As a result, Equation 4 can be explained as:

Equation 22

$$N_e = 5\times10^{18}\frac{h_v}{h_l}$$

In practice, the values of the length ratios are between 0.3 and 2, resulting to Te excess concentrations from 10^{18} to $10^{19}cm^{-3}$.

Accordingly the total deviation from the exact stoichiometry of the melt is:

Equation 23

$$N_T = \pm N_w + N_e$$

There are many effective ways to minimize the formation of inclusions and precipitates such as control of stoichiometric composition, postgrowth annealing under controlled partial pressure.

Cd rich annealing is usually used for the reduction of Te inclusions and enhancement of the IR transmittance, and Te rich annealing is used for the elimination of Cd inclusions.

P.Rudolph et al. described Te inclusions as nonstoichiometric defects that formed during the melt growth of the crystals. In fact, during growth, the CdTe interface acts as a ″pulsating″ phase boundary due to the temperature fluctuations. Thus, the crystallizing CdTe growth front progress rapidly and captures liquid Te separating it from the rest of the solution zone (89). It has been established that the shape of Te inclusions strongly depends on radial and axial temperature during cooling process. R.Schwarz et al. have demonstrated that under small gradients between 9-15K/cm, hexagonal polygons tend to form, while using larger temperature gradients between 40-51 K/cm, triangular shaped inclusions take place. In fact, the proper choice of superheating and post growth annealing conditions may be used to reduce the size and density of Te inclusions.

It has been shown that Te inclusions can act as affective gettering sites for impurities such as Na, Ag, In and Bi. This phenomenon originates from the diffusion mechanism during crystal growth and from the segregation mechanism during cooling (40).

In CdTe and CdZnTe both tellurium and cadmium inclusions have been found (90). This depends on the melt composition from which the crystal was grown, Te or Cd rich. Usually, Cd inclusions have star shape and are in the range of 5μm to 120μm (90), while Te inclusions have triangular or hexagonal shape.

For the first time, J.Zhu et al. have observed Zn inclusions in CdZnTe crystals grown by Bridgman which are possibly due to the Zn segregation effects resulting from the deviation from the congruent melting point (91).

Although there is no agreement concerning the minimum size of Te inclusion which can affect the detector resolution; it has been found that inclusions < 1μm do not affect the energy resolution, as they behave as ordinary electron traps whose effect on the charge collection efficiency and it can be corrected (92). It has been also established that the effect of Te inclusions > 3μm is to lower the devices performance, and thereby restricting the ability to use thick detectors (93).

Te inclusions can be easily identified by using transmission IR microscopy; they absorb the infrared light and show up as distinct black spots as shown in **Figure 18**.

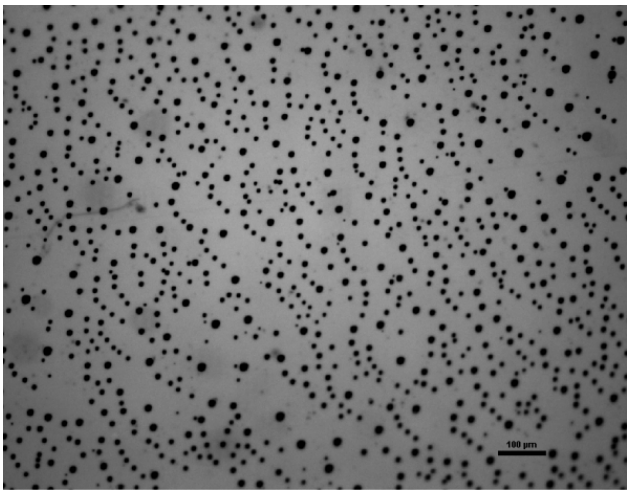

Figure 18: IR microscopy image for CZT sample

Precipitates are different from Te inclusions, where experiments show that the size of precipitates is in the range of 10-50nm and are invisible using IR microscopy, and so precipitates can behave like point defects. Calculations suggest that they form in about 100s and are separated by tens of nm (94) (95). The concentration of Te inclusions may exceed $10^{7}cm^{-3}$, but is still several orders of magnitude less than that of Te precipitates which can exceed $10^{12}cm^{-3}$ (96).

G.A.Carini et al. have defined Te precipitates as any volume of Te material with a size smaller than 30μm (85). G.S.Camarda et al. have indicated that the typical size of Te precipitates is between 1 and 20μm (97).

It has been demonstrated that Te precipitates affect the electron charge collection efficiency and thus the performance of nuclear radiation detectors. Te precipitates on the surface can also increase the leakage current, thereby deteriorating the device performance. Te inclusions and precipitates also act as traps for the charge carriers.

I.6. Applications of CdZnTe

Currently there is a huge range of applications in which CdZnTe detectors have been widely used. Various fields such as medical imaging, homeland security and astronomy have currently taken advantage of the desirable properties of this material and its potential uses. CdZnTe crystals are not only important as a substrate material for growing $Hg_{1-x}Cd_xTe$ films, but are also used to prepare X-ray and γ-ray detectors, photoelectric modulators, solar cells, etc. In fact, CdTe is versatile semiconductor which enables to convert radiation to electron effectively, which will reform radiography and radiation measurement in medical and industrial area.

Gamma rays are emitted by a variety of radioactive materials, some of the better known being ^{60}Co and^{137}Cs. X rays, in contrast, are produced by radiation-producing machines, the most common being the X-ray machines used in medicine and dentistry. Neither gamma rays nor X-rays are radioactive. They are pulses of energy that move through space at the speed of light. In general, gamma rays have higher energies than X-rays.

I.6.1. Medical applications

The uses of X-rays in the fields of medicine and dentistry have been extremely important. X-ray photographs utilize the fact that portions of the body such as bones and teeth with higher density are less transparent to X-rays than other parts of the human body. X-rays are widely used for diagnostic purposes in these fields. Examples might include the observation of the broken bones and torn ligaments of football players, the detection of breast cancer , or the discovery of cavities and impacted wisdom teeth. A relatively new technique for using X-rays in the field of medicine is called computerized axial tomography, producing what are called CAT scans. These scans produce a cross-sectional picture of a part of the body which is much sharper than a normal X-ray. It has been reported that the CdTe imaging sensor is suitable for the digital radiography. The principal advantages of using CdTe sensor are the simple structure of CdTe facilitating down-sizing, then high sensitivity and high signal to noise S/N ratios; additionally, X-ray photons are directly converted into electrical signals and energy information relative to the incident X-ray photons can be obtained (98).

The use of high density and high atomic number detector such as CdZnTe semiconductor substrates will allow for fabrication of high efficiency thin detectors with enhanced image quality.

Single photon emission computed tomography (SPECT), using gamma rays, has become a major tool for the in vivo localization of radiopharmaceuticals in nuclear medicine and now is performed routinely with commercially available radiopharmaceuticals to answer important clinical questions including those in cardiology, neurology, psychiatry, and oncology. SPECT produces images that represent the three dimensional distribution of radioactivity. This improves both image quality as well as the potential for the quantification of the radioactivity distribution in vivo.

Computed tomography (CT) has always been considered as a valuable tool in radiotherapy treatment planning due to the increased accuracy offered in tumor

localization and tissue inhomogeneity corrections. A schematic illustration of CT imaging is presented in **Figure 19.**

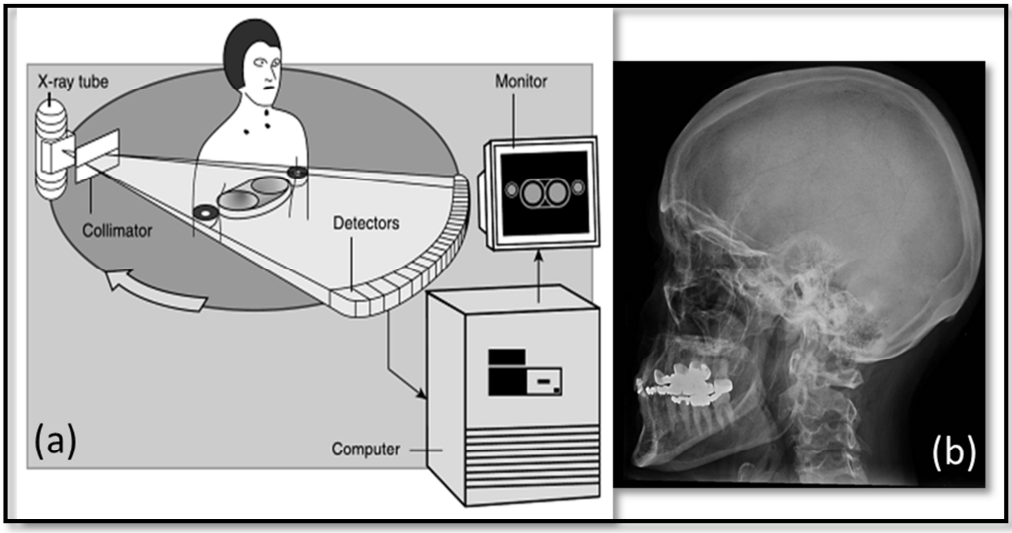

Figure 19: (a) Schematic illustration of CT imaging operation and (b) scan image of a human skull (99)

I.6.2. National security

In undertaking national security and non-proliferation inspection, radiation detectors mainly serve to locate and identify special radioactive nuclear materials. CdTe and CdZnTe detectors have proven well-suited for these purposes, because they are providing good energy resolution and high detection efficiency. The International Atomic Energy Agency (IAEA) has used CdTe and CZT detectors for over three decades (100) (101). The IAEA employs hemispheric CdTe/CZT to verify irradiated nuclear material, that is, spent-fuel assemblies; generally, they must measure high count rates and high gamma energies.

CdZnTe and CdTe detectors have been used in International Safeguards for more than 10 years. With their properties, they complement the classical NaI and liquid nitrogen cooled Ge detectors (102) (103).

I.6.3. Space and astrophysics applications

Both CdTe and CdZnTe detector play a crucial role for space and astrophysics applications. Operating in the range of 10-500KeV, CdTe and CdZnTe processes prominent advantages compared with scintillators and Ge detector. The International Gamma Ray Astrophysics Laboratory`s (INTEGRAL) Soft Gamma Ray imager (ISGRI) of the European Space Agency (ESA) is the first space instrument using good spectral resolution CdTe (104) (105). It provided faultless operations in space since the

launch of INTEGRAL in October 2002 (106). The ISGRI mainly is devoted to detecting and precisely measuring celestial gamma ray photons between 15KeV and 1MeV. It supports research on violent processes occurring near black holes, neutron stars, or in supernovae (105). The ISGRI camera produces the best images ever obtained in the soft gamma-ray domain. Without any doubt, CdTe and the similar but more popular CdZnTe will play a key role in the future of instrumental high-energy astrophysics (106). Presented in **Figure 20** is a schematic view of the INTEGRAL satellite and its payload. The IBIS instrument is basically in two parts: the coded mask and the detection unit. The detection unit comprises two detection layers ISGRI and PICsIT actively shielded by an anticoincidence system. ISGRI is located 3.2 m below the coded mask.

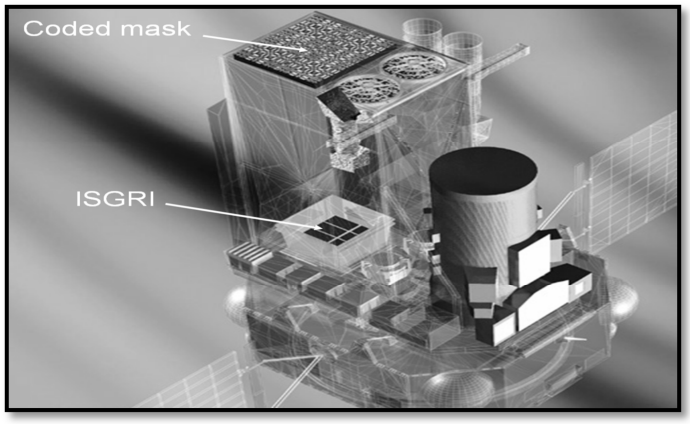

Figure 20: Schematic view of the INTEGRAL satellite and its payload (106)

The Goddard Space Flight Center, NASA, leads the InFOCμS project, whose focal plane consists of a CZT detector with a 12×12 array of 2mm pixels. The telescope was flown twice, in 2001 and 2004, and achieved an angular resolution of 2.2 arc-min (HPD) and spectral resolution of 4 at 32 keV. The good performance of CZT facilitated the successful detection of the astrophysical source Cyg X-1, even with an on-target observation time of only about a minute (105).

I.7. Bibliography

1. **Triboulet, R.** Fundamentals of the CdTe and CdZnTe bulk growth. 2005, Vol. 5, pp. 1556 – 1565.
2. **A. Iller, G. Karczewski, G. Kolmhofer, E. Lusakowska ,H. Sotter.** AES Investigation of Chemical Treatment Effect on CdTe and CdZnTe Surfaces. *Cryst. Res. Technol.* 1998, Vol. 33, pp. 401-408.
3. **M. Schenk, H. Ahnert, T. H. Duong, H. Nieusch.** Validity of the Lattice Parameter Vegard Rule in Cd1-xZnxTe Solid Solutions. 1996.
4. **Sivaraman, Gowri.** *Characterization Of Cadmium Zinc Telluride Solar Cells.* 2003.
5. **Adachi, S.** *Properties of Group IV, III-V, and II-VI semiconductors.* 2005.
6. **G. Zha, W. Jie, X. Bai, T. Wang, L. Fu, W. Zhang, J. Zhu, F. Xu.** The study on the work function of CdZnTe with different surface states by synchrotron radiation photoemission spectroscopy. 2009, Vol. 106.
7. **G. Zha, W. Jie, T. Tan, P. Li, W. Zhang, F. Xu.** The atomic and electronic structure of CdZnTe (111) A surface. 2006, Vol. 427, pp. 197-200.
8. **W. Xiaoqin, J. Wanqi, L. Qiang, G. Zhi.** Surface passivation of CdZnTe wafers. 2005, Vol. 8, pp. 615-621.
9. **Szeles, C.** CdZnTe and CdTe materials for X ray and gamma ray radiation detector applications. *Phys.Stat.Sol.(b).* 2004, 3, pp. 783-790.
10. **U.N. Roy, S. Weiler, J. Stein, Y. Cui, M. Groza, V. Buliga, A. Burger.** Zinc mapping in THM grown detector grade CZT. *Journal of Crystal Growth.* 2012, Vol. 347, pp. 53–55.
11. **P. Fougeres, L. Chibani, M. Hageali, J.M. Koebel, G. Hennard, A. Zumbiehl, P. Siffert, M. Benkaddour.** Zinc segregation in HPB grown nuclear detector grade Cd1-xZnxTe. *Journal of Crystal Growth.* 1999, Vol. 197, pp. 641-645.
12. **K. Boujdaria, O. Zitouni.** Energy-band structure of CdTe and Si: a sp3(sp)2 k.p model. *Solid State Communications.* 2004, Vol. 129, pp. 205–210.
13. **M. Cohen, T.K. Bergstresser.** Structure, Band Structures and Pseudopotential from factors for fourteen Emiconductor of the Diamond and Zinc Blende. *Physical Review.* 1966, Vol. 141.
14. **S. Del Sordo, L. Abbene, E. Caroli, A.M. Mancini, A. Zappettini, P.Ubertini.** Progress in the Development of CdTe and CdZnTe Semiconductor Radiation Detectors for Astrophysical and Medical Applications. *Sensors.* 2009, Vol. 9, pp. 3491-3526.
15. **S. Sen, W.H. Konkel, S.J. Tighe, L.G. Bland, S.R. Sharma, R.E. Taylor.** Crystal growth of large-area single-crystal CdTe and CdZnTe by the computer-controlled vertical modified-Bridgman process. 1990, Vol. 86, pp. 111-117.
16. **C. Martinez-Tomas, V. Muñoz, R. Triboulet.** Heat transfer simulation in a vertical Bridgman CdTe growth configuration. 1999, Vol. 197.
17. **S. Hassani, A. Lusson, A. Tromson-Carli, R. Triboulet.** Seed-free growth of (1 1 1) oriented CdTe and CdZnTe crystals by solid-state recrystallization. *Journal of Crystal Growth.* 2003, Vol. 249, pp. 121–127.
18. **Jordan, A.S.** Estimated thermal diffusivity, Prandtl number and Grashof number of molten GaAs, InP, and GaSb. 1985, Vol. 71, pp. 551–558.
19. **L. Luna, A. Yeckela, M. Reedc, C. Szeles, P. Daoutidisa, J.J. Derby.** On the effects of furnace gradients on interface shape during the growth of cadmium zinc telluride in EDG furnaces. 2006, Vol. 290, pp. 35–43.
20. **A. Zappettini, M. Zha, L. Marchini, D. Calestani.** Control of the interface shape in vertical Bridgman grown CdZnTe crystals for X-ray detector applications. 2012, Vol. 14, pp. 5992-5995.

21. **S. Mnasri, S. Abdi-Ben Nasrallah, N. Sfina, N. Bouarissa, M. Said.** Electronic, lattice vibration and mechanical properties of CdTe, ZnTe,MnTe, MgTe, HgTe and their ternary alloys. *Semicond. Sci. Technol.* 2009.
22. **D. Zeng, w. Jie, T. wang, G. Zha.** Residual stress and strain in CdZnTe wafer examined by X-ray diffraction methods. *Appl. Phys.* 2007, Vol. 86, pp. 257–260.
23. **Z. Zhang, H. Gao, W. Jie, D. Guo, R. Kang, Y. Li.** Chemical mechanical polishing and nanomechanics of semiconductor CdZnTe single crystals. *Semicond. Sci. Technol.* 23.
24. **T. Fukuda, H.J. Scheel.** *Crystal Growth and Technololy.* 2003.
25. **Wohlfarth, E.P.** *The growth of crystals from liquids.* 1973.
26. **Greenberg, J.H.** P-T-X phase equilibrium and vapor pressure scanning of non-stoichiometry in CdTe. *Journal of Crystal Growth.* 1996, Vol. 161, pp. 1 - 11.
27. *P-T-X phase equilibrium and vapor pressure scanning of non-stoichiometry in the CdZnTe system.* **Greenberg, J.H.** 2003, Vol. 47, pp. 196-238.
28. **V.N. Guskov, J.H. Greenberg.** Vapor pressure scanning of non-stoichiometry in Cd0.9Zn0.1Te and Cd0.85Zn0.15Te. *Journal of Crystal Growth.* 2006, Vol. 289, pp. 552-558.
29. **J.H. Greenberg, V.N. Guskov.** Vapor pressure scanning of non-stoichiometry in Cd0.9Zn0.1Te and Cd0.85Zn0.15Te. *Journal of Crystal Growth.* 2006, Vol. 289, pp. 552–558.
30. **M. Bruder, H.J. Schwarz, R. Schmitt, H. Maier, M.O. Möller.** Vertical Bridgman growth of Cd1−yZnyTe and characterization of substrates for use in Hg1−xCdxTe liquids phase epitaxy. 1990, Vol. 101, pp. 266-269.
31. **Rudolph, P.** Fundamental Studies On Bridgman Growth Of CdTe. *Prog. Crystal Growth and Charact.* 1994, Vol. 29, pp. 275-381.
32. **M. Fiederle, A. Fauler, A. Zwerger.** Crystal Growth and Characterization of Detector Grade (Cd,Zn)Te Crystals. 2007, Vol. 54.
33. **M. Mühlberg, P. Rudolph.** The correlation between superheating and supercooling in CdTe melts during unseeded bridgman growth. *Journal of Crystal growth.* 1993, Vol. 128, pp. 571-575.
34. **P. Rudolph, H.J. Koh, N. Schaifer, T. Fukuda.** The crystal perfection depends on the superheating of the mother phase too - experimental facts and speculations on the "melt structure" of semiconductor compounds. *Journal of Crystal Growth.* 1996, Vol. 166, pp. 578-582.
35. **Capper, P.** *Bulk crystal growth of electronic, optical & optoelectronic materials.* 2005.
36. **Fang, H.** *To study crystal cracking and melt inclusion during laser crystal growth by Czochralski method.* 2008.
37. **M. Azoulay, S. Rotter, G. Gafni.** Zinc segregation in CdZnTe grown under Cd/Zn partial pressure control. *Journal of Crystal Growth.* 1992, Vol. 117, pp. 276—280.
38. **Y. Xu, W. Jie, P.J. Sellin, T. Wang, L. Fu, G. Zha, P. Veeramani.** Characterization of CdZnTe Crystals Grown Using a Seeded Modified Vertical Bridgman Method. *IEEE Transactions On Nuclear Science.* 2009, Vol. 56.
39. **Y. Tao, S. Kou.** Segregation reduction in vertical Bridgman crystal growth of CdZnTe. *Journal of Crystal Growth.* 1997, Vol. 181, p. 301 303.
40. **G. Yang, A.E. Bolotnikov, Y. Cui, G.S. Camarda, A. Hossain, R.B. James.** Impurity gettering effect of Te inclusions in CdZnTe single crystals. 2008, Vol. 311, pp. 99–102.

41. **T. Asahi, O. Oda , y. Taniguchi , A. Koyama.** Growth and characterization of 100 mm diameter CdZnTe single crystals by the vertical gradient freezing method. 1995, Vol. 149, pp. 23-29.
42. **C.E. Chang, V.F.S. Yip, W.R. Wilcox.** Vertical gradient freeze growth of gallium arsenide and naphthalene: Theory and practice. *Journal of Crystal Growth.* 1974, Vol. 22, pp. 247–258.
43. **C. Szeles, S.E. Cameron, J.O. Ndap, and W.C. Chalmers.** Advances in the Crystal Growth of Semi-Insulating CdZnTe for Radiation Detector Applications. *IEEE Transactions On Nuclear Science.* 2002, Vol. 49, 5.
44. **T. Asahi, O. Oda, Y. Taniguchi, A. Koyama.** Growth and characterization of 100 mm diameter CdZnTe single crystals by the vertical gradient freezing method. *Journal of Crystal Growth.* 1996, Vol. 161, pp. 20-27.
45. **A. Koyama, A. Hichiwa, R. Hirano.** Recent Progress in CdZnTe Crystals. *Journal of Electronic Materials.* 1999, Vol. 28, pp. 683-687.
46. **M. Fiederle, T. Feltgen, J. Meinhardt, M. Rogalla, K.W. Benz.** State of the art of (Cd,Zn)Te as gamma detector. *Journal of Crystal Growth.* 1999, Vol. 197, pp. 635-640.
47. **M. Fiederle, V. Babentsov, J. Franc, A. Fauler, J.P. Konrath.** Growth of high resistivity CdTe and (Cd,Zn)Te crystals. *Cryst.Res.Technol.* 2003, Vol. 38, pp. 588-597.
48. **V. Komar, A. Gektin, D. Nalivaido, I. Klimenko, V. Migal, O. Panchuk, A. Rybka.** Characterization of CdZnTe crystals grown by HPB method. *Nuclear Instruments and Methods in physics Research A.* 2001, Vol. 458, pp. 113-122.
49. **G. Li, W. Jie, Z. Gu, H. Hua.** Growth of Cd1−xZnxTe crystals with different x values and their qualities comparison. *Journal of Crystal Growth.* 2004, Vol. 263, pp. 332-337 .
50. **G. Li, W. Jie, T. Xang, G. Yang.** Impurities in CdZnTe crystal grown by vertical Bridgman method. *Nuclear Instruments and Methods in Physics Research A.* 2004, Vol. 534, pp. 511-517.
51. **G. Li, X. Zhang, W. Jie.** Correlation between the low-temperature PL spectra and Cd0.9Zn0.1Te quality. *Semicond.Sci.Technol.* 2005, Vol. 20, pp. 86-89.
52. **G. Yang, W. Jie, Q. Li, T. Wang, W. Li, G. Li, H. Hua.** Effects of In doping on the properties of CdZnTe single crystals. *Journal of Crystal Growth.* 2005, Vol. 283, pp. 431-437.
53. **P. Gille, F.M. Kiessling, M. Burkert.** A new approach to crystal growth of Hg1_xCdxTe by the travelling heater method (THM). *Journal of Crystal Growth.* 1991, Vol. 114, pp. 77—86.
54. **N. Audet, B. Levicharsky, A. Zappetini, N. Zha.** Composition Study of CdTe Charges Synthesized by the travelling Heater Method. *IEEE Transtactions on Nuclear Science.* 2007, Vol. 54.
55. **H. Shiraki, M. Funaki, Y. Ando, S. Kominami, K. Amemiya, R. Ohno.** Improvement of the productivity in the growth of CdTe single crystal by THM for the new PET system. *IEEE Nuclear Science Symposium Conference Record.* 2007.
56. **Rudolph, P.** Defect Formation During Crystal Growth from the Melt. 2010.
57. **L. Yujie, M. Guoli, J. Wanqi.** Point defects in CdTe. 2003, Vol. 256, pp. 266-275.
58. **R. Grill, J. Franc, P. H. oschl, E. Belas, I. Turkevych, L. Turjanska, P. Moravec.** Semiinsulating CdTe. 2002, Vol. 487, pp. 40-46.
59. **J. Gutowski, K. Sebald, T. Voss.** CdTe: defect formation energies, entropy of point defects, migration energy. 2008.
60. **Muren Chu, Sevag Terterian, David Ting, C. C. Wang, H. K. Gurgenian, and.** Tellurium antisites in CdZnTe. 2001, Vol. 79.
61. **Berding, M.A.** Annealing conditions for intrinsic CdTe. 1999, Vol. 74.

62. **C. Szeles, Y. Y. Shan, K. G. Lynn, A. R. Moodenbaugh.** Trapping properties of cadmium vacancies in Cd1-xZnxTe. 1996, Vol. 55.
63. **H. Elhadidy, J. Franc, P. Moravec, P. Hoschl, M. Fiederle.** Deep level defects in CdTe materials studied by thermoelectric effect spectroscopy and photo-induced current transient spectroscopy. 2007, Vol. 22, pp. 537-542.
64. **R. Gul, K. Keeter, R. Rodriguez, A.E. Bolotnikov, A. Hossain, G.S. Camarda, K.H. Kim, G. Yang, Y. Cui, V. Carcelen, J. Franc, Z. Li, R.B. James.** Point Defects in Pb-, Bi-, and In-Doped CdZnTe Detectors: Deep-Level Transient Spectroscopy (DLTS) Measurements. 2012, Vol. 41.
65. **R. GUL, A. Bolotnikov, H.K. Kim, R. Rodriguz, K. Keeter, Z. Li, G. Gu, R.B. JAMES.** Point Defects in CdZnTe Crystals Grown by Different Techniques. 2011, Vol. 40.
66. **R.B.James.** Cd1-xZnxTe Spectrometers for Gamma and X-Ray Applications-Semiconductors and Semimetals, Chapter 9. 1995, Vol. 43.
67. **Kh. Allachen, M. Tapiero, Z. Guellil, J.P. Zielinger, J.C. Launay.** Photoconductivity studies in vanadium-doped CdTe and Cd1-xZnxTe. 1998, Vol. 184, pp. 1142-1146.
68. **S. Seto, K. Suzuki, V.N. Abastillas, K. Inabe.** Compensating related defects in In-doped bulk CdTe. 2000, Vol. 214/215, pp. 974-978.
69. **L. Shcherbak, P. Feichouk, P. Fochouk, O. Panchouk.** Self-compensation studies in Cd-saturated In-doped CdTe. 1996, Vol. 161, pp. 219- 222.
70. **G.F.Knoll.** *Radiation detection and measurements.* 2000.
71. **J. R. Heffelfinger, D.L.Medlin, R.B.James.** Analysis of Grain Boundaries, Twin Boundaries and Te Precipitates in Cd1-xZnxTe Grown by Hhigh Pressure Method. 1997.
72. **C. Szeles, M.C. Driver.** Growth and properties of semi-insulating CdZnTe for radiation detector applications. 1998.
73. **J.Crocco.** *Crystal Growth & Technology, Device Fabricaiton, and Material Properties of Cd(Zn)Te for Radiation Detector Applications.* 2012.
74. **Kuvvetli, I.** *Development of CdZnTe detector.* 2003.
75. **G. Li, S. Jushih, Y. Huang, T. Wang, W. Jie.** Nanostructure sof defects in CdZnTe single crystals. 2008, Vol. 311, pp. 85-89.
76. **Carcelen, V.** *Growth and Characterization of Cd0.85Zn0.15Te Crystals Doped With Bi:1019 at/cm3.* 2011.
77. **Y. Jianrong, G. Huiming, C. Xinqiang, F. Weizheng, H. Li.** Dislocation assessment of CdZnTe by chemical etching on both {1 1 1}B and {2 1 1}B faces. 2002, Vol. 234, pp. 337-342.
78. **D.Rose, K.Durose, W.Palosz, A.Szczerbakow, and K.Grasza.** Methods of dislocatiojns distribution analysis and inclusion identification with application to CdTe and (Cd,Zn)Te. 1998, Vol. 31, pp. 1009-1016.
79. **G. Zha, W. Jie, Q. Li, Z. Wang, Y. Xu, D. Zeng.** The effect of dislocations in Cd0.96Zn0.04Te single crystal on IR transmittance. 2006, Vol. 9, pp. 160–163.
80. **J.R. Heffelfinger, D.L. Medlin, H. Yoon, H. Hermon, R.B. James.** Analysis of grain boundaries, Twin boundaries and Te precipitates in CdZnTe Grown by High-Pressure Bridgman Method. 1997.
81. **A. Hossain, L. Xu, A.E. Bolotnikov, G.S. Camarda, Y. Cui,G. Yang, K-H. Kim, and R.B. James.** Distribution of Te inclusions in a CdZnTe wafer and their effects on the electrical properties of fabricated devices. 2011, Vol. 652, pp. 146–148.
82. **C. Szeles, M.C. Driver.** Growth and properties of semi-insulating CdZnTe for radiation detector applications. 1998.

83. **M.E. Rodriguez, O. Zelaya-Angel, J.J. PeHrez Bueno, S. Jimenez-Sandoval, L. Tirado.** Influence of Te inclusions and precipitates on the crystalline and thermal properties of CdTe single crystals. *Journal of Crystal Growth.* 2000, Vol. 213, pp. 259-266.
84. **A. E. Bolotnikov, N. M. Abdul-Jabbar, O. S. Babalola, G. S. Camarda, Y. Cui, A. M. Hossain, E. M. Jackson, H. C. Jackson, J. A. James, K. T. Kohman, A. L. Luryi, R. B. James.** Effects of Te Inclusions on the Performance of CdZnTe Radiation Detectors. 2008, Vol. 55.
85. **G.A. Carini, A.E. Bolotnikov, G.S. Camarda, G.W. Wright, R. B. James.** Effect of Te precipitates on the performance of CdZnTe detectors. 2006, Vol. 88.
86. **P. Rudolph, M. Neubert, M. Muhlberg.** Defects in CdTe Bridgman monocrystals caused by nonstoichiometric growth conditions. 1993, Vol. 128, pp. 582-587.
87. **Rudolph, P.** Basic problems of vertical Bridgman growth of CdTe. 1993, Vol. 16, pp. 8-16.
88. **K. Peters, A. Wenzel, P. Rudolph.** The p-T−x projection of the system Cd-Te. 1990, Vol. 25, pp. 1107-1116.
89. **R. Schwarz, K.W. Benz.** Thermal field influence on the formation of Te inclusions in CdTe grown by the travelling heater method. 1994, Vol. 144, pp. 150-156.
90. **E. Belas, M. Bugar, R. Grill, J. Franc, P. Moravec, P. Hlidek, P. Hoschl.** Reduction of Inclusions in (CdZn)Te and CdTe:In Single Crystals by Post-Growth Annealing. 2008, Vol. 37.
91. **J. Zhu, J. Chu, X. Zhang, J. Cheng.** Study of zinc inclusions/precipitates in CdZnTe crystals. 1997, Vol. 171, pp. 357-360.
92. **A.E. Bolotnikov, G.S. Camarda, G.A. Carini, Y. Cui, K.T. Kohman.** Performance-limiting defects in CdZnTe detectors. 2007, Vol. 54, pp. 821-827.
93. **U.N. Roy, S.Weiler, J. Stein, A. Hossain, G.S. Camarda, A.E. Bolotnikov, R.B. James.** Size and distribution of Te inclusions in THM as-grown CZT wafers: The effect of the rate of crystal cooling. 2011, Vol. 332, pp. 34–38.
94. **R. D. S. Yadava, R. K. Bagai, W. N. Borle.** Theory of Te Precipitation and Related Effects in CdTe Crystals. *Journal of Electronic Materials.* 1992, Vol. 21.
95. **A. E. Bolotnikov, N. Abdul-Jabber, S. Babalola, G. S. Camarda, Y. Cui, A. Hossain, E. Jackson, H. Jackson, J. James, K. T. Kohman,A. Luryi, and R. B. James,.** Effects of Te inclusions on the performance of CdZnTe radiation detectors. *IEEE Nuclear Science Symposium Conference Record.* 2007.
96. **P. Rudolph, A. Engel , I. Schentke, A. Grochocki.** Distribution and genesis of inclusions in CdTe and (Cd,Zn)Te single crystals grown by the Bridgman method and by the travelling heater method. 1995, Vol. 147, pp. 297-304.
97. **G. S. Camarda, A. E. Bolotnikov, G. A. Carini, R. B. James, L. Li.** Effects of Telluriuem Precipitates on Charge Collection in CZT Nuclear Radiation Detectors. 2006.
98. **Scheiber, C.** New developments in clinical applications of CdTe and CdZnTe detectors. 1996, Vol. 380, pp. 385-391.
99. **Iniewski, K.** *Medical imaging, Principles, Detectors and Electronics.* 2009.
100. **Schlesinger, T. E.** *Semiconductors for Room Temperature Nuclear Detector Applications.* 1995.
101. **M. de Carolis, T. Dragnev, A. Waligura.** IAEA Everinnce in the Development and Use of CdTe Gamma Spectrometric Systems for Safeguards Application. 1976, Vol. 23.
102. **R. Arlt, K.H. Czock, D.E. Rundquist.** Overview of the use of CdTe detectors for the verification of nuclear material in nuclear safeguards. 1992, Vol. 322, pp. 575–582.

103. **R. Arlt, D.E. Rundquist, D. Bot, P. Siffert, M. Richter, A. Khusainov, V. Ivanov, A.Chrunov, Y. Petuchov, F. Levai, S. Desi, M. Tarvainen, I. Ahmed.** Use of Room Temperature Semiconductor Detectors for the Verification of Nuclear Material in International Safeguards - Recent Advances. 1993.
104. **Limousin, O.** New trends in CdTe and CdZnTe detectors for X- and gamma-ray applications. 2003, Vol. 504, pp. 24–37.
105. **R.Triboulet.** *CdTe and Related Compounds; Physics, Defects, Hetero- and Nano-structures.. Part II.* 2010.
106. **Lebrun, F.** The ISGRI CdTe Gamma Camera In-Flight Performance. 2005, Vol. 52.

Chapter II: Experimental processes and characterization

Table of Contents

II.1. Introduction

The crystal growth process plays an essential role in determining the properties of CdZnTe crystals. The control of crystal growth parameters of CdZnTe is an experimental challenge for achieving large single grain and high resistivity material useful for gamma radiation and other applications. Furthermore, surface treatment is a critical and sensitive process in the fabrication of CdZnTe detectors, and plays a critical role in determining the detectors performance. For this reason, it was fundamental to develop both crystal growth as well as detectors fabrication processes.

This chapter provides a complete study of the experimental methods which have been used is this investigation. This includes (i) crystal growth, (ii) samples preparation (iii) detectors fabrication, and finally (iv) the techniques used for characterizing the materials and detectors.

II.2. Crystal growth

II.2.1. Selection of the crucible

In the Bridgman and Vertical Gradient Freeze (VGF) techniques, a sealed quartz ampoule for crystal growth of CdZnTe is usually used. Nevertheless, to maintain the purity of the starting materials and avoid impurities such as Na, Ag and Li, it is important to prevent interaction between the quartz ampoule and CdZnTe melt. Deposition of a quite thin layer of carbon, on the order of microns, on the quartz surface is also used. Another approach is to use a high purity crucible, such as pyrolytic boron nitride (pBN). The crystal structure of pBN is hexagonal. The preferred orientation of the c-axis is parallel to the direction of growth. The pBN crucibles are not porous and they can resist any chemical attack because of its density. PBN is the only material that is resistive to anhydrous HF attack at temperature above 1600°C.

Semiconductor materials of very high purity can be grown in pBN due to its several interesting properties such as the anisotropic thermal conductivity. The thermal anisotropy is a result of low thermal conductivity along the c-axis direction (2W/m) and higher thermal conductivity perpendicular to the c-axis (50W/m). As a result, radial heat flow is suppressed, being perpendicular to the c-axis.

It was demonstrated for CdZnTe that pBN crucibles led to the growth of ingots with low concentration of impurities and etch pit density (1). There are other important properties; some of them are presented in **Table 1**.

Table 1: Properties of Pyrolytic Boron Nitride at 1000°C

Properties	"a" direction	"c" direction
Maximum temperature (°C)	2500	-
Density (g/cm^3)	2.22	-
Total impurities (ppm)	<10	-
Resistivity (Ω.cm)	3×10^7	5×10^9
Thermal conductivity (W/m)	2	50

One disadvantage of pBN crucibles is correlated with the interaction with the melt during the growth cycle. It has been shown for III-V materials that the texture of a pBN crucible can have an influence on crystal growth (2). To avoid this interaction, a carbon coating to pBN crucibles has been developed.

Glow Discharge Mass Spectroscopy (GDMS) has been implemented for the analysis of CZT purity using both PBN and using ccpBN (carbon coating to pBN). From the results shown in **Table 2**, we observe that the ingot grown using cc-pBN exhibited lower concentrations of B and N incorporated into the matrix. The slightly higher concentrations of iron and chromium could be related to the stainless steel tools which are used for charging the crucible. We also observe a high concentration of Cl for pBN and cc-pBN grown ingot, this may be due to the cleaning with hydrochloric acid (HCl).

Table 2: GDMS data (ppb) for CZT ingots grown using pBN and cc-pBN

Elements	pBN	cc-pBN
B	30	<3
N	65	8
P	28	<2
Li	26	6
Cl	2000	1200
Fe	<5	74
Cr	14	13

II.2.2. Cleaning of the ampoule

Quartz ampoules from Heraeus were used for crystal growth of CdZnTe. Quartz glass is a very pure material consisting of SiO_2 and some impurities.

The analysis of impurities in Quartz tube is presented in **Table 3**. One can observe that the most common impurities are metals such as Al, Na and Fe. These foreign elements can influence the properties of the material processed in contact with the quartz glass.

Table 3: Impurities measured in quartz tube in ppm

	Al	Ca	Cr	Cu	Fe	K	Li	Mg	Mn	Na	Ti	Zr
Quartz tube	15	0.5	<0.05	<0.05	0.1	0.4	0.6	0.05	<0.05	0.3	1.1	0.7

Besides its high purity, quartz glass has more important properties as shown in **Table 4.** Quartz has a very low thermal expansion coefficient which is much lower than that of other common materials (for example glass $85\times10^{-7}K^{-1}$) and a very high thermal shock resistance. Additionally it has a low thermal conduction. Due to these properties quartz is one of the most valuable materials used in science and industry.

Table 4: Properties of quartz tube

	Density (g/cm^3)	Compressive strength (N/mm^2)	Max. working temperature (°C)	Heat conductivity ($W/m\cdot K$)	Mean expansion coefficient (K^{-1})
Quartz	2.203	1150	1160	1.38	5.1×10^{-7}

To prepare ampoule for crystal growth the following processes were used:

a) First the ampoule was rinsed with Alconox concentrated detergent in order to remove the surface contaminants, followed by a rinsing with distilled water, trichloroethylene, methanol and acetone (DI, TCE, MeOH, and acetone)

b) The ampoule was filled with aqua regia (nitric acid HNO_3 and hydrochloric acid HCl in a volume ratio of 1:3 respectively) for a period of 24 hours, followed by DI, TCE, MeOH, and acetone.

c) The ampoule was then etched with Hydrofluoric acid for 3 hours, followed by DI, TCE, MeOH, and acetone. Finally the ampoule was dried in the oven.

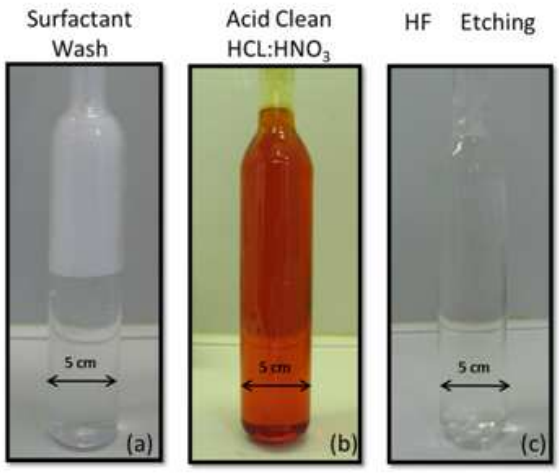

Figure 1: Ampoule preparation for crystal growth. (a) Ampoule being cleaned with Alconox detergent (b) acid cleaning using 3HCl:HNO_3 solution (c) quartz etching using HF acid

II.2.3. Vertical Gradient Freeze furnace (VGF)

A five-zone Vertical Gradient Freeze (VGF) furnace was used to grow 25mm diameter CdZnTe ingots. As shown in **Figure 2**, the hot zone of the system consisted of five independent 1KW furnace elements each 10cm in height. S-types Thermocouples were located in the center of each zone in order to measure the temperature. To improve the thermal isolation in the furnace, high temperature refractory wool was used.

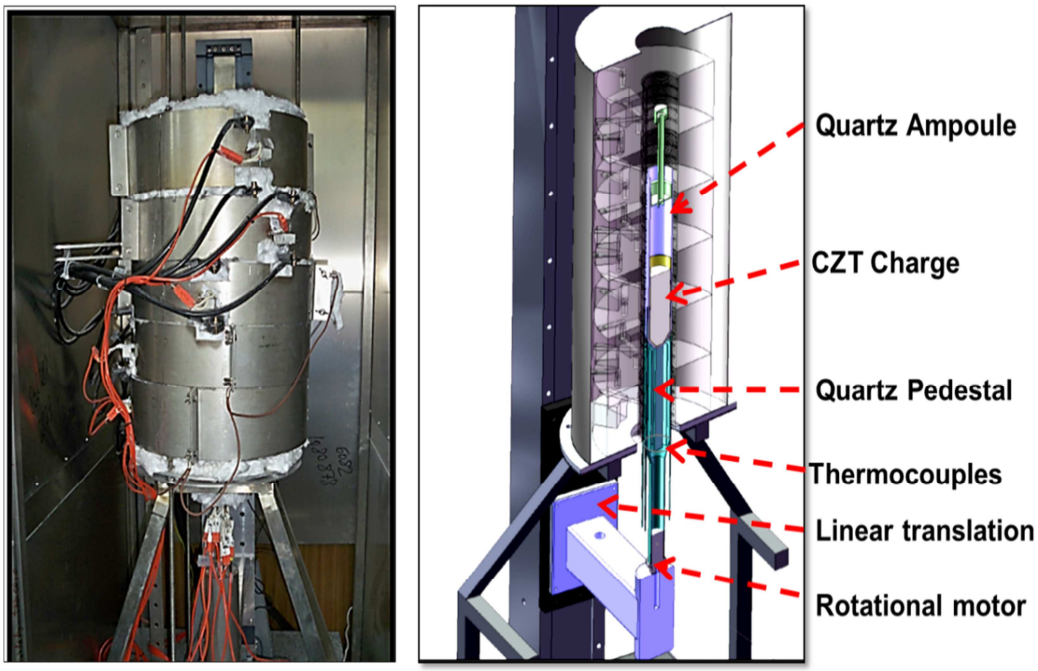

Figure 2: As built (left) and designed (right) VGF furnace

A linear actuation system was used for positioning the crystal growth ampoule inside the furnace. This system consisted of a linear column actuated by a stepper motor which

was controlled by software. A second DC motor was housed inside the linear actuator column head and provided the capability for rotation of the ampoule during the process. The positioning system was coupled to a quartz pedestal, upon which the ampoule would be placed. This quartz pedestal consisted of a central quarts/SiC rod, intended to support the weight of the ampoule at high temperatures, surrounded by a separate set of a type-s thermocouples for measuring the temperature gradients near the ampoule wall as shown in **Figure 3**. The SiC pedestal acts as a cold-finger due to its high thermal conductivity properties and increase the axial heat flow and the temperature gradient at the first to freeze of the ingot. J. Crocco et al. demonstrated that the first to freeze part of the CZT ingot grown using a SiC is substantially better than the first to freeze part using only quartz. In fact, the first to freeze crystal is only composed from two large grains. However, the grain size of the first to freeze crystal of the ingot grown without Sic pedestal are much smaller and does not show the same continuity from wafer to wafer (3).

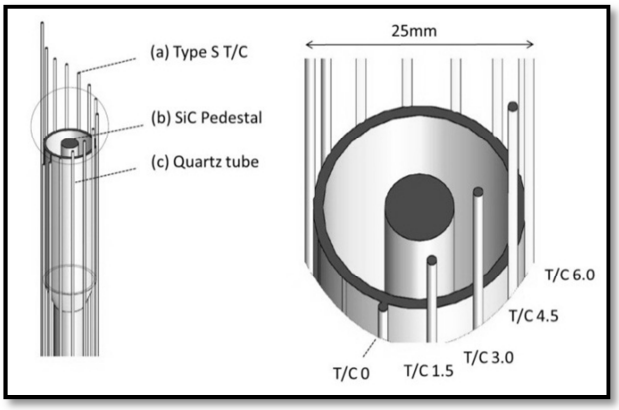

Figure 3 : Thermocouples distribution and Sic pedestal used for the growth

The thermocouples (T/C) used in this work were made in the laboratory. S-type platinum-Platinum Rhodium (10%) thermocouples with a wire diameter of 0.5mm were chosen. These thermocouples are resistant to oxidation in air and, because of their high melting points, can be used up to very high temperatures. The upper temperature limit of use for types S thermocouples in an oxidizing atmosphere is quoted as high as 1600°C (for 0.5mm diameter wires). An S-type T/C is presented in **Figure 4**. The temperatures measured by the thermocouples are automatically saved in the computer, using the Picolog program.

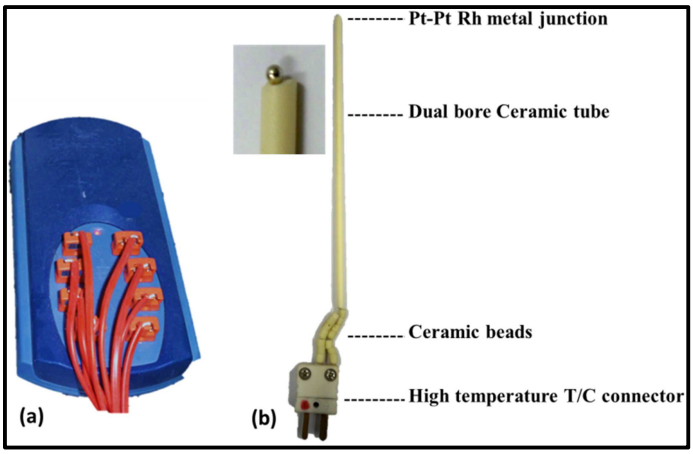

Figure 4: (a) Picolog (b) S-type thermocouple constructed in the laboratory

A software and hardware developed at SEGAINVEX in conjunction with an electrical cabinet were used to control the furnace. The various elements comprising the electrical cabinet used for controlling the furnace temperature include six 1kW single phase transformers, thyristor units, used in conjunction with two Eurotherm temperature controllers, connections for thermocouple terminations, communication ports, and circuit breaking elements. The Graphical User Interface (GUI) is performed to program the temperature ramps for each zone of the furnace as presented in **Figure 5.**

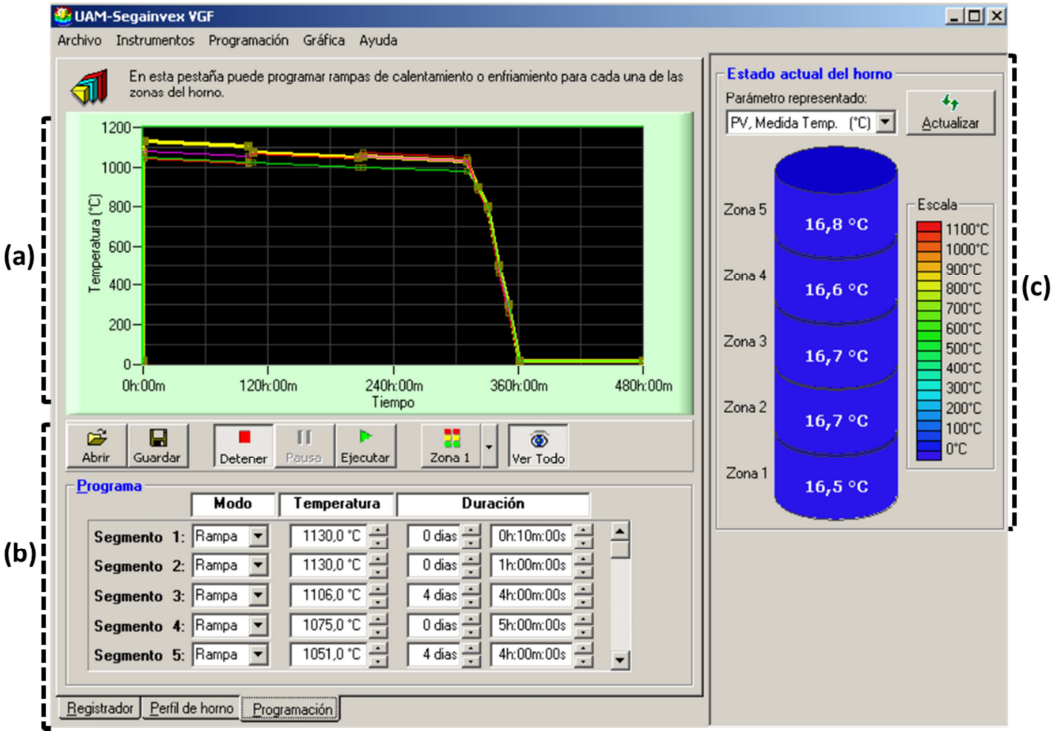

Figure 5: GUI software used to control VGF furnace (a) temperature plot window showing the programmed temperature, (b) the program window where the temperature ramps are created, (c) window related to the furnace temperature.

II.2.4. Material synthesis

The starting materials play an important role in the homogenization process and also in the reduction of the impurities in the grown CdZnTe crystals. It is well known that the presence of various impurities introduces different defect levels, which distinctly affect the electrical properties of CZT (4).

High purity 7N elemental Cd, Zn, and Te from 5N plus company were used in this work. 7N is the highest quality material for CdZnTe starting material. This purity level is determined by the net concentration of impurities not more than 100ppb. In **Table 5** are presented the GDMS analysis for some impurities in Te, Cd and Zn starting material**.** We observe that there exists a background concentration of impurities which may act as acceptors or donors. This behavior of the impurities has the effect of changing the electrical compensation of the material.

Table 5: GDMS analysis (ppb) for Te, Cd and Zn starting material

	Te	Cd	Zn
Li	<10	<4	<2
In	<2	<10	0.9
Mn	<2	<20	<0.3
Fe	<1	<15	18
Na	<7	<1	<1
P	<5	<0.8	<0.8
Cu	<5	<1	<30
Te	Matrix	<6	<1
Cd	<14	Matrix	7
Zn	<16	72	Matrix

The loading of material were carried out inside an argon purged glove box, the elemental material was loaded in order from bottom of the pBN crucible to top: tellurium, zinc, and cadmium. This crucible is then loaded into the ampoule to be used for crystal growth. The sizes of the charges grown in this work were between 120-180g for the 25mm ingot diameter. After charging, the ampoule is immediately placed under vacuum.

The vacuum system used in the present crystal growth is composed of a turbo pump Pfeiffer. In order to speed up the rate of air extraction, we have added a cooling trap that

can be filled with liquid nitrogen before the pump worked. Due to the low temperature caused by the liquid nitrogen, the vapor molecules was cooled and shortened the time for extracting air. With this process, a high vacuum of 10^{-7}mbar is finally achieved.

The ampoule is then sealed with a quartz rod located on the top of the ampoule and placed inside the furnace to start the growth.

The thermal cycle which has been used for CdZnTe synthesis is presented in **Figure 6**.

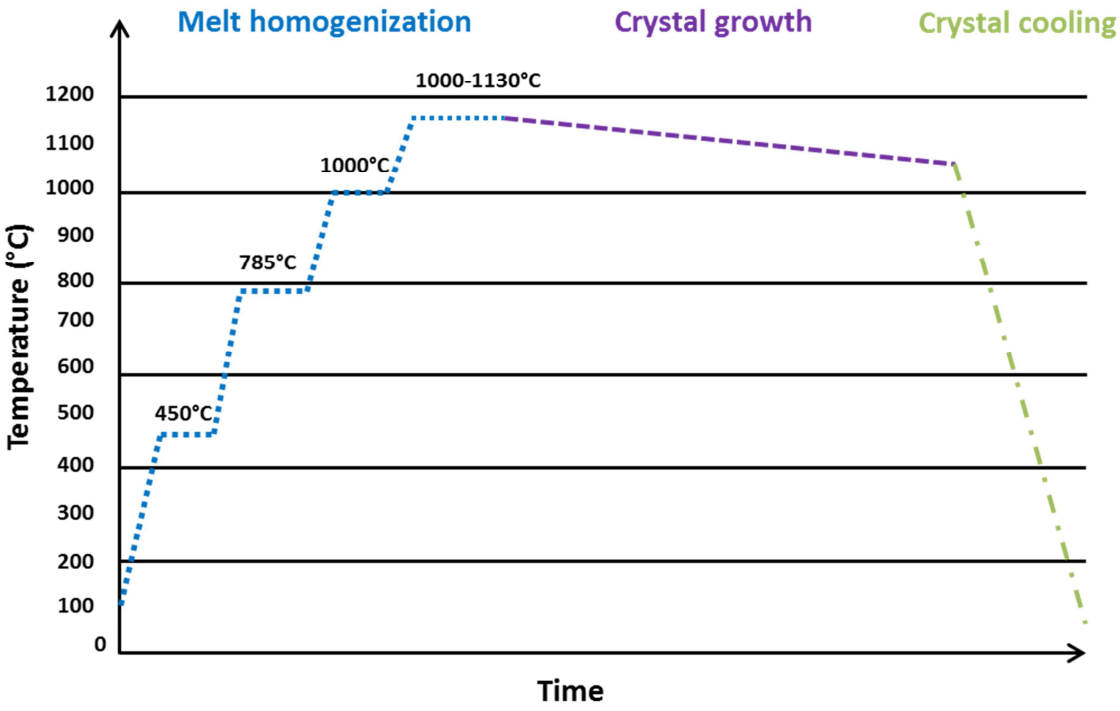

Figure 6: Thermal cycle for CdZnTe synthesis

This cycle is divided into three steps: melt homogenization, crystal growth, and crystal cooling. The temperatures and times used for each process have a great impact on the crystals properties. The homogenization process of CdZnTe could be divided into four phases:

Temperature ramp to 450°C:

This temperature is related to the reaction between Cd and Te to form CdTe. It is important to note that this temperature is above the melting point of Cd (320°C), Zn (419°C) and Te (450°C).

Temperature ramp to 785°C:

The temperature set point of 785°C which is above the boiling point of Cd(765°C), was of interest to observe if there were any exothermic reactions associated with unreacted Cd and Te.

Temperature ramp to 1000°C:

This temperature is above the boiling point of Cd, Zn (907°C), and Te (990°C) but still below the melting point of CdZnTe. In some cases small exothermic reactions could be observed to take place, and could be associated with the fusion of unreacted Cd and Te.

Temperature ramp to 1100-1130°C:

This temperature is above the melting point of CdZnTe with the objective to break of Te particles in the melt. This phase is very important to achieve homogeneous material with good optical and electrical properties.

II.3. Sample preparation

The performance of the detector is influenced by the techniques used to treat the surface. This includes the preparation of the samples prior to the deposition of the contacts.

Surface treatment is a critical and sensitive process in the fabrication of cadmium zinc telluride (CZT) radiation detectors, and plays a critical role in determining the detectors performance (5). In fact, CdZnTe is a very difficult material to prepare, especially to lap and polish with very little mechanical damage.

II.3.1. Cutting

After removing the ingot from the ampoule, the ingot is sliced in small pieces depending of the required geometry. As shown in **Figure 7**, an horizontal 3032 Well diamond machine, with a diamond wire of 170µm diameter was used for cutting the CdZnte samples. The sample holder is attached to a counter-balanced arm that uses appropriated weights to establish and maintain the proper amount of force throughout the entire cut. A microscope was also mounted to accomplish an accurate positioning of the diamond wire and watch the cutting. In order to avoid the cracking of the samples, the wire must be soaked continuously. For this, we use a solution of 1000ml of distilled water and 2ml of the solution recommended by Well.

It important to note that cutting can introduce defects such as microcracks and dislocations which can deteriorate the detector performance. Therefore, lapping and polishing processes are necessary to remove these damages and improve the surface of the samples.

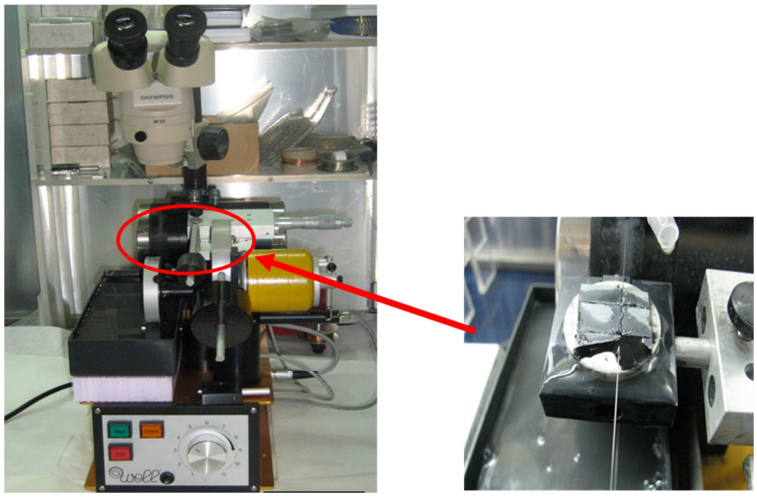

Figure 7: cutting machine and CdZnTe wafer being cut using diamond wire

II.3.2. Lapping

CZT samples were lapped in order to remove subsurface damage caused by sawing and produce the required thickness and flatness (5). As presented in **Figure 8**, the process was carried out using a Logitech PM5 machine with a standard glass plate operating at 50RPM. The abrasive slurries used for bulk material removal were generally following the order of 9µm and 3µm Al_2O_3 powders, supplied by Logitech. The PM5 system was used in conjunction with a jig for controlling the pressure and material removal rates. The samples were fixed with a wax on a glass sacrificial piece by using a hot plate.

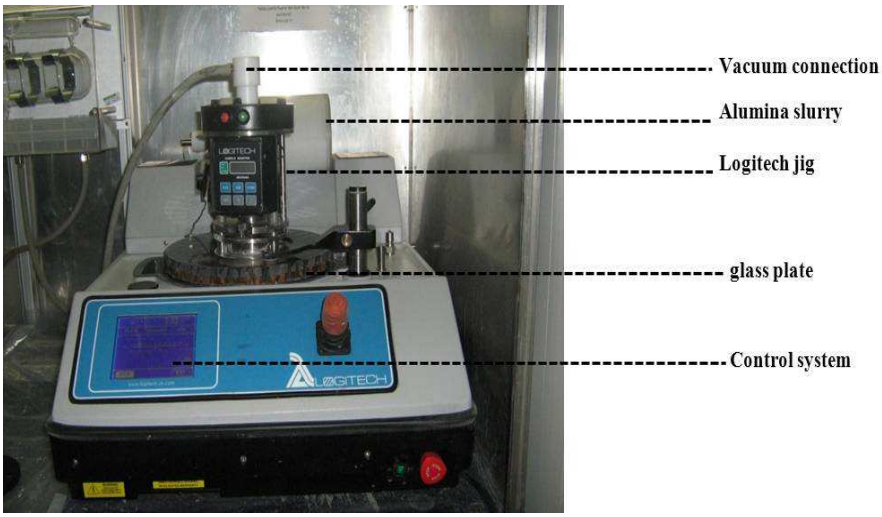

Figure 8: PM5 Logitech lapping and polishing machine of CdZnTe

The principle of lapping process is to press the wafer against a moving plate, while slurry is added continuously. The slurry contains abrasives, which play a significant role during lapping. The plate is in direct contact with the sample and removes the material. The abrasives in the slurry support this mechanical removal.

The Preston equation is a basic attempt to describe the material removal rate (MRR) on the surface during lapping (6).

Equation 1 $$\boldsymbol{MRR = C \times P \times v}$$

Where, C is a multipurpose constant that includes the effects of chemistry, temperature, and other process parameters. P is the applied pressure and *v* is the velocity of the plate. This equation assumes that the MRR depends on the pressure and relative velocity between sample and plate.

The material removal rate for lapping process using 9 and 3µm Al_2O_3 and different pressures is shown in **Figure 9**. For smaller samples, a pressure of no more than 1 g/mm^2 was applied during the process. One can observe that using 9µm Al_2O_3 lapping the removal material rate is higher than 25µm/min using a pressure of 10kPa, while using the same pressure for 3µm Al_2O_3 lapping only 10µm/min was removed. In fact, lapping process using 9µm Al_2O_3 could be used for achieving large stock removal after cutting damage. Using pressure higher than 15kPa can let to the breaking of the samples, and therefore it was avoided.

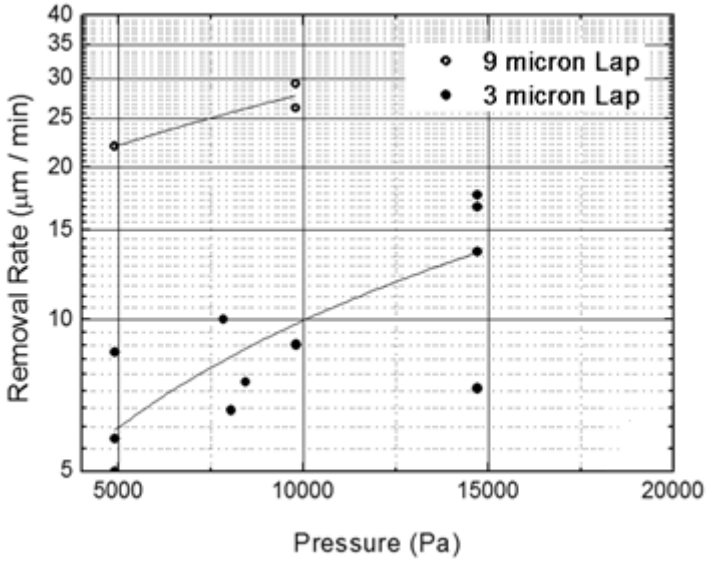

Figure 9: Material removal rate for lapping using different slurries and pressures

II.3.3. Mechanical polishing

While the lapping process removes a significant damage layer induced after cutting, the objective of the mechanical polishing was to reduce the thickness of the amorphous subsurface damage layer and to improve the surface quality. This treatment is also performed with the same Logitech system, but using a pad (Chemcloth) and, again, 3µm Al_2O_3 and 1µm diamond powder.

The material removal rate for polishing process has been also studied using 3 and 1µm at different pressures, and is shown in **Figure 10**. Despite the high pressure used for polishing compared with lapping process, the removal material rate is very low. 1µm polishing has a very low removal rate, but is effective to reduce the surface roughness. Using 3µm Al_2O_3 and a pressure of 30kPa, we can only remove 5µm/min.

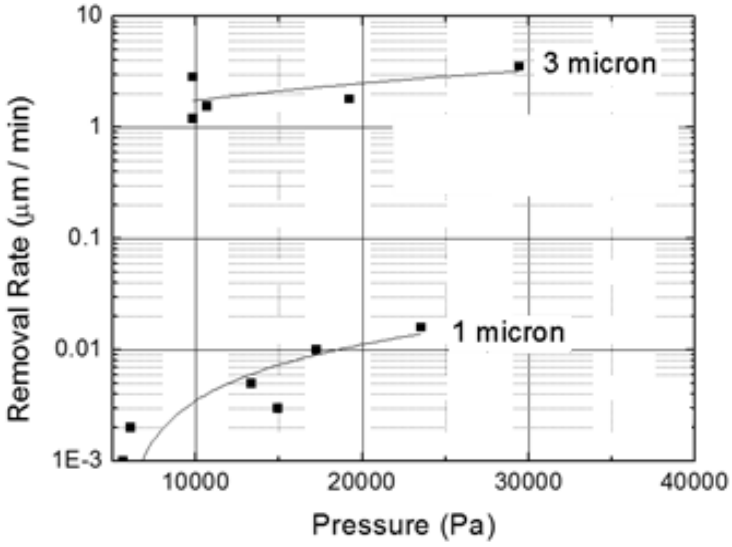

Figure 10: Material removal rate for polishing using different slurries and pressures

II.3.4. Chemical mechanical polishing

In order to improve the surface quality of the detector fabrication, the process is continued by using a fine chemical mechanical polishing (CMP), carried out by using a CP3000 Logitech system with 1µm diamond slurry.

CMP is a technique that combines both chemical and mechanical polishing principles to achieve uniform removal rates of a highly composite specimen. CMP is typically done using a polishing pad combined with a slurry of finely dispersed alumina or silica particles in an alkaline solution. CMP combines the selectivity of chemical polishing with the mechanical removal properties of standard mechanical polishing techniques. This conbination give excellent selectivity and planarity and can be tailored to many different materials.

The system, presented in **Figure 11**, consisted of the CP3000 chemical polishing system, a peristaltic pump used for slurry delivery, and a holding tank from which the fresh slurry was pumped (a), and to which the used slurry was deposited (b).

It is important to note that the choice of polishing pads, slurries, pressure on samples, pad velocity, drip rate of slurries are fundamental factors to control the quality and uniformity of the samples.

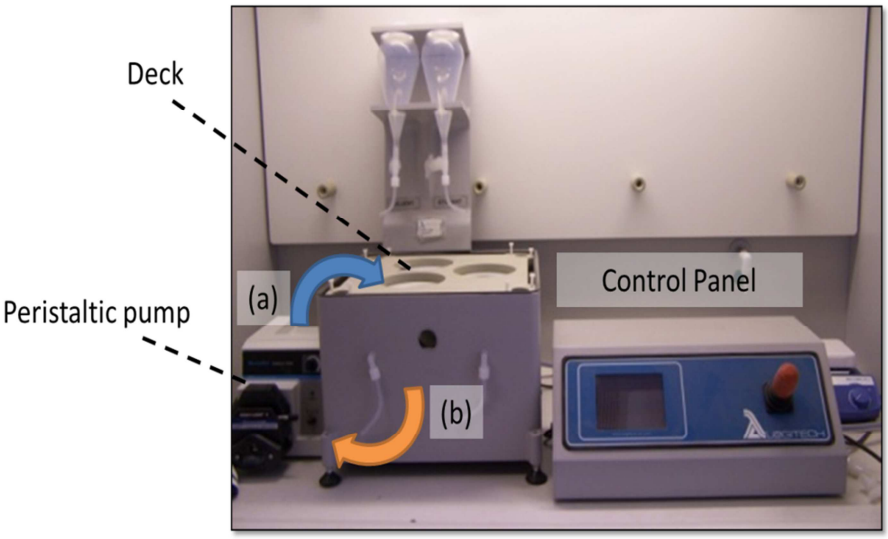

Figure 11 : PM5 Logitech chemical polishing machine of CdZnTe

II.4. Detector preparation

CdZnTe detector devices are fabricated by applying metallic contacts on the finely prepared parallel surfaces. The contacts serve as electrodes, cathode and anode that collect charges mobilized by an internal electric field due to the applied bias.

The three major device configurations for room temperature detector are simple planar, co-planar grid and pixellated configurations. Simple planar and co-planar grid configurations are generally used for large-volume single detectors. Pixellated detectors are used in imaging systems where position information is obtained in signals from individual pixels. Photolithography is used to design complex electrode structures such as co-planar and pixellated electrodes.

II.4.1. Etching

For radiation detector application, etching is usually performed before contact deposition to remove the damaged layer produced after wafer cutting, lapping, and polishing.

The chemical etching process can be achieved in three steps. The first step involves the transport of the reactants to the surface. The second step is the surface reactions involving electron transfer process, while the third step is the transport of the products from the surface to the solution, leaving a clean material surface thereby reducing the surface states and in consequence the leakage current.

The composition of the surface depends on the pH, chemical composition and aging of the solutions used (7). For CdTe or CdZnTe, chemical etching solution is based on a mixture of bromine and alcohol. Traditionally, methanol has been used to etch CdZnTe. The samples react with Br-MeOH solution following (this reaction will be discussed in details in chapter 4):

Equation 2 $$CdTe + 3Br_2 \rightarrow CdBr_2 + TeBr_4$$

This process results in a smooth, clean surface however the surface composition is usually tellurium rich due to the preferential etching of cadmium by the bromine solution. It has been reported that if this Te layer is exposed to air, it will rapidly oxidizes, therefore Te atoms oxidize to TeO_x and in majority to TeO_2.

The interaction of the metal film with the etched surface will control the electrical characteristics of that contact, so a good understanding of morphology and electrical properties of surfaces prepared in this way is essential.

II.4.2. Metallization

Wafer metallization is the deposition of a thin film of conductive metal onto the wafer surface. The type of metal used for the contact is an important selection parameter. High work function metals such as gold or platinum will form ohmic (charge injecting) contacts on p-type semiconductors, whereas low work function metals such as indium will form ohmic contacts on n-type semiconductors. Gold and platinum are the most used contacts materials with CdZnTe (8) (9). They are applied trough sputtering, thermal evaporation, or electroless deposition.

II.4.2.1. Electroless

Electroless method with $AuCl_3$ is the most commonly used commercially (10). Electroless is frequently used for CdZnTe in order to create a strong chemical bond between semiconductor and metal compared to sputtering and evaporation, and at the same time minimize the formation of oxides at the metal/CZT interface. During the gold electroless process, the Cd is preferentially removed creating a layer of gold which adheres strongly to the substrate as a result of the strong chemical bond between Au and Te. As shown in **Figure 12** electroless deposition must be done immediately after etching in order to avoid the formation of Te oxide.

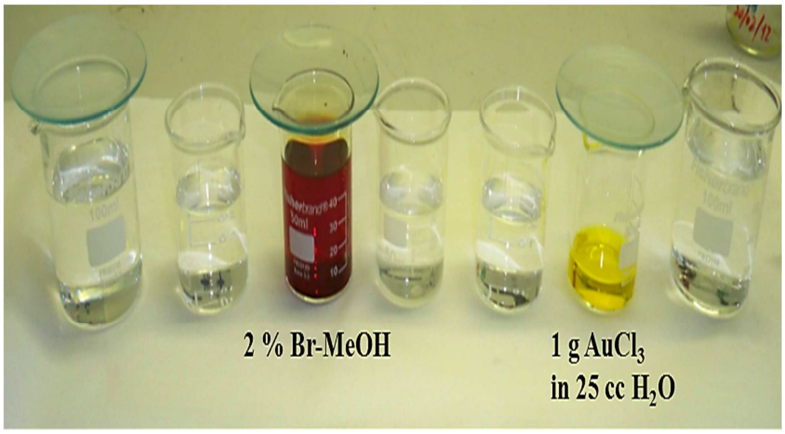

Figure 12: Electroless process

Figure 13 presents a CZT sample after polishing, Au deposition process with electroless, and after lateral edge polishing. We can observe smooth gold contacts deposited on the sample due to a good polishing done before the contact.

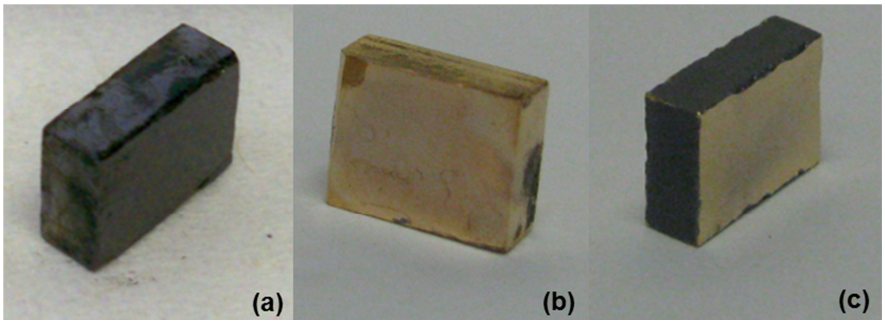

Figure 13: CZT simple after: (a) Polishing step, (b) Au contact and (c) lateral edge polishing

II.4.2.2. Sputtering

Thin film deposition via sputtering involves the physical removal of atoms from a metallic or pressed target through bombardment with high energy ions. Sputtered atoms are ejected from the target and fly across the chamber where they condense onto the substrate. In sputtering methods, a voltage is applied between the target and the substrate to generate ions and accelerate them toward the target.

Sputtering, a form of physical vapor deposition (PVD) is widely used for depositing gold. It is a physical process that dislodges atoms from a metal target and deposits the atoms on the wafer surface. **Figure 14** shows the sputtering machine and the deposition chamber used for Au deposition.

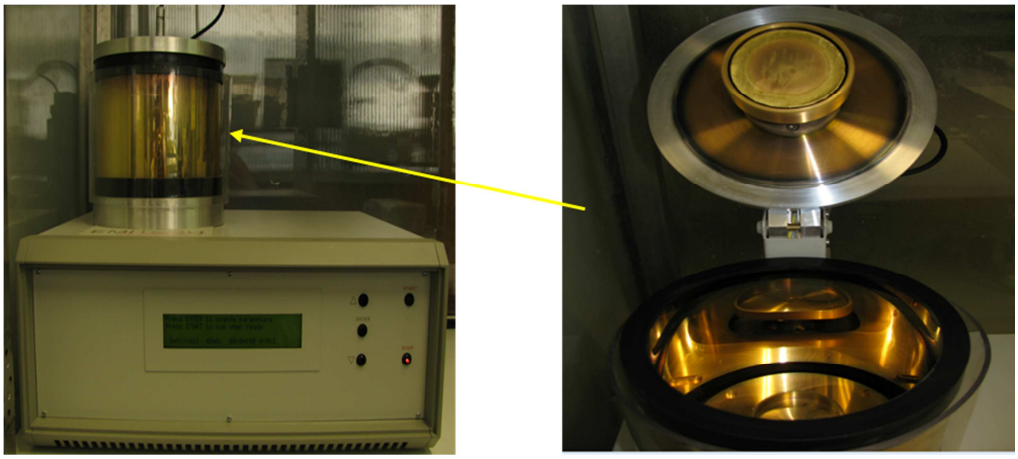

Figure 14: Sputtering equipment used for gold deposition

II.4.2.3. Thermal evaporation

Evaporation is a common physical vapor deposition method of thin film. The source material is heated and evaporated in a vacuum. The vacuum allows vapor particles to travel directly to the target object (CZT samples), where they condense back to a solid state. Generally, if the substrate has a rough surface, the evaporated material deposit from a single direction leading to a non-uniform layer.

II.4.3. Lateral edges passivation

Surface passivation is the process by which the semiconductor surface is rendered inert and does not change semiconductor properties as a result of interaction with air or other materials in contact with the surface or edge of the crystal (11).

Mechanical polishing followed by bromine-methanol etching is routinely employed for CZT surface preparation prior to device fabrication. This treatment removes the native oxide but leaves a Te-rich surface of the lateral edges. The surface passivation of CdZnTe detectors is an important step in the device manufacturing. Therefore, the process of passivation had been typically required to reduce the conductivity of the Te-enriched surface layer and decrease the surface leakage current (12).Various methods have been studied for the CZT surface passivation, which could oxide the surface. Previous studies have shown that hydrogen peroxide (H_2O_2) forms oxides tellurium on the CZT surface, thus acting as a good passivating agent (13). The KOH aqueous solution leaves a more stoichiometric and smoother CZT surface (14). NH_4F/H_2O_2 is an effective passivant which reports the most stoichiometric surface and the lowest leakage current (15) (16) (12). It has been demonstrated that passivation using $(NH_4)_2S$ reconstructs the surface due to the effective removal of CdO and TeO_2 and saturation of the dangling bonds with the formation of CdS, making a chemically stable and highly

resistive surface (17). Presented below in **Table 6** is a summary of the different passivants used for CdZnTe. The passivation process in our investigation was carried out by using 2.68g NH_4F 8ml H_2O_2 17ml H_2O for 10min (12). These results will be discussed in chapter 4.

Table 6: different passivants used for CdZnTe

Passivants	Composition	Time (min)	References
NH_4F:H_2O_2: H2O	2.68g:8ml:17ml	10	(12) (18)
NH_4F:H_2O_2: H2O	3g:2.05ml:24ml	15	(19)
		45	(20)
		6-12	(21)
KOH : H_2O	4.5g:25ml	30	(19)
		40	(20)
KOH:H_2O_2:H_2O	4.5g:3.07ml:21ml	5	(19)
H_2O_2: H_2O	10.25ml:15ml	2	(22)
		5	(19)
H_2O_2 followed by KOH	10.25ml:15ml /4.5g:25ml	5/30	(19)

II.5. Techniques of characterization

During this investigation, various techniques of characterization have been used in order to study the compositional, structural, optical and electrical properties of CdZnTe material.

II.5.1. Structural and compositional characterization

II.5.1.1. High resolution of X-ray diffraction (HRXRD)

High resolution of X-ray diffraction (HRXRD) is an important non-destructive method to study the crystallographic structure of the crystalline materials. Typical routine applications of this technique include rocking curves, X-ray reflectivity measurements, coupled scans, and reciprocal space mapping. Particularly, rocking curves can provide information about the defects such as dislocation density, mosaic spread, curvature, misorientation, inhomogeneity, and lattice mismatch.

Rocking curve is widely used to evaluate the structural quality of CdZnTe. The full width at half-maximum (FWHM) is commonly used as a measure of the crystalline quality. The narrower the FWHM means better crystalline quality (23).

The experimental set-up used during this investigation consists in a rotating anode generator which allows the monochromatization and collimation of the necessary radiation to obtain high resolution. It incorporates a 4 circles goniometer with large format which can work at high and low temperatures. The incident angle, ω, is defined between the X-ray source and specimen. The diffracted angle, 2θ, is defined between the incident beam and detector angle.

The characteristics of the diffractometer are operated by four Ge monochromator optimized with the (220) and (440) reflections, equipment with electronic motors, the output of these only obtain photons with the wavelength CuKα1 (λ = 1.540562Å).

II.5.1.2. Inductively coupled plasma- mass spectroscopy (ICP-MS)

Inductively coupled plasma- mass spectrometery (ICP-MS) is an analytical technique that performs elemental analysis with excellent sensitivity. The technique was commercially introduced in 1983 and has gained general acceptance in many types of laboratories. It is capable of analyzing all elements from lithium to uranium and can be applied to solutions, solids and gasses. It can perform qualitative, semiquantitative, and quantitative analysis. This technique is able to analyse only positive ions, so the elements like C, N, O and halogens cannot be quantified.

In this work, this technique has been used to determine the concentration of dopants, impurities, and at the same time to obtain concentration of the main elements Te, Cd, and Zn. The schematic of inductively coupled plasma mass spectrometer is summarized in **Figure 15**. The samples are introduced either as solutions in the form of a fine aerosol in Ar or Ar-He gas mixture or, alternatively, solid materials can be sampled directly using laser ablation. The fine aerosol from the solution, or the ablated material from the laser sampling, enters the RF-generated argon plasma where virtually all atoms and molecules are converted to ions before they enter the high vacuum stage of the mass spectrometer through a small entrance hole in the interface. The ions are accelerated and focused into an ion beam by a series of electrostatic lenses. The ion beam is then analysed by a fast switching mass filter (the quadrupole). The mass filter selects particles on the basis of their mass/charge ratio so that only specific isotopes are allowed through the filter and can enter the electron multiplier detector mounted at the

end of the quadrupole. Fast switching of the quadrupole settings enables scanning or peak jumping over the mass spectrum. Detected signals of individual isotopes can be converted to isotopic ratios or, when standards are measured along with the unknowns, to the element concentrations.

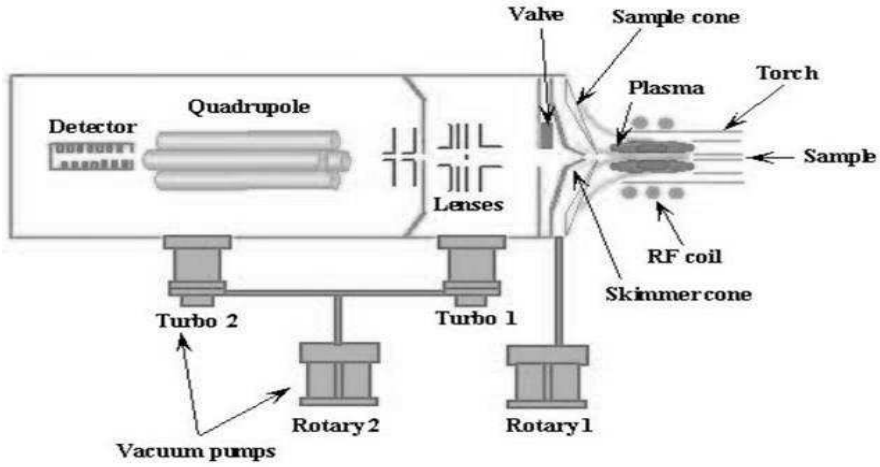

Figure 15: Schematic of inductively coupled plasma mass spectrometer

II.5.1.3. X-Ray photoemission spectroscopy (XPS)

X-Ray Photoemission Spectroscopy (XPS), also known as Electron Spectroscopy for Chemical Analysis (ESCA), is the most widely used surface analysis technique because of its relative simplicity in use and data interpretation. The sample is irradiated with X-rays causing photoelectrons to be emitted from the sample surface. From the binding energy and intensity of a photoelectron peak, the elemental identity, chemical state, and quantity of an element could be determined. This technique is used to characterize the surface of solids to a depth of 10-100Å, or 5-10nm, depending on the material studied.

XPS detects all elements with an atomic number higher than 3. It cannot detect hydrogen or helium because the diameter of these orbitals is so small.

The sample analysis is conducted in a vacuum chamber, under the best vacuum conditions achievable, typically ~10^{-10}torr. This facilitates the transmission of the photoelectrons to the analyser but more importantly minimizes the re-contamination rate of a freshly cleaned sample. This is crucial because XPS is very surface-sensitive, with a typical “sampling depth” of only a few nanometres.

X-ray photoelectron spectroscopy operates on the principle of the photoelectric effect, which occurs via excitation process by X-ray irradiation producing electrons (photoelectrons) of discrete energy, containing chemical information regarding the surface analyse. It should be noted that X-rays are only one of many types of excitation

sources that can be used to induce emission of electrons for analysis. In XPS, the energy of a photon is transferred to the electron in the sample. Electrons released are analysed for their kinetic energy, which can be used to determine the binding energy level of the electron.

The equation describing the energetics of the photoionization process is:

Equation 3 $$h\nu = E_B + E_K$$

where $h\nu$ is the X-ray photon energy, E_B is the binding energy of the electron from a particular energy level, and E_K is the kinetic energy of the ejected photoelectron.

Taking into account that the binding energies of energy levels in solids are conventionally measured with respect to the Fermi-level of the solid, rather than the vacuum level. To correct this discrepancy with **Equation 3**, a constant is added, accounting for the difference between the Fermi level and vacuum level. This constant is known as the work function (Φ) of the solid.

XPS counts electrons ejected from a sample surface when irradiated by X-rays, and a spectrum representing the number of electrons recorded at a sequence of energies includes both a contribution from a background signal and also resonance peaks characteristic of the bound states of the electrons in the surface atoms.

XPS spectra are, for the most part, quantified in terms of peak intensities and peak positions. The peak intensities measure how much of a material is at the surface, while the peak positions indicate the elemental and chemical composition. Other values, such as the full width at half maximum (FWHM) are useful indicators of chemical state changes and physical influences.

XPS is used to not only to identify the elements but also to quantify the chemical composition. The atomic concentration on the surface of a sample can be expressed as (24):

Equation 4 $$C_i = \frac{I_i/S_i}{\sum_i I_i/S_i}$$

Where I_i is the peak area for element i, and S_i is the sensitivity factor for the peak i.

II.5.2. Surface characterization

II.5.2.1. Scanning electron microscopy (SEM)

The scanning electron microscope (SEM) is a powerful characterization technique that uses a beam of highly energetic electrons to examine objects on a very fine scale. The signals that derive from electron sample interactions can give information about the

topography (surface features of a sample), morphology (shape and size of the particles on the surface of the sample), and composition.

Accelerated electrons in an SEM carry significant amounts of kinetic energy, and this energy is dissipated as a variety of signals produced by electron-sample interactions when the incident electrons are decelerated in the solid sample as shown in **Figure 16**. These signals include secondary electrons (that produce SEM images), backscattered electrons (BSE), diffracted backscattered electrons (EBSD that are used to determine crystal structures and orientations of minerals), and visible light (cathodoluminescence). Secondary electrons and backscattered electrons are commonly used for imaging samples. In fact, secondary electrons are most valuable for showing morphology and topography on samples while backscattered electrons are most valuable for illustrating contrasts in composition in multiphase samples.

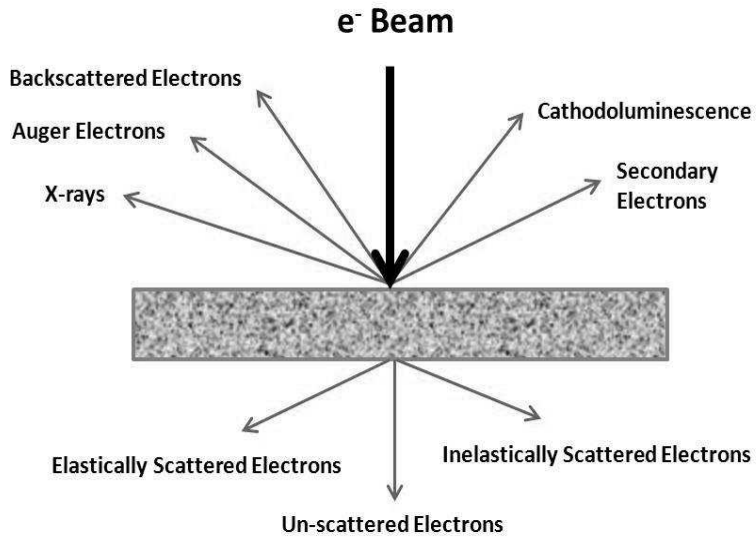

Figure 16: Electron beam interactions with a solid sample relevant to scanning electron microscopy

In this work SEM measurements were made using (Hitachi S-3000N) coupled to an energy dispersive X-ray (EDX) analyser (Oxford Instruments, INCAx-sight model).

II.5.2.2. Atomic force microscopy (AFM)

The atomic force microscope (AFM) or scanning force microscope (SFM) was invented in 1986 by Binnig, Quate and Gerber. Similar to other scanning probe microscopes, the AFM raster scans a sharp probe over the surface of a sample and measures the changes in force between the probe tip and the sample.

Figure 17 illustrates the working concept for an atomic force microscope. A cantilever with a sharp tip is positioned above a surface, and depending on this separation distance, long range or short range forces will dominate the interaction. This force is measured by the bending of the cantilever by an optical lever technique: a laser beam is focused on the back of a cantilever and reflected into a photodetector. Small forces between the tip and sample will cause less deflection than large forces. By raster-scanning the tip across the surface and recording the change in force as a function of position, a map of surface topography and other properties can be generated.

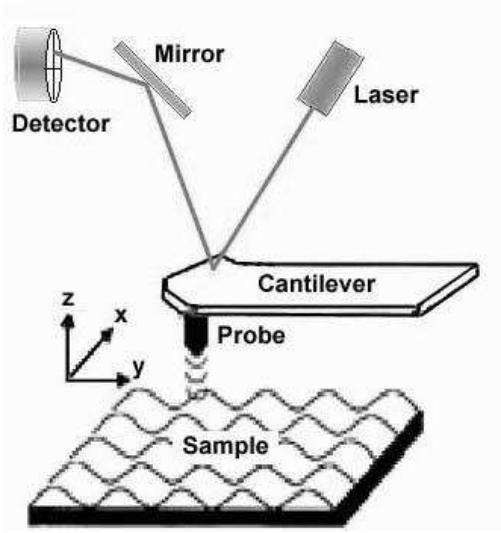

Figure 17: Scheme of the principle of atomic force microscope

The AFM may be operated in contact mode or non-contact mode, both of which are determined by the cantilevers position with respect to the surface.

The surfaces in this work have been investigated using the non-contact mode of the AFM. The non-contact mode has the advantage that the tip never makes contact with the sample and therefore cannot disturb or destroy the sample.

The AFM is useful for obtaining three-dimensional topographic information of insulating and conducting structures with lateral resolution down to 1.5 nm and vertical resolution down to 0.05nm. In general, the AFM is an industry standard for measuring the surface roughness. The AFM system used in this work is presented in **Figure 18.**

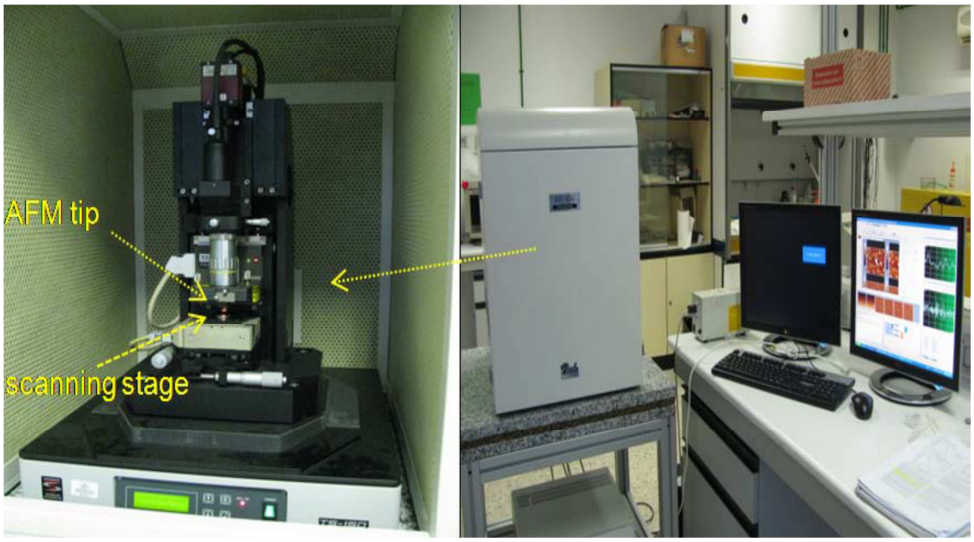

Figure 18: The AFM used for investigation of CdZnTe

II.5.3. Optical characterization

II.5.3.1. IR imaging microscopy

Te precipitates or inclusions are one of the defects formed during the crystal growth process in the ternary CdZnTe compound. These inclusions are considered as one of the factors limiting the performance of the radiation detector. CZT crystals are transparent when illuminated with infrared light while the internal defects such as tellurium inclusions are not, therefore, Te inclusions will act to either scatter or absorb the infrared light and show up as distinct black spots as shown in **Figure 19** which present an examples of Te inclusions distribution which have been measured for CZT sample. Image-pro Plus 6.0 software was used to calculate the size, diameter and concentrations of Te inclusions in the crystal.

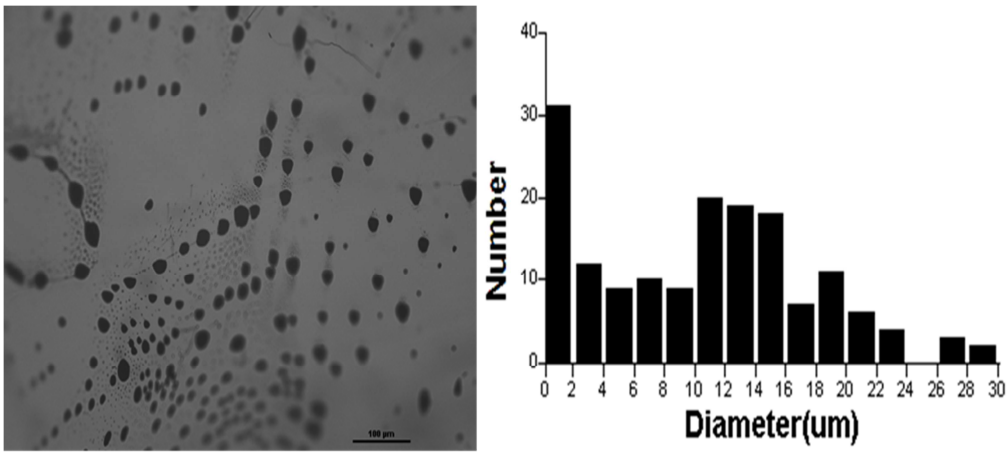

Figure 19: IR images of Te inclusions and diameter distribution (μm) of CZT sample

A Nihon 90i Infrared (IR) microscope imaging system has been developed and was used for optical characterization and measuring the size and density of Te inclusions in the CZT crystals. The system mainly consists of:

- An infrared back light.
- IR sensitive CCD camera with long objective microscope lens and a 7.8x10.6 mm^2 sensor with 2208x3000pixels, and
- The 3D translation stage.

To study the surface morphology bright-field (BF), dark-field (DF), and phase-contrast filter cubes were purchased. In the BF imaging mode, differences in absorption at the surface of the sample is used for differentiating materials or features at the surface. This mode has been used in conjunction with the phase-contrast filter cube for imaging of surface morphology and surface roughness.

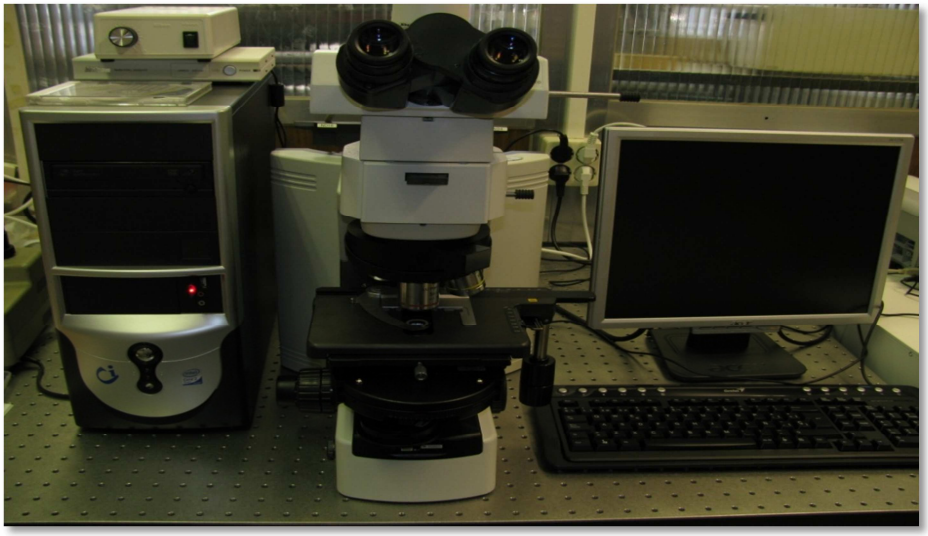

Figure 20: Nikon 90i IR microscope

Different objectives were used for the characterization of the surface and bulk crystals, ranging from 1x to 50x magnification.

By using the 3D translation stage, the system can perform a one, two, or three dimensional scan. At each XYZ position of the crystal, an image of the area is taken and saved, and then the translation stage moves to the next position where this is repeated. The system setup allowed us to acquire stacks of images, each focused at a different depth of the crystal. Te inclusions present within the bulk of CZT samples have been characterized using the transmission mode of the microscope.

II.5.3.2. Fourier transform infrared spectroscopy (FTIR)

Fourier transform infrared spectroscopy (FTIR) is most useful for identifying chemicals that are either organic or inorganic. It can be utilized to quantitate some components of an unknown mixture. It can be applied to the analysis of solids, liquids, and gasses. This technique can identify unknown materials, determine the quality of a sample, and determine the amount of components in a mixture.

In infrared spectroscopy, IR radiation is passed through a sample. Some of the infrared radiation is absorbed by the sample and some of it transmitted. The basic components of an FTIR are shown schematically in **Figure 21**.

The infrared source emits a broad band of different wavelength of infrared radiation. The IR radiation goes through an interferometer that modulates the infrared radiation, and then the interferometer performs an optical inverse Fourier transform on the entering IR radiation. The modulated IR beam passes through the sample where it is absorbed to various extents at different wavelengths by the various molecules present. Finally the intensity of the IR beam is detected by a detector. The detected signal is digitised and Fourier transformed by the computer to get the IR spectrum of the sample.

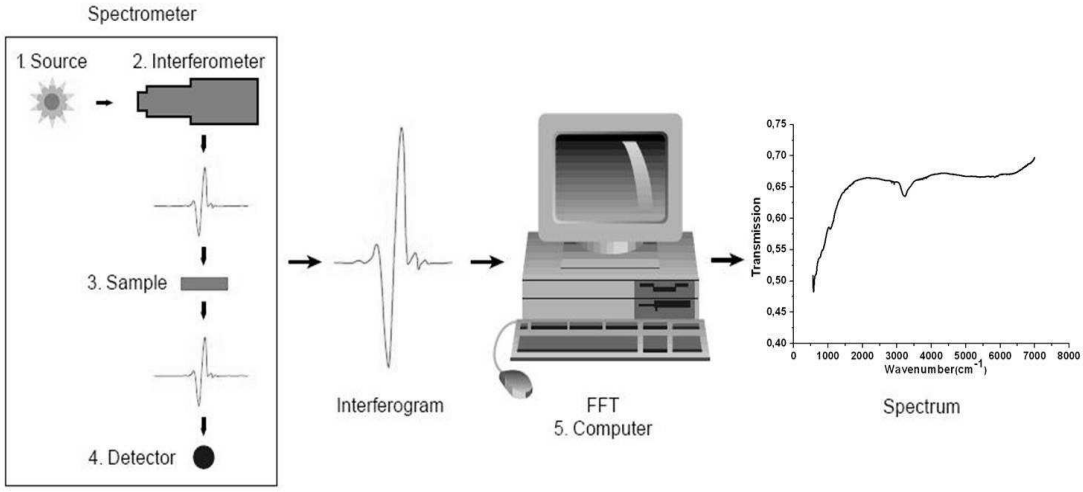

Figure 21: Basic components of FTIR

It has been thought that there is definitely a correlation between the presence of inclusions/precipitates and optical transmittance. However, free carrier absorption must also be considered. Yang et al. (25) suggested that the extinction of infrared light is dominated at higher energy by scattering of inclusions, and at lower energy by the absorption of free carriers. While, Qiang et al. (26) found that the density of Te precipitates/inclusions seems to have no obvious influence on the IR transmittance. According to the trends that IR transmission spectra change with the wavenumber, four

types of IR transmittance spectra were defined. Wafers with the descending type IR transmission spectrum had high dislocation density. Wafers with the ascending type spectrum had low resistivity. Wafers with the low straight type spectrum had high dislocation and low resistivity, whereas wafers with the high straight type spectrum had low dislocation and high resistivity.

II.5.3.3. Photoluminescence (PL)

Photoluminescence is a widely non-destructive technique used for the characterization of optical transitions in semiconductors.

In PL spectroscopy, photons are used to excite the surface of the semiconductor material; the incident monochromatic photon beam is partially reflected, absorbed, and transmitted by the material. The absorbed photons create electron-hole pairs in the semiconductor. The electrons are excited to the conduction band, or to the energy states within the gap. In consequence, the photons produced in respect to the various recombinations of electrons and holes are emitted from the sample surface and resulting to the photon emission spectrum that is studied in photoluminescence. The photon energies reflect the variety of energy states that are present in the semiconductor. Different energy states are produced by different defects, and by the impurities which are incorporated into the lattice. Consequently, a PL emission spectrum provides information concerning the point defect nature of a material by determining not only the presence, but also the type of these defects such as vacancies, interstitials, and impurities in the lattice.

The energy of the incident photons on the surface of a material can be higher or lower energy than its band gap energy (Eg). When this energy is greater than Eg, it is sufficient to excite carriers from the valence band to the conduction and generates an excess density of electrons and holes. If the energy is lower than Eg the transmission of photons through the material occur without absorption.

A free hole in the valence band and a free electron in the conduction band experience a Coulomb force as a pair of opposite charges and form a composite particle called an “exciton”. The electron and the hole are weakly bound to each other by their attractive electrostatic interaction and the electron can orbit about the hole as in the hydrogen atom. When the exciton is not trapped by a defect or impurity, it is called a free exciton. The energy states of the free exciton can be described by the hydrogen model as follows:

Equation 5 $$E_x = E_g - 2\pi^2 m_r^* q^4 / h^2 \varepsilon^2$$

where Eg is the band gap energy, h is the Plank's constant, Ɛ is the dielectric constant, and m_r* is the reduced effective mass of the electron-hole pair. The reduced mass is given by:

Equation 6 $$1/m_r^* = 1/m_e^* + 1/m_h^*$$

where m_e* is the electron effective mass and m_h * is the effective mass of the hole.

In a real material, there exist many kinds of impurities or defects. When excitons are near defects, the defects can either increase or decrease the binding energy of the exciton. When the defects reduce the total system energy of the exciton, excitons will be trapped about the defects, which lead to the formation of bound excitons. When the total system energy of the exciton is increased by a particular defect, the exciton will remain free.

In CdZnTe, excitons bound to ionized donors (D^+, X), excitons bound to neutral donors (D^0, X), and excitons bound to neutral acceptors (A^0, X) PL emission bands are observed (27) (28). However, excitons bound to ionized acceptors (A^-, X) PL emission band is not detected in this material. The observation of (D^+, X) emission or (A^-, X) PL emission bands in a particular material will depend on the ratio of electron and hole effective masses m_e and m_h. An exciton can be bound to an ionized donor if $m_h/m_e>1.4$. Similarly, an exciton can be bound to an ionized acceptor if $m_e/m_h>1.4$. Therefore, it is not expected that (D^+, X) and (A^-, X) PL emission bands coexist in the same material. In CdZnTe, mh/me is about 3, thus only (D^+, X) emission bands are observed, as has been verified by many experimental studies (25). In CZT, excitons bound to donors and acceptors exhibit PL emission peaks just below the free exciton PL emission line. The recombination process can also include electron transitions from neutral donor levels to the valence band (D^0, h) and electron transitions from the conduction band to neutral acceptor levels (e, A^0). In CdZnTe, DAP recombination between shallow donors and the shallow acceptors is also observed. **Figure 22** shows a summary of various energy levels in $Cd_{1-x}Zn_xTe$ relative to the valence and conduction band.

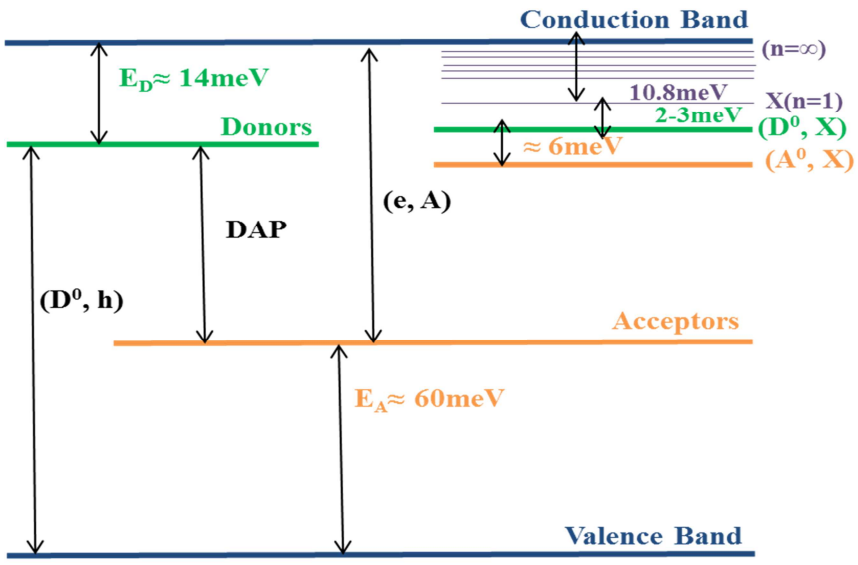

Figure 22: Energy level diagram showing various radiative transitions in $Cd_{1-x}Zn_xTe$

II.5.3.4. Raman spectroscopy

Raman scattering was first observed in 1928 and was used to investigate the vibrational states of many molecules in the 1930s. Initially, spectroscopic methods based on the phenomenon were used in research on the structure of relatively simple molecules. Over the past 20 years, however, the development of laser sources and new generations of monochromators and detectors has made possible the application of Raman spectroscopy to the solution of many problems of technological interest.

Raman spectroscopy is a technique based on inelastic scattering of monochromatic light, usually from a laser source. Photons of the laser light are absorbed by the sample and then reemitted. Frequency of the reemitted photons is shifted up or down in comparison with original monochromatic frequency, which is called the Raman effect. This shift provides information about vibrational, rotational and other low frequency transitions in molecules. In fact, Raman spectroscopy can be used to study solid, liquid and gaseous samples.

As shown in **Figure 23**, when a sample is irradiated with an intense monochromatic light source (usually a laser), most of the radiation is scattered by the sample at the same wavelength as that of the incoming laser radiation in a process known as Rayleigh scattering. Some of this scattered light is directed to the detector, which records the Raman spectrum.

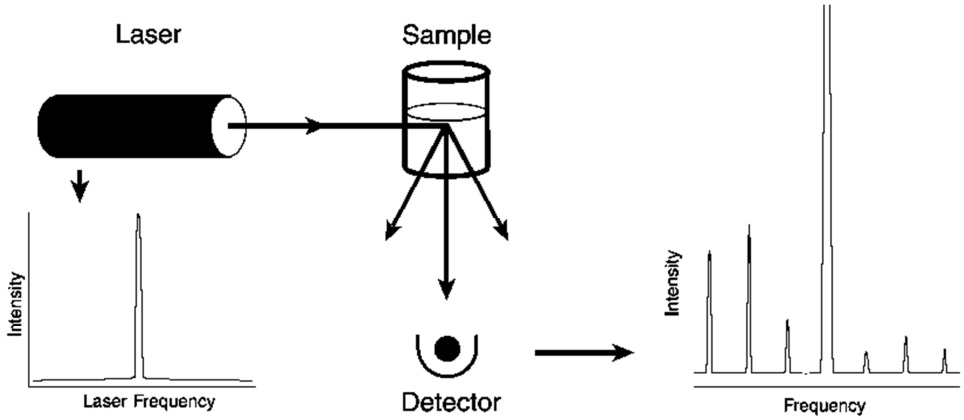

Figure 23: experimental design of Raman spectroscopy

In this investigation, Raman spectra were obtained with a HRLabRam spectrometer attached to a metallographic microscope. The excitation was done with He–Ne laser line at 633 nm, through a 100x microscope objective, which also collected the scattered light.

II.5.3.5. Cathodoluminescence (CL)

Cathodoluminescence (CL) is a surface sensitive characterization technique used for studying the electrical and optical properties of materials (29) (30). In materials science and semiconductor engineering, cathodoluminescence will mostly be performed in either a scanning electron microscope or a scanning transmission electron microscope. CL is a powerful technique to characterize defects, impurity concentration and phase composition in composite materials. CL offers a contactless and nondestructive method to characterize optical and electronic properties of nanostructures in many kinds of materials.

Cathodoluminescence is a phenomenon in which a beam of electrons**,** generated by an electron gun, is incident upon a material, causing the material to luminesce through the excitation of its electrons by the beam's current. The excitation depth from a crystal is commonly in the range of 2-8µm, which is depending on the energy of electrons. The energy transfer may occur in a crystal provided by the lattice, interaction of neighbouring lattice defects, or anion groups, and thus the emission site may have a distance from the site of excitation. The CL intensity is proportional to the accelerated voltage and the current density, however, the power level used is limited by the destruction of the specimen or the specific defects including luminescence centers under electron bombardment.

The CL signal is formed by detecting photons of the ultraviolet, visible, and near infrared regions of the spectrum. These photons are emitted as the result of electronic transitions between the conduction and valence bands and levels lying into the band gap of the material.

For CdTe and CdZnTe crystals, CL characterization has been used to identify the dominant acceptor bound exciton (A^0,X) and the free electron-to-bound acceptor (eA^0) transitions (30), to study the presence of Cd and Te vacancies (31), and also to study dislocations (32).

In this work, CL measurements were carried out at liquid nitrogen temperature (80 K) with a XiCLOne system (Gatan UK) attached to a LEO 1530-Carl Zeiss FESEM microscope. The luminescence signal was detected with a Peltier cooled CCD.

II.5.4. Electrical characterization

II.5.4.1. Contactless resistivity mapping (COREMA)

COREMA is a commercial device which is used to map the resistivity across an entire wafer. The measurement is non-contacting which avoid the problems connected with the fabrication of ohmic contacts. In addition, it allows the examination of wafers without degrading surface quality.

The concept of COREMA is based on the measurement of the dielectric relaxation time of the semiconductor τ defined as (33):

Equation 7

$$\boldsymbol{\tau = \varepsilon\varepsilon_0\rho}$$

where ε_0 and ε represent the permittivity of free space and the dielectric constant of the material. The sample is inserted into a capacitor as a lossy dielectric substance as shown in **Figure 24** and the resistivity is evaluated by measuring a time dependent charge transient observed after application of a voltage step.

The exponential time dependence of the charge Q(t) allows to measure the relaxation constant as well as the charges Q(0), Q(∞). To obtain the resistivity of the material, one can use the **Equation 8**. The measurements range of this equipment is 10^5-10^{11}Ω.cm.

Equation 8

$$\boldsymbol{\rho = \frac{\tau\, Q(0)}{\varepsilon_0 \varepsilon Q(\infty)}}$$

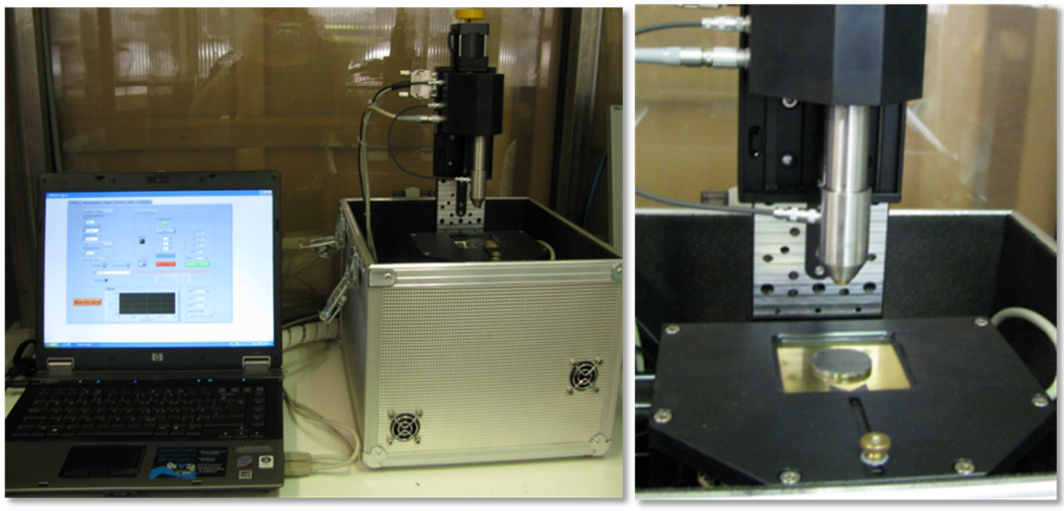

Figure 24: COREMA system

II.5.4.2. Current-voltage characteristics (I-V)

The current-voltage (I-V) characterization is used to measure the resistivity of the samples and check the contact's ohmicity. In this work, I-V was used to evaluate the detector performance, compare the effect of defects and surface preparations on the leakage current.

I-V measurements were done at room temperature using a Keithley 2400. The samples were measured applying a bias voltage from -200V to 200V. The resistivity was calculated following the equation:

Equation 9 $$\rho = \frac{R \times A}{L}$$

Where R and A are the resistance and contact area of the sample and L is the thickness.

The sample should be protected from light during the measurements in order to prevent free carrier absorption and excitation, which can increase carrier concentration and therefore decrease the resistivity.

The contact's ohmicity can be also extracted from these measurements:

Equation 10 $$I = aV^b$$

where *a* is constant and *b* is called the ohmicity. The parameter *b* implies the quality of the ohmic contact. For an ideal ohmic contact b equals to unity (34).

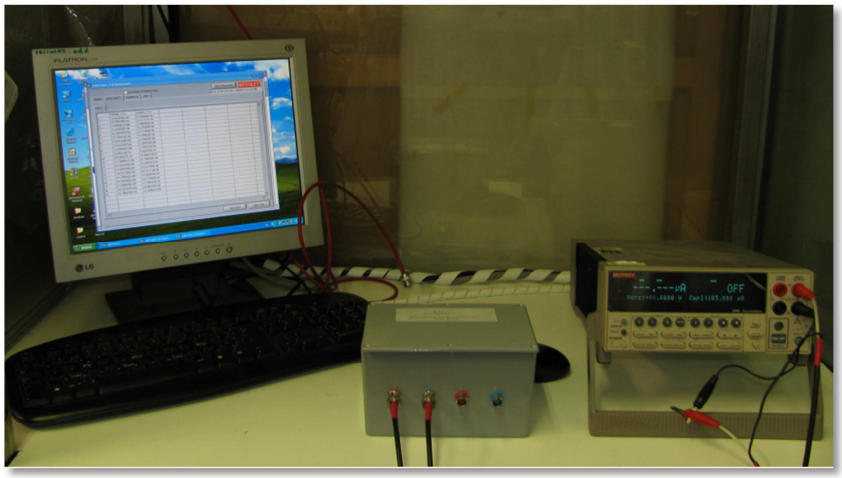

Figure 25: I-V system

II.5.4.3. Transient current technique (TCT)

The principle of TCT measurements is based on a direct time resolved measurement of the current arising from the drift of free charge carriers in an electric field. The transient current technique has been adapted to study the distribution of the electric field and calculate the mobility of electrons in CZT single crystals.

Figure 26 shows the experimental setup used for our TCT measurements. The sample was placed inside a copper shielding box and irradiated with a 5.5MeV ^{241}Am α-particle source at a distance of 3–5mm. the incident radiation creates an electron–hole plasma near the electrode. During the drift process electrons and holes can be trapped which leads to a reduction of current signal if the charge-carrier lifetime is in the order of or below the transit time (35). To collect the charge carriers, the detector was biased by a Tennelec TC 952 voltage supply. Charged carriers drifting through the detector create a current pulse that is amplified by a 2-GHz Miteq AM-1607–2000R amplifier. The signal is converted into a voltage pulse with a conversion factor of 6.536 mV/µA, and is then recorded by a 350-MHz digital oscilloscope LeCroy WaveSurfer 434. Since this method is very sensitive to electromagnetic interference, we placed two anti-parallel Schottky diodes at the input of the preamplifier to protect it from unexpectedly large pulses that could damage the input stage. It was proven that these diodes do not distort the signal. A second copper shielding was placed around the detector's shielding and the amplifier to improve the signal-to-noise ratio (36).

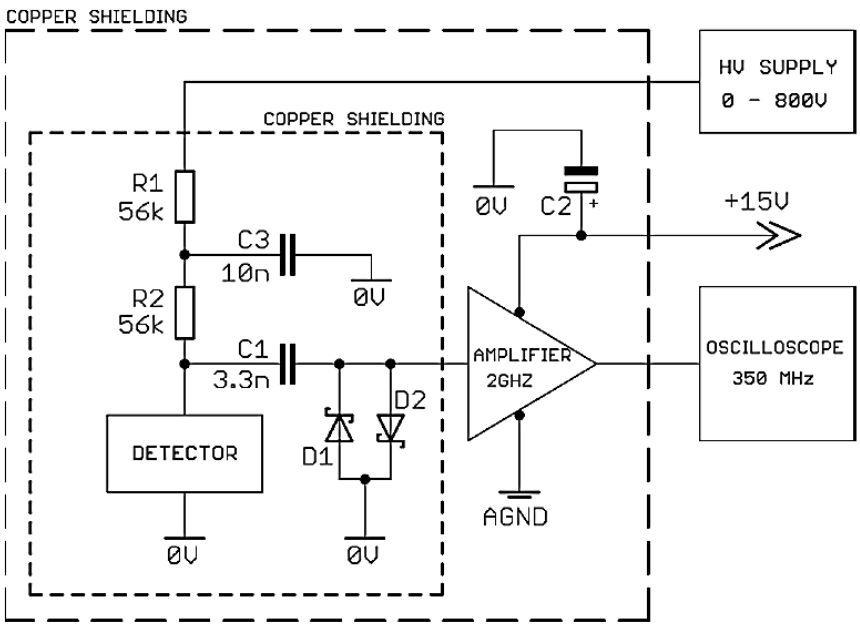

Figure 26: Schematic view of the TCT experiment

II.5.4.4. Gamma response

The equipment used for testing the CZT detectors was based on set of A250 charge sensitive preamplifiers from Amptek. **Figure 27** displays the experimental configuration for testing the CZT radiation detectors in our work at CIEMAT. As shown in this figure, the first stage of the preamp circuit shown on the right part is the Amptek A250 integrating amplifier with the 2SK152 Nchannel FET mounted onto the PC250 board. The PC250 board provides a convenient way to test the A250. From the noise performance curves given by Amptek, this FET seems to be the best solution for small capacity detectors. The preamp transfers the charge signal of the test detector into the 1 pF internal feedback capacitor of the A250. The decay time of the A250 circuit is expected to be 300μs. The PCB boards each contain the FET and A250 charge sensitive pre-amplifier.

The detector was mounted on a Teflon fixture designed by our laboratory, the mounting plate was made of gold and was connected to the anode, and the cathode side is made of a gold cantilever. The cathode of the detector was connected to high voltage, while the anode of the detector was connected to the input of the FET.

The bias voltage across the detector is filtered in the preamp box by a low pass filter with a time constant of 1s. The values of the default bias voltage circuit are optimised for bias currents up to a few nA. For higher bias currents the bias voltage across the detector will deviate considerately from the bias voltage that is set by the HVPS control.

The BNC connections of this configuration are used to connect the cathode to the bias voltage (left) and also connect the output of the A250 pre-amplifier with the input of the Ortec Dual Spec Amp 855 post-amplifier (right). All the BNC connections were made by using 50Ω coaxial cables with BNC terminations. The measurements were controlled and maintained at 20°C.

The measurements were carried out in the pulsed detector modes, in contrast to the current modes or mean square voltage (MSV) modes. In order to operate this mode properly, it is necessary to note that the time constant of the charge sensitive preamplifier is substantially larger than the time constant of the detectors.

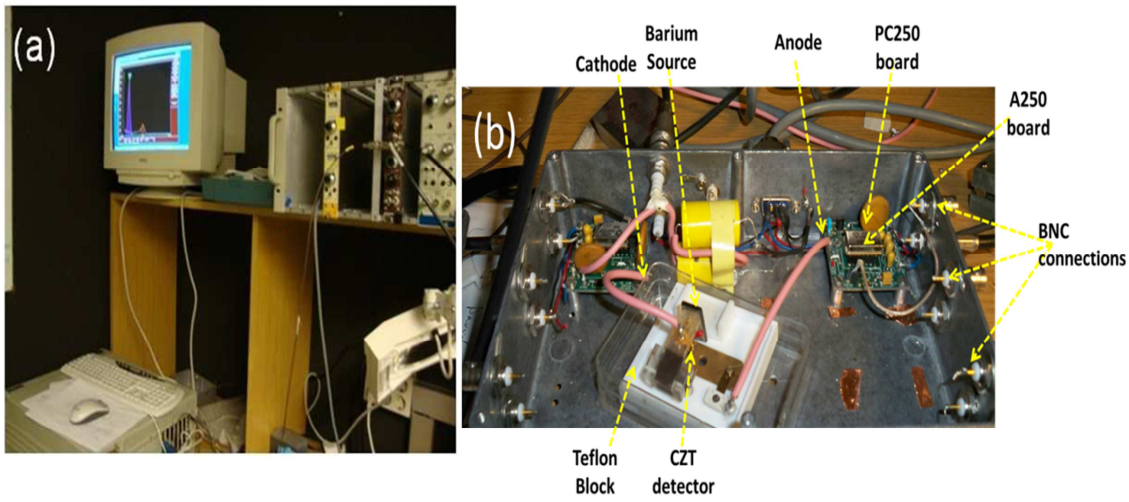

Figure 27: Testing equipment (a) test box with an installed CZT detector (b)

II.5.4.5. Thermoelectric effect spectroscopy (TEES)

The basic idea of the thermoelectric effect spectroscopy method is based on the temperature gradient induced diffusion of free charge carriers towards the electric contact at the cold end of the sample. If the deep traps are filled by illumination at low temperature, the subsequent rise of temperature causes the release of trapped carriers. Therefore, application of the thermal gradient across the sample results in thermoelectric current (I_{TEE}). TEES spectrum shows the dependence of I_{TEE} current measured as a function of the sample temperature (T). The different sign of peaks in TEES curves corresponds to the different types of charge carriers. Due to the low thermal conductivity of our semi-insulating CZT samples, temperature gradient (2-10K/cm) is obtained during heating the samples at heating rate below 0.16K/s.

An experimental setup for TEES measurements as shown in **Figure 28** is based on a liquid nitrogen cooled cryostat operating in the temperature range of 80-300K. High resistivity sample is placed inside of the cryostat by using a holder and its electrical

contacts are fed via vacuum coaxial feed trough. The sample is cooled down to ≈ 90K in the absence of light, where the traps are filled by optical excitation using a 25mW He-Ne laser. The duration of irradiation was 1200s. Temperature dependence of thermoelectric current, which is generated by the temperature gradient during the sample warming up, is measured by an electrometer (Keithley, model 6574). The sample temperature is precisely measured by Keithley, model 2000. Control computer is used for data acquisition and storing by using GPIB interface bus.

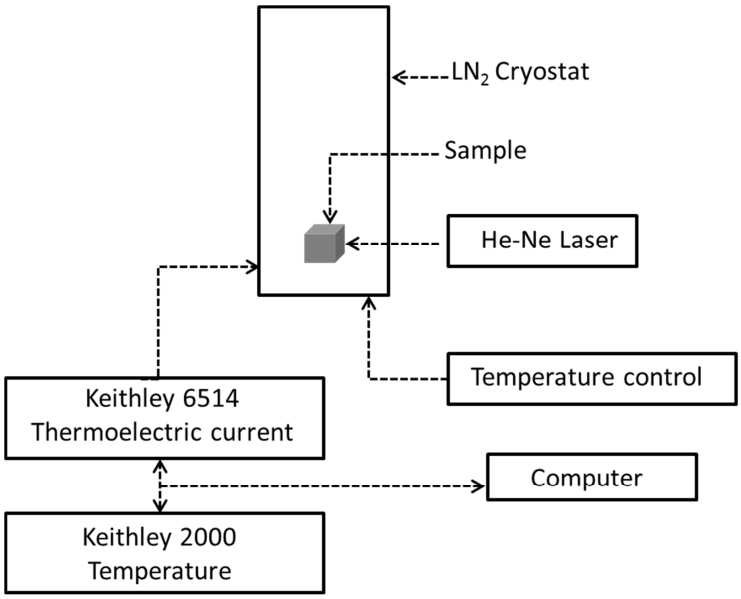

Figure 28: Schematic of Thermoelectric Effect Spectroscopy experimental setup

II.5.4.6. Photoconductivity (PC)

Photoconductivity is a technique which involves applying the sample to constant and continuous electric field illuminated by a light source of variable wavelength. Changing the wavelength of incident light the photo-current is measured through the sample and plotted on a graph the values of photocurrent as a function of λ. From the chart above we can estimate the band-gap of the material that corresponds to the wavelength where the photo-current drops to half its maximum value at the absorption edge. Information can be also obtained about the existence of deep centers and their approximate energy photosensitive, and the mechanisms driving the material.

A continuous and constant voltage (V) is applied to the sample, using a voltage source NHQ-105L and is illuminated with a monochromatic light source. The monochromator has a tungsten lamp as a source of enlightenment. Light incident on the sample is modulated using a mechanical chopper Bentham. The generated signal is measured with a Stanford SR830 lock-in DSP in parallel with an electrical resistance (R) which in turn

is in serie with the sample. The value of this resistance is adjusted for the value of the resistance of the sample itself because they must be of the same order of magnitude.

The photo-voltage measured compared with photo-currents as it has two main advantages. First, the voltages measure itself by a lock-in is less susceptible to electronic noise and can be measured with much greater accuracy than the current, decreasing the measurement error, since the same lock-in amplifier is used and acts as second term, to modulate the light generates in the sample as an alternating current. In this way in the lock-in phase with the chopper was able to eliminate the noise, both electronic and thermal one.

II.6. Summary of techniques of characterization

	Technique	Objetive	Sample preparation
Compo-sitional	ICP-MS	Concentration of main elements and impurities	Powder
	EDX	Superficial composition	Polished, etched, passivated
	XPS	Composition and thikness of TeO_2	Etched, Passivated
Superficial and Optical	AFM	Surface roughness	Lapped, polished, etched and passivated
	SEM	Surface morphology	Lapped, polished, etched
	PL	Crystalline quality, defects, and Zn mapping	Etched
	TEES	Bandgap defects level	Contacted
	Raman	Te peak	Polished and irratdiated
	CL	Defects	Polished and irratdiated
	FTIR	IR transmittance	Polished sample
	IR microscopy	Te inclusions	Polished
Electrical	I-V	Electrical resistivity	Contacted
	CoReMa	Resistivity mapping	Polished
	TCT	Electric field, mobility life time	Contacted
	Gamma response	Detector performance	Contacted

II.7. Bibliography

1. **H. L. Glassa, A. J. Sochaa, D. W. Bakkena, V. M. Spezialea and J. P. Flinta.** Control of Defects and Impurities in Production of CdZnTe Crystals by the Bridgman Method. 1998, Vol. 487.

2. **L. Fischer, U. Lambert, G. Nagel, H. Riifer, E. Tomzig.** Influence of pyrolytic boron nitride crucibles on GaAs crystal growth process and crystal properties. 1995, Vol. 153, pp. 90-96.

3. **J. Crocco, H. Bensalah, Q. Zheng, V. Carcelén, E. Diéguez.** Influence of SiC pedestal in the growth of 50 mm CZT by Vertical gradient freeze method. 2012, Vol. 360, pp. 92–94.

4. **G. Yang, A.E.Bolotnikov, Y.Cui, G.S.Camarda, A.Hossain, R.B.James.** Impurity gettering effect of Teinclusions in CdZnTe single crystals. *Journal of Crystal Growth.* 2008, Vol. 311, pp. 99–102.

5. **H. Bensalaha, J.L. Plaza, J. Crocco, Q. Zheng, V. Carcelen, A. Bensouici, E. Dieguez.** The effect of etching time on the CdZnTe surface. 2011, Vol. 257, pp. 4633–4636.

6. **C. Ludwig, M. Kuna.** An Analytical Approach to Determine the Pressure Distribution During Chemical Mechanical Polishing. 2012, Vol. 41.

7. **A. A. Rouse, C.Szeles, J.O.Ndap, S. A. Soldner, K. B. Parnham, D. J. Gaspar, M. H. Engelhard, A. S. Lea, S. V. Shutthanandan, T. S. Thevuthasan, D. R. Baer.** Interfacial Chemistry and the Performance of Bromine-Etched CdZnTe Radiation Detector Devices. *IEEE Transactions on Nuclear Science.* 2002, Vol. 49.

8. **E.J. Morton, M.A. Hossain, P. De Antonis, A.M.D. Ede.** Investigation of Au-CdZnTe contacts using photovoltaic measurement. 2001, Vol. 458, pp. 558-562.

9. **A. Burger, H. Chen, J. Tong, D. Shi, M. A. George, K.-T. Chen,W. E. Collins, R. B. James, C. M. Stahle, andL. M.-Bartlett.** Investigation of Electrical Contacts for Cd1-x,Zxn,Te Nuclear Radiation Detectors. 1997, Vol. 44.

10. **Qiang Li, Wanqi Jie, Li Fu, Xiaoqin Wang, Xinggang Zhang.** Metal–CdZnTe contact and its annealing behaviors. 2006, Vol. 253, pp. 1190–1193.

11. **D.J.Wagenaar.** *CdTe and CdZnTe Semiconductor Detectors for Nuclear Medicine Imaging.* 2004.

12. **H. Bensalah, J. Crocco, V. Carcélen, J. L. Plaza, Q. Zheng, L. Marchini, M. Zanichelli,G. Domínguez, L. Soriano, and E. Diéguez.** Study of ammonium fluoride passivation time on CdZnTe bulk crystal wafers. *Cryst. Res. Technol.* 2011, Vol. 46, pp. 659 – 663.

13. **K.T.Chen, D. T. Shi, B. Granderson, M.A. George, W.E. Collins, A. Burger, and R.B. James.** Study of oxidized cadmium zinc telluride surfaces. *J. Vac. Sci.Technol. A.* 1997, Vol. 15.

14. **K. Chattopadhyay, M. Hayes, J. O. Ndap, A. Burger, W. J. Lu, H. G. McWhinney, T. Grady, and R. B. James.** Surface Passivation of Cadmium Zinc Telluride Radiation Detectors by Potassium Hydroxide Solution. *J.Electron. Mater.* 2000, Vol. 29.

15. **X. Cheng, S.Zhu , B. Zhao, Z. He, D.Gao, J.Fang.** Effect of surface preparation on the properties of Au/p-Cd1-xZnxTe. 2007, Vol. 253, pp. 8404–8407.

16. **G.W. Wright, R.B. James, D. Chinn, B.A. Brunett, R.W. Olsen, J.Van Scyo,M. Cliftl.** Evaluation of NH4F/H2O2 Effectiveness as a Surface Passivation Agent for Cd1-xZnxTe Crystals. 2000, Vol. 4141, pp. 324-335.

17. **Shin Hang Cho, Jong Hee Suh, Jae Ho Won, Ki Hyun Kim, Jin Ki Hong, Sun Ung Kim.** Surface leakage current control with heterojunction-type passivation in semi-insulating CdZnTe material. 2008, Vol. 591, pp. 203–205.

18. **A. Kargar, A. M.Jones, W.J. McNeil, M.J. Harrison, D.S. McGregor.** *Nucl Instrum Meth A.* 2006, Vol. 558, pp. 497–503.
19. **W.Xiaoqin, J.Wanqi, L.Qiang, G.Zhi.** Surface passivation of CdZnTe wafers. *Materials Science in Semiconductor Processing.* 2005, Vol. 8, pp. 615–621.
20. **A.J. Nelson, A.M. Conway, C.E. Reinhardt, J.L. Ferreira, R.J. Nikolic, S.A. Payne.** X-ray photoemission analysis of passivated Cd1-xZnxTe surfaces for improved radiation detectors. *Materials Letters.* 2009, Vol. 63, pp. 180–181.
21. **S.Wenbin, J.Wei, Z.Qi, M.Jiahua, Z.Minglong, T.Jianyong, Q.Yongbiao.** A novel surface passivation process for CdZnTe detector packaging. *Proceeding paper.* 2004, pp. 377 - 379 .
22. **Y.Xu, W.Jie, P.Sellin, T.Wang, W.Liu, G.Zha, P. Veeramani, C.Mills.** Study on temperature dependant resistivity of indium doped cadmium zinc telluride. *J. Phys. D: Appl. Phys.* 2009, Vol. 42.
23. **G. A. Carini, G. S. Camarda, Z. Zhong, D. P. Siddons, A. E. Bolotnikov, G. W. Wright, ,B. Barber, C. Arnone,R. B. James.** High-Energy X-ray Diffraction and Topography Investigation of CdZnTe. 2005, Vol. 34.
24. **Balaz, P.** *Mechanochemistry in Nanoscience and Minerals Engineering.* 2008. p. 138.
25. **B. Yang, Y. Ishikawa , Y. Doumae , T. Miki , T. Ohyama , M. Isshiki.** Growth and characterization of high purity CdTe single crystals. 1997, Vol. 172, pp. 370-375.
26. **LI Guo-Qiang, JIE Wan-Qi, GU Zh, HUA Hui.** Correlation Between the IR Transmission Spectra and the CdZnTe Qualities. 2003, Vol. 20.
27. **K. Suzuki, T. Sawada, K. Imai, M. Adachi, K. Inabe.** Photoluminescence Measurements on Undoped CdZnTe Grown by the High-Pressure Bridgman Method. *Journal of Electronic Materials.* 2001, Vol. 30.
28. **J.Teng, W.Sang, G.Li, Z.Shi, J.Min and D.Hu.** Influence Of In Dopant On Pl spectra of CdZnTe. *Journal of the Korean Physical Society.* 2008, Vol. 53.
29. **N. Armani, C. Ferrari, G. Salviati, F. Bissoli, M. Zha, L. Zanotti.** Crystal defects and optical transitions in high purity, high resistivity CdTe for device applications. 2002, Vol. 91, pp. 353-357 .
30. **J.K. Radhakrishnana, G. Salviati.** Cathodoluminescence investigations on CdTe and Cd0.96Zn0.04Te crystals. 2005, Vol. 113, pp. 235–242.
31. **J. Rodríguez-Fernández, ,V. Carcelén, P. Hidalgo, N. Vijayan, J. Piqueras.** Relationship between the cathodoluminescence emission and resistivity in In doped CdZnTe crystals. 2009, Vol. 106.
32. **P. Hidalgo, J. Piqueras, N. V. Sochinskii, M. Abellan. E.Saucedo, E. Dieguez.** Cathodoluminescence study of CdTe crystals doped with Bi and Bi:Yb. 2008, Vol. 43, pp. 5605–5608.
33. **R Stibal, J Windscheif and W Jantr.** Contactless evaluation of semi-insulating GaAs wafer resistivity using the time dependent charge measurements. *Semicond. Sci. Technol.* 1991, Vol. 6, pp. 995-1001.
34. **Q.Li, W.Jie, L.Fu, X.Wang, X. Zhang.** Metal–CdZnTe contact and its annealing behaviors. *Applied Surface Science.* 2006, Vol. 253, pp. 1190–1193.
35. **H. Pernegger, S. Roe, P. Weilhammer.** Charge-carrier properties in synthetic single-crystal diamond measured with the transient-current technique. 2005, Vol. 97.
36. **Š. Uxa, E. Belas, R. Grill, P.Praus, R B. James.** Determination of Electric-Field Profile in CdTe and CdZnTe Detectors Using Transient-Current Technique. 2012, Vol. 59.
37. **Nicholas, K.H. and J. Woods.** Evaluation of Electron Trapping Parameters from Conductivity Glow Curves in Cadmium Sulphide. 1964, Vol. 15, pp. 783-795.

38. **Awadalla.S.A, Hunt.A. W, Tjossem, R.B, Lynn, K. G, Szeles.C, Bliss.M.** Evidence for dislocations or related defects present in CdTe and Cd1-xZnxTe crystals. 2001, Vol. 264.

Chapter III: The effect of superheating, cooling and annealing processes on Te inclusions in CdZnTe

Table of content

III.1. Introduction

Several studies have shown that inclusions and precipitates may influence optical transmission, electrical recombination, and mobility-lifetime product (1). For example, M. Fiederle et al. found that the formation of Te-clusters is the essential reason for the polycrystalline structure (2). In this way, a large amount of work has been done in order to eliminate or avoid the formation of inclusions. P. Capper et al. demonstrated a reduction in the density of inclusions present in melt growth using the accelerated crucible rotation technique (3). Post growth annealing under Cd vapor was found to be effective to reduce Te inclusions superior to 1µm but less effective to remove smaller one (<1µm) (4). Szeles et al. reported that growth process under Cd excess correct the stoichiometry which reduce the formation of Te inclusions (5).

Taking into account the ionic character of the Cd-Te chemical bond, CdTe melts is highly associated close to the melting point, resulting in the presence of extremely organized particles affecting nucleation process and growth kinetics (6). Therefore large superheating ΔT^+ ($\Delta T^+ = T-T_m$), where T is the maximum melt temperature before the crystal growth and T_m is the melting point is necessary to destroy this associated melt complexes (7) (8).

The quality of the as grown CZT crystal is related to the temperature of the mother phase before the growth process starts (9). In fact, P. Rudolph et al demonstrated that slight superheating temperature affect the crystal growth by generating subgrains and twins, while for higher superheating temperature these defects disappear. Therefore, the crystal growth process could be improved by using a defined superheating and holding time before the crystallization.

The cooling rate after growth is one of the most important parameters for crystal growth and is an essential issue in the quality of CdZnTe crystals (10). The sizes and densities of the inclusions were found to be related to the melt stoichiometry and cooling process of the growth (11). The retrograde solubility of Te is also responsible for the formation of the Te-rich precipitates during the cooling down process (12).

The effects of cooling rate on the size distribution and concentration were studied for two inch ingots by L. L. Xu et al. It was observed that fast-cooled (30K/h) crystal contains high density of dislocations and sub-grain boundaries decorated with high concentration of Te inclusions, while, the slow-cooled (10K/h) has smaller number of defects (13).

Bruder et al. demonstrated that the cooling rate after the growth strongly affect the crystalline quality. In fact, with cooling rates in the range of 30K/h strain and small angle boundaries occur, while cooling rates in the range of 10K/ h show an absence of low angle structures and crystals are largely free of strain (14).

Different cool down techniques were used by K. Swain et al. to observe the effects on the size, distribution, and density of Te inclusions. From the results, it was observed that growth with excess cadmium and slow cool down rates (14 and 7°C/h) was possible to achieve near stoichiometric growth. Cool down with a radial gradient in order to realize thermo-migration of tellurium but no significant difference was observed. Quenching after growth was successful in reducing the secondary phases by an order of magnitude and also reducing the sizes of the inclusions (15) (11).

An additional process for controlling the properties of the grown CdTe is post-annealing of the as grown ingot during the cooling process and/or of the cut slices (10). In general, the effect of annealing on CdTe and CdZnTe has been widely studied, and the results indicate that annealing process can reduce Te inclusions trough thermo-migration process.

There is increasing interest in applying a post-growth in situ annealing to the whole ingot before cooling to room temperature. Sen et al. found that the post growth annealing of the ingot under Cd saturated conditions was partially effective in reducing the size of Te inclusions (16). It has been also demonstrated that the possibility to produce high quality CdTe and CdZnTe crystals depends strongly on the temperature and time of annealing. A long time annealing at 975°C remove completely small tellurium inclusions, while Annealing at 900 - 1050°C for 40 hours was successful to reducing the size and density of precipitates, inclusions and residual strain (10).

Several authors used two zones annealing furnace for sliced wafers, and showed that is an effective method for the elimination of point and structural defects and therefore to improve the quality of CdZnTe crystals. However, Biao Li et al (17) demonstrate that after annealing the lattice perfection is degraded because of the regrowth of CdZnTe during the thermo-migration process of Te precipitates.

In this chapter, several growth parameters will be used including superheating, cooling and annealing. This investigation will be mainly focused on the influence of the size and distribution of Te inclusions, deep defects, the homogeneity, the optical and electrical properties of CdZnTe detectors using different techniques of characterization.

III.2. Experimental procedure

III.2.1. Crystal growth process

$Cd_{1-x}Zn_xTe$ ingots (x=10%) were grown by Vertical Gradient Freeze (VGF) method using a 5-zone furnace. The pBN crucible was filled with 7N high purity as starting materials, Te (450°C), Zn (419°C), Cd (320°C) in the order of their melting points. The concentration of indium used for each experiment was 3ppm.

To measure thermal gradients applied throughout the growth process, type S thermocouples were placed below the nucleation tip of the ampoule and circumferentially along the axial direction of growth as shown in **Figure 1**.

A SiC pedestal was used in conjunction with the pBN crucible in order to improve the thermal dynamics, axial heat flow and to reduce the effects of undercooling during crystal growth. The SiC was used due to its high thermal conductivity properties, and for increasing the temperature gradient at the first to freeze part. As a result, large crystal grains and volumes have been obtained (18).

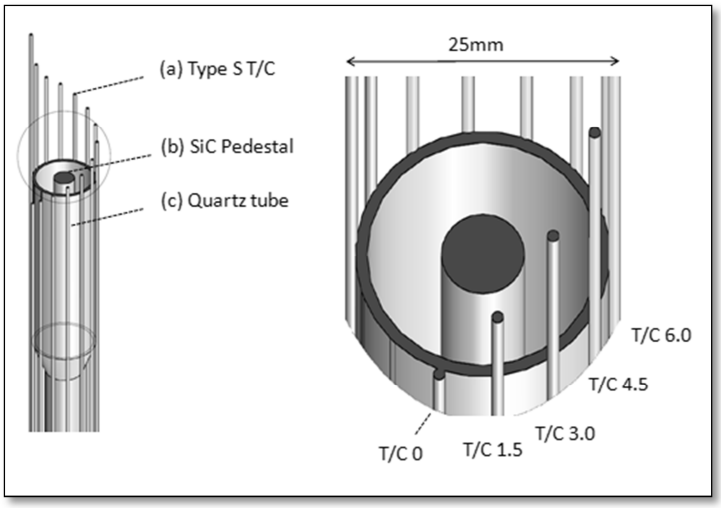

Figure 1: Thermocouples distribution and Sic pedestal used for the growth

Presented in **Figure 2** are two different thermal profiles applied to the ingots during the homogenization step of the growth. In the first homogenization ramp, the temperature at the bottom of the crucible (Z=0) is considered to be near to the melting point of CdZnTe (T_m=1104°C). In the second homogenization ramp, the process was evaluated by bringing the bottom of the crucible up to 26°C above the melting point of CZT for 15min. The temperature of the melt was then cooled down before the growth cycle was started. This higher temperature is intended to push the reaction further, and break apart secondary phases in the melt (19). It is important to note that the thermocouple used for

measuring the superheating temperature was T/C 0, located near the bottom of the ampoule as shown in **Figure 1.**

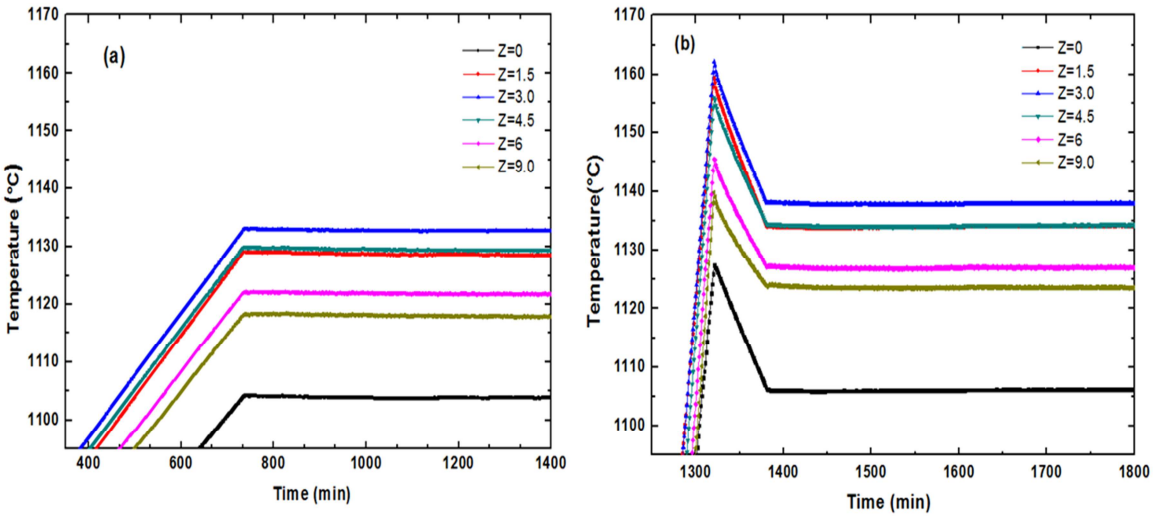

Figure 2: Temperature profile for (a) No superheated ingots and (b) 26°C superheated ingots

Standard grown ingots have been cooled using a rate of 20°C/h and some ingots have been cooled by using a faster decreasing ramp of 110°C/h, calling this processes "slow" and "fast cooling", respectively in the next paragraphs. In **Table 1** is presented a summary of the crystal growth nomenclature.

Table 1: Crystal growth nomenclature used in the chapter

Crystal growth	Nomenclature in the chapter
No superheating+slow cooling	*Ingot A*
Superheating+slow cooling	*Ingot B*
Superheating+Fast cooling	*Ingot C*

III.2.2. Samples preparation

The grown ingots were sliced into wafers perpendicular to the growth direction. The samples were firstly lapped and then polished using 3µm Al_2O_3 powder.

Etching process was done with 2% Br-MeOH for 2min to remove the damaged surface layer. Immediately after etching, Au was deposited on both sides of the CZT samples by the electroless method. In **Table 2** is presented the sample preparation needed for the characterization techniques used in this chapter.

Table 2: Summary of techniques of characterization and sample preparation

Technique of characterization	Sample preparation
IR Microscopy	*Polished*
FTIR	*Polished*
PL	*Etched*
TEES	*Contacted*
TCT	*Contacted*
I-V	*Contacted*
Gamma response	*Contacted*

III.3. Effect of superheating and cooling on Te inclusions and intrinsic defects

III.3.1. Consequences of superheating process on the quality and compositions of the ingots

In order to establish and demonstrate repeatable behavior, three ingots were grown for each process. A picture of the as grown ingots is shown in **Figure 3**. One can observe that in the case of no superheating, the ingots exhibited large volumes of polycrystalline material and high void content at the top of the ingots, which is obviously detrimental to the yield of the material, whereas, this behavior was not observed in the three ingots grown using 26°C superheating. Strictly based on these macroscopic features of the ingots, superheating of 26°C appears to have some positive effects on the as grown crystals.

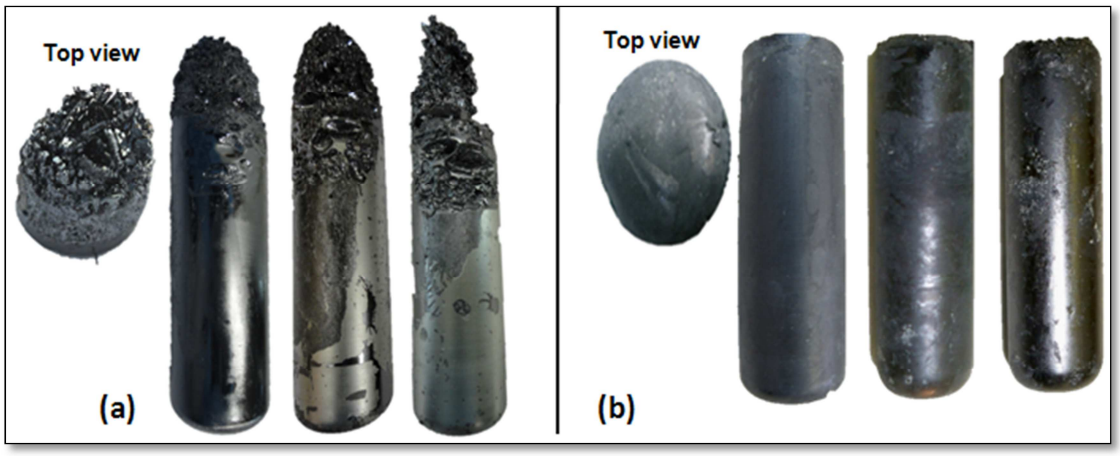

Figure 3: As Grown 25mm diameter CZT ingots (a): No superheated (b): 30°C superheated

In fact, these differences between no superheated and superheated ingots were also observed in the 50mm diameter ingots as shown in **Figure 4**. One can observe that the ingot grown without superheating, exhibited a similar conical polycrystalline region at the top of the ingot, while the second ingot was grown using superheating protocol for 15 min. As can be seen, the volume of this conical region has been reduced. Moreover, the third ingot was grown using the same protocol, however the melt was held 5 hours this time. As can be seen, this polycrystalline conical region has been eliminated. Increasing the superheating temperature of the melt to about 1130ºC, substantially improved the material homogeneity.

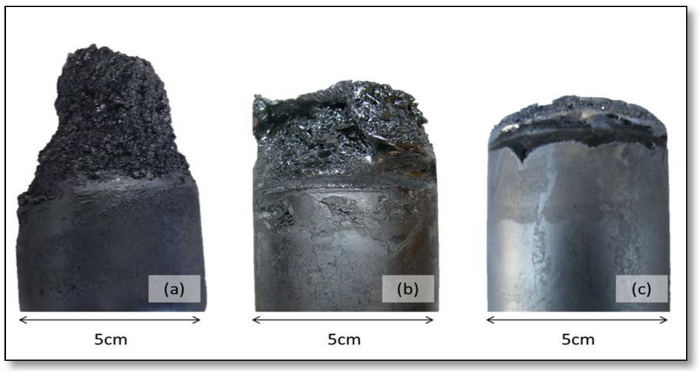

Figure 4: 50mm diameter CdZnTe ingots grown using (a) No superheating (b) 15min superheating and (c) 5h superheating

These results could be explained by a numerical model which has been used for modeling the crystal growth process. These simulation results have been obtained using the CGsim software package developed for modeling global heat transfer arising from conduction, convection and radiation as presented in **Figure 5**.

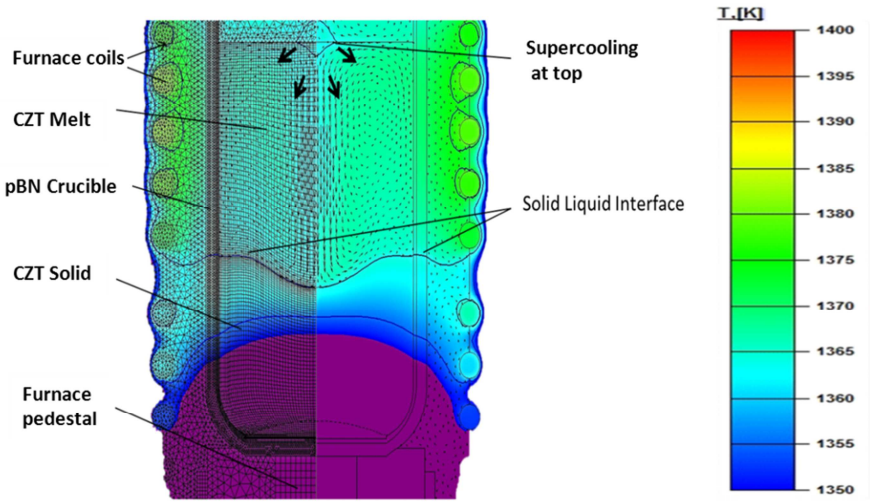

Figure 5: CGsim numerical simulation

The formation of the polycrystalline cap may be attributed to the type of the axial temperature profile which has been used throughout the crystal cycle. Therefore it is conceivable that supercooling at the melt surface, midway through the growth cycle, may lead to the formation of a polycrystalline cap. But this just begs the question: why is this polycrystalline cap only observed in the ingots that have not been superheated, if the axial temperature profile is the same for all ingots?

The real key to understand and hopefully explain this behavior rests upon understanding the effect of superheating and supercooling and their effects on nucleation events. Returning to the work published by Rudolph on melt superheating and supercooling (10). It appears clearly from

Figure 6 that for melts with small superheating, a small supercooling is required for nucleation to occur, while for melts with significant superheating, on the other hand, a high supercooling is required for nucleation to occur. Therefore, when the top of the melt becomes supercooled, the melt that has not undergone superheating will easily nucleate, whereas the melt that has been previously superheated will not reach the required degree of supercooling for nucleation to occur.

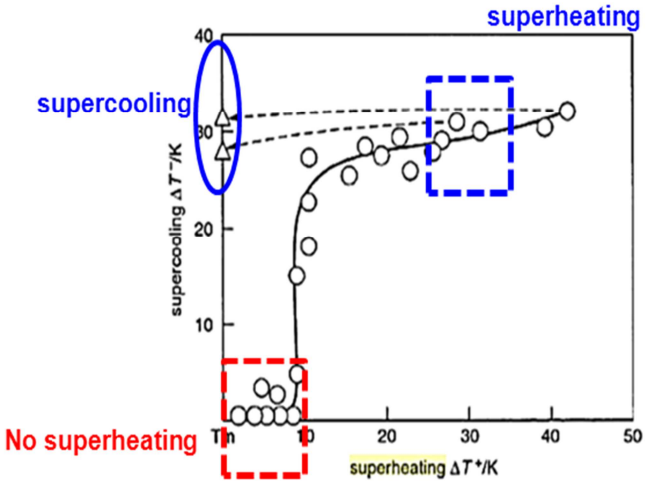

Figure 6: Results adapted from P. Rudolph illustrating experimental results about the effect of superheating and supercooling of the CdTe melt **(10)**

Other important consequence of superheating process is the material composition along the ingot. The axial composition of zinc for the ingots grown without and with superheating was characterized using ICP-MS to measure the axial zinc segregation. Results are illustrated in **Figure 7.** Using Pfann equation presented by **Equation 1,** the segregation coefficient for both processes has been calculated to be between 1.34 and 1.37.

Equation 1 $$C_s = C_0 . k(1-g)^{k-1}$$

where C_0 is the initial concentration of zinc, C_s is the concentration of zinc in the solid, k is the segregation coefficient, and g is the solidified fraction.

The values obtained for k are consistent to the commonly reported values found in literature (k=1.35) (20) (21). We observe that the axial concentration profile in the solid increased to a maximum and then decreases uniformally for both cases. The variation in the axial zinc concentration could be divided to three regions. In the first region for g close to 0.2, which correspond to the first to freeze, the segregation coefficient is close to unity, and reflects the bulk concentration of the melt which is 10% in our case. This behavior is generally ascribed to an effect of supercooling during the first part of of the growth. This effect has been studied by others authors (22) (23). In the second region, the segregation of zinc follows closely the Pfann equation. Nevertheless, in last region, the concentration of zinc falls rapidly to lower values and reaches the value of 5-8%. In fact, we can observe that superheating process did not affect the zinc segregation phenomenon.

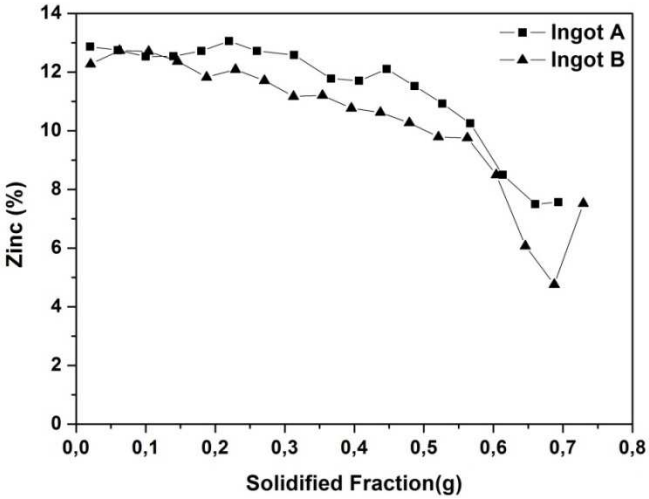

Figure 7: Zinc concentration for ingots A and B

It was also interesting to know the composition of Te, Cd and Zn along both ingots. ICP data showing the changes in content of Cd and Zn with respect to Te are presented in **Figure 8.** One can observe that the ingot grown without superheating exhibited larger fluctuations of Te, Cd, and Zn composition. These fluctuations could be attributed to the non-uniform melt composition, associated with the incomplete reaction of CdZnTe as has been discussed previously.

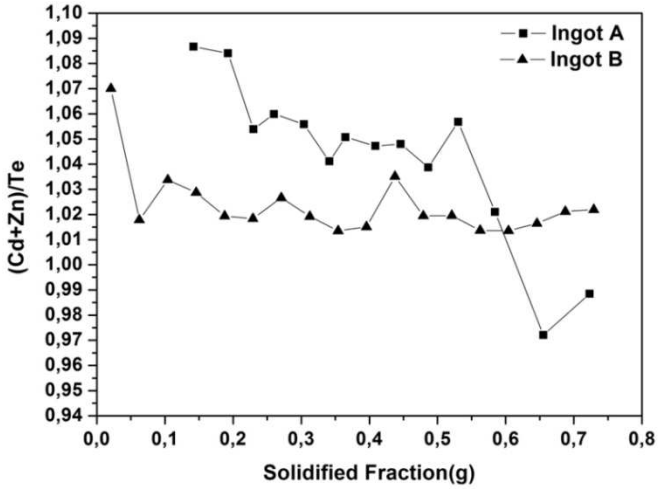

Figure 8: Composition of ingots A and B

Taking into account these results, we conclude that superheating process of the melt by 26ºC was effective to improve material homogeneity and eliminate the conical shape and voids at the top of the ingots.

III.3.2. The size and density of Te inclusions

While the macroscopic properties of the crystals provide useful information with respect to the general dynamics of the growth, the optical properties play a major role in CZT used as detectors. Therefore it was necessary to determine how the melt homogenization and cooling process affects the formation of secondary phases.

IR microscopy is an adequate technique to visualize Te inclusions in CZT samples. As we know, inclusions are formed from pure Te which strongly absorb light and appear as dark spots in the IR images. **Figure 9** and **Figure 10** show the IR microscopy images and diameter distribution (μm) of Te inclusions for samples harvested from different positions of each ingot. We observe that no superheated samples (ingot A) contain larger Te inclusions, probably a consequence of an incomplete reaction between Cd and Te in the melt. After superheating (ingot B), the clusters were broken and the size of Te inclusions reduces. After fast cooling (ingot C), the ingot present the smallest Te inclusions due to the retrograde solubility of the phase diagram, where Te does not have time to agglomerate (24) (25). Other possible reason for the formation of Te inclusions is the high dissociation energy of Te–Te bound and the less volatile nature of Te_2 atoms in comparison with Cd and Zn atoms (26).

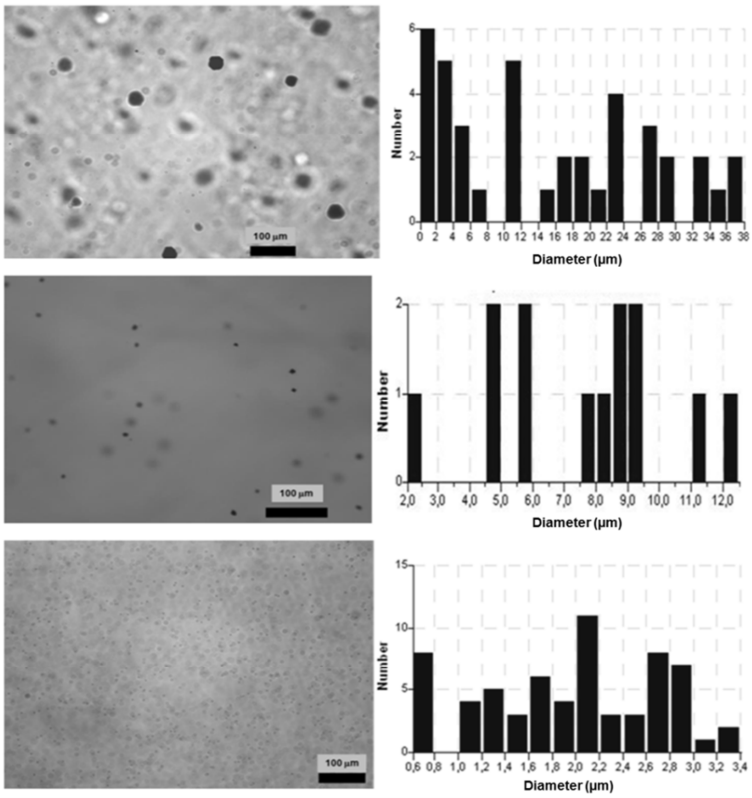

Figure 9: IR microscopy images and diameter distribution (µm) of the inclusions for samples from the first part to freeze of the ingots A, B and C successively

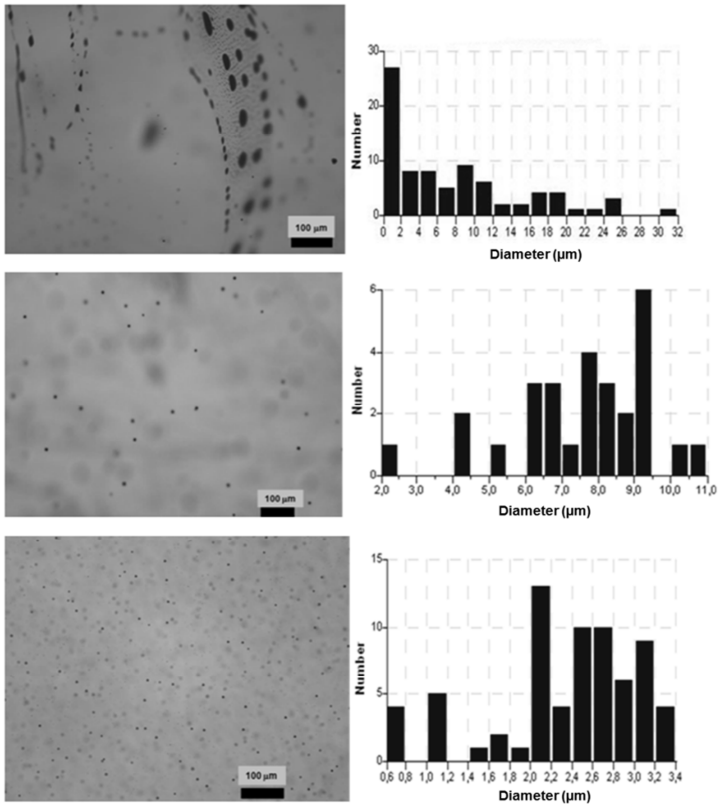

Figure 10: IR microscopy images and diameter distribution (µm) of the inclusions for samples from the last part to freeze of the ingots A, B and C successively

It is also interesting to study the size and density of Te inclusions along the ingot. Presented in **Figure 11** is the distribution of Te inclusion diameter for the three 25mm ingots on samples harvested perpendicularly to the growth direction and analyzed at the center part. One may observe that ingot A has very large inclusions or clusters in the first to freeze region, in excess of 160 µm, an example of these clusters is shown **Figure 12**. In the rest of ingot A, the diameter drops to between 20µm and 40µm, however they are considered relatively large in comparison with the ingots B and C. On the other hand, ingot B has a more or less constant inclusion size between 10 and 20µm, also the clusters are not present in the first to freeze region. Further improvements are made regarding ingot C grown with both superheating and fast cooling, we observe that the diameter distribution is more uniform throughout the crystal and do not exceed 4.6 µm (11).

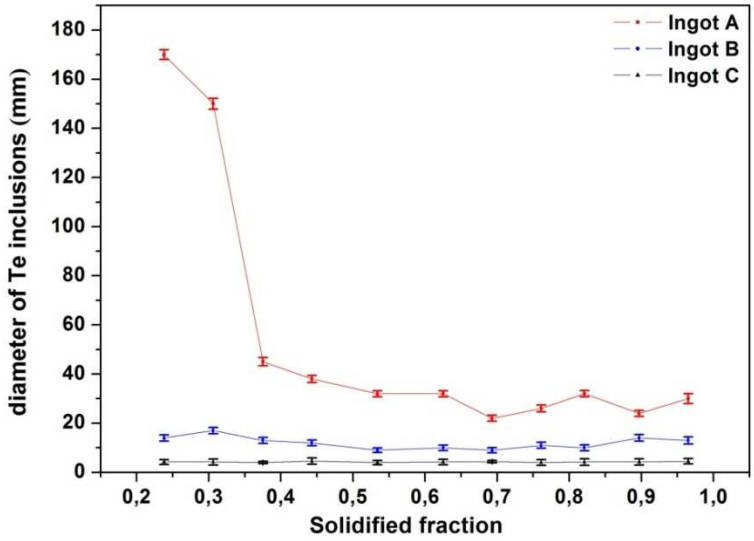

Figure 11: Diameter distribution of Te inclusions along the ingots A, B and C

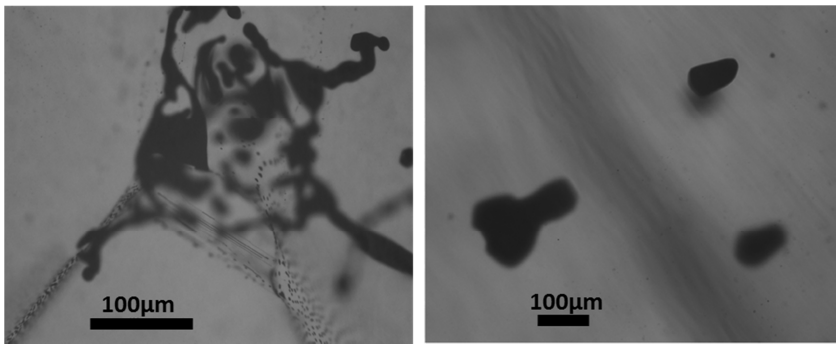

Figure 12: Te clusters in the first to freeze region of the ingot A

Figure 13 The density of Te inclusions along the three ingots has been also studied and the results are shown in **Figure 13**. One can observe that ingot A has the least uniform distribution in inclusion density, with wide fluctuations in density between $4.5\times10^{5}cm^{3}$

to less than $1.0\times10^5 cm^3$. Ingot B has a significantly lower density between 0.5-$1.0\times10^5 cm^3$, whereas ingot C has elevated Te density in the range 3.5-$4.5\times10^5 cm^3$.

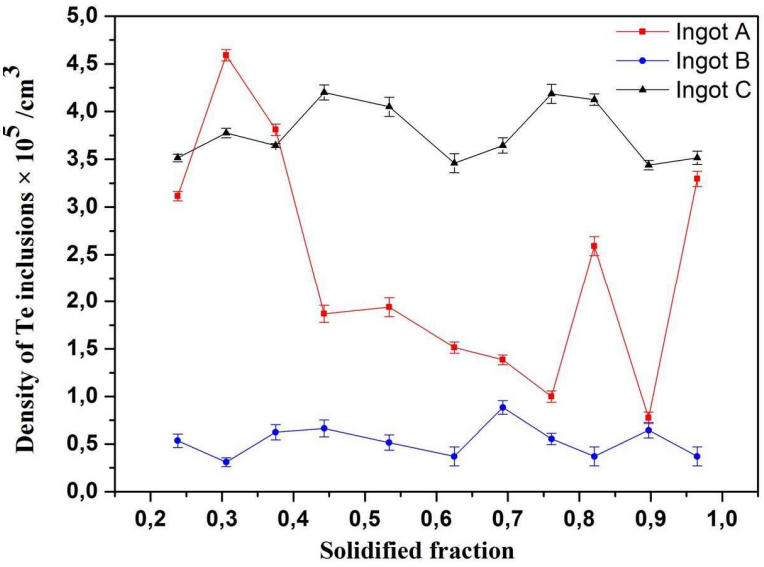

Figure 13: Density of Te inclusions along the ingots A, B and C

Finally, to really demonstrate the difference between ingots grown without and with superheating at macroscopic level, an IR transmission for two wafers is presented in **Figure 14**. This figure shows that the inclusions are much smaller in ingot B in comparison with ingot A, clearly demonstrating the problems with incomplete homogenization.

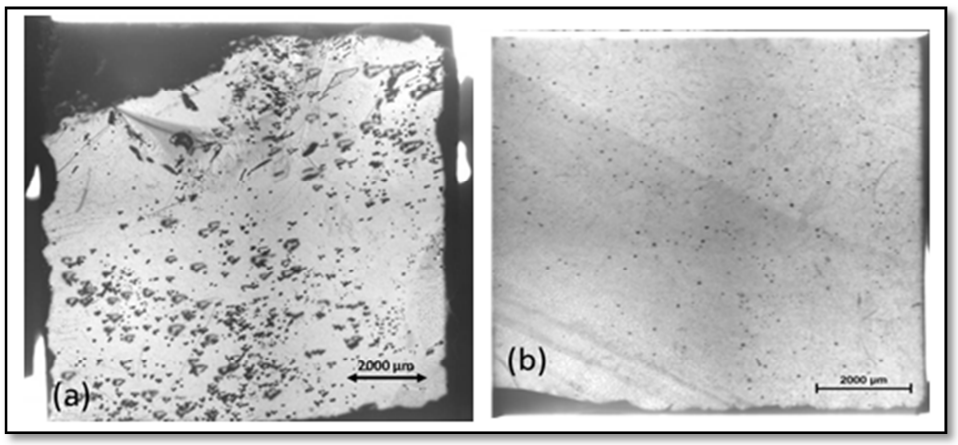

Figure 14: IR microscopy images of 1cm x 1cm CZT wafers: (a) ingot A (b) ingot B

The evaluation of the quality of the ingots A, B and C is completed by The IR transmittance measurements. The IR transmission spectra for samples harvested from each of the ingots is presented in **Figure 15**.

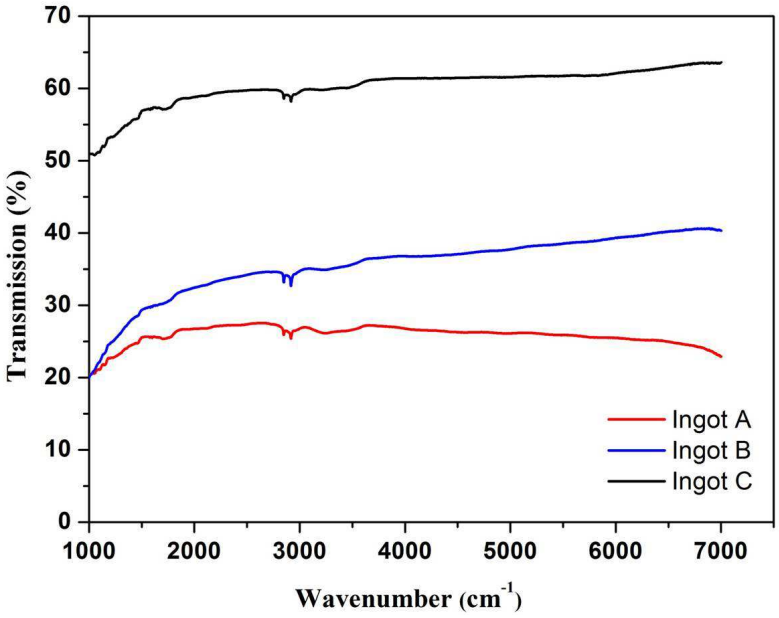

Figure 15: IR transmittance spectra for the CZT samples from the ingots A, B, and C

In this figure on can observe that the samples harvested from ingot A not only exhibit the lowest IR transmission, but this transmission decreases with increasing wavenumber which is generally attributed to the large size of Te inclusions which scatter the incident IR light. In addition to scattering, another possible reason for the decreased transmission is the absorption mechanism which in CZT material may be attributed to lattice absorption and free-carrier absorption. In fact, the lattice absorption changes the electric dipole moment via the displacement of atoms. The larger the electric dipole moment is, the more the lattice absorption will be. The change in the local lattice parameter brought by dislocations and Te inclusions may help to explain the increased absorption. These second phase particles can change the lattice parameter and destroy the periodicity of the lattice, consequently enlarging the electric dipole moment (27).

The effect of superheating, which has been applied to ingot B, reduces the size of the inclusions and in consequence increases the IR transmission. However, these samples still contain relatively large inclusions, which helps explain the lower IR transmission, less than 40%.

Nevertheless, IR transmission was further improved for ingot C with the implementation of both superheating and fast cooling process. The IR transmission for these samples exceeds 60 % for wavenumbers from 1500cm^{-1} to 7000cm^{-1}, a transmission values near the theoretical limit (28) (29). This is a direct result of the smaller diameter inclusions within the sample, resulting in less scattering. Similar

transmission data was also observed for other samples harvested from the same ingot in different solidified positions.

III.3.3. Study of intrinsic defects

The goal of this section is to investigate and analyze in detail the shallow and deep defects in CdZnTe:In samples grown using different growth conditions.

PL measurements were performed to characterize the point defects and mapping, while thermoelectric emission spectroscopy technique **(**TEES) was used to calculate the thermal ionization energy and capture cross section of shallow and deep trapping levels in the samples.

III.3.3.1. Shallow defects

The identification and control of point defects in CZT detector is an important research issue. PL spectroscopy is a non-contact and non-destructive tool, best suited to characterize these defects, such as impurities (donors, acceptors) and native, or intrinsic defects in CZT crystals such as vacancies and vacancy-impurity complexes which are produced during growth.

In this study PL was used to evaluate the material quality and defect in the samples grown using different growth conditions. A representative low temperature (4.2K) PL spectrum displaying detected recombination features in the near-edge emission range 1.35-1.70eV from the bulk of CdZnTe samples is shown in **Figure 16**. The intensities of the PL spectra were normalized to the (D^0, X) peak for better comparison. In this figure, one can see that the main neutral donor bound exciton (D^0, X) peak at 1.657eV is observed in all samples. The emission peak at 1.646 is the neutral acceptor bound exciton (A^0, X) at 1.648eV. The peak at 1.623eV is the shallow donor–acceptor pair (DAP) followed by its longitudinal optical photon replica (LO) (21meV separation) located at 1.603 and 1.583eV, respectively. In $Cd_{1-x}Zn_xTe$, the direct electron-phonon interaction is dominated by the longitudinal optical mode because of the associated polarization fields (30).

A wideband centered at 1.472eV, known as the A-center band, is also visible in all the samples (31) (32). In addition, an emission due to the free exciton (FX) recombination is observed at 1.667eV.

In the literature, the A-center band is related to a complex defect involving a Cd vacancy and In donor impurity, $[In_{Cd}]^{+}$, by the following interaction (32):

Equation 2 $$\boldsymbol{In + [V_{Cd}]^{2-} \Leftrightarrow [In_{Cd}]^{+} + 3e^{-}}$$

Equation 3 $$\boldsymbol{[In_{Cd}]^{+} + [V_{Cd}]^{2-} \Leftrightarrow \left[In^{+}_{Cd}V^{2-}_{Cd}\right]^{-}}$$

Equation 4 $$\boldsymbol{[In_{Cd}]^{+} + \left[In^{+}_{Cd}V^{2-}_{Cd}\right]^{-} \Leftrightarrow \left[2In^{+}_{Cd} - V^{2-}_{Cd}\right]^{0}}$$

where $[In_{Cd}^{+}]$ is an ionized shallow donor, formed by the compensation with Cd vacancy. The shallow donor $[In_{Cd}^{+}]$ attracts one $[V_{Cd}]^{2-}$ shallow acceptor, thereby the singly negative donor-vacancy complex can be formed $[In_{Cd}^{+}V_{Cd}^{2-}]^{-}$. The complex A-centers can further recombine with the extra accumulated In donors forming the neutral entity $[2In_{Cd}^{+}\text{-}V_{Cd}^{2-}]^{0}$. It has been reported that A-center plays an important role in the compensation process, namely in the neutralization of the native acceptor defects (V_{Cd}) (33).

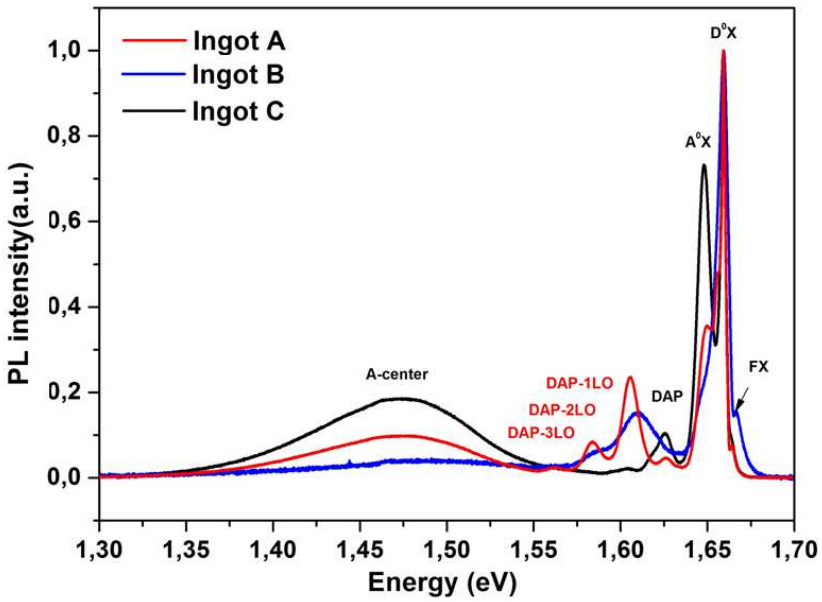

Figure 16: Low temperature (4.2K) PL spectra of CZT samples from the ingots A, B, and C

At the same figure, one can observe that for ingot A, the intensity of the (A^{0}, X) peak is lower comparing with ingot C, while this peak disappear for ingot B. The high intensity of (A^{0}, X) peak imply that the shallow acceptors concentration (V_{cd} and some impurities such as Li, Na Cu) is higher and were not fully compensated for ingot C.

The DAP peak of sample from ingot B is much higher than the others ingots, indicating a relative increase in the concentration of shallow donors or acceptors. This could be attributed to Te antisites which act as a shallow acceptor (34) or the segregation of impurities (35). In addition, the intensity of the A-center peak is much higher for ingot C, while it disappears for ingot B. the intensity of A-center indicates that the indium donors recombined with Cd vacancies acceptors, which decreases the concentration of V_{Cd}. It has been found that the increase of the concentration of A-center complexes to reduce the deleterious effects of V_{Cd} is one approach to achieving high resistivity material. However, the A-centers are shallow hole traps (between 0.1 and 0.2 eV above the valence band), and should have therefore a negligible effect on the transport properties of CZT (36).

III.3.3.2. A-center mapping

PL mapping can be used as a sensitive probe of lateral variations in structural quality, impurity concentration, and stoichiometry and hence in measuring the homogeneity of composition and doping. PL at low temperature is the most used for Zn mapping as well as for crystal defects mapping.

In order to visualize the distribution of defects in the CdZnTe samples, PL at low temperature was used. The PL maps of A-center defects are presented in **Figure 17**. Each map shows the distribution of PL intensity along the sample. For ingot A and B we observe that A-center defects are uniformly distributed while the sample from ingot C shows a clear non-uniformity distribution; in fact the intensity is very high comparing with the others samples. The results are in agreement with PL spectra shown above in **Figure 16**, where we observe that the peak of A-center is higher for the sample from ingot C, which indicates exact compensation between In shallow donors and Cd vacancies acceptors.

The non-uniformity distribution of A-center could be attributed to the fast cooling used for the growth process of ingot C.

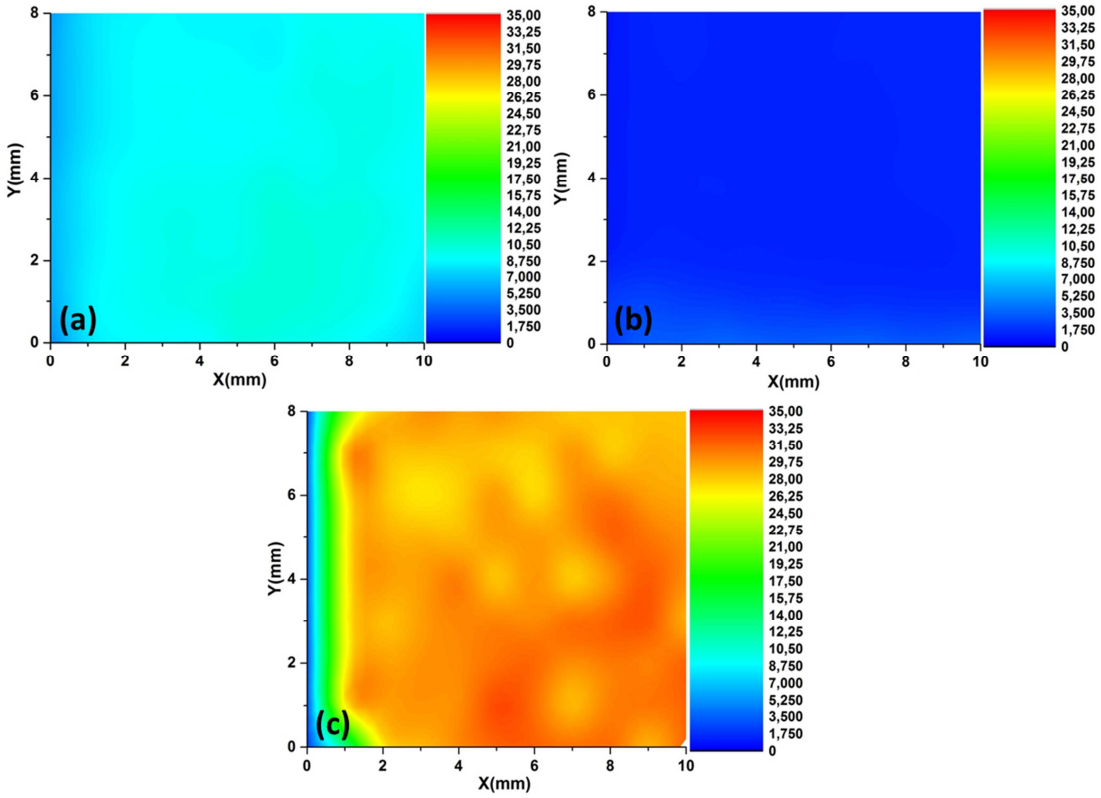

Figure 17: Pl maps of A-center defects of samples from ingots A, B and C

III.3.3.3. Zinc mapping

In general, PL has been used as a method providing informations on defects and impurities as well as on material composition.

In the ternary compound $Cd_{1-x}Zn_xTe$, the band gap and free-exciton energies depend on zinc concentration (x). In fact, the band gap E_g can be adjusted from 1.606eV in CdTe to 2.4eV in ZnTe at liquid helium temperature as shown in **Figure 18**. We observe that as x increases, the lattice parameter decreases, this reduction in the inter-atomic spacing increases the repulsive interaction between core electrons and thus increases the band gap.

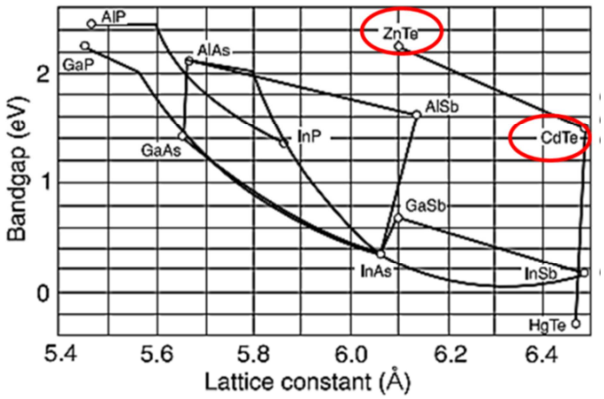

Figure 18: Lattice Parameter and Bandgap Data for III-V and II-V semiconductors

The energy gap can be calculated from photon energy of bound (D^0X and A^0X) or free exciton (FX) peaks in the luminescence spectra, using the following formula (37) (38):

$$\mathbf{E_g = E_D{}^0{}_X + 13meV}$$

$$\mathbf{E_g = E_A{}^0{}_X + 24meV}$$

$$\mathbf{E_g = E_{FX} + 10.8meV}$$

where $E_D{}^0{}_X$ is the energy attributed to a neutral donor-bound exciton, $E_A{}^0{}_X$ is the neutral acceptor-bound exciton energy, and E_{FX} is the free exciton energy.

Once the E_g value is calculated, zinc concentration *x* is obtained from (38):

Equation 5 $$\boldsymbol{E_g = 1.606 + 0.520x + 0.254x^2 \quad (eV)}$$

Shown in **Figure 19** are the PL maps of zinc distribution in CZT samples grown from different growth conditions. We observe that the three samples have the same concentration of Zn because they are from the same position from each ingot. We also observe that in both samples harvested from ingot A (No superheated and slowly cooled) and ingot B (Superheated and slowly cooled) exhibit good Zn uniformity; in fact the superheating process did not affect the zinc distribution. However, the distribution of zinc in the sample from the ingot C is not uniform which could be attributed to the fast cooling used for this ingot.

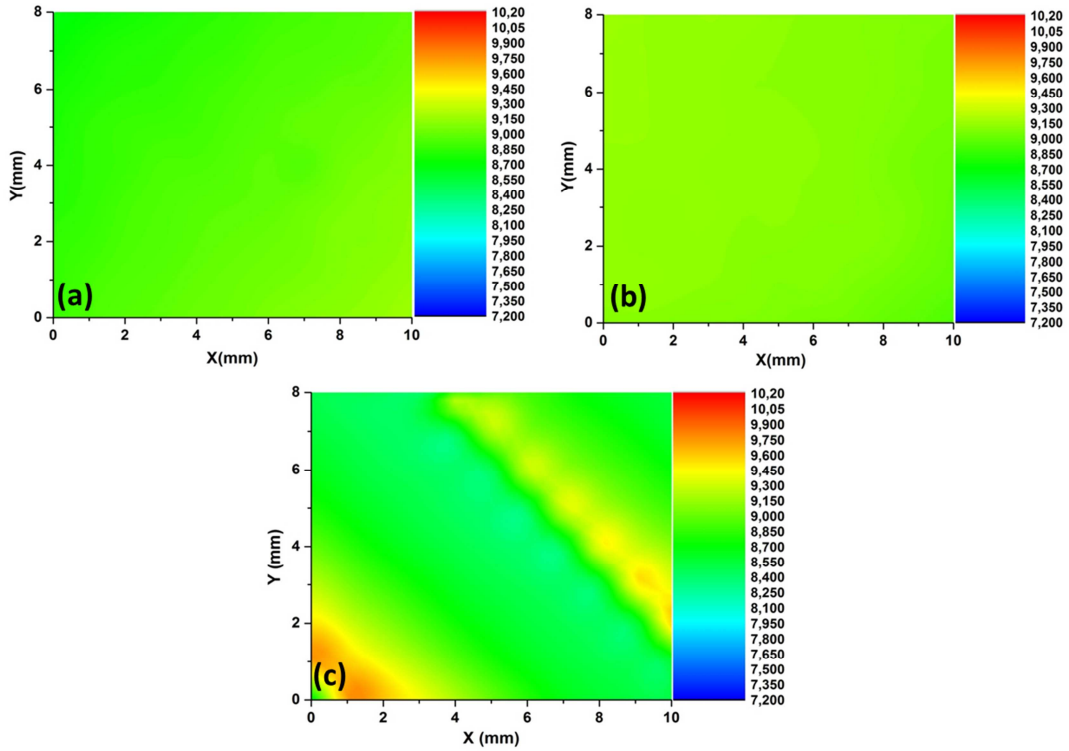

Figure 19: Zinc concentration maps from different CZT samples: (a) Ingot A, (b) Ingot B, (c) Ingot C

Because the segregation coefficient of zinc in CdZnTe is greater than one (1.35), the zinc content of the crystal decreases as solidification proceeds. Taking into account that these samples are from the last-to-freeze part of the ingots, the concentration of Zn does not exceed 9%, due to the segregation of Zn along the ingot.

From the results presented in this section, one can conclude that fast cooling can affect the compensation process of impurities and intrinsic defects and also lead to a non-uniform distribution of defects and Zinc. In **section III.4**, we are going to study if these defects will destroy the detector performance or there are other parameters which can affect the electrical properties of CZT detectors.

III.3.3.4. Deep defects and traps

Deep electronic levels in CZT play an important role in stabilizing compensation conditions for defects in the material, however, at the same time they can degrade the transport properties of carriers acting as trapping centers (39). To determine the main traps in the CZT samples, the thermoelectric emission spectroscopy technique (TEES) was used. For this technique, only high resistivity samples can be used, as a results ingot B will not be characterized because it showed low resistivity.

TEES spectra at four different rates are shown in **Figure 20** and **Figure 21**. The induced current from the emitted charge is plotted as a function of sample temperature. One can note that all observed peaks are positive, which means that all corresponding traps are holes.

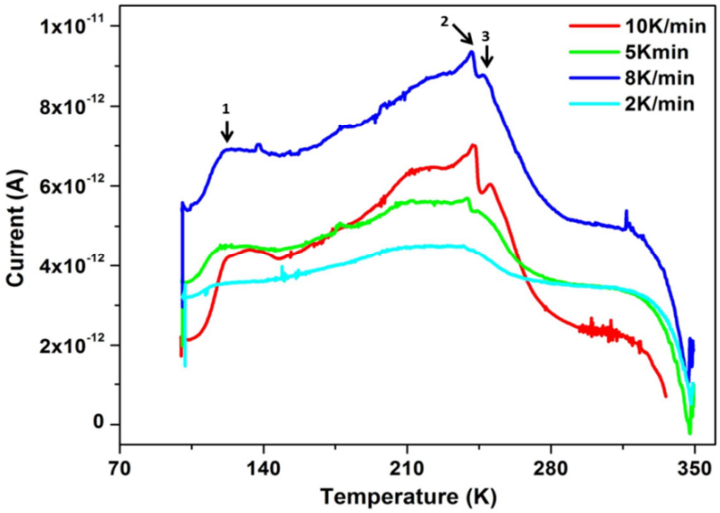

Figure 20: TEES spectra of sample harvested from the ingot A at different rates

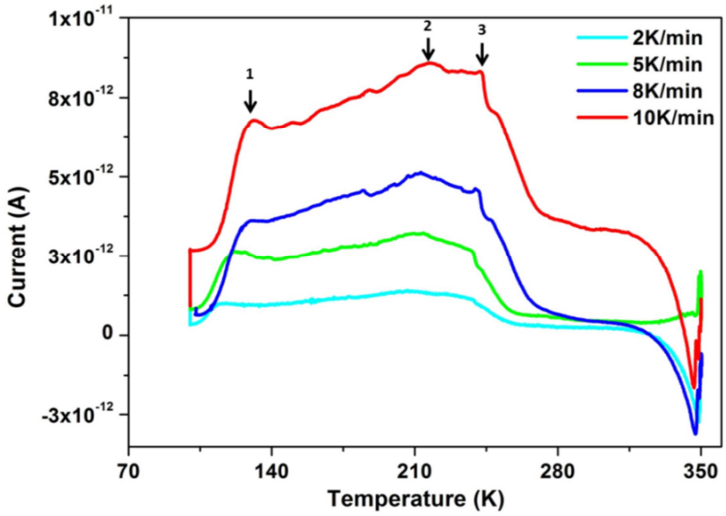

Figure 21: TEES spectra of sample harvested from the ingot C at different rates

The thermal ionization energy (E_t) and capture cross section (S_t) of trapping levels were extracted using heating rate method. **Figure 22** shows an example of the Arrhenius plots, from which the trap's energy and hence their capture cross section can be calculated using the following equation:

Equation 6 $$\ln(T_M^2/R) = (E_t/kT_M) - ln(S_t v_e N_c k/E_t)$$

Where, T_M is the temperature of the maximum current, R is the heating rate, k is the Boltzmann constant, N_C=1.44*10^{14}*$T^{3/2}$$cm^{-3}$ is the effective density of states in the conduction band, υ_e=2.18*10^6*$T^{1/2}$cm/s is the electron thermal velocity (40).

If several heating rates are used and T_M is determined as a function of R, it is possible to derive E_t from the slope of the straight line which should be obtained by plotting $\ln(T^2_M/R)$ against $1/kT_M$. Knowing E_t, the carrier cross section values can be obtained from **Equation 6.**

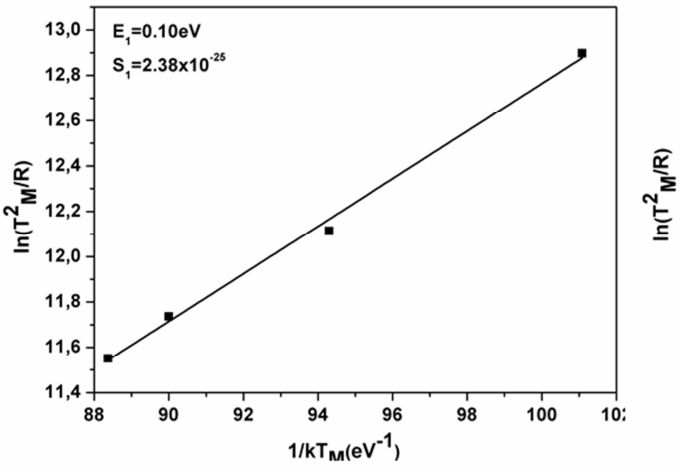

Figure 22: Example of Arrhenius plots showing the thermal ionization energy and trap cross section

The calculated values of the energy and capture cross section of the traps are presented in **Table 3**.

For the sample from ingot A, we observe that the measured thermoelectric current is positive, which means that the peaks are the results of hole emission and the corresponding energy levels are 0.10, 0.42 and 0.90eV above the valence band. The trapping cross section of the levels are 2.71×10^{-25}, 5.43×10^{-20} and $2.30\times10^{-11}cm^2$, respectively. The first shallow level at $E_1=E_v+0.10eV$ is associated with a complex of Cd vacancy with donors or A-center (41) (42) (43). These defects are shallow hole traps and should have therefore a negligible effect the transport properties of CZT (36). It has been demonstrated that these defects can affect the detector performance when they form complexes with deep levels.

The level at E_2= 0.42eV could be attributed to a second ionized Cd Vacancies V_{cd}^{2-}, and finally the deep level at 0.90eV could be associated to doubly ionized Te_{cd} (44). In fact, Te antisite alone cannot pin the Fermi level.

For the sample from ingot C, one can observe also that the peaks are corresponding to hole traps with energy levels of 0.10, 0.70 and 0.86eV, and capture cross section value of 2.38×10^{-25}, 5.37×10^{-13} and $3.42\times10^{-12}cm^2$, respectively. Similarly to ingot A, the shallow level at 0.10 eV is ascribed with A-center. Typically, defects levels of less than 0.2 eV, in our case A-center play a minor role in the deterioration of CZT detector (45).

We suggest that the deep trap near the middle of the gap at 0.70eV could be identified as a complex of V_{Cd} and Te_{cd} (46). It could be the transition to one of the higher charge state levels of the Te_{cd}-V_{Cd} pair (Te_{Cd} + V_{Cd}); these levels are supported to play a fundamental role in determining the material resistivity (47). The level at 0.86eV is assigned to doubly ionized Te_{cd}.

Table 3: Calculated thermal ionization energies and capture cross section

Sample	Trap sign	Energy, E_t (eV)	Capture cross section, S_t (cm^2)
Ingot A	**hole**	**0.10**	**2.71×10^{-25}**
	hole	**0.42**	**5.43×10^{-20}**
	hole	**0.90**	**2.30×10^{-11}**
Ingot C	**hole**	**0.10**	**2.38×10^{-25}**
	hole	**0.70**	**5.37×10^{-13}**
	hole	**0.86**	**3.43×10^{-12}**

From TEES results, we can conclude that three hole traps have been detected for each sample. A-center and the doubly ionized Te_{cd} were observed in both samples, while some were unique to one sample. We suppose that this difference may be associated with the size and distribution of Te inclusion. The detector performance of these samples will be studied in the next part and we can conclude which traps can lead to the deterioration of electrical properties of CZT samples. These results allow us to conclude that fast cooling was successful to reduce the size of Te inclusions but it can introduce some defects into the crystal. This could be attributed the high cooling rate used in this investigation. For this reason it will be necessary to try lower cooling rate in the future work.

III.4. Influence of Te inclusions on the electrical properties of CZT detectors

One important and often overlooked factor that deteriorates the properties and performance of CdZnTe detector device is the size and distribution of Te inclusions (48). Therefore, it is essential to study the electrical properties in order to identify the parameters that deliver the best detector performance.

In order to study how Te inclusions affect CZT detectors, two samples with different size and distribution of Te inclusions as shown in **Figure 23** have been selected. These samples were harvested from ingot A (CZT-A) and ingot C (CZT-C).

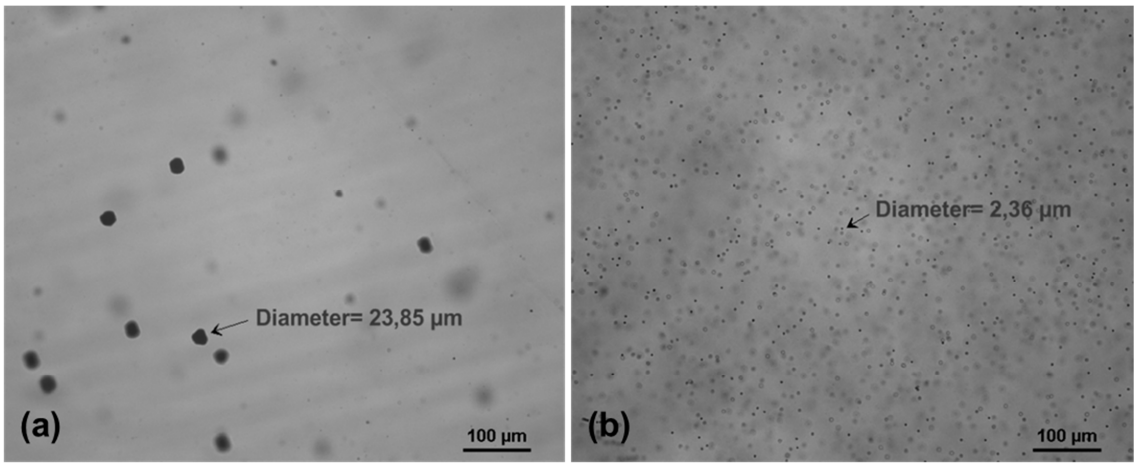

Figure 23: IR microscopy images of CZT samples with different Te inclusions distribution (a) big inclusions CZT-A and (b) small inclusions CZT-C

III.4.1. Transient current technique measurements

In this section, the transient current technique (TCT) has been used to study the profile of the electric field distribution and calculate the electron mobility in CZT single crystals. TCT is based on a direct time resolved measurement of the current arising from

the drift of free charge carriers in an electric field. The applied bias voltage dependence of current pulses measured for samples CZT-A and CZT-C are illustrated in **Figure 24** and **Figure 25** respectively. For both samples, the maximum current signal was attained after applying the higher voltage. One can also observe that the rise time of current is decreasing with increasing bias voltage, where it decreases from 20s at 300V to 4s at 800V for CZT-A, while for CZT-C decreases from 38s at 400V to 5s at 1000V. After arising the maximum, the waveform decrease exponentially. The exponential decay ends upon the arrival of the first electronic "cloud" at the anode. This behavior of the current could be explained in terms of a positive space charge within the sample.

The subsequent final fall of the amplitude is attributed to the longitudinal diffusion of the charge carriers, which take place during their movement across the sample. For low voltages the charge carrier cloud can reach larger dimensions and, as a consequence, the signal falls off slowly after the first carriers arrive at the electrode.

The average signal durations (transit time t_{tr}), which is defined as the time taken by a carrier to traverse the entire detector decreased as the voltage is increased, which means that carriers are affected highly by the produced electric field within the detector. For sample CZT-A this value for a given bias of 300V is 150ns, while for the same applied voltage bias for sample CZT-C is 250ns. We observe that the transit time is shorter in CZT-A sample which indicate that electrons take less time to drift through the detector. It has been also demonstrated that shorter transit times lead to lower probability of recombination and trapping, therefore, the carrier will be collected more completely (49) (50) (51).

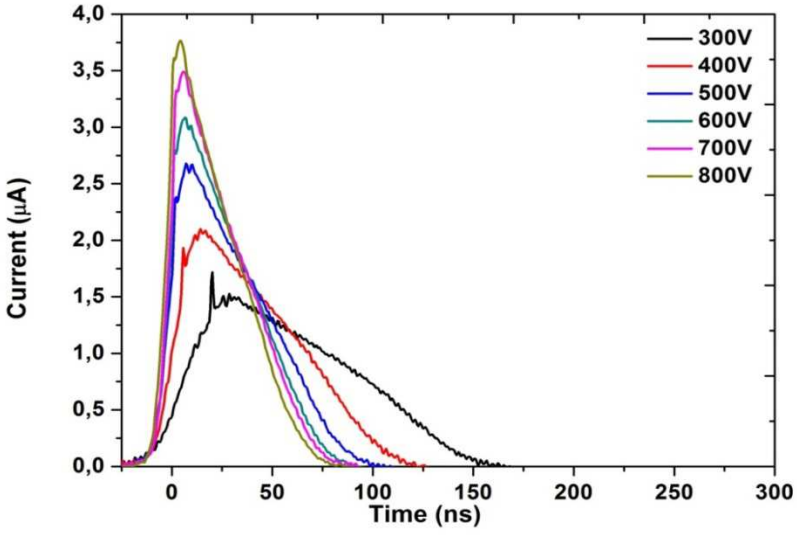

Figure 24: TCT measurements in CZT-A for different applied bias

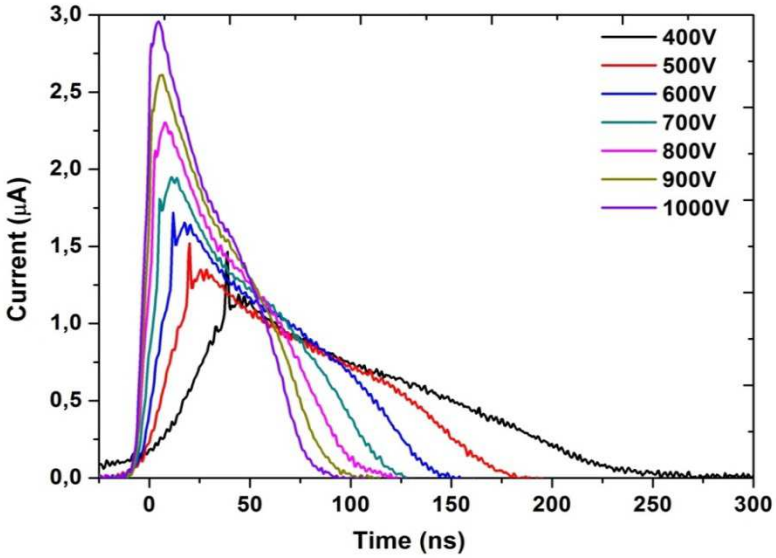

Figure 25: TCT measurements in CZT-C for different applied bias

III.4.1.1. Calculation of electron mobility

To calculate the electron mobility of each sample, one can take into consideration the conventional model of detector polarization (52) (53), where a constant space charge density may be anticipated which results in a linear electric field defined as:

Equation 7 $$E(x) = E_0 - ax$$

With E_0 is the electric field under the irradiated cathode (x=0), and "a" is the slope induced by the space charge density N and defined as:

Equation 8 $$a = \frac{eN}{\varepsilon_0 \varepsilon_r}$$

With ε_0 and ε_r =10.3, are the vacuum and relative permittivity, e is the electronic charge, and N the space charge density.

Positive space charge formed on trap levels below the Fermi energy is estimated, which implies a > 0 in this investigation. The loss of drifting charge due to carrier trapping is expressed by:

Equation 9 $$Q(t) = Q_0 e^{-t/\tau}$$

Where τ is the trapping time

Using **Equation 7**, the kinetic equation of carrier drift through the detector could be defined as:

Equation 10 $$\frac{dx}{dt} = v(t) = \mu E(x)$$

Since at t=0, the carrier is at x=0 and the electric field is E_0 as given by **Equation 7**, **Equation 10** can be solved as:

Equation 11 $$\boldsymbol{x(t) = \frac{E_0}{a}(1 - e^{-a\mu t})}$$

Therefore, the current induced on the detector with a thickness L is:

Equation 12 $$\boldsymbol{i(t) = \frac{Q(t)v(t)}{L} = \frac{Q_0 E_0}{L} e^{-(a+\frac{1}{\mu\tau})\mu t} \propto e^{-ct}}$$

With $$\boldsymbol{c = \left(a + \frac{1}{\mu\tau}\right)\mu}$$

Taking into consideration the equation presented by S. Uxa et al. (53), $U = E_0 L - \frac{1}{2} a L^2$ and **Equation 11,** we can obtain the final equation to calculate "a":

Equation 13 $$\boldsymbol{ct_{tr} = \left(1 + \frac{1}{a\mu\tau}\right) \ln\left(\frac{1+\frac{aL^2}{2U}}{1-\frac{aL^2}{2U}}\right)}$$

With U is the applied bias and L the thickness of the sample.

Fitting the experimental data according to **Equation 12** which gives the values of the parameter c, and estimating t_{tr} from **Figure 24** and **Figure 25,** and "a" from **Equation 13**, we can obtain the electron mobility μ by solving the equation $c = \left(a + \frac{1}{\mu\tau}\right)\mu$.

The values of μτ were calculated using a charge sensitive preamplifier according to the fit to a single carrier Hecht equation. CZT-A has a value of 0.96×10^{-3}cm^2/V, while the μτ of CZT-C is 1.00×10^{-3}cm^2/V. CZT-C has slightly higher value of μτ which mean that this detector is expected to be of higher energy resolution value than that of CZT-A detector (50).

Averaging the mobilities calculated for different bias, we result in $\mu_{CZT\text{-}A}$= (1032±31)cm^2/Vs and $\mu_{CZT\text{-}C}$= (1039±38)cm^2/Vs.

III.4.1.2. Electric field profile

The electric field uniformity is one of the most important factors for the practical application of CdTe/CZT detectors. The polarization of the space charge distribution can causes a disturbance of electric field in the detectors and produces a progressive degradation of energy resolution. In fact, when a radiation interaction occurs, the created electrons and holes could be trapped by the defects existing inside the sample and in consequence affect the internal electric field. If the trapping lifetime is long, the distribution of electric field in CdZnTe material decreases slowly which lead to the decrease of the carriers drift velocity.

The profiles of the electric field of the CZT-A and CZT-C were calculated using $U = E_0 L - \frac{1}{2} a L^2$ and **Equation 7**.

The results are presented in **Figure 26** and **Figure 27**. For both samples, we observe that the electric field shows a maximum near the cathode and then linearly decreases at the anode. This behavior is consistent with the positive space charge within the sample. For our detectors, the depletion width can extend to the entire sample, therefore the charge was collected by the whole volume of the detector and is operating under compete depletion.

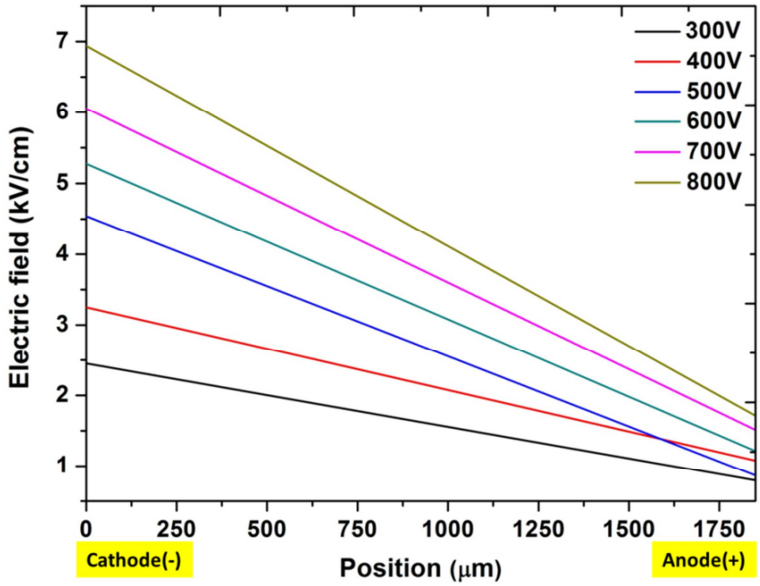

Figure 26: Calculated strength of the electric field in CZT-A detector as a function of the distance from cathode for different applied bias voltages

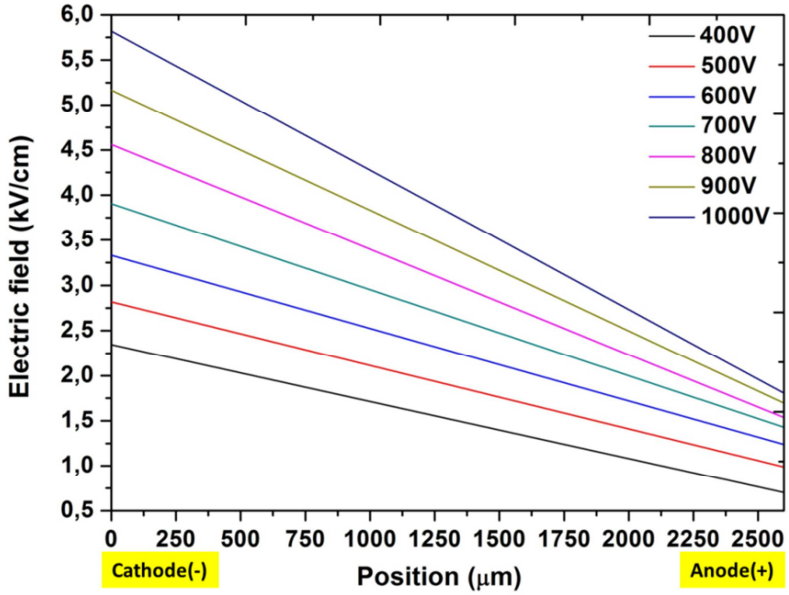

Figure 27: Calculated strength of the electric field in CZT-C detector as a function of the distance from cathode for different applied bias voltages

CZT-C sample results in a slightly higher mobility lifetime and high applied voltage. We assume that CZT-C sample could result in much better detector performance.

III.4.2. Detector performance

I-V measurements were used for testing detector performance and comparing the effects of Te inclusions on detector resistivity.

I-V characteristics (-800 to -100V) of CZT-A and CZT-C detectors are shown in **Figure 28**. As can be seen, the detector CZT-A which contains bigger and low concentration of Te inclusions display higher leakage current than the detector CZT-C which contains smaller and high concentration of Te inclusions. In fact, this high leakage current can affect the electric field distribution, resulting in poor charge collection efficiency (54).

One can observe that, for the sample CZT-A the leakage current is 27.55×10^{-8}A whereas for the sample CZT-C the leakage current is only 22.63×10^{-9}A at -800V, which is an order of magnitude lower. We can conclude from the I-V results that the size of Te inclusions can strongly affect the leakage current.

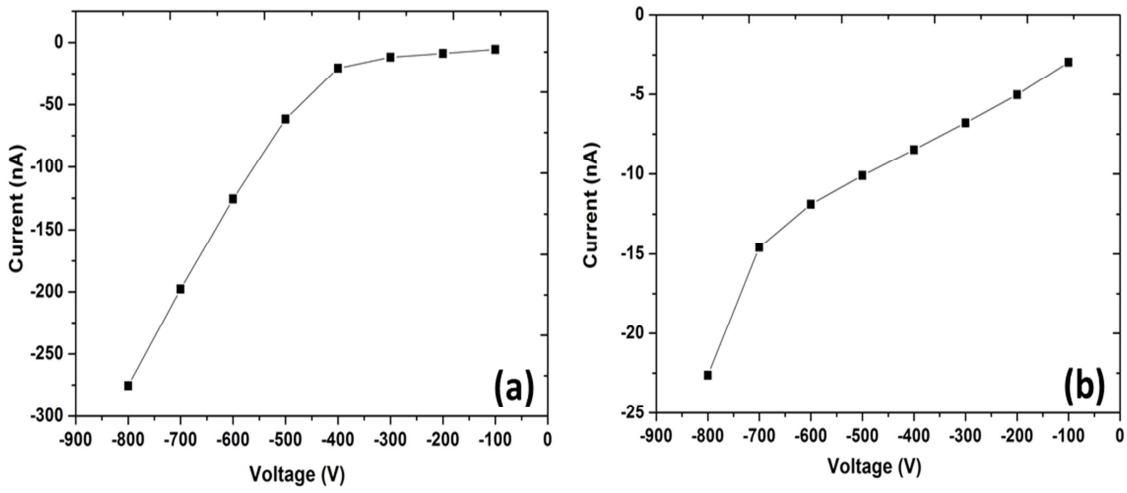

Figure 28: I-V curves of (a) CZT-A and (b) CZT-C detectors

The radioactive source ^{241}Am has been used in this part for comparing the performance of the detectors achieved from two ingots with different size and distribution of Te inclusions. **Figure 29** and **Figure 30** exhibit the gamma spectroscopy of CZT-A and CZT-C detectors, respectively. One can observe that the peak at 59.54keV was detected for both detectors.

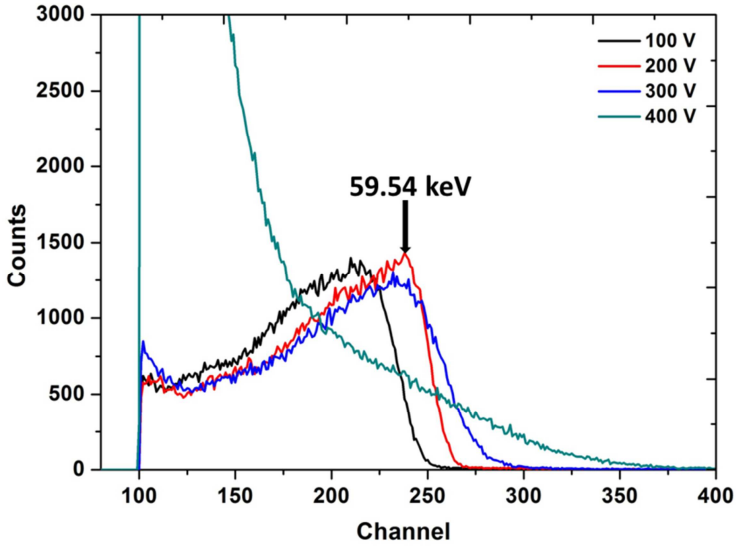

Figure 29: Gamma response with ^{241}Am source of CZT-A detector

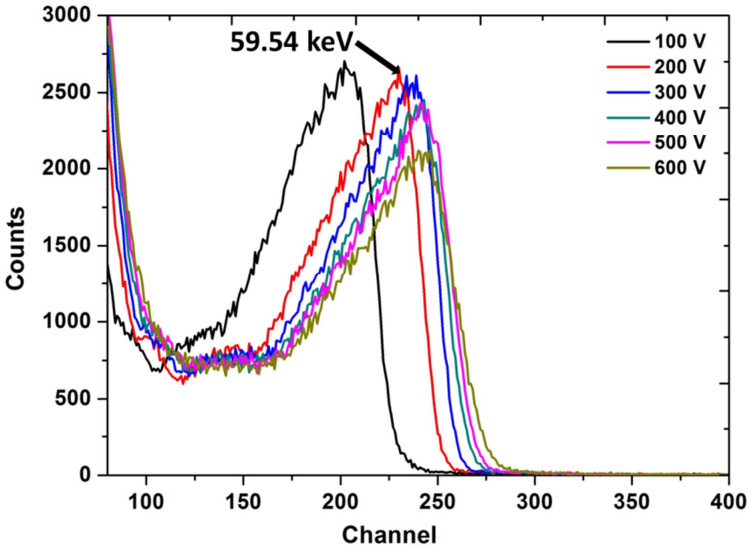

Figure 30: Gamma response with ^{241}Am source of CZT-C detector

By comparison, we can observe that the performance of the detector CZT-C obtained from the ingot with smaller Te inclusions is better than the one with bigger Te inclusions. Additionally, for CZT-A detector, the maximum voltage that we can apply is 300V, and no peak is observed at 400V, while CZT-C detector can operate at even higher voltage than 400V without the degradation of the device. Indeed, increasing the breakdown voltage of CdZnTe devices is a primary goal for advanced device fabrication technology (55). At the same figure, one can observe that when the bias voltage increases, the peak shifts to higher energies, indicating the improvement of charge collection.

The summary of the gamma spectra of the planar detectors fabricated at the applied bias of 200V is presented in **Table 4**.

For gamma ray detection, the detector performance is usually estimated by the photopeak resolution and peak/valley ration. These parameters contribute to the quality factor which is expressed as:

Equation 14

$$Quality\ factor = \sqrt{\frac{\frac{peak}{valley} ratio}{\%FWHM}}$$

Table 4: Information of the gamma response with 241Am for CZT-A and CZT-C

	CZT-A	CZT-C
FWHM% (200V)	54	47
P/V (200V)	2.86	4.34
Quality factor (200V)	0.23	0.30

The FWHM values are 54% and 47% for the detectors CZT-A and CZT-C, respectively. The peak/valley ratio of CZT-A is 2.85, which is lower than that of CZT-C (3.94), indicating that less noise appears with CZT-C sample. The noise level is associated with the value of the applied voltage and increases with the increasing leakage current. Finally, the quality factor of CZT-C is 0.30, which is slightly higher than that of detector CZT-A. In fact, the performance of the CZT-C detector with smaller Te inclusions is better than the detector with bigger Te inclusions.

^{241}Am alpha response has been also used to study the effect of Te inclusions on the planar detector performance.

The alpha response with ^{241}Am radioactive source for CZT-A and CZT-C at different voltage bias are presented in **Figure 31** and **Figure 32.**

For CZT-C, we can observe when the voltage increases, the pulse height of the photopeaks increases and shifts to higher energies side, indicating the improvement of charge collection, while, for CZT-A, the pulse height stop increasing at 400V, and the signal is noisy and then the resolution is very poor.

As expected, the CZT-C detector which contains smaller size of Te inclusions achieves a good response as indicted by 26% FWHM energy resolution at 800V, in contrast to sample CZT-A whichshows very large FWHM. One explanation for the poor response is that big Te inclusions (>20μm) can lead to non-uniformity in the electron transport properties and produce a charge trapping and in consequence affect the detector performance (56).

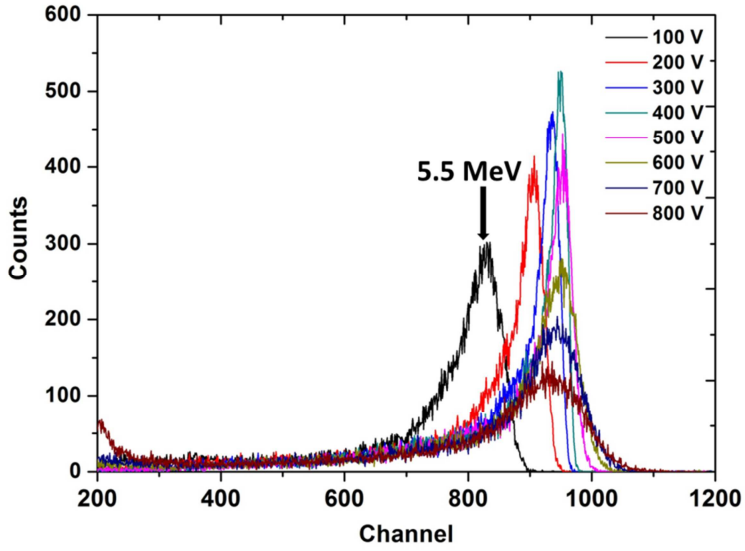

Figure 31: Alpha response with ^{241}Am source of CZT-A detector

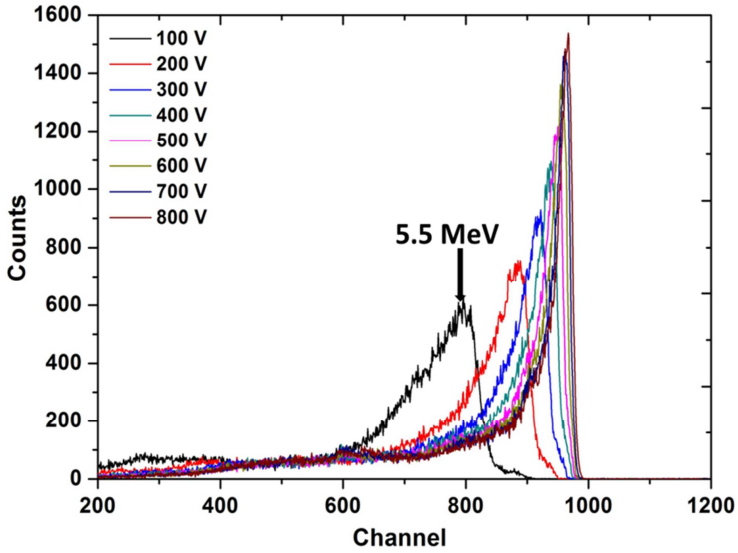

Figure 32: Alpha response with ^{241}Am source of CZT-C detector

As a consequence of high mobility lifetime, high applied voltage and low leakage current, the sample CZT-C shows the best detector performance. These results allow us to conclude that the size and distribution of Te inclusions can have a substantially larger effect on the bulk electrical properties of CZT crystals.

III.5. The effect of in-situ post growth annealing process

Post-growth annealing is a promising method for reducing Te inclusions defects, adjusting the concentration of native defects (57), and then improving the properties of CZT for fabricating room temperature gamma-ray detectors.

In this investigation, the in-situ annealing process was carried out at 950°C for 10 and 24h, and then followed by fast cooling.

Figure 33 shows the IR images of CZT crystals harvested from different ingots grown with and without annealing. One can observe that the concentration of Te inclusions is reduced after 10h at 950°C, while annealing for 24h at the same temperature annealing was successfully developed to eliminate Te inclusions. The incomplete elimination of Te inclusions could be ascribed to the insufficient time of annealing.

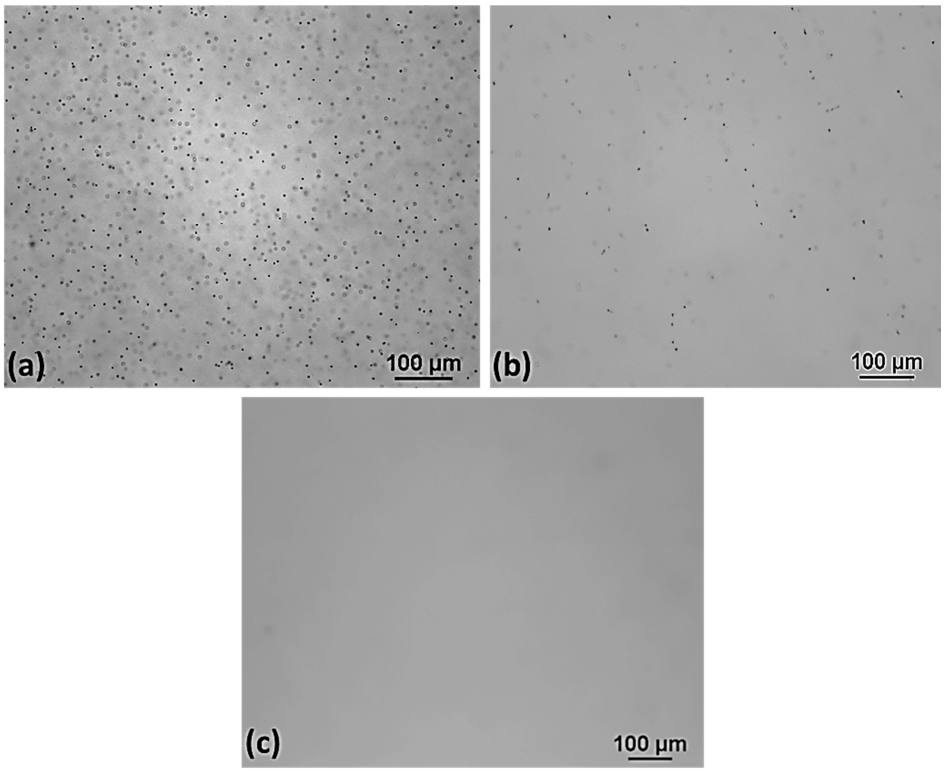

Figure 33: IR images for CZT samples from different ingots: (a) No annealed, (b) Annealed for 10h and (c) annealed for 24h

The mechanism which could be possible for eliminating Te inclusions after annealing of 24h in temperature gradient is the thermo-migration or the movement of Te inclusions under the influence of a temperature gradient. Is has been demonstrated that thermo-migration is the principle mechanism responsible for elimination of Te inclusions during annealing process, and annealing above the melting point of Te (450℃) show significant decrease in Te inclusions compared to the temperatures below the melting temperature of Te (58).

At 950°C which is higher than the melting point of Te, tellurium is in liquid phase and in the presence of temperature gradient they migrate from the lower to the higher temperature zone.

It has been reported that the relation between thermo-migration velocity and effective diffusion coefficient is expressed by (59) (60):

Equation 15

$$\nu = \frac{D}{1-X}\left(\frac{\partial X}{\partial T}\right)\nabla T$$

Equation 16

$$D = D_0 exp\left(-\frac{Q}{RT}\right)$$

where ν is the velocity of the Te droplet in CZT (cm/s), D_0 is the diffusion coefficient of Te in CZT ($1.6\times10^4 cm^2/s$ for CdTe), Q is the heat of fusion of CZT (12.0 kcal/mol for CdTe), R is the gas constant (1.985 cal/mol K), T is the temperature (K), X is the atomic fraction of Te in liquid, (∂X/∂T) is the atomic change with respect to temperature (1/K), and ∇T is the temperature gradient through the CZT wafer (K/cm).

From these equations we understand that thermo-migration velocity strongly depend on the temperature and temperature gradient. Thermo-migration velocity is also depending on the size of the Te inclusions. In fact, when the compositional changes in small Te droplets are minimal (∂X/∂T«1), so thermo-migration will be slow.

High resistivity is one of the most important parameter for CZT material used for gamma radiation. Unfortunately, while thermal annealing can eliminate Te inclusions, this process usually cause a loss of resistivity as shown in **Figure 34**. Several studies have shown that the re-annealing under Te overpressure is successful to restore the high resistivity (61) (62) (63).

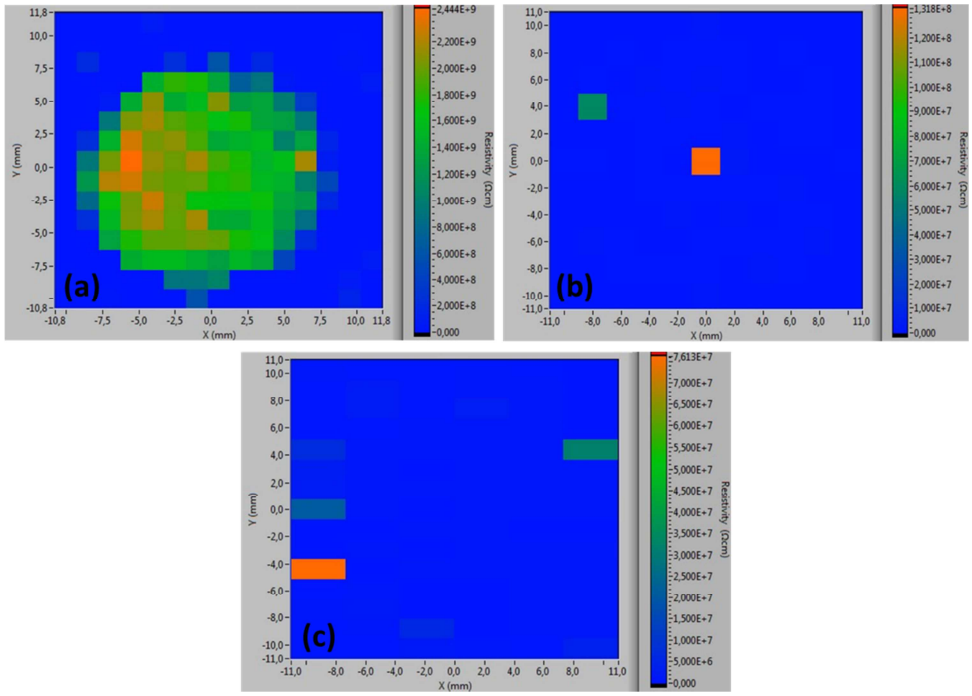

Figure 34: COREMA measurements for CZT samples from different ingots: (a) No annealed, (b) Annealed for 10h and (c) annealed for 24h

To understand better the effect of annealing, we used low temperature PL spectroscopy in order to characterize the change of defects in CZT. The typical low-temperature PL spectra of CZT samples grown without and with annealing for 24h are shown in **Figure 35.**

The spectra can be divided into three regions: near-band-edge region: bound exciton (D^0,X) peaks situated at 1.64–1.68eV; donor–acceptor region covering the donor–acceptor pairs (DAP) recombination; a defect band centered at 1.46–1.50eV ascribed to the A-center related to Cd vacancies in complex with a donor. One can observe that The (A^0,X) representing the acceptor-bound-exciton disappear for the annealed sample. We also observe that the DAP peak has relatively high emission intensity for the no annealed sample. However, the intensity becomes relatively low for the annealed sample. The decrease of the intensity of the DAP peak is due to the decrease of the impurities. Also, the intensity of the A-center peak slightly decreases after annealing because of the reduction of Cd vacancies acceptors. It is also important to note that the FWHM of (D^0,X) increase after annealing, and at the same time the FX peak disappear, which could means that the crystallinity was degraded. This behavior could be related to the regrowth of CdZnTe during the thermo-migration process of Te inclusions (17).

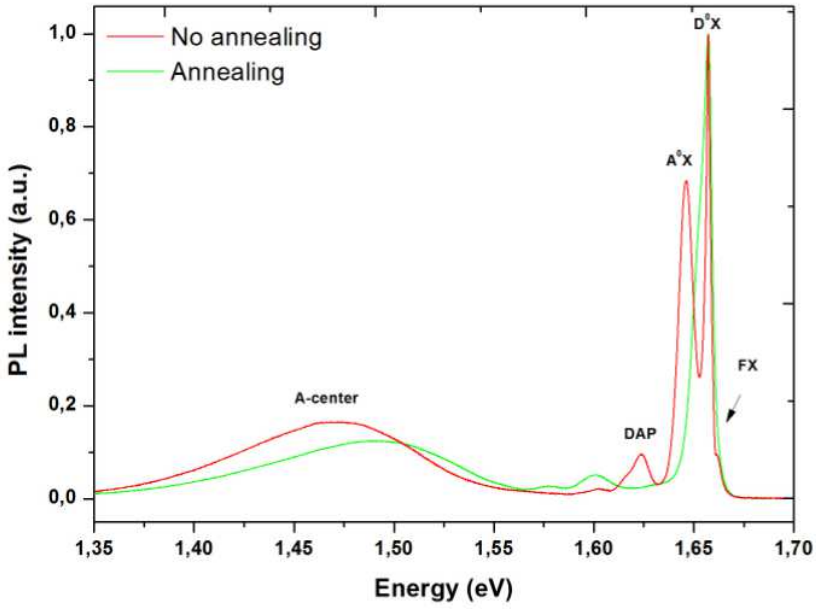

Figure 35: PL spectra of CZT samples without and with annealing

The production of homogeneous CdZnTe crystals is a key requirement for high quality detectors. In this work, we have studied the radial uniformity of Zn concentration in annealed and no annealed CdZnTe samples.

To evaluate the Zn concentration, EDX measurements were carried out. The radial composition of zinc for the sample grown without and with annealing is illustrated in **Figure 36**. One can observe that the ingot grown without annealing exhibited larger fluctuations of Zn composition, while the uniformity of Zn was improved after annealing. This behavior could be explained by the redistribution of atoms by solid state diffusion during thermal annealing (64).

The same behavior was observed for the (D^0,X) peak which is directly related to the band gap and Zn concentration. The maps are presented in **Figure 37**.

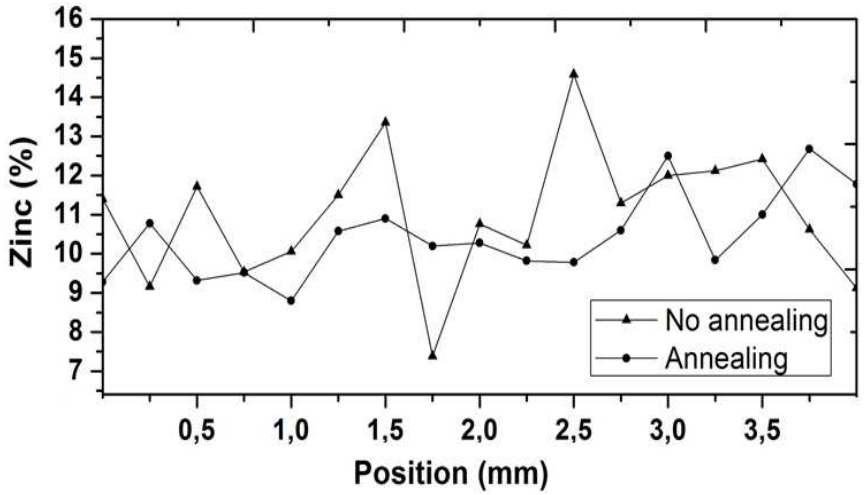

Figure 36: Radial Zn composition in no annealed and annealed CZT samples

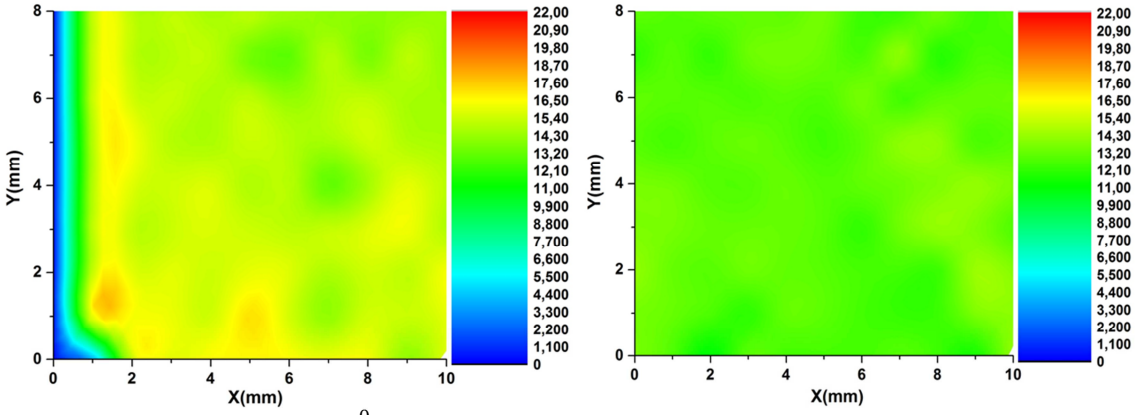

Figure 37: Pl maps of (D^0,X) peak of samples from (left) no annealed and annealed ingots (right)

III.6. Conclusions

In summary, high quality CdZnTe detectors have been harvested from ingot C, effectively demonstrating the advantages of crystal growth conditions. The summary of this investigation are as follows:

- Superheating of the melt by 26ºC was sufficient to (i) improve material homogeneity, (ii) eliminate of the conical shape and voids at the top of the ingots, and (iii) break down the Te clusters within CdZnTe crystals.
- Ingots grown using fast cooling present the smallest Te inclusions due to the retrograde solubility of the phase diagram, where Te does not have time to agglomerate.
- Fast cooling can affect the shallow defects of CZT samples leading to the increase of shallow acceptors concentration. In fact, fast cooling can also influence the zinc uniformity.
- Bigger Te inclusions can degrade the detector performance by distorting the internal electric field. In addition, big Te inclusions can reduce the active volume of the detectors leading to a voltage breakdown and increasing the leakage current.
- Annealing for 24 hours at 950°C creating a temperature gradient was successful to eliminate Te inclusions. However, annealing lowers the resistivity.

III.7. Bibliography

1. **S. Sitharaman, R. Raman, L. Durai, S. Pal, M. Gautam, A. Nagpal, S. Kumar, S.N. Chatterjee, S.C. Gupta.** Effect of hydrogenation on the electrical and optical properties of CdZnTe substrates and HgCdTe epitaxial layers. *Journal of Crystal Growth.* 2005, Vol. 285.
2. **M. Fiederle, A. Fauler, V. Babentsov, J. Franc, J. Konrath, M. Webel,J. Ludwig, K.W. Benz.** Characterization of CdTe crystals grown by the Vertical Bridgman. *Nuclear Instruments and Methods in Physics Research A.* 2003, Vol. 509, pp. 70–75.
3. **J. Franc, R. Grill, P. Hlídek, E. Belas, L. Turjanska, P. Höschl, I. Turkevych, A. L Toth, P. Moravec, H. Sitter.** The influence of growth conditions on the quality of CdZnTe single crystals. *Semicond. Sci. Technol.* 2001, Vol. 16, pp. 514-520 .
4. **A. Koyama, A. Hichiwa, R. Hirano.** Recent progress in CdZnTe crystals. *Journal of Electronic Material.* 1999, Vol. 28.
5. **C. Szeles, S. E. Cameron, J. O. Ndap, W. C. Chalmers.** Advances in the crystal growth of semi-insulating CdZnTe for radiation detector applications. *IEEE Trans. Nucl. Sci.* 2002, Vol. 49, pp. 2535–2540.
6. **Fukuda, Hans J.Scheel and Tsuguo.** *Crystal growth and technology.* 2003.
7. **A. Fauler, A. Zwerger, M. Dambacher, M. Fiederle.** Crystal growth and characterization of detector grade (Cd,Zn)Te crystals. 2006.
8. **M. Miihlberg, P. Rudolph, M. Laasch.** The correlation between superheating and supercooling in CdTe melts during unseeded Bridgman growth. *Journal of Crystal Growth* . 1993, Vol. 128, pp. 571-575.
9. **P. Rudolph, H.J. Koh, N. Schäfer, T. Fukuda.** The crystal perfection depends on the superheating of the mother phase too-experimental facts and speculations on the “melt structure” of semiconductor compounds. *Journal of Crystal Growth.* 1996, Vol. 166, pp. 578-582.
10. **P.Rudolph.** Fundamental Studies On Bridgman Growth Of CdTe. *Prog. Crystal Growth and Charact.* 1994, Vol. 29, pp. 275-381.
11. **L.Congfeng.** The formation and elimination of inclusions in CdZnTe crystal. *Proc.SPIE 6835, 68350I.* 2007.
12. **U.N. Roy, A. Burger, R.B. James.** Growth of CdZnTe crystals by the traveling heater method. In press.
13. **L. Xu, W. Jie, A.E. Bolotnikov, U.N. Roy, J. Stein, A. Hossain, G.S. Camarda, K.H. Kim, G. Yang, R. Gul, Y. Cui, Y. Xu, T. Wang, G. Zha, R.B. James.** Concentration of extended defects in CdZnTe single crystals: Effects of cooling rate after growth. 2012, Vol. 355, pp. 84–87.
14. **M. Bruder, H.J. Schwarz, R. Schmitt, H. Maier, M.O. Möller.** Vertical Bridgman growth of Cd1−yZnyTe and characterization of substrates for use in Hg1−xCdxTe liquids phase epitaxy. 1990, Vol. 101, pp. 266-269.
15. **S. K. Swain, K.A. Jones, A. Datta, K.G. Lynn.** Study of Different Cool Down Schemes During the Crystal Growth of Detector Grade CdZnTe. 2011, Vol. 58, p. 2341.
16. **S. Sen, W.H. Konkel, S.J. Tighe, L.G. Bland, S.R. Sharma, R.E. Taylor.** Crystal growth of large-area single-crystal CdTe and CdZnTe by the computer-controlled vertical modified-Bridgman process. 1990, Vol. 86, pp. 111-117.
17. **B. Li, J. Zhu, X. Zhang, J. Chu.** Effect of annealing on near-stoichiometric and non-stoichiometric CdZnTe wafers. 1997, Vol. 181, pp. 204-209.
18. **J. Crocco, H. Bensalah, Q. Zheng, V. Carcelen, E. Dieguez.** Influence of SiC pedestal in the growth of 50 mm CZT by Vertical gradient freeze method. *Journal of Crystal Growth.* 2012, Vol. 360, pp. 92–94.

19. **M. Fiederle, A. Fauler, A. Zwerger.** Crystal Growth and Characterization of Detector Grade (Cd,Zn)Te Crystals. *IEEE Transactions on Nuclear Science.* 2007, Vol. 54.
20. **A. Tanaka, Y. Masa, S. Setoand T. Kawasaki.** Zinc and Selenium Co-Doped CdTe Substates Lattice Matched To HgCdTe. *Journal of Crystal Growth.* 1989, Vol. 94, pp. 166-170.
21. **P. Fougeres, L. Chibani, M. Hageali, J.M. Koebel, G. Hennard, A. Zumbiehl,P. Siffert, M. Benkaddour.** Zinc segregation in HPB grown nuclear detector grade Cd1-xZnxTe. *Journal of Crystal Growth.* 1999, Vol. 197, pp. 641-645.
22. **S. Kuppurao, S.Brandon, J.J. Derby.** Modeling the vertical Bridgman growth of cadmium zinc telluride II. Transient analysis of zinc segregation. *Journal of Crystal Growth.* 1995, Vol. 155, pp. 103-111.
23. **A. Zappettini, L.Marchini , M.Zha , G. Piacentini , N.Zambelli , G. Benassi D. Calestani.** Study of the anomalous zinc distribution in vertical Bridgman grown CdZnTe crystals. *CrystEngComm.* 2012.
24. **M. Fiederle, C. Eiche, M. Salk, R. Schwarz, K. W. Benz, W. Stadler, D. M. Hofmann, B. K. Meyer.** Modified compensation model of CdTe. 1998, Vol. 84.
25. **J.H. Greenberg, V.N. Guskov.** Vapor pressure scanning of non-stoichiometry in Cd0.9Zn0.1Te1±δ and Cd0.85Zn0.15Te1±δ. *Journal of Crystal Growth.* 2006, Vol. 289, pp. 552-558.
26. **Wang, Junning Gao ·Wanqi Jie · Yihui He · Jie Sun ·Hao Zhou · Gangqiang Zha · Yanyan Yuan Junli Tong · Hui Yu · Tao.**Study of Te aggregation at the initial growth stage of CdZnTe films deposited by CSS. 2012, Vol. 108, pp. 447–450.
27. **Q. Zheng, F. Dierre, J. Crocco, V. Carcelen, H. Bensalah, J.L. Plaza, E. Dieguez.** Influence of surface preparation on CdZnTe nuclear radiation detectors. *Applied Surface Science.* 2011, Vol. 257, pp. 8742– 8746.
28. **Anand, K.G.** Te Precipitates and Impurity Gettering Effect in CdZnTe (Zn=4%) Crystals. 2013, Vol. 4, pp. 4-7.
29. **Li.Guo-Qiang, Jie.Wan-Qi, Gu.Zhi, Hu A. Hui.** Correlation between the IR Transmission Spectra and the CdZnTe Qualities. *Chin.Phy.Lett.* 2003, Vol. 20.
30. **Jain, S.** *Photoluminescence Study of Cadmium Zinc Telluride.* 2001.
31. **G. Yang, W.Jie, Q. Li, T. Wang, G. Li, H. Hua.** Effects of In doping on the properties of CdZnTe single crystals. *Journal of Crystal Growth.* 2005, Vol. 283, pp. 431–437.
32. **Q.Li, W. Jie, L. Fu, T. Wang, G.Yang, X. Bai, G.Zha.** Optical and electrical properties of indium-doped Cd0.9Zn0.1Te crystal. *Journal of Crystal Growth.* 2006, Vol. 295, pp. 124–128.
33. **A. Castaldini, A. Cavallini, B. Fraboni, L. Polenta, P. Fernandez, J. Piqueras.** Compensation and deep levels in II–VI compounds. 1996, Vol. 42, pp. 302-305.
34. **K.H. Kim, J.Suh, A.E.Bolotnikov, P.M.Fochuk, O.V.Kopach, G.S.Camarda , Y.Cui , A.Hossain,G. Yang.** Temperature-gradient annealing of CdZnTe under Te overpressure. *Journal of Crystal Growth.* 2012, Vol. 354, pp. 62–66.
35. **S. Seto, A. Tanaka, M. Kawashima.** Correlation between electrical and photoluminescence measurements in high-quality p-type CdTe. 1988, Vol. 64, p. 3658 .
36. **Crocco, J.** *Crystal Growth & Technology, Device Fabrication, and Material Properties of Cd(Zn)Te for Radiation Detector Applications.* 2012.
37. **K. Hjelt, M. Juvonen, T. Tuomi, S. Nenonen, E. E. Eissler, M. Bavdaz.** Photoluminescence of Cd1- xZnxTe Crystals Grown by High-Pressure Bridgman Technique. 1997, Vol. 162.

38. **J. Franc, P. Hlídek, P. Moravec, E. Belas, P. Höschl, L. Turjanska, R. Varghová.** Determination of energy gap in Cd1-xZnxTe (x=0-0.06). *Semicond. Sci. Techno.* 2000, Vol. 15.
39. **V. Babentsov, J. Franc, P. Höschl, M. Fiederle, K. W. Benz, N. V. Sochinskii, E. Dieguez, R. B. James.** Characterization of compensation and trapping in CdTe and CdZnTe: Recent advances. 2009, Vol. 44.
40. **Awadalla.S.A, Hunt.A. W, Tjossem, R.B, Lynn, K. G, Szeles.C, Bliss.M.** Evidence for dislocations or related defects present in CdTe and Cd1-xZnxTe crystals. 2001, Vol. 264.
41. **M. Samini, B.Biglarmi, M. Haje.Ali, J. M. Koebel, P. Siffert.** About the Origin of the 0.15 to 0.20 eV Defect Level in Cadmium Telluride. *phys. stat. sol. (a).* 1987, Vol. 100.
42. **H. Elhadidy, J.Franc, E. Belas,P. Hlidek, P. Moravec, R. Grill, P.Hoschl.** Thermoelectric Effect Spectroscopy and Photoluminescence of High-Resistivity CdTe:In. *Journal of Electronic Materials.* 2008, Vol. 37.
43. **M. Pavlović, M. Jakšić, H. Zorc, and Z. Medunić.** Identification of deep trap levels from thermally stimulated current spectra of semi-insulating CdZnTe detector material. *Journal of Applied Physics.* 2008, Vol. 104.
44. **M. Chu, S. Terterian, D. Ting, C. C. Wang, H. K. Gurgenian, S. Mesropian.** Tellurium antisites in CdZnTe. 2001, Vol. 79.
45. **R.Triboulet.** *CdTe and Related Compounds; Physics, Defects, Hetero- and Nano-structures.. Part II.* 2010.
46. **M. Fiederle, V. Babentsov, J. Franc, A. Fauler, J.P. Konrath.** Growth of high resistivity CdTe and (Cd,Zn)Te crystals. *Cryst. Res. Technol.* 2003, Vol. 38, pp. 588 – 597 .
47. **R. Soudararajan, K.G. Lynn, S.Awadallah.** Study of Defect Levels in CdTe Using Thermoelectric Effect Spectroscopy. *Journal of Electronic Materials.* 2006, Vol. 35.
48. **A.E. Bolotnikov, G. S. Camarda, Y. Cui, K. T. Kohman, L. Li, M. B. Salomon, R. B. James.** Performance-limited Defects in CdZnTe detectors. 2007, Vol. 54.
49. **Z. GangQiang, X. Hang, L. Ting, X. YaDong, W. Tao, J. WanQi.** The analysis of X-ray response of CdZnTe detectors. 2012, Vol. 55.
50. **L.A. Najam, N. Y. Jamil, R. M. Yousif.** Comparison in Mobility, Transit Time and Quality Factor Between CdMnTe and CdZnTe Detectors. 2012, Vol. 7.
51. **R. B. James, T. E. Schlesinger, J. C. Lund , M. Schieber.** Cd1-xZnxTe Spectrometers for Gamma and X-ray Applications. *Semiconductors and Semimetals.* 1995) Chap.9., 9.
52. **R. Grill, E. Belas, J. Franc, M. Bugár, S. Uxa, P. Moravec, P. Höschl.** Polarization Study of Defect Structure of CdTe Radiation Detectors. 2011, Vol. 58.
53. **Š. Uxa, E. Belas, R. Grill, P.Praus, R B. James.** Determination of Electric-Field Profile in CdTe and CdZnTe Detectors Using Transient-Current Technique. 2012, Vol. 59.
54. **A.E. Bolotnikov, C.M. Hubert Chen, W.R. Cook, F.A. Harrison.** The effect of cathode bias (field effect) on the surface leakage current ofCdZnTe detectors. 2003, Vol. 510.
55. **C. Szeles, S.A. Soldner, S. Vydrin, J. Graves, D.S. Bale.** CdZnTe Semiconductor Detectors for Spectroscopic X-ray Imaging. 2008, Vol. 55.
56. **H.Chen, S.A. Awadalla, J. Mackenzie, R.Redden, G.Bindley,A. E. Bolotnikov, G. S. Camarda, G. Carini, R. B. James.** Characterization of Traveling Heater Method (THM) Grown Cd0.9Zn0.1Te. 2007, Vol. 54.

57. **E. Belas, J. Franc, R. Grill, A. Toth, P. Horodysky, P. Moravec, P. Hoschl.** Regular and Anomalous-Type Conversion of p-CdTe during Cd-Rich Annealing. 2005, Vol. 34.
58. **H.R. Vydyanath, J.A. Ellsworth, J.B. Parkinson.** Thermomigration of Te Precipitates and Improvement of (Cd,Zn)Te Substrate Characteristics for the Fabrication of LWlR (Hg,Cd)Te Photodiodes. 1993, Vol. 22.
59. **T.S. Lee, J.W. Park, Y.T. Jeoung, H.K. Kim, C.H. Chun, J.M. Kim.** Thermomigration of Tellurium Precipitates in CdZnTe Crystals Grown by Vertical Bridgman Method. 1995, Vol. 24.
60. **K.H. Kim, J. Suh, A.E. Bolotnikov, P.M. Fochuk, O.V. Kopach, G.S. Camarda, Y. Cui, A. Hossain, G. Yang, J. Hong, R.B. James.** Temperature-gradient annealing of CdZnTe under Te overpressure. 2012, Vol. 354, pp. 62–66.
61. **J. Franc, E. Belas, M. Bugáa, P. Hlídek, R. Grill, G. Yang, A. Cavallini, B. Fraboni, A. Castaldini, S. Assali.** Semi insulating CdTe:Cl after elimination of inclusions and precipitates by post grown annealing. 2012, Vol. 7.
62. **M. Bugar, E. Belas, R. Grill, J. Prochazka, Š. Uxa, P. Hlidek, J. Franc, R. Fesh, P. Hoschl.** Inclusions Elimination and Resistivity Restoration of CdTe:Cl Crystals by Two-Step Annealing. 2011, Vol. 58.
63. **P. Yu, W. Jie. T. Wang.** Effect of Te atmosphere annealing on the properties of CdZnTe single crystals. 2011, Vol. 643.
64. **J. K. Radhakrishnan, B. S. Sunderseshu, Meenakshi Srivastava, G. L. Seth, R. Raman, R. C. Narula, R. K. Bagai.** Homogenization of zinc distribution in vertical Bridgman grown Cd0.96Zn0.04Te crystals. 2001, Vol. 24, pp. 659-663.

Chapter IV: The effect of surface preparation on the properties of CdZnTe

Table of content

IV.1. Introduction

There has been a great interest in CdZnTe (CZT) semiconductors in recent years due to its several applications. CZT has been investigated for many potential uses in medical imaging and can also be used in the field of national security, nuclear detecting, astrophysical research and industrial measurement. This is due to the interesting properties including high resistivity, high average atomic number, large band gap, and room temperature operability. In spite of these fundamental advantages, the use of CZT material is still limited by some problems such as the presence of secondary phases, impurities, and surface quality.

Surface treatment is a critical and sensitive process in the fabrication of CZT radiation detectors, and plays a critical role in the detectors performance (1). As it is known, surface preparation influence the uniformity of the electric field inside the device and can significantly affect charge transport and signal formation. In this way, various studies have shown that surface properties control many aspects of device operation and performance. For example, the maximum bias voltage is often limited by surface leakage current and the conductivity of the detector surface, which depends on surface processing. Furthermore, high leakage currents affect the electric field line distribution near the contacts, and can degrade the charge collection efficiency. Therefore, it is desirable to have the leakage current of the detector as low as possible (2). For these reasons it is important to study CZT surface treatment to obtain an optimal surface condition that would result in high quality radiation detectors.

In this chapter, the surface preparation processes which have been developed during this thesis investigation are presented. This includes cutting, lapping, polishing, chemical etching, as well as lateral edges passivation. These processes are fundamental to prepare the surface of the CdZnTe crystals for electrode deposition. Our objective is to study the influence of each process on the morphological, optical and electrical properties of CZT and then select the best process to be followed for the preparation of CZT detectors.

IV.2. Experimental details

IV.2.1. Samples preparation

The samples used in this section have been harvested from an ingot of $Cd_{1-x}Zn_xTe$ (x = 10%) grown by the Bridgman method (3). The crystals were cut into $5\times5\times3mm^3$ samples using horizontal Well 3032 machine with a diamond wire of 170µm diameter.

In the surface preparation process, different steps were carried out with the objective to obtain high quality detectors. These steps will be discussed as follows:

The samples were first ***lapped*** to remove the saw damage, and to obtain flat surfaces with controlled thickness. This process was carried out using a Logitech PM5 machine with a standard glass plate operating at 50rpm. The abrasive used for bulk material removal was 3µm Al_2O_3 powder.

Afterwards ***mechanical polishing*** was done in the objective to reduce the thickness of the amorphous subsurface damage layer and to improve the surface quality. This process is performed with the same PM5 Logitech system, but using a pad (Chemcloth) and 3µm Al_2O_3 powder and also by CP3000 Logitech system with 1µm diamond. **Table 1** summarizes the parameters used for lapping and polishing. The pressure is controlled with the JIG adapted to the machine.

Table 1: Lapping and polishing parameters

Parameter	Lapping	Polishing	
Plate	Glass	Pad	Pad
Plate velocity (rpm)	50	50	50
Abrasive	3µm Al_2O_3	3µm /1µm Al_2O_3	1µm diamond
Pressure (kPa)	<10	<15	<15
Duration (min)	20	15	15
Machine	PM5	PM5	CP3000

The material preparation operations such as cutting, lapping, and polishing create surface and sub-surface damage. To remove this damage layer, a ***chemical etching*** process is used. Chemical etching is needed prior to the metal deposition process in order to form a tellurium-rich surface, while removing surface contaminants and oxides. The standard chemical solution for CZT etching is Br-MeOH (4). The enrichment of elemental Te on the surface is one favourable characteristic useful for electrode deposition and adhesion. However, this surface layer of Te can also lead to increased leakage current, which is unfavourable to the performance of CdZnTe detector (5).

In this work, the samples were chemically etched with 2 % Br-MeOH solution for 2min, and react following the **Equation 1**. In fact, the reaction of Br_2 at the surface can be explained by the redox reactions between Bromine and Cd or Te (6).

Equation 1 $$Cd_{0.9}Zn_{0.1}Te + Br_2 \rightarrow 0.9CdBr_2 + 0.1ZnBr_2 + Te$$

Equation 2 $$Br_2 + Cd \rightarrow 2Br^- + Cd^{2+} \quad \Delta E = +1.469\,V$$

Equation 3 $$2Br_2 + Te \rightarrow 4Br^- + Te^{4+} \quad \Delta E = +0.498\,V$$

It can be observed in these reactions that Br_2 preferentially reacts with Cd, therefore the sample surface changes to Te-rich due to the deposition of Te product on Cd Face. Afterward the samples were rinsed with methanol to dissolve the Br remaining on the surface and then dried with nitrogen gas.

Immediately after etching, Au was deposited on both sides of the CZT samples by the ***electroless*** method (1g of $AuCl_3$ in $25cm^3$ of H_2O) for measuring I-V characteristics. In this process the sample is immersed in the $AuCl_3$ aqueous solution for 2min.

The $AuCl_4^-$ ions are supposed to react with Cd, Zn, and Te. Due to the fact that the composition of Zn in the $Cd_{1-x}Zn_xTe$ crystal is in minority concentration (~10 % in our case), the reaction of Au ions with Zn is negligible in comparison of Cd. As shown in **Equation 4** and **Equation 5** the difference of standard potentials of the reaction between $AuCl_4^-$ and Cd is higher than the one of Te, which means that Au reacts in preference with Cd. In fact, when Cd react with $AuCl_4^-$, an oxide-reduction reaction occurs, where the oxidation reaction was chosen as $AuCl_4^- + 3e^- \leftrightarrow Au + 4Cl^-$, with a standard potential of +1.00V, and the reduction reaction occurring with Cd is $Cd^{2+} + 2e^- \leftrightarrow Cd$, with a standard potential of –0.4V.

Equation 4 $$2AuCl_4^- + 3Cd \rightarrow 2Au + 8Cl^- + 3Cd^{2+} \quad \Delta E^0 = +1.40V$$

Equation 5 $$2AuCl_4^- + 3Zn \rightarrow 2Au + 8Cl^- + 3Zn^{2+} \quad \Delta E^0 = +1.76V$$

Equation 6 $$4AuCl_4^- + 3Te \rightarrow 4Au + 16Cl^- + 3Te^{4+} \quad \Delta E^0 = +0.43V$$

Equation 7

$$4AuCl_4^- + 3Te + 6H_2O \rightarrow 4Au + 16Cl^- + 3TeO_2 + 12H^+ \quad \Delta E^0 = +0.41V$$

It is necessary to note that only when the potential difference is positive, the reaction is supposed to occur favorably. The potential difference of redox reaction means that the reaction is total and consequently shifted to one direction. In consequence, the reaction of Au deposition is a direct reaction. For the redox reactions between $AuCl_4^-$ ions and Te, two possible reactions are presumed (**Equation 6** and **Equation 7**).

The Au reacts with the CZT surface forming a conductive TeAu layer, considering that cadmium is removed from the surface and replaced by gold (7).

After Au deposition, the sample was dried with nitrogen. Then the anode and cathode surfaces were protected by a thin wax film. Afterward the edges were lapped manually with Al_2O_3 powder 3μm to remove the gold from the lateral edges and then etched. For

lateral edges ***passivation***, the samples were i) immersed in 2.68g NH_4F 8ml H_2O_2 17ml H_2O for 10min, and then rinsed with ionized water (8), and finally, ii) the wax is removed through dissolution in trichloroethylene.

IV.2.2. Characterization

The study of the surface was carried out using a Scanning Electron Microscope (Hitachi S-3000N) coupled to an Energy Dispersive X-ray (EDX) Analyser (Oxford Instruments, INCAx-sight model) for surface quality and elemental composition. An Atomic Force Microscope (PSI100 Park Systems) was used for analyzing the surface roughness. The samples were also characterized using X-Ray Photoelectron Spectrometer (XPS) formed by a CLAM4 electron energy analyzer, and an X-ray Source Mg Kα from Thermo-scientific. Photoconductivity (PC) measurements were performed by using a NHQ-105L voltage source and monocromated CM110 light source. A Brucker D5000 X-ray diffractometer was used for carrying out high-resolution X-ray rocking-curve measurements. The source was a Cu K_α (λ=1.54178A°) radiation, the system has had an angular deviation of 0.0002°, and the generator settings were 45kV and 100mA. The photoluminescence spectra were recorded with a Hamamatsu R453 photomultiplier and an HRS-2 monochromator with a spectral resolution of 0.6nm and the samples were excited with the 488 nm line of an Ar-ion laser. The I-V results have been obtained using a Keithley 2400 sourcemeter.

IV.3. Results and discussion

The most important results obtained in the sample surface preparation will be presented in the next paragraphs. First, the characterization of the surface after lapping, polishing and etching will be discussed in order to understand the influence of each step in the surface preparation. In the second part, the effect of etching time will be studied considering that etching is necessary for detector preparation. Finally, the lateral edges passivation with ammonium fluoride will be further investigated.

IV.3.1. Effect of lapping, polishing and etching

The morphology of the surface of CdZnTe samples after lapping and polishing with different slurries were analysed using SEM technique, as shown in **Figure 1**. One can observe that the lapped sample has a very rough surface, while the 3µm mechanically polishing process produces a more reflective surface, but with a high density of scratches on the surface. Using 1µm polishing, the density of scratches decreases. In

fact for the polishing with 1µm diamond, we observe that the surface is smooth in comparison with the others, and the density of scratches is too low which generate a uniform surface.

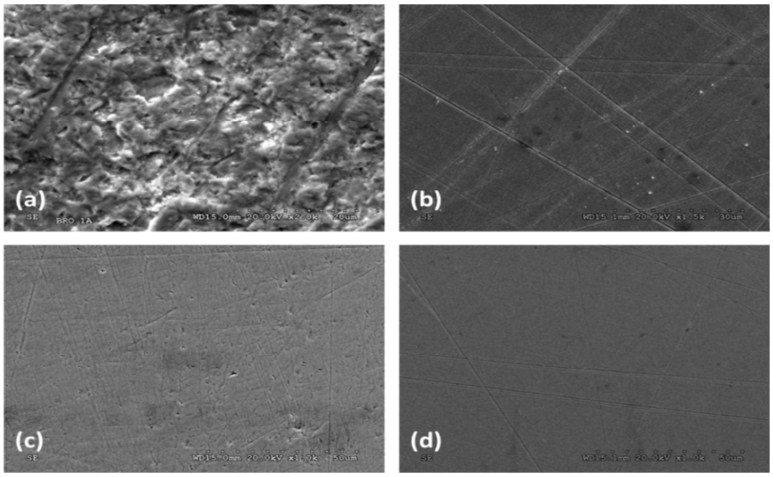

Figure 1: SEM images of samples after: (a) 3µm lapping (b) 3µm Al_2O_3 polishing, (c) 1µm Al_2O_3 polishing, (d) 1µm diamond polishing

In order to analyze the surface composition, EDX measurements were carried out and the results are illustrated in **Figure 2**. Using this technique, the surface composition for each sample can be obtained, taking into account that the area under each peak is proportional to the concentration of the element. One can see in this figure that in addition to the three principal elements Te, Cd and Zn, more peaks are also observed due to the chemical composition of the slurry. Al and O were observed for the samples polished using Al_2O_3, while C for polishing using Diamond. It is important to note that these polishing residues could be removed after etching with Br-MeOH.

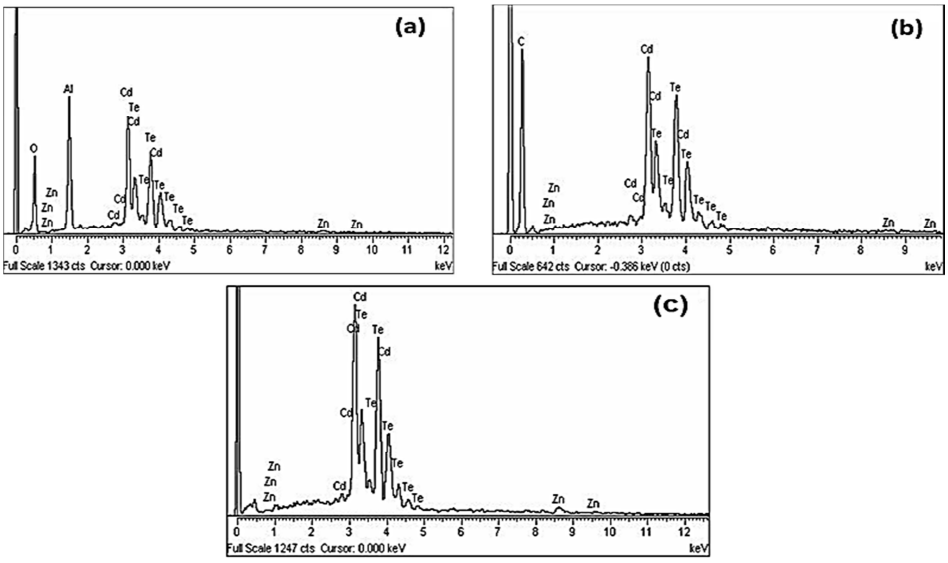

Figure 2: EDX analysis spectra after using: (a) polishing Al_2O_3, (b) polishing Diamond and (c) etching Br-MeOH

It is also important to take into consideration that surface crystallinity plays an important role in determining the quality of CZT crystals. For this reason, the high resolution X-ray diffraction (HRXRD) technique has been used in order to have information about the surface quality of the samples after different processes.

One can observe in **Figure 3** that the HRXRD rocking curves exhibit a significant difference after each surface treatment, where the variation in the FWHM is clear (9). The rocking curve shape after lapping and polishing show that the crystal quality is very poor. The most intense peak and the lower FWHM (68") has been obtained after etching process, which means that etching process is necessary to remove the damage created by cutting, lapping and polishing (10) and taking into consideration that the rocking curve of the CZT bulk crystal is similar to the behaviour of the etched sample shown in **Figure 3**. The HRXRD demonstrate the strong influence of lapping and polishing on the crystalline quality at the surface.

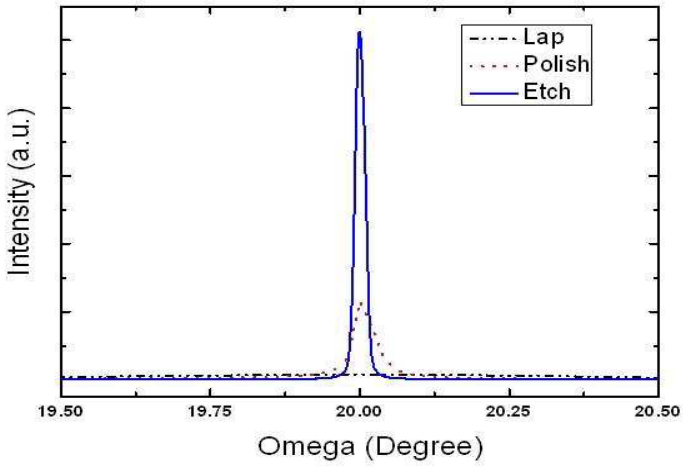

Figure 3: Recorded HRXRD pattern of CZT sample after different surface treatments

In order to complete the previous results about the influence of lapping, polishing and etching, PL at low temperature has been realized to study the defects introduced during surface preparation processes. In this situation, lapping, polishing and etching have been investigated. PL spectra after the surface preparation are shown in

Figure 4. It is clearly visible that no peaks can be observed after the lapping process, which indicates that the surface quality is very low. As can be seen, in the same figure the peaks (D^0,X) at 1.66eV and (A^0,X) at 1.64eV are observed after polishing and etching processes. In fact, the intensities of (D^0,X) and (A^0,X) peaks after etching are more higher after etching process, which means that the surface has been ameliorated. The shallow donor–acceptor pair recombination DAP at 1.61eV is also existing and its

intensity increases for the etched sample which demonstrates that the impurities and defects are compensated after etching. The A-center band at 1.505eV which is related to the formation of surface defects such as complexes of cadmium vacancies and Indium donors is also visible after polishing and etching processes.

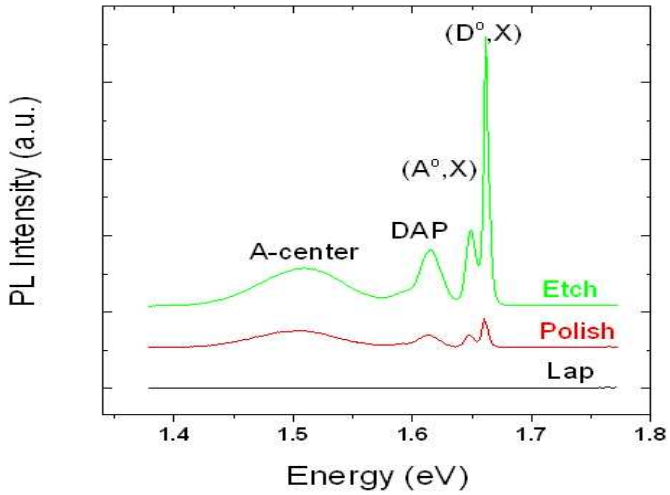

Figure 4: Low temperature (22K) PL spectra of CZT sample after different surface treatment

A summary of these peaks and their intensities is illustrated in **Table 2**. We note that the sample after etching process has the highest $I_{(D0,\ X)}/I_{A\text{-center}}$ intensity ratio which means that etching using bromine-methanol is an adequate process to remove the damages and defects introduced by cutting, lapping and polishing (11) (12). Additionally, the FWHM of (D^0, X) peak is too narrow after chemical etching and the $I_{(D0,\ X)}/I_{DAP}$ is the highest.

Table 2: PL results for the CZT surface after lapping, polishing and etching

	Lap	Pol	Etch
(D^0,X) (eV)	-	1.660	1.661
(A^0,X) (eV)	-	1.647	1.649
DAP (eV)	-	1.614	1.614
A-center (eV)	-	1.507	1.509
$I_{(D0,X)}/I_{(A0,X)}$	-	2.3	3.50
$I_{(D0,X)}/I_{DAP}$	-	2.23	4.71
$I_{(D0,X)}/I_{A\text{-center}}$	-	1.69	6.95
FWHM	-	5.9	4.6

The previous results show that chemical etching process produces the desired surface composition: low surface roughness, low defects and high quality for electrode deposition. With these arguments, it is important to study the electrical behavior of the samples after each process.

Figure 5 present the I–V characteristics (0 V to +170 V) for the detectors prepared after lapping, polishing and etching. It can be seen that the chemically etched detector shows a reduction of the dark current in comparison with the lapped and polished one. These data support the fact that leakage current increases when the surface damage increases.

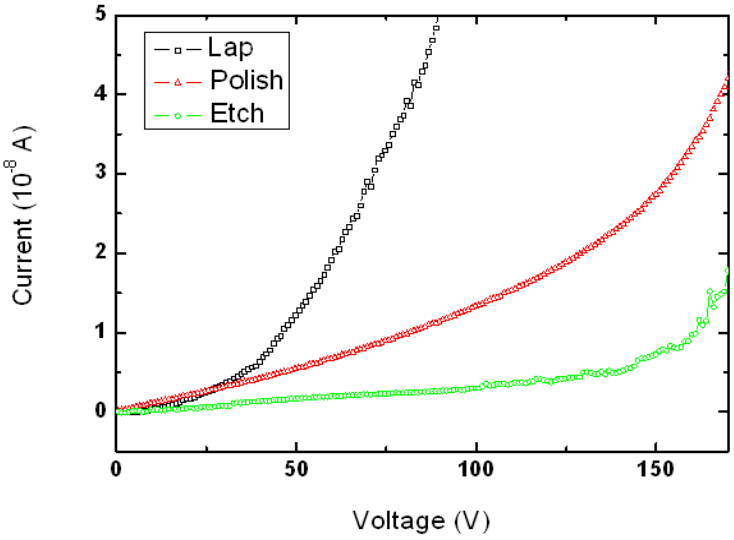

Figure 5: I–V curves after different surface treatment

From these results, we conclude that mechanical polishing cannot be suitable as a final step for detectors fabrication, and chemical etching is necessary to remove defects from the surface and then reduce the leakage current.

IV.3.2. Selection of the best etching time of CdZnTe

As previously has been discussed, the etching process using Br-MeOH is an important step to be carried out before the metal deposition in order to form a tellurium-rich surface, while removing, scratches, contaminants and oxides from the surface. In this section we are going to study how the etching time affects the properties of CdZnTe samples, and find out the suitable time to achieve good detector material.

CZT samples previously lapped and polished were treated with the same concentration of 2% Br-MeOH for different etching times (30 s, 2, 4, 6, 8min).

In order to optimize the etching time and achieve smooth and clean surfaces for electrode deposition, AFM was selected to study the surface uniformity of the samples. 3D images of CZT crystals after different etching time with 2% Bromine methanol are presented in

Figure 6. The AFM images show that the etching process for 30 seconds results in a surface with low density of small particles, while etching for 2 minutes presents high density of particles. When the time of etching is increasing, we can observe that the density of the particles decreases but it contains bigger size of particles.

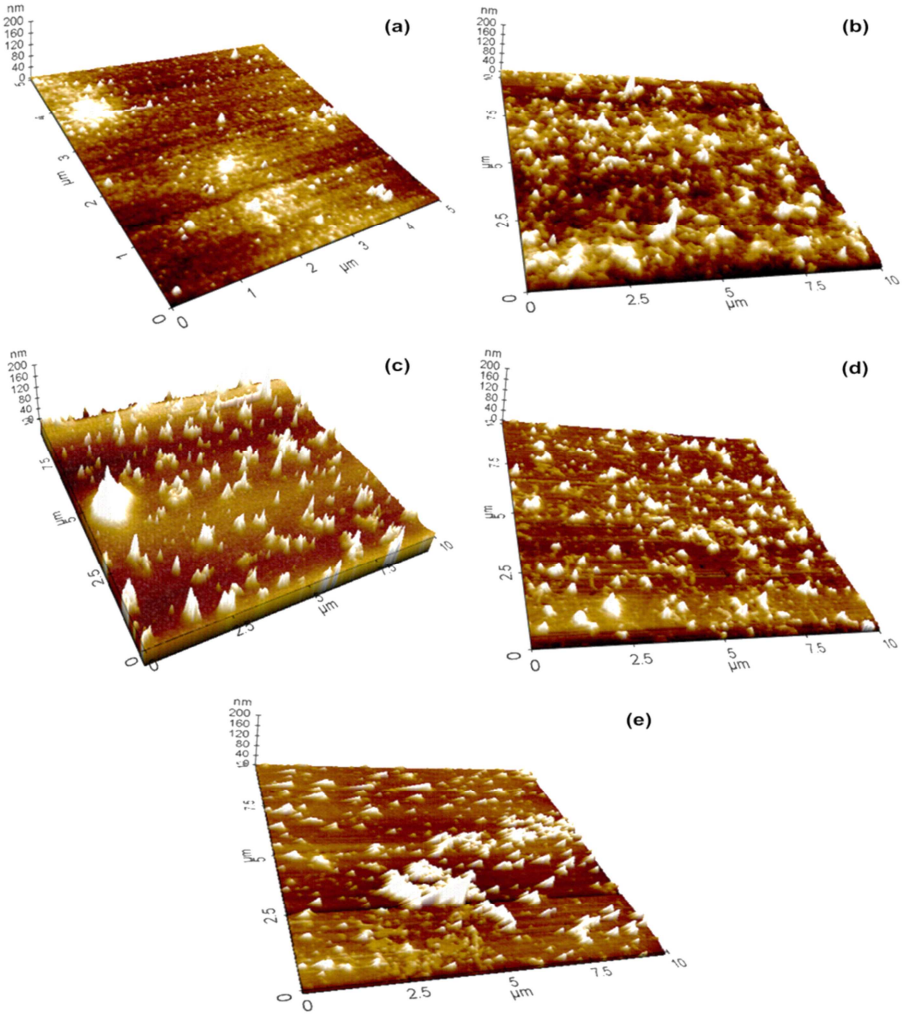

Figure 6 : 3D AFM images of CZT samples after etching: (a) 30s, (b) 2min, (c) 4min, (d) 6min, (e) 8min

Complementary to this, the surface roughness, the samples were also examined with AFM as presented in **Figure 7**. One can observe that the surface roughness decreases when the surface is etched with 2% Br/methanol solution for 30s. However this trend changes and the roughness increases when the sample is etched for more than 2min. It is clear that 30s of chemical etching is sufficient to significantly reduce the damage imparted by the mechanical polishing, as evidenced by the reduced surface roughness observed after etching. For etching time greater than 2min, the surface morphology is degraded with increasing roughness. Indeed, it has been demonstrated that the roughness of the surface degrades the detector efficiency (13).

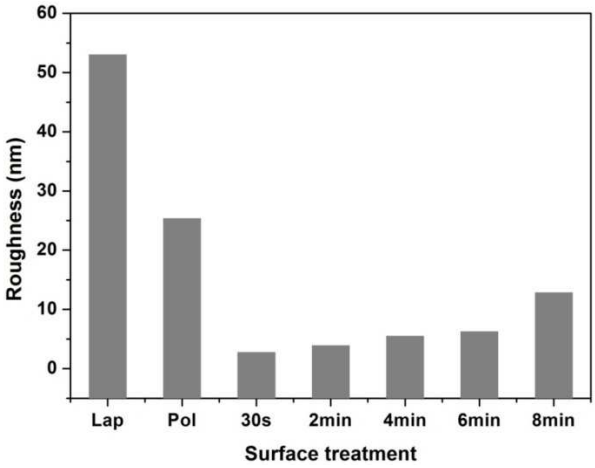

Figure 7: Roughness values after lapping, polishing, and chemical etching process with different times

In fact, rougher surfaces tend to contain a higher concentration of surface trapping centers which greatly disturb the near-surface electrical field and cause injecting contacts, thus increasing the surface leakage currents (14).

Following these results, one can justify the use of Br-MeOH solution to remove the surface damaged layer introduced by cutting and mechanical polishing in order to obtain a clean surface prior to electrode deposition.

The surface composition for each sample has been obtained by EDX and is presented in **Figure 8**. The results indicate that the surface concentration of Te/Cd+Zn varies greatly for each process. We also observe that the surface is enriched with Te for the chemical etching processes (30s and 2min), while the Te concentration is reduced for the others processes, and the etching time of 30s produces the largest concentration of Te. This is an interesting result because a Te rich surface is necessary for Au deposition in order to facilitate the formation of Au/Te layer.

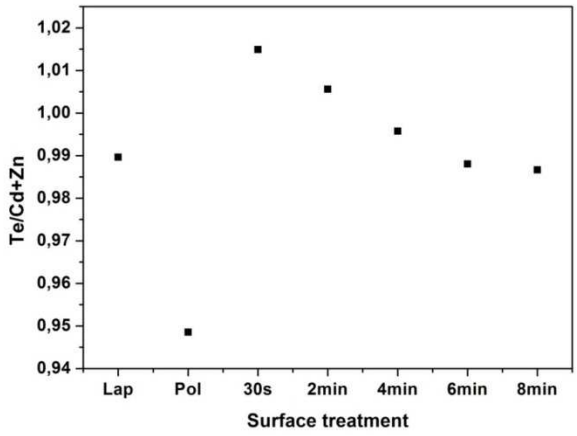

Figure 8: Chemical composition from EDX after lapping, polishing, and chemical etching processes with different times

Both previous results show that the 30s and 2min chemical etching processes produce the desired surface composition: low surface roughness with enriched Te surface for optimum electrode deposition. With these arguments, it is important to know the behavior of the leakage current of the samples submitted to the processes discussed above. **Figure 9** compares the *I–V* characteristics for detectors prepared with different etching time. It can be observed that the chemically etched detector shows a reduction of the dark current in comparison with the polished one which indicates that the leakage current increases when surface roughness increases. We also observe that the leakage current increases with increasing etching time. With these results we confirm that the improvement of the surface quality can decrease the trapping centers which are responsible of the increase of leakage current by supplying more conductive and altered electric-field distributions (15).

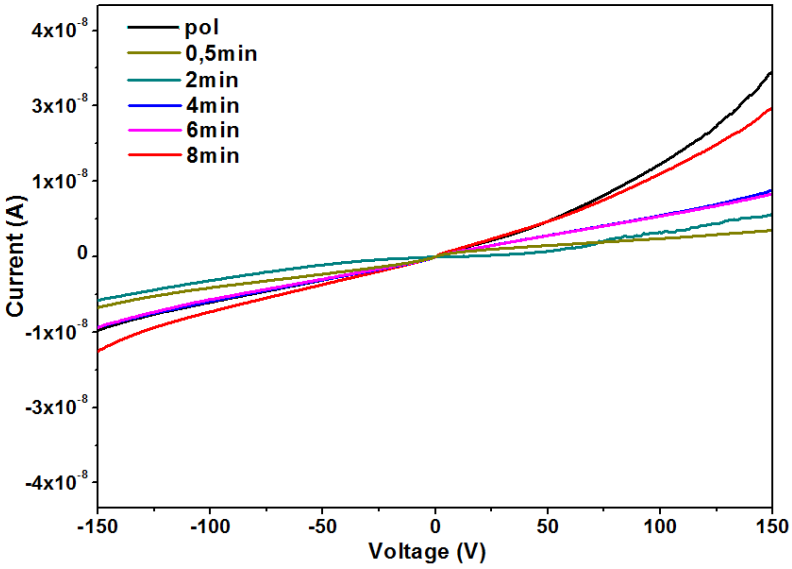

Figure 9: *I–V* curves after different surface treatment

These results support the conclusion that an etching time between 30s and 2min produces the minimum leakage current in the detector.

In summary, by comparison of the results obtained using different characterization techniques, an etching time for 30s is considered as the best etch time regarding Te concentration, surface roughness and leakage current.

IV.3.3. Study of lateral edges passivation with ammonium fluoride

Passivation of lateral edges of CdZnTe detectors through the formation of an oxide film is an important step in the device manufacturing. Therefore, the process of passivation had been typically required to reduce the conductivity of the Te-enriched surface layer and decrease the surface leakage current (16).Various methods have been studied for the CZT surface passivation, which could oxidize the surface. Previous studies have shown that hydrogen peroxide (H_2O_2) forms oxide tellurium on the CZT surface, thus acting as a good passivating agent (17). The KOH aqueous solution leaves a more stoichiometric and smoother CZT surface (18).

In order to study the surface roughness of the CZT samples after different surface treatment processes, the samples were analyzed by SEM and AFM as shown in **Figure 10**. One can observe that mechanical polishing leaves on the surface high density of scratches. After chemical etching these scratches were totally removed but it produces surface pitting. Passivation treatment leaves the surface more clean and remove the pitting on the surface.

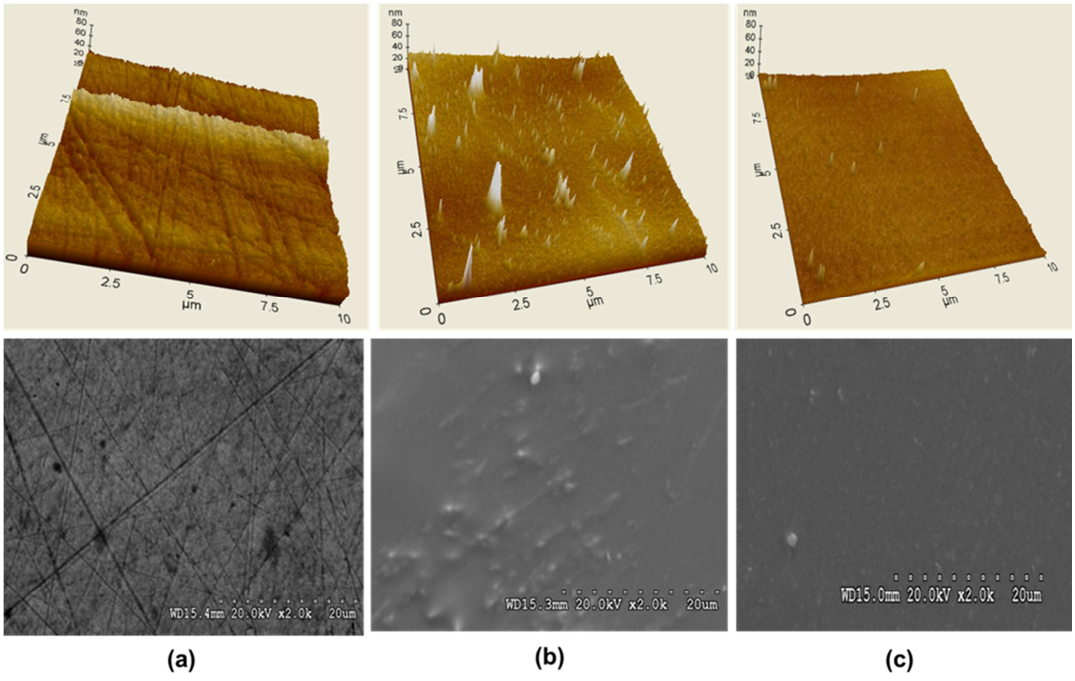

Figure 10: AFM and SEM images of CZT samples after polishing (a), etching (b) and passivation (c)

To understand the surface uniformity of the different processes used, the roughness has been calculated using AFM data as presented in **Figure 11**. The average roughness values have been determined from an imaged area of 10μm^2.The results show that the surface roughness decreases when the surface is etched with 2% Br/Methanol solution and decreases deeply when the surface is passivated immediately after etching. However this trend changes and the roughness increases when the sample is passivated after 24h after etching process.

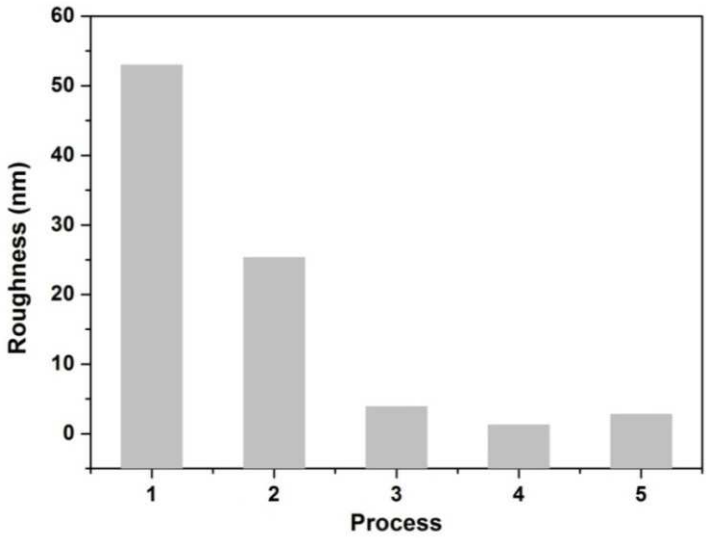

Figure 11: Roughness values after different surface treatment: 1- Lapping, 2- Polishing, 3- Etching, 4- Passivation immediately after etching and 5- Passivation 24h after etching

In order to complete the previous information on the morphology and surface composition, EDX measurements have been carried out and the results are illustrated in **Table 3**. The results show that after polishing the concentration of Cd is higher, while chemical etching reduces Cd and leaves the surface rich on Te. After passivation appear an important concentration of oxygen and the concentration of Cd and Te decreased which means that Te and Cd were oxidized.

Table 3: EDX analysis results of CdZnTe samples after different surface treatment

	%Te	%Cd	%Zn	%O
Polishing	48.49	49.36	2.15	-
Etching	51.52	47.29	1.19	-
Passivation	30.62	27.02	3.13	39.23

XPS is a highly surface sensitive technique, with the ability to measure the elemental composition and chemical binding information for the top 1–5nm depth of the surface region. **Figure 12** illustrates the XPS survey spectra for CdZnTe samples and show distinct Te, Cd and Zn peaks around 400, 600 and 1000eV respectively.

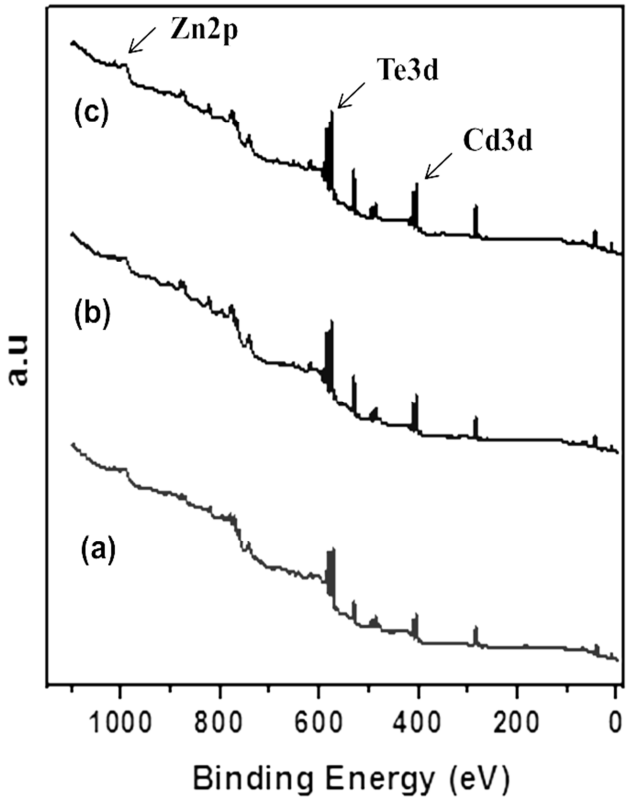

Figure 12: XPS survey spectra for CdZnTe surface submitted to different treatments: a) after etching, b) passivation immediately after etching, c) passivation 24h after etching

Figure 13 shows the Te3d peaks where the etched sample has two sharp peaks with a binding energy of 572.8eV for $Te^0 3d_{5/2}$ and 583.2eV for $Te^0 3d_{3/2}$,characteristic of Te^0 (19). After passivation treatment we observe a shift towards higher energy, and two peaks at 576eV and 586.4eV appear and become sharper, whereas the two previous $Te^0$3d peaks become weaker. This could mean that the surfaces of CdZnTe wafers are covered with oxide after the passivation treatment (20).

The shift of binding energy in Te is caused by the charge transfer effect (21). The chemical state change from Te^0 to Te^{4+} (TeO_2) is resulting in an energy shift of 3.2eV, which is similar to the value calculated in our samples (22). This indicates that the oxide formed after passivation is TeO_2.

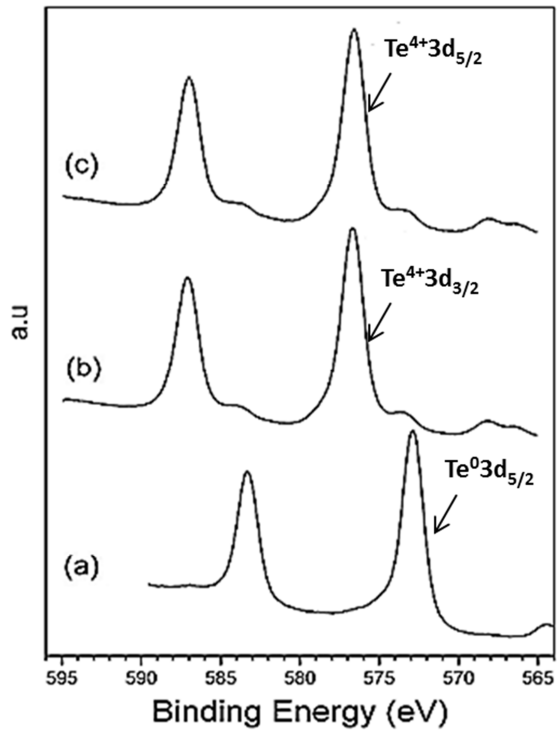

Figure 13: Te3d XPS spectra for CdZnTe surface submitted to different treatments: a) after etching, b) passivation immediately after etching, c) passivation 24h after etching

Considering the results of XPS, and taking into account the process for calculation of the surface composition (Te, Cd, and Zn elements) (23), and considering the peak area of each chemical state (Te^{+4}/Te^{0}) the quantitative analysis of the studied samples calculated using the equation in chapter 3 section 5.1.3, are shown in **Table 4**. In this Table we can observe that for the samples passivated immediately after etching, the Te/(Cd+Zn) ratio approximates to 1, which means that the stoichiometry is restored near the surface region, and the crystallinity could be improved.

In the same table, the tellurium oxide layer thickness on CdZnTe surface calculated following the **Equation 8** (24).

Equation 8

$$\boldsymbol{d = -\lambda ln\left[1 - \left(Te^{4+}d_{5/2} + Te^{0}d_{5/2}\right)\right]}$$

where λ is the inelastic mean free path, which in our XPS experiment has a value of 14 Å according to the Tanuma, Penn and Powell formula (25) for TeO_2, and $Te^{4+}3d_{5/2}/Te^{0}3d_{5/2}$ is the ratio of Te atom obtained from the XPS spectra. The results of the thickness d of oxide layer with different treatment is calculated individually and listed in **Table 4** .

It is clear that after etching the surface is rich on Te, and the surface of the sample passivated immediately after etching has the greatest $Te^{4+}3d_{5/2}/Te^{0}3d_{5/2}$ value, which shows that its oxide layer is thicker than the one passivated 24h after etching. In consequence, the sample passivated immediately after etching is the most stoichiometric, with the thickest TeO_2 oxide layer. In the same table we observe that there is a high quantity of carbon after etching which is due to rinsing for the sample with methanol after the process. The objective of passivation is to oxide the Te on the surface to TeO_2, for this reason we observe that the highest concentration is for oxygen.

Table 4: Quantitative XPS analysis results of CdZnTe wafer surface after different surface treatment

Surface treatment state	Etching	Passivation immediately	Passivation after 24h
%Te	43.17	18.22	18.56
%Cd	27.73	15.25	13.64
%Zn	1.26	1.20	0.78
%O	1.73	54.95	57.14
%C	26.10	10.34	9.86
[Te]/([Cd]+[Zn])	1.48	1.10	1.28
Binding energy	572.8	576.7	576.7
Chemicals state	Te^{0}	Te^{4+}	Te^{4+}
Te^{4+}/Te^{0}	0	0.98	0.93
$d_{oxide\ layer}$(Å)	0	53	37

Concerning Cd3d peaks presented in **Figure 14**, the binding energy are 405eV and 412eV of Cd $3d_{5/2}$ and Cd $3d_{3/2}$, respectively. One can observe that there is no change in the chemical state of Cd. In fact, the chemical shift of CdO is 0.2eV, which is not always possible to distinguish from the Cd peak since the resolution of our XPS system is about 0.9 eV (26). These peaks become wider which could be attributed to oxidation on the surface. This behavior could mean that Cd is partially oxidized at the surface although broadening by disorder after oxidation cannot be neglected. These results are in agreement with the previous EDX analysis.

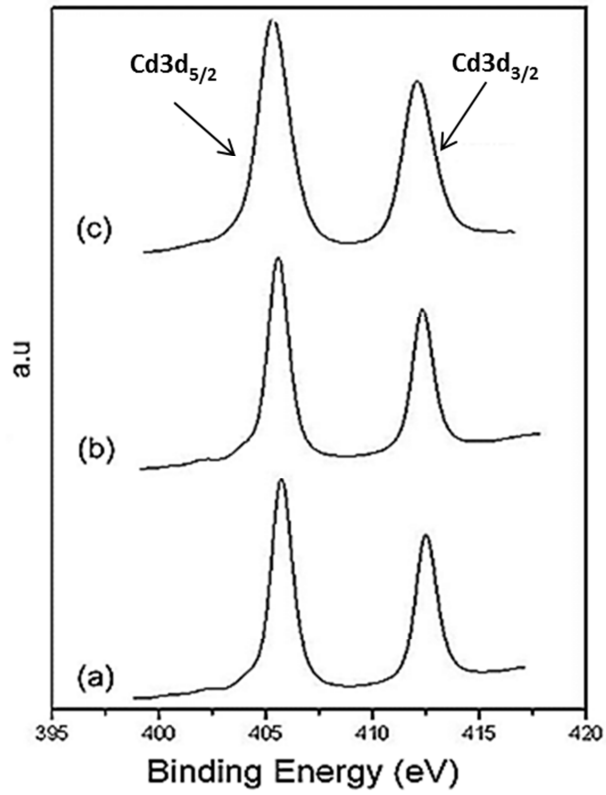

Figure 14: Cd3d (right) Peaks of XPS spectra for CZT surface: after polishing (a), etching (b) and passivation (c)

It was observed previously by XPS that in the case of passivation after 24h, more oxides could be generated on the surface of CZT samples. To demonstrate this, photoconductivity (PC) measurements of the same samples submitted to the same processes have been also performed. The PC results for V=±200V are shown in **Figure 15** for the sample passivated immediately after etching and **Figure 16** for the sample passivated 24h after etching. The investigated energy interval can be divided in three regions: I) a high energy region (200-700nm) in which it can be found the contributions from surface oxides; II) the CZT band-edge around 800nm, III) a low energy region (900-1600nm) characterized by shallow and deep levels of CZT or other unwanted complexes. The comparison between the spectra with positive and negative bias highlights the different charge collection mechanisms. For a negative bias, the contribution in the PC spectrum is mostly due to the electrons drifting toward the anode, while for the positive bias the contribution is mainly due to holes. In fact, the higher mobility of electrons implies a higher PC signal for the negative bias. The two peaks in region (I) could be the consequence of the surface levels like $CdTeO_3$ or CdO due to the difference of time between etching and passivation.This behaviour cannot be observed in the PC spectrum for the sample passivated immediately after etching (27).

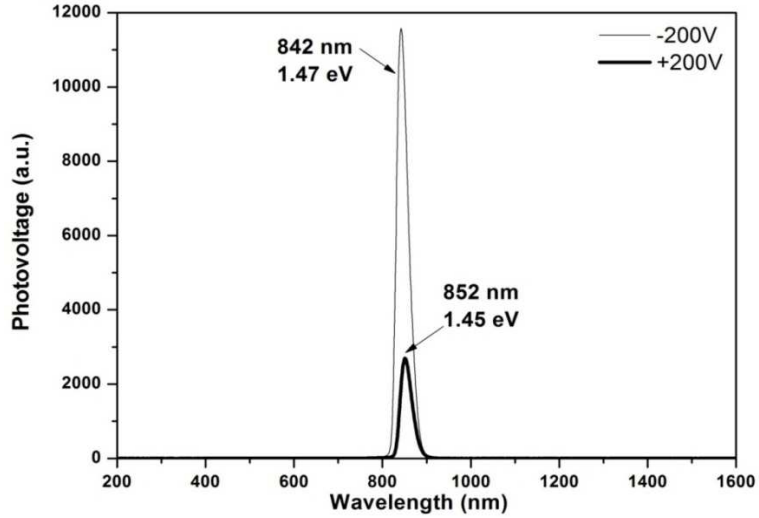

Figure 15: Photoconductivity spectrum for the sample passivated immediately after etching, at 300K

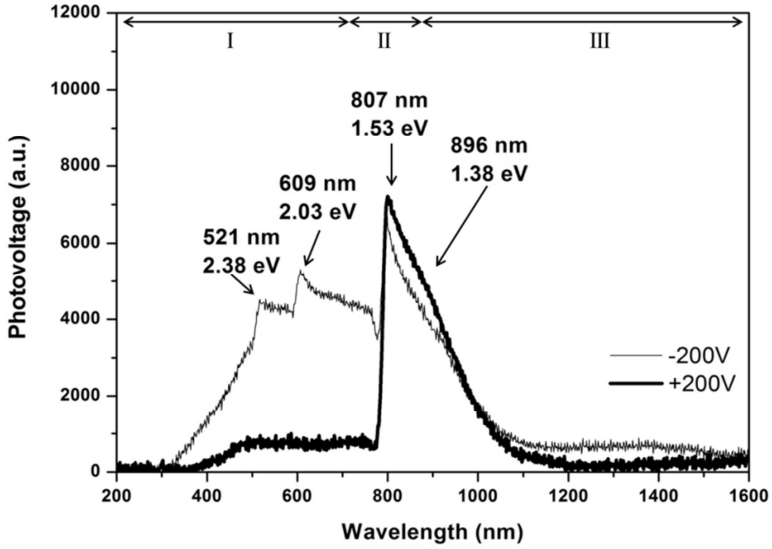

Figure 16: Photoconductivity spectrum for the sample passivated 24h after etching, at 300K

In order to study the effect of the passivation time on the leakage current, I-V experiments were carried out in the same samples and the results are shown in **Figure 17**. The **Figure 17-a** shows the results of the sample passivated immediately after etching, while **Figure 17-b** presents the results concerning the sample passivated 24h after etching. One can observe that, for the sample passivated immediately after etching the leakage current is 5.27×10^{-9}A/cm^2 whereas the sample passivated 24h after etching the leakage current is 1.33×10^{-7}A/cm^2 at 1000V/cm, a difference which could be attributed to the different composition which appear in the samples after different treatment, a possible consequence of the oxide tellurium layer, as it has been previously discussed.

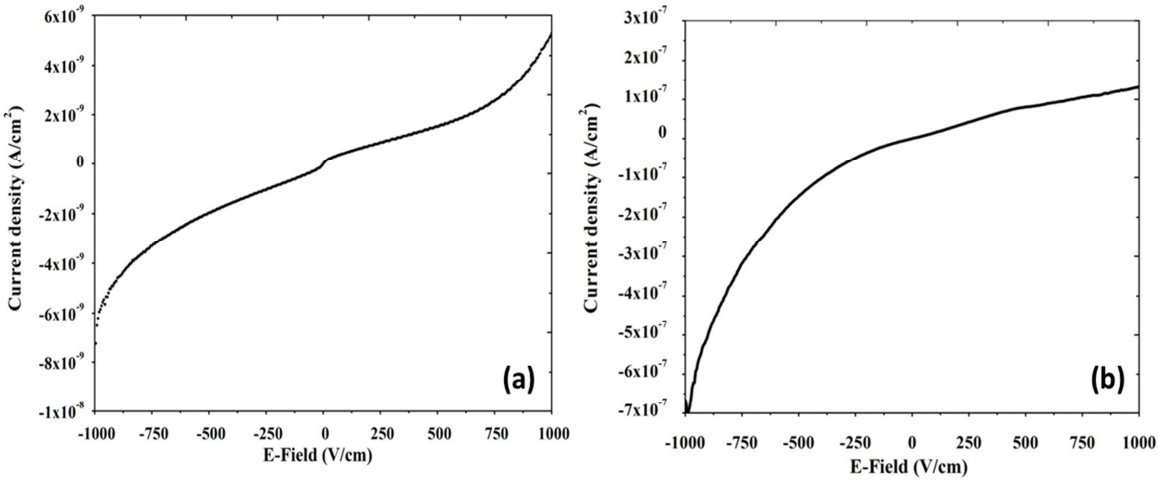

Figure 17: I-V characteristics of sample passivated (a) immediately and (b) 24h after etching

This study examined the effect of passivation time on CdZnTe bulk crystal. XPS analysis showed that the sample passivated immediately after etching has the best passivation efficiency because the enriched Te on the surface was almost completely oxidized to TeO_2, which results in the thickest oxide layer, and the most stoichiometric surface. The I-V measurement showed that the surface leakage current was reduced by two orders of magnitude in comparison with the sample passivated 24h after passivation. At the same time the photoconductivity showed the absence of the CdTeO/CdO peaks on the surface passivated immediately after etching.

IV.4. Conclusions

In this chapter has been described the different processes for surface preparation of CdZnTe detectors, including lapping, mechanical polishing, chemical etching and passivation. These results can be summarized as following:

- Lapping and mechanical polishing introduce surface damage and scrashes, which can increase leakage current and then deteriorate detector performance. Chemical etching is an important step to eliminate scrashes, decrease surface roughness and reduce at the same time the leakage current.
- It has been found that etching process for 30s can be considered as the best etching time regarding Te concentration, surface roughness and leakage current.
- It has been demonstrated that the lateral edges passivated immediately after etching has the best passivation results because the enriched Te layer present on the surface is completely oxidized to TeO_2, and the surface leakage current is reduced by two orders of magnitude.

IV.5. Bibliography

1. **A. Hossain, A.E. Bolotnikov, G.S. Camarda, Y. Cui, S. Babalola, A. Burger, R.B. James.** Effects of Surface Processing on the Response of CZT Gamma Detectors: Studies with a Collimated Synchrotron X-Ray Beam. *Journal of Electronic Materials.* 2008, Vol. 37.

2. **H. Bensalah, J.L. Plaza, J. Crocco, Q. Zheng, V. Carcelen, A. Bensouici, E. Dieguez.** The effect of etching time on the CdZnTe surface. *Applied Surface Science.* 2011, Vol. 257, pp. 4633–4636.

3. **V. Carcelen, N. Vijayana, E. Dieguez, A. Zappettini, M. Zha, L. Sylla, A. Fauler, M. Fiederle.** New approaches in order to enlarge the grain size of bulk CdZnTe (CZT) crystals. *J. Optoelectron. Adv. Mater.* 2008, Vol. 10, pp. 3135–3140.

4. **A. Bensouici, V. Carcelen, J.L. Plaza, S. DeDios, N. Vijayan, J. Crocco, H. Bensalah, E. Dieguez, M. Elaatmani.** Study of effects of polishing and etching processes on Cd1−xZnxTe surface quality. *J. Cryst. Growth.* 2010, Vol. 312, pp. 2098–2102.

5. **W. Xiaoqin, J. Wanqi, L. Qiang, G. Zhi.** Surface passivation of CdZnTe wafers. *Mat. Sci. Semicon. Proc.* 2005, Vol. 8, pp. 615-621.

6. **Zheng, Q.** *Preparation and Development of CdTe and CdZnTe Detectors for Gamma Ray Radiation Applications.* 2012. Thesis.

7. **A. Kargar, A.M. Jones, W.J. McNeil, M.J. Harrison, D.S. McGregor.** CdZnTe Frisch collar detectors for gamma ray spectroscopy. *Nucl. Instrum.Methods: Phys. Res. A.* 2006, Vol. 558, pp. 497–503.

8. *CdZnTe Frisch collar detectors for gamma ray spectroscopy.* **A. Kargar, A. M.Jones, W.J. McNeil, M.J. Harrison, D.S. McGregor.** 2006, Vol. 558, pp. 497–503.

9. **Q. Zheng, F. Dierre, J. Crocco, V. Carcelen, H. Bensalah, J.L. Plaza, E. Dieguez.** Influence of surface preparation on CdZnTe nuclear radiation detectors. *Applied Surface Science.* 2011, Vol. 257, pp. 8742–8746.

10. **H. Yoon, J.M. Van Scyoc, M.S. Goorsky.** Investigation of the Effects of Polishing and Etching on the Quality of Cd1-xZnxTe Using Spatial Mapping Techniques. 1997, Vol. 26, 6.

11. **H. Chen, J. Tong, Z. Hu, T. Shi, G.H. Wu, K.T. Chen, M.A. George, W.E. Collins, A. Burger, R.B. James, C.M. Stahle, L.M. Barlett.** Low-temperature Photoluminescence of Detector Grade Cd1-xZnxTe Crystal Treated by Different Chemical Etchants. Vol. 80, pp. 3509-3512.

12. **J.Wanqi, L.Qiang.** Surface passivation and electrical properties of p-CdZnTe crystal. 2006, Vol. 21, pp. 72–75.

13. **A. Hossain, A.E. Bolotnicov, G. S. Camarada, Y. Cui, S. Babalola, A. Burger, R.B. James.** Effects of Surface Processing on the Response of CZT Gamma Detectors: Studies with a Collimated Synchrotron X-Ray Beam. *J. Electron. Mater.* 2008, Vol. 37.

14. **Y.H. Kim, S.Y. An, J.Y. Lee, I. Kim, K.N. Oh, S.U. Kim, M.J. Park.** Photoluminescence study on the effects of the surface of CdTe surface passivation. 1999, Vol. 85.

15. **Y. Cui, M. Groza, A. Burger, R. B. James.** Effects of Surface Processing on the Performance of Cd1-xZnxTe Radiation Detectors. 2004, Vol. 51.

16. **Y. Lu, W. Sang, J. Xia, J. Min, Y. Qian, J. Teng.** Investigation of Passivation Layer of CdZnTe Detector. *IEEE.* 2006, pp. 962- 964.

17. **K.T. Chen, D.T. Shi . H. Chen, B. Granderson, M.A.George, W.E. Collins, A. Burger, R.B. James.** Study of Oxidized Cadmium Zinc Tellurium Surfaces. *J. Vac. Sci. Technol, A.* 1997, Vol. 15, pp. 850-853.

18. **K. Chattopadhyay, M. Hayes, J.O. Ndap, A. Burger, W.J. Lu, H.G. McWhinney, T. Grady, R.B. James.** Surface passivation of cadmium zinc telluride radiation detectors by potassium hydroxide solution. *J. Electron. Mater*. 2000, Vol. 29.
19. **W.Xiaoqin, J.Wanqi, L.Qiang, G.Zhi.** Surface passivation of CdZnTe wafers. *Mat. Sc. in Semicon. Proc.* 2005, Vol. 8, pp. 615-621.
20. *Surface passivation of CdZnTe wafers.* **W.Xiaoqin, J.Wanqi, L.Qiang, G.Zhi.** 2005, Vol. 8, pp. 615-621.
21. **Paul S. Bagus, H.J. Freund, T. Minerva, G. Pacchioni, F. Parmigiani.** Charge transfer effects and photoemission in transition metal oxides. 1996, Vol. 25.
22. **K. Kim, S. Cho, J. Suh, J. Hong, S. Kim.** Gamma-Ray Response of Semi-Insulating CdMnTe Crystals. 2009, Vol. 56.
23. **X. Cheng, S. Zhu, B. Zhao, Z. He, D. Gao, J. Fang.** Effect of surface preparation on the properties of Au/p-Cd1-xZnxTe. *Appl. Surf. Sci.* 2007, Vol. 253, pp. 8404-8407.
24. **M. P. Seah, D. Briggs.** *Practical Surface Analysis.* 1990. Vol. 1.
25. **S. Tanuma, C. J. Powell, D. R. Penn.** Calculations of electorn inelastic mean free paths. II. Data for 27 elements over the 50–2000 eV range. *Surf. Interface Anal.* 1991, Vol. 17, pp. 911-926.
26. **F. Aqariden, S. Tari, K. Nissanka, Jin Li, N. Kioussis, R. E. Pimpinella, M. Dobrowolska.** Influence of Surface Polishing on the Structural and Electronic Properties of CdZnTe Surfaces. 2012, Vol. 41.
27. **Carcelen, V.** *Growth and Characterization of Cd0.85Zn0.15Te Crystals Doped With Bi:1019 at/cm3.* 2011. Thesis.

Chapter V: The influence of argon ions and laser irradiation on the surface of CdZnTe

Table of content

V.1. Introduction

CdZnTe (CZT) crystals can be used in a variety of detector type applications. This is due to several interesting material properties including large absorption coefficient, high resistivity, high average atomic number, and large band gap. As a consequence of these properties, CZT is a very promising material for its use as room temperature gamma detector (1). Historically, the performance of CZT has typically been adversely affected by point defects and structural and compositional heterogeneities within the crystals, such as twinning, grain boundaries and Te inclusions, etc.

Te inclusions and precipitates are created during the growth and the cooling down phases (2). They are the result of the retrograde solid solubility of Te and, in general, they are created when the growth system offers a poor stoichiometric control (3).

In fact, the concentration and distribution of Te inclusions within a device are one of the major contributions to the degradation of CZT detectors. Te precipitates on the surface can also increase the leakage current (4) (5), thereby deteriorating the device performance. Te inclusions and precipitates also act as traps for the charge carriers. This trapping affects the charge collection efficiency as well as the energy resolution of the detector. For this reason it is necessary to study these defects and adopt appropriate techniques to minimize their influence.

This chapter presents the importance of irradiation process for CdZnTe crystals. The investigation is mainly focused on the irradiation of the surface by argon ion beam and Nd:YAG laser in order to modify the properties of CdZnTe. Two sections are described about the irradiation and characterization of the samples. In the first section, we describe the effects of Argon ion beam bombardment at different fluences on the surface composition, luminescence and mechanical properties of $Cd_{0.9}Zn_{0.1}Te$ crystals.

In the second section, the effect of powerful laser radiation on Te inclusions and the electrical properties of CZT detectors will be investigated.

V.2. Effect of argon ion beam irradiation

Ion beam sputtering (IBS) has come to play an important role in science and technology. The sputtering phenomenon is caused by the interaction of incident particles with the target surface atoms. IBS is employed in many applications, such as ion doping, surface cleaning and etching, thin film deposition, ion milling (6) (7). One of the largest applications of ion irradiation in biomedicine is for cancer therapy, with

usage of proton and He beams of 230 MeV per nucleon, and more recently 320-430 MeV per nucleon ^{12}C, as an alternative to X-ray therapy (8).

Some important results have been reported by different authors about the effect of argon irradiation on the surface of different semiconductors like GaSb, CdTe and CdZnTe. For instance, argon irradiation has been used to inverse the conductivity from p to n type in GaSb (9). G. Panin et al. found that low energy Ar ions results in the formation of an n-type surface layer on p-type CdTe crystals which is caused by the suppression of cadmium vacancies acting as the main acceptors in these crystals (6). J. Olvera et al. demonstrated that the luminescent properties of CdTe samples increased after greatly irradiation with low energy argon ions (0.5-2keV); this enhancement is due to the removal of surface damage produced after sample cutting and polishing processes (7) (10). L.F. Voss et al. reported that the Ar ions bombardment of $Cd_{0.46}Zn_{0.04}Te_{0.50}$ results in a modified surface atomic ratio, with Cd being preferentially removed compared to Te; in addition, the native oxide is removed and the leakage current decreases approximately 2.5 orders of magnitude compared to non-irradiated samples (11). IBS can be also used to produce different nanostructures on a semiconductor surface depending on the incidence angle. The formation of nanodots by IBS has been reported on GaSb and InP (12) (13).

V.2.1. Fundamentals of argon ion-material interaction

The phenomenon of sputtering has been discovered for more than 150 years and it has long been established that the sputtering process can modify surface morphology (14). Sputtering is a widely used technique for the erosion of surfaces and the deposition of films. Sputtering, also known as sputter etching, is used for patterning semiconductor wafers, for cleaning surfaces, for micromachining, depth profiling, and a number of applications which require careful, microscopic erosion of a surface (15) (16) (17).

Sputtering is usually carried out by plasmas which generate charged particles and can be accelerated towards a surface. It can occur for any incident species, including atoms, ions, electrons, and photons. Commonly, sputtering utilizes ion bombardment with inert gas ions such as Ar^+ or small molecular ions such as N_2^+. Sputtering depend on the transfer of physical momentum and kinetic energy from the incident particle to the surface. To understand the sputtering process, consideration of the interaction between an ion beam and the surface will be required.

The sputtering process is presented with a schematic diagram in **Figure 1**. This figure shows the basic ion-material interactions which can happen during ion bombardment of a solid. The incident particles hit the surface of the solid with sufficient energy and results in a series of elastic collisions. If an energetic ion with a kinetic energy greater than the surface binding energy (SBE) impacts with the surface target, atoms will be ejected from the surface. Inelastic interactions also can occur and results in the emission of secondary electrons (SE). The ion will be implanted within the target at some depth below the surface if the ion is not backscattered out of the target surface.

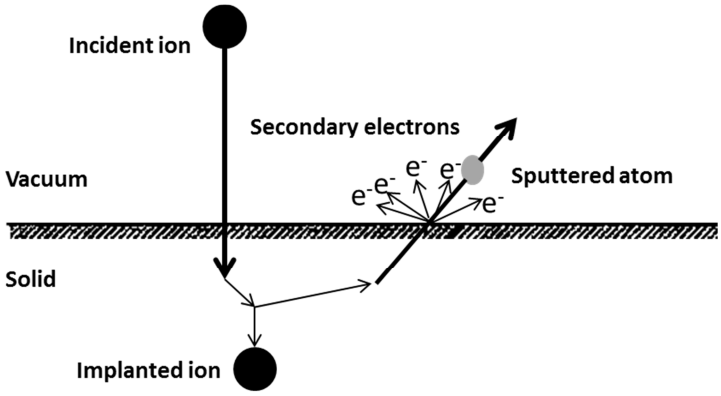

Figure 1: Schematic of sputtering process

Sputtering is quantified by the sputter yield, S_Y, the mean number of atoms removed or sputtered per incident particle.

Equation 1

$$S_Y = \frac{Sputtered\ atoms}{Incident\ particle}$$

S_Y values are typically in the range of 10^{-5} and 10^3 atoms per incident particle and increase with the energy of the sputtering gas (18).

Sputter yield is strongly dependent on the kinetic energy of the bombarding ion, ion incidence angle, ion mass, and surface material properties.

The sputter yield as a function of the applied argon ion energy for different materials is also presented in **Figure 2**. One can observe that the sputter yield increases with the increasing of the ion energy. It is also important to comment that the sputter yield is independent of the atomic number. Indeed, material with atomic number (Z_{Bi}=83 and Z_{Pb}=82) results in the lowest sputter yield and material with atomic number (Z_{Hg}=80) shows the highest sputter yield.

As can be seen also from this figure, the sputter yield of Cd is higher than Te. This will be discussed in next section in order to demonstrate if this behavior will be the same in CdZnTe compound taking into account that the preferential sputtering phenomenon.

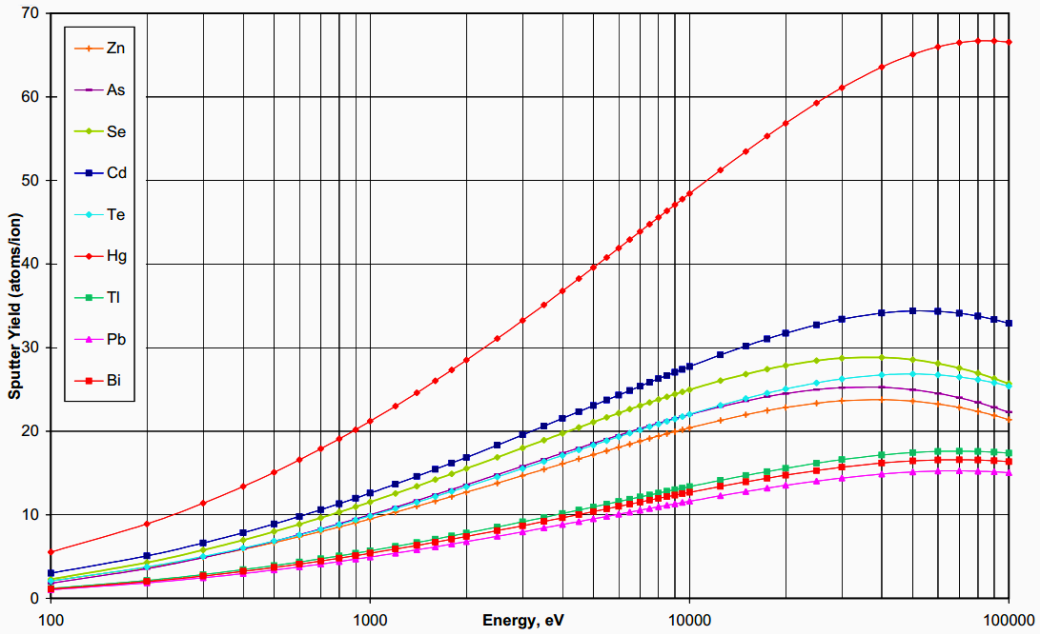

Figure 2: Sputter yield of different material using Ar at incidence angle of 45°

The sputtering velocity or sputter rate S_R of a surface also can be calculated and is expressed as:

Equation 2

$$S_R = \frac{M}{\rho N_A e} S_Y j_p$$

where, M is the molar weight of the target, ρ is the density of the material, N_A is the Avogadro number, e is the electron charge, S_Y is the sputtering yield and j_p is the primary ion current density.

Sputter rates depend on different parameters, such as the incident ion flux, background pressure of the sputtering species, gas phase composition. The sputtering rate could change due to filament degradation as a function of time, even these parameters are held constant (19). Sputter rate of a variety of materials using 500eV argon at 1mA/cm^2 is shown in **Table 1.**

Table 1: Measured Sputter rate for 500eV Argon at 1mA/cm^2 **(20)**

Material	Sputter rate (A°/min)
GaAs	1500
GaP	1400
$LiNbO_3$	400
CdS	2100
PbTe	3300

Physical sputtering can be done in several energy ranges, from few eV to MeV energies. Incident ion energies in the range of 1–100eV are extensively used in surface cleaning (21) where no damage occurs. This is due to the presence of a sputter threshold in this energy regime below which no sputtering occurred. The sputter yields in this energy range are typically too low. A sputtering yield around 10^{-2}atoms/ion was calculated at very low bombarding argon ion energy of 60eV for SiO_2 (22).

At ion energies from 1keV to 50keV, the incident particle has sufficient energy to affect the surface of the target and create some defects. Using 50keV Ar^+ ion irradiation of semi-insulating GaAs results in the formation of nano-dots on the surface (23). This regime has generally higher yields and is used for sputter deposition applications.

At ion energies above 50keV, the incident particle can travel well into the bulk of the solid and can create significant damage on the surface. In addition, the incident particle is often trapped or implanted within the sample. C. W. Rischau et al. demonstrated the damage formation in CdTe single crystals irradiated with 270keV argon (24).

Over the years, investigations mainly on semiconductors such as GaSb, InP and InSb have been performed to understand the surface topography evolution during argon ion beam sputtering.

The morphology of sputtered surfaces is essentially caused by the dynamic competition between roughening (sputtering atoms off the surface) and smoothing (diffusion of defects and atomic species) processes. The variation of these two processes with temperature, ion flux, ion energy and incident angle defines the resultant surface morphology (25).

Christopher K. Egan et al. (26) performed sputtering on different surface orientations of CdTe but no differences were found in the surface morphology. However by changing the angle of incidence, greatly change in the surface morphology was observed.

The physical process taking place during ion bombardment is explained as follows: An ion strikes the surface and stops at a distance “a” after all its energy is dissipated due to elastic and non-elastic interactions with the atoms of the material. The energy deposited at point r_0=(0,0,0) by the ion reaching the point r=(x,y,z) is well described by the Gaussian distribution (27):

$$\boldsymbol{E(r,z) = \frac{\epsilon}{(2\pi)^{3/2}\sigma\mu^2} exp\left\{-\frac{z^2}{2\sigma^2} - \frac{x^2+y^2}{2\mu^2}\right\}}$$

where ϵ is the kinetic energy of the incident ion and the material-dependent parameters σ and μ characterize the widths of the energy distribution along z and x(y) directions,

respectively. The parameters σ and μ are material dependent and vary with the physical properties of the target material and the incident ion energy (28).

The Bradley Harper (BH) theory predicts that the sputtering yield at a particular point on the surface was proportional to the local surface curvature at that point. So a point with positive curvature (bottom of valleys) has more material removed from it compared to a point with negative curvature (top of hills). This leads to an instability that tends to increase the rate of roughening with increasing surface roughness. This rapid roughening is balanced by surface diffusion which acts to smooth the surface (29) (30) (31).

The evolution of the surface during the sputter process is described by a partial differential equation, which incorporates the characteristic dependence of the erosion rate on the local surface curvature. Under certain conditions a surface instability is induced with a roughening rate proportional to the second derivative of the surface contour. The resulting equation describing the dynamics of the surface morphology was originally considered for the description of chemical waves and flame fronts and is known as the Kuramoto-Sivashinsky (KS) equation. In the special case of isotropic ion sputtering at normal incidence or non-normal incidence in conjunction with a rotating surface, the isotropic KS equation describes the temporal evolution of the surface height function $h(x,y)$ as

Equation 3

$$\frac{\partial h(x,y)}{\partial t} = \nu_0 + \nu\nabla^2 h - D\nabla^2(\nabla^2 h) + \frac{\lambda}{2}(\nabla h)^2 + \eta(x,y,t)$$

Equation 4

$$\nu = -\frac{a\mu^2}{2\sigma^2}\left[\frac{J\epsilon p}{\sqrt{2\pi\sigma}} exp\left(-\frac{a^2}{2\sigma^2}\right)\right]$$

Equation 5

$$\lambda = \frac{\mu^2}{2}\left(\frac{1}{\sigma^2} - \frac{a^2}{\sigma^4} - \frac{1}{\mu^2}\right)\left[\frac{J\epsilon p}{\sqrt{2\pi\sigma}} exp\left(-\frac{a^2}{2\sigma^2}\right)\right]$$

where v_0 is the average erosion velocity of the surface during sputtering, v is the effective surface tension induced by ion sputtering, D is the coefficient related to relaxation by surface diffusion, λ is the tilt-dependent erosion rate, and h (x,y,t) is white noise incorporating the stochastic nature of the ion-sputtering process. The coefficients ν and λ are calculated from the distribution of the energy deposited by the incident ions, which is assumed to be Gaussian, as given in **Equation 4** and **Equation 5**. They are functions of ion current density J, ion energy ϵ, and of the parameters describing the Gaussian energy distribution, i.e., ion range a, longitudinal width σ, and lateral width μ. p is the proportionality factor coupling the energy deposited with the erosion rate.

V.2.2. Experimental details

The system used for argon ion beam bombardment during this study, consists of an ion source mounted to the main vacuum system. Argon ions impinge on the end of rotary manipulator where the sample is mounted. The experimental set-up is shown in **Figure 3**. Ion beam sputtering utilizes an ion source to generate a relatively focused ion beam directed at the target to be sputtered. Applying a high voltage field of 2-10 kV to the anode creates an electrostatic field inside the ion source. When argon gas is injected into the ion source, the high electric field causes the gas to ionize, creating plasma inside the source region. The ions are then accelerated from the anode region to the exit aperture (cathode) creating a "collimated" ion beam.

The beam is focused by a set of biased lens electrodes. The target sample is kept at ground potential to prevent charge build up. The beam energy is given by the acceleration voltage applied to the cathode. The sputtering is performed at a chamber pressure of $\sim 1\times10^{-5}$mbar where the argon gas is admitted via a leak valve into the front of the sputtering source.

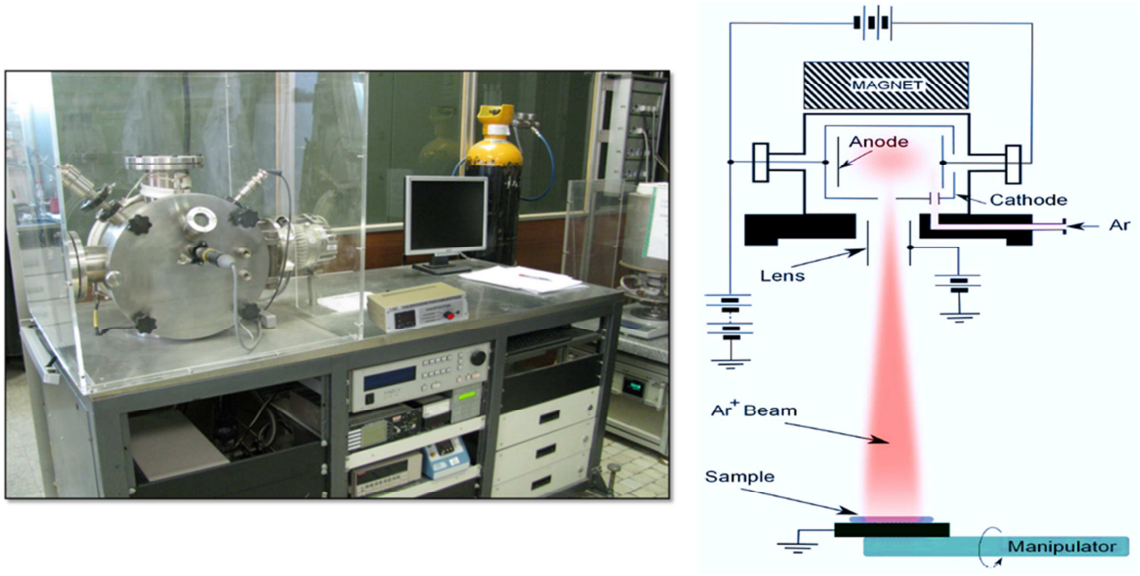

Figure 3: Sputtering system in CGL and its schematic diagram

$Cd_{0.9}Zn_{0.1}Te$ ingot with a diameter of 25mm and length of 60mm was grown by the vertical Bridgman method. The ingot was sliced perpendicular to the growth direction into single wafers, and a series of samples were obtained as a function of axial positions. The dimension of the samples was $8\times5\times2mm^3$. The samples were then lapped and polished by using 3μm Al_2O_3 powder.

A Specs PQ10 broad beam ion gun was used for the ion irradiation. A filament current of 10 mA with an energy of 5 keV was selected. Three sputtering times were studied: 1, 3 and 8 hours, which resulted in fluences of 2, 4, and $8\times10^{17}cm^{-2}$, respectively. The experimental conditions used for the irradiation are summarized in **Table 2**. The fluence is calculated using **Equation 6**, where I_{sc} is the current of the sample (It is important to comment that this current is in the order of μA and is different from the filament current), t is the time of irradiation, A is the area irradiated, and $1.6\times10^{-19}C$ is the electron charge.

Equation 6

$$\boldsymbol{Fluence(cm^{-2}) = \frac{I_{sc}(A)\times t(s)}{A(cm^2)\times 1.6\times 10^{-19}C}}$$

In order to study the effect of argon beam bombardment on the properties of CdZnTe, the samples were characterized before and after irradiation using a Scanning Electron Microscope (SEM), Hitachi S-3000N to have information about the morphology and topography of the surface. An Atomic Force Microscope (AFM), PSI100 Park Systems, was used for analyzing surface roughness. Micro-photoluminescence (μPL) and micro-Raman (μR) spectra were obtained with a HRLabRam spectrometer attached to a metallographic microscope. The excitation was done with He–Ne laser line at 633nm, through a 100X microscope objective, which also collected the scattered light. CL measurements (panchromatic images as well as CL spectra) were carried out at liquid nitrogen temperature (80K) with a XiCLOne system (Gatan UK) attached to a LEO 1530-Carl Zeiss-FESEM microscope. The luminescence signal was detected with a Peltier cooled CCD.

Table 2: Summary of experimental conditions used for irradiation

Experimental conditions	
Base Pressure (torr)	10^{-6}
Working pressure (torr)	10^{-4}
Time (h)	1, 3 and 8
Fluence (ions/cm^2)	$2\text{-}8\times10^{17}$

V.2.3. Results and discussion

In this section the effect of argon irradiation on the surface, optical and mechanical properties will be discussed.

a) Surface characterization

In order to analyze the surface morphology and surface roughness, the surface of the samples before and after irradiation was carried out using an AFM and SEM.

Figure 4 shows the AFM images of irradiated surfaces with fluences of 2, 4 and $8\times10^{17}cm^{-2}$ respectively. From these images we can observe different surface structural development regimes. The scratches observed in the polished crystals are removed for all the fluences used in this study, thus leading to a cleaner surface after the irradiation process. An additional effect has been observed as the irradiation fluence increases; after irradiation with the lower fluence ($2\times10^{17}cm^{-2}$) we observe the generation of pitting on the surface while for medium ($4\times10^{17}cm^{-2}$) fluence surface waviness is observed. For the highest fluence, deeper holes start to form on the surface accompanied by a rough surface with the formation of two kinds of pits: (i) void craters and (ii) craters with a particle in the middle.

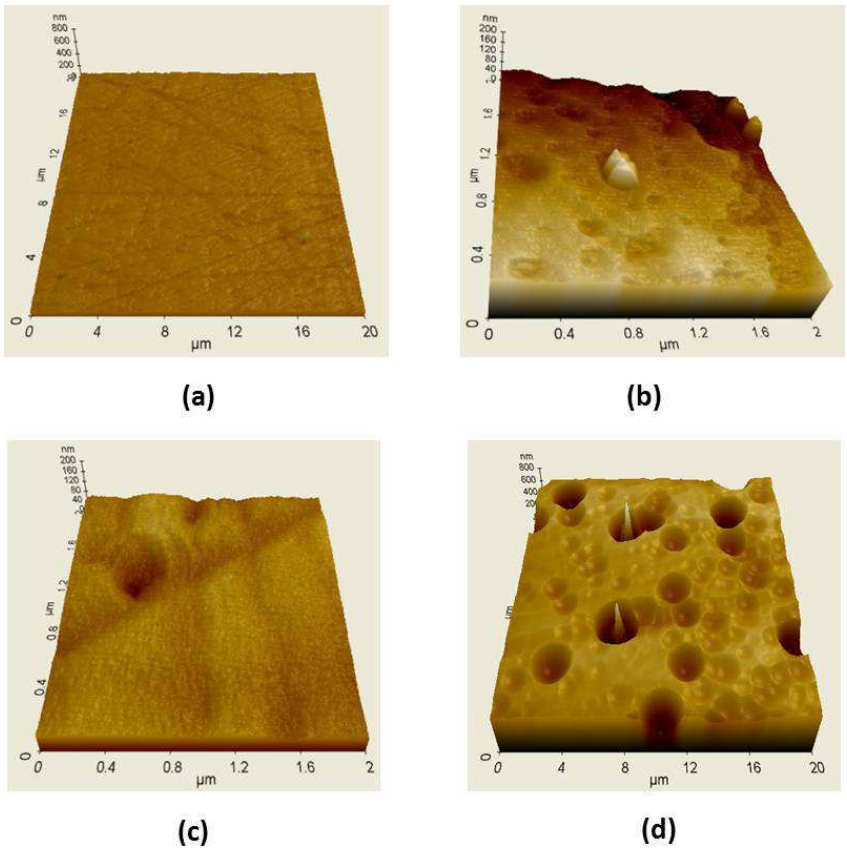

Figure 4: AFM images of CZT samples: (a) no irradiated and irradiated with fluences of (b) $2\times10^{17}cm^{-2}$, (c) $4\times10^{17}cm^{-2}$ and (d) $8\times10^{17}cm^{-2}$

The evolution of surface morphology during ion bombardment process could be a result of a balance between the removal of material which tends to roughen the surface and the transport driven by surface energy minimization which leads to smooth the surface. In fact, SEM images of the surface of the sample irradiated at the highest fluence are presented in **Figure 5**. The above mentioned pits created by the ion beam, can be clearly observed in this figure. The typical size of the craters and the particles is about 2μm and 0.5μm respectively. One can conclude that the surface roughness evolution strongly depends on the argon fluence. Extremely low fluence leads to a smooth surface while increasing the fluence leads to much faster roughness development.

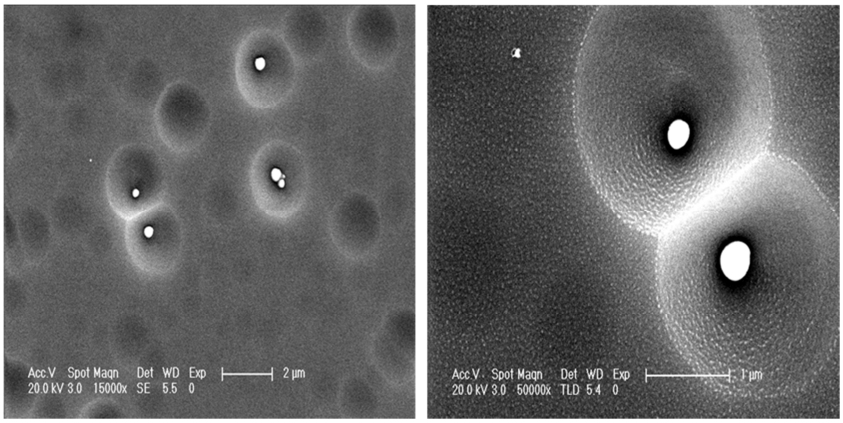

Figure 5: SEM images of the sample irradiated with a fluence of $8\times10^{17}cm^{-2}$

The mechanism of the formation of craters on the surface is illustrated in **Figure 6** and could be explained as follows: a) we take in consideration that our starting CZT crystals are rich in Te, so a high amount of Te interstitials (Te_i) is present in the material, as well as a random distribution of Te inclusions and precipitates in the sample volume (32); b) the ion bombardment process implies to supply energy to the crystal lattice, which can locally induce Gibbsian segregation of Te due to the minimization of the surface free energy (33), thus allowing for an extra formation of Te aggregates; c) in consequence larger Te clusters could be created; d) as the surface is eroded, some of the Te cluster, those close to the surface are unburied and exposed to the ion beam; e) as these clusters are different material (pure Te) than the surroundings (CZT), the sputtering yields are also different for both. It happens that the sputtering yield for Te is higher than CZT (33) (34).

As the Te are more “resistive” to the ion erosion than CZT, the Te clusters act like small “masks” and the surroundings are eroded faster than the clusters leading to the crater formation. Those craters with a Te cluster inside are those in which the ion beam did not have time for the complete erosion of the cluster; in those cases, the central part presents a peak, as is observed in the AFM image of **Figure 4-d**.

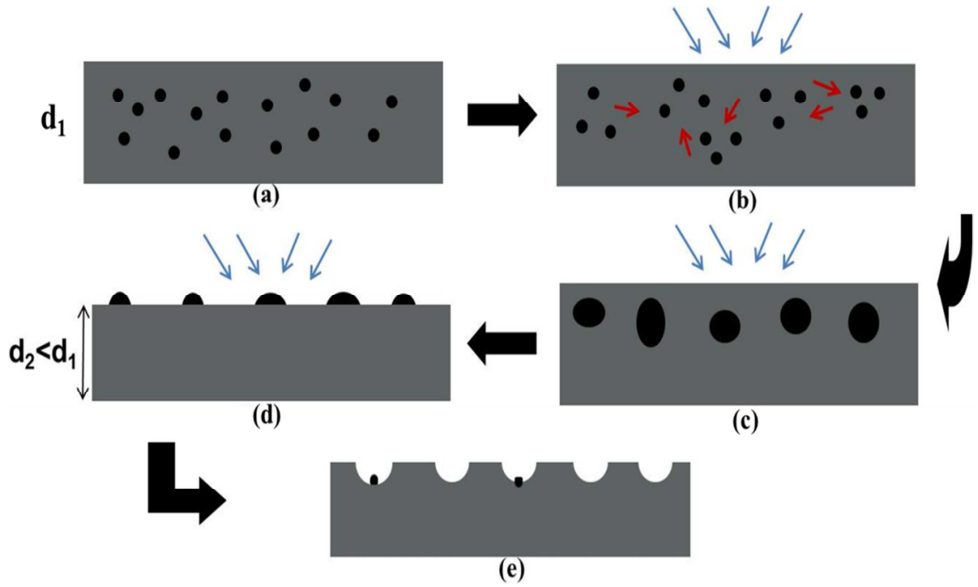

Figure 6: Schematic representation of the elimination of Te inclusions during the bombardment with argon ions

b) Optical characterization

The optical properties of no irradiated and irradiated CdZnTe crystals were investigated in detail by Photoluminescence, Cathodoluminescence and Raman spectroscopy.

Figure 7 shows PL spectra at room temperature of the CdZnTe samples obtained at both irradiated and no irradiated areas. We see that the PL spectrum is composed of a single broad peak at energy close to the band gap. The important difference concerns the peak intensity, which greatly increases after irradiation. This increase should be related to the improved quality of the CdZnTe surfaces after irradiation, due to the removal of the surface defects created during the cutting, lapping, and polishing processes. The PL peak position also shifts to higher energies after the irradiation process, this effect being more marked for increasing fluences. This should be likely related to a depletion of Cd atoms in the surface after the irradiation process, leading to a CdZnTe alloy with an increased Zn content and a decreased Cd content.

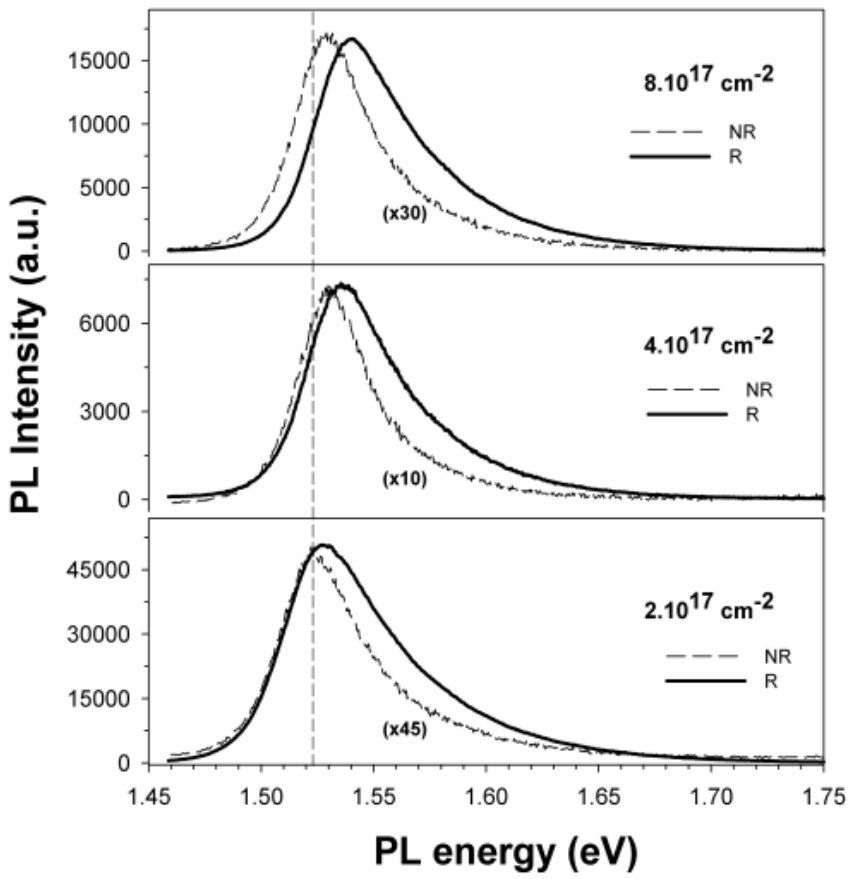

Figure 7: Room temperature PL spectra of the studied CdZnTe samples at both irradiated (R) and no irradiated (NR) areas for different fluences: $2\times10^{17}cm^{-2}$, $4\times10^{17}cm^{-2}$, and $8\times10^{17}cm^{-2}$

The luminescence properties of the sample have been also studied by means of low temperature (80K) Cathodoluminescence (CL) spectroscopy. **Figure 8** shows the CL spectra of the samples before and after irradiation. The CL spectrum of the CdZnTe samples before irradiation shows (i) a prominent acceptor bound exciton transition (A°,X) at 1.61eV, (ii) an emission at 1.57eV, with the characteristics of free to bound acceptor transition (e,A°), and (iii) a weak broad emission at 1.49eV, related to surface defects (35). After irradiation we observe both an increase of the intensity of the excitonic emission as well as a decrease of its full width at half maximum, these effects being more marked for the highest fluence used. Also, we observe that the broad band at 1.49eV was removed after irradiation for all the analyzed fluences. These observations support the removal of surface defects due to the Ar irradiation process. On the other hand, the CL peak at 1.57eV is observed to be slightly reduced after irradiation with a fluence of $2\times10^{17}cm^{-2}$, while it completely disappears when using higher fluences.

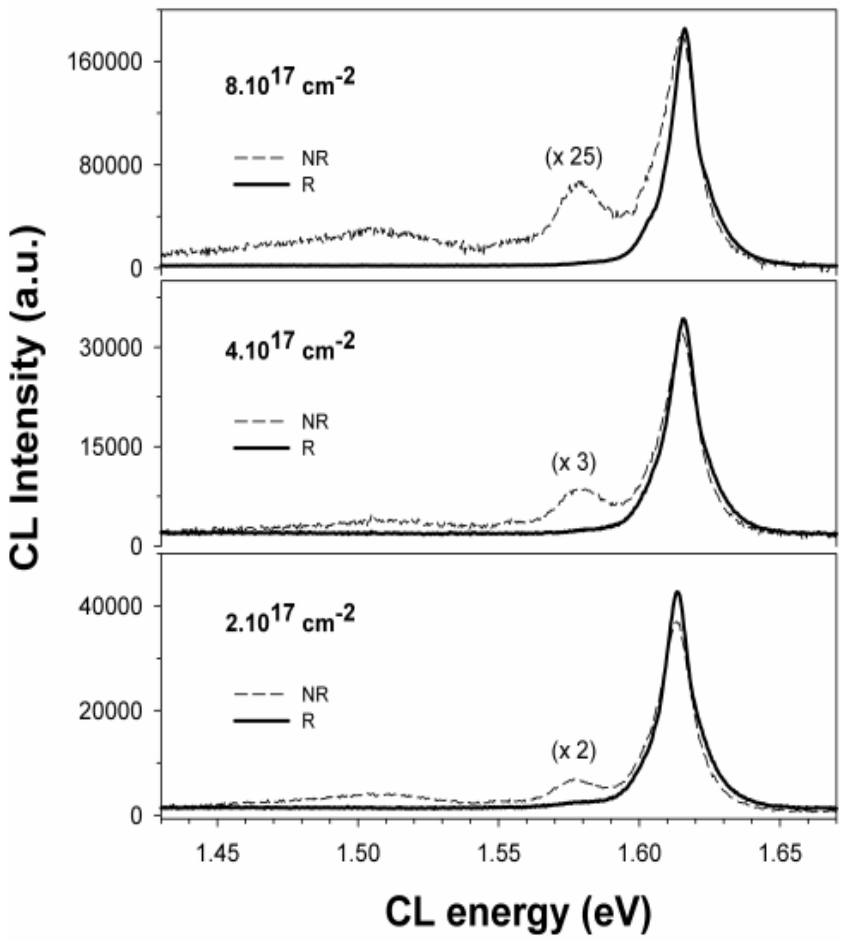

Figure 8: CL spectra of the CdZnTe samples at both irradiated (R) and no irradiated (NR) areas for different fluences: $2\times10^{17}cm^{-2}$, $4\times10^{17}cm^{-2}$, and $8\times10^{17}cm^{-2}$

The samples have also been analysed by means of Raman spectroscopy. Typical Raman spectra of the no irradiated and irradiated CdZnTe areas of the studied samples are presented in **Figure 9**. The Raman peaks at 123 and $141cm^{-1}$, observed with great intensities for the no irradiated sample, are attributed to the presence of Te inclusions (36). It is observed that the intensities of both peaks decrease after irradiation, for all the fluences used, although the change is better observed as the fluence increases. In fact, the irradiation with the smallest fluence produces a very small reduction of the intensities of these two peaks, while for the highest fluence used the two Raman peaks disappear completely. This indicates that the irradiation process lead to an elimination of Te precipitates from the surfaces of the CdZnTe samples as has been previously mentioned in our model depicted in **Figure 6**.

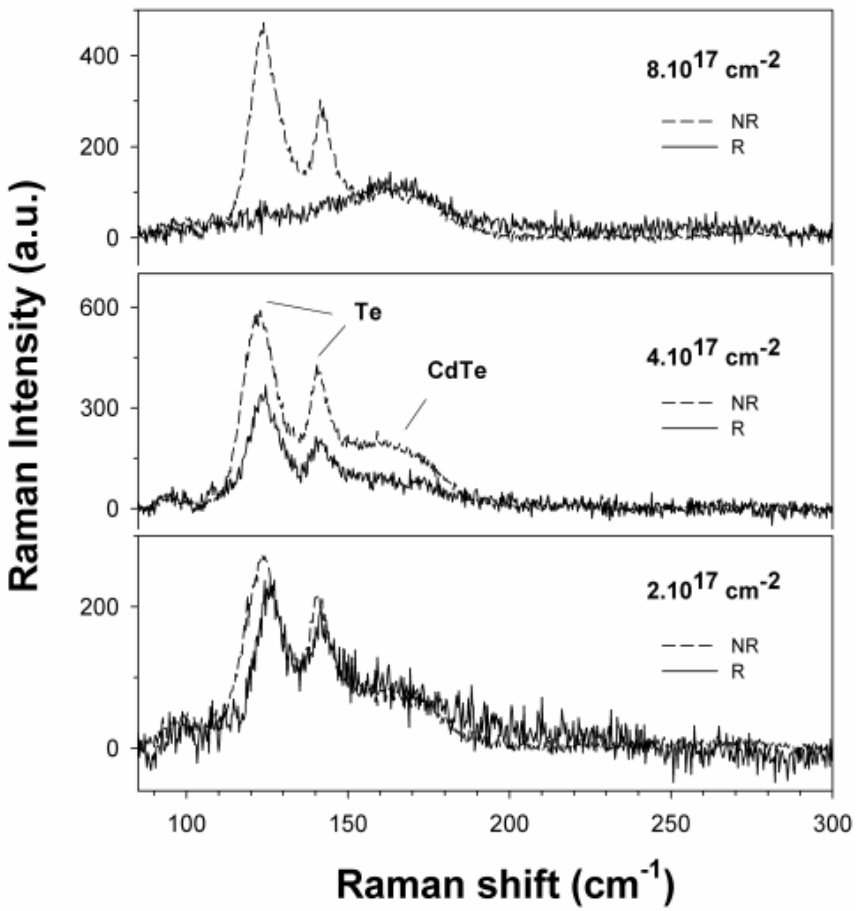

Figure 9: Raman spectra of irradiated (R) and no irradiated (NR) areas for the different fluences investigated

There are two physical mechanisms which can explain the preferential sputtering effect in alloy semiconductors: differences in the masses of the atoms in the sample, what is called mass effects, and differences in the surface binding energies between atoms, called bonding effects (37). If mass effects are the dominant mechanism for preferential sputtering, the lighter atom should be sputtered preferentially since for a given energy transfer, the lighter atom has a larger range than the heavier atom so that the lighter atom can escape from deeper inside the sample. As a result, the lighter atom has a greater probability of leaving the sample surface than the heavier atom. If bonding effect is the dominant mechanism, the atom which has the lowest surface binding energy should be sputtered preferentially since that atom can leave the surface more easily.

Taking into account that Te, the heaviest element is preferentially sputtered in CdZnTe, the mass effect is not the dominant for preferential sputtering mechanism. In this case, the surface binding energy of Te in CdZnTe is probably lower that of Cd due to the fact

that Te is bound to both Cd and Zn. So, preferential removal of Te during ion irradiation could be attributed to bonding effect.

c) Mechanical characterization

The mechanical properties of semiconductors are a topic of practical and theoretical interest. The mechanical properties relate to changes that arise during processing of semiconductor devices, particularly from dislocations and Te inclusions that are formed during growth process or slicing and polishing that are introduced during samples preparation. Young's modulus (E) and hardness (H) are essential parameters of structural materials and the relationship between them play an important interest for material scientists.

Young's modulus is usually considered to be an increasing function of hardness and is expressed as (38):

$$\boldsymbol{H = \left(^{2}/_{3}\right)\left[1 + \ln\left(E\cos\theta/3\sigma_{y}\right]\sigma_{y}}$$

where σ_y is the compressive yield stress and θ is the half angle of indenter.

Nanoindentation is a non-destructive technique developed over the last decade for probing the mechanical properties of materials. It can work from 50 nN to 500 mN and can be used for mechanical characterization of thin films, surface layers and bulk materials (39).

In order to study how argon irradiation affects the mechanical properties of CZT, two samples with different size and distribution of Te inclusions as shown in **Figure 10** have been prepared.

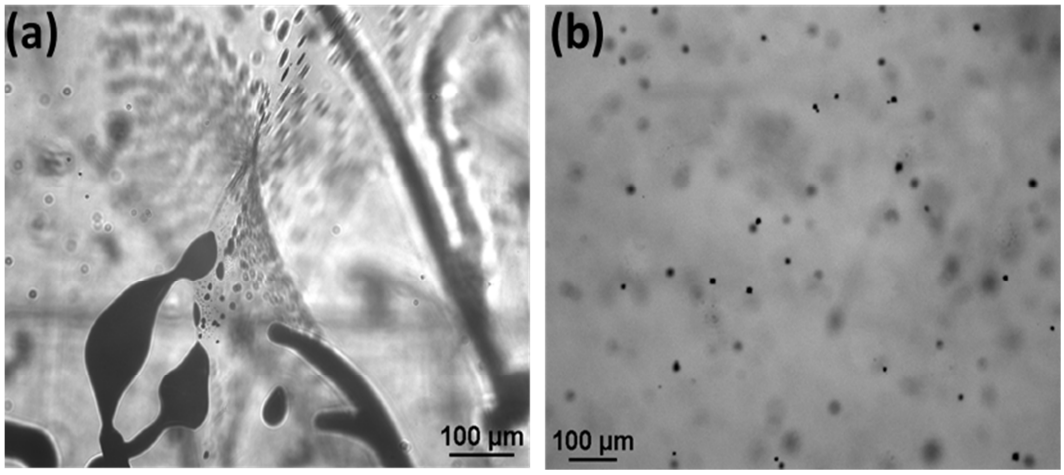

Figure 10: IR images of the samples prepared for irradiation (a) big inclusions and (b) small inclusions

Nanoindentation test were performed using a MTS Nano Indenter with continuous stiffness measurements (CSM) at 2nm oscillation amplitude and 45Hz frequency. Strain rate was held constant at $0.05s^{-1}$. Experiments were carried out at room temperature using a Berkovich tip. **Figure 11** shows the nanoindentation observed by scanning electron microscopy (SEM). Nanoindentation tests were performed at two different depths (100 and 500nm).

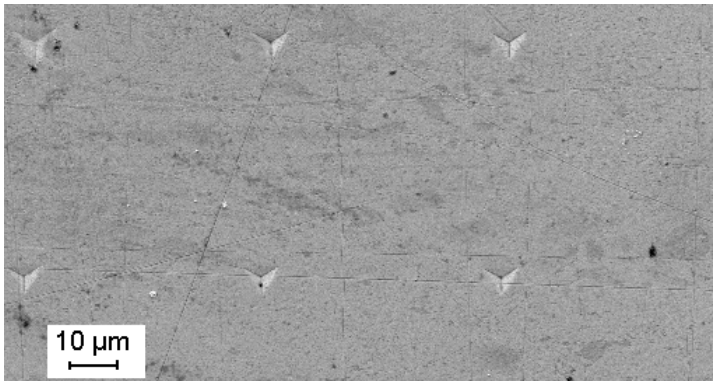

Figure 11: SEM image of nanoindentation made with a Berkovich indenter

Each hardness and Young's modulus value listed in **Table 3**, are an average of 25-100 measurements performed on two different samples in order to achieve statistical significance.

Table 3: Hardness and Young's modulus for CZT samples before and after irradiation

Sample	State	Depth Limit (nm)	Young's modulus (GPa)	Hardness (GPa)
Sample a	Before irradiation	100	40.273	1.483
		500	41.847	1.079
	After irradiation	100	37.538	1.148
		500	39.463	1.045
Sample b	Before irradiation	100	39.734	1.428
		500	41.523	1.099
	After irradiation	100	36.752	1.327
		500	40.608	0.927

From this table, we observe that both Young's modulus and hardness decrease after irradiation. One can also observe that Young's modulus and hardness in sample a, which contains big inclusions, are higher in comparison with sample b. This difference could be explained with the higher amount of Te element which has a Young's modulus value of 43GPa. From this, one can deduce that the decrease of mechanical parameters after irradiation is due to the removal of Te from the surface.

These again confirm the results demonstrated previously, and we can conclude that argon irradiation was successful to remove Te inclusions from the surface of CZT samples.

While argon irradiation provides useful informations with respect to the optical and mechanical properties which play a major role in CZT detectors. Therefore, in the next section the effect of laser irradiation on the properties of CZT and especially on Te inclusions will be discussed.

V.3. Improvement of CZT after Nd:YAG laser irradiation

V.3.1. Fundamentals of laser irradiation

Laser processing is a very interesting technique in sensor technology. Special interest has been shown in the application of laser pulses to treat semiconductors with light that is strongly absorbed. In particular laser irradiation of CdTe semiconductor has been greatly used for different kinds of surface processing including cleaning, etching, oxide film removal, local annealing, nanostructure formation, doping and producing diode junctions (40) (41). In fact, any surface treatment is accompanied by changes of morphology or transformation of structure (41). Doping technique using laser radiation to diffuse impurity atoms into the semiconductor has been developed by several groups. For example, by depositing impurity materials such as Na_2Te on CdTe surface and using a KrF laser can help to decompose the compound and diffuse Na atoms into Cd sites by heating the film surface, and result in p-type conductivity material (42) (43) (44).

Lasers have been also applied to the synthesis and deposition of thin films. In fact, CdTe thin films were prepared at room temperature using a Nd:YAG laser at 1064 and 532nm by F. de Moure-Flores at al. (45). It has been demonstrated that using laser processing of high-resistivity CdZnTe crystals with ruby laser of intensities in the range of 7-20MW/cm^2 was possible to improve the surface, increase the photosensitivity, and decrease the surface recombination rate (46).

In general, during the interaction of the laser with solids a variety of physical processes occur. The first step in any structural modification of a material by laser radiation is the deposition of a certain amount of laser energy. The laser–solid interaction process is the excitation of electrons from their equilibrium states to some excited states by absorption of photons (47). For example, in the case of semiconductors, electrons can be excited from the valence band to the conduction band by absorption of single photons. The energy absorption depends on a wide variety of physical and chemical properties of the target material. In consequence, these properties govern the depths of penetration of the laser light.

For laser irradiation, the beam intensity *I* at a depth *x* for the normally incident beam of initial intensity I_0 (in W/m^2) is given by:

Equation 7 $$\boldsymbol{I(x,t) = I_0(t)(1-R)\exp(-\alpha x)}$$

where, I_0 is the incident intensity, t is the time, R and α are the reflectivity and absorption coefficient, respectively. Since α is greater than $10^3 cm^{-1}$ in the case of CdTe, as a consequence high amount of light will absorbed.

Laser irradiation could be also accompanied by heating of the material, inducing a pronounced modification of its real structure and significantly influencing the electrical properties of the devices. The high temperatures generated can enhance diffusion rate which lead to the reorganization of the crystal structure, and sintering of porous materials (48). In order to calculate thermal fields in the material the heat transfer equation could be solved (49):

Equation 8: $$\boldsymbol{\rho C_p \frac{\partial}{\partial t} T(x,t) = \frac{\partial}{\partial x}\left(K \frac{\partial T(x,t)}{\partial x}\right) + S(x,t)}$$

where T(x,t) is the temperature at depth *x* in moment t, *K* is the thermo-conductivity coefficient, *ρ* is the density, C_p is the specific heat, *S*(x,t) is the heat generation function expressed as:

Equation 9 $$\boldsymbol{S(x,t) = (1-R)\alpha I(t) e^{-\alpha x}}$$

where R is the reflectivity, α is the absorption coefficient, I(t) is the time dependence of laser pulse.

Another effect which can happen during laser irradiation is the removal of material or ablation which involves two phenomena: photochemical and photothermal ablation.

The photochemical ablation (PCA) process is mainly dependent upon the absorption coefficient of the materials (α) according to the Beer–Lambert law at a given laser wavelength. The optical penetration depth (L_0) is defined as the reciprocal of the absorption coefficient (α^{-1}). The L_0 gives an estimated depth through which the laser energy will be absorbed efficiently and consequently the depth through which photochemical ablation will take place. On the other hand, the photothermal ablation (PTA) process is dependent on materials properties and laser pulse duration according to the thermal penetration depth L_e which is expressed as:

Equation 10 $$L_e = 2(\kappa\tau)^{1/2}$$

where τ is the laser pulse duration in seconds and κ the thermal diffusivity defined as:

Equation 11 $$\kappa = \frac{K}{\rho C_p}$$

where K is the thermal conductivity, ρ the density and C_p is specific heat capacity. For materials with low κ and/or laser pulse duration below 1ns, L_e is generally much smaller than L_0. For example in CdZnTe, taking in consideration that the thermal diffusivity is $7.5\times10^{-7}m^2/s$ and laser pulse duration of 15ns, the thermal penetration depth will be in the order of 0.15μm.

There are many different types of lasers. Solid-state lasers such as Nd:Glass and Nd:YAG, gas lasers such as He, HeNe, and CO_2, and diode laser such as GaAlAs/GaAs and InGaAlAs. Among solid state lasers, Nd:YAG laser has an important role due to its high efficiency, possibility to tune it in different wavelengths from infrared (λ=1064 nm) till ultraviolet (λ=213nm) and change pulse duration from milliseconds down to picoseconds.

V.3.2. Samples preparation

The samples used for the study of laser irradiation were grown by the VGF method. The harvested $Cd_{0.9}Zn_{0.1}Te$ crystals have high resistivity in the order of $10^9\Omega$.cm. $10\times5\times3mm^3$ samples were cut from the grown ingot and then lapped and polished using 3μm Al_2O_3 powder. Several samples cut from the same position were irradiated. As shown in **Figure 12**, the samples were prepared in this form and were irradiated in in the center in order to analyze the same zone before and after irradiation.

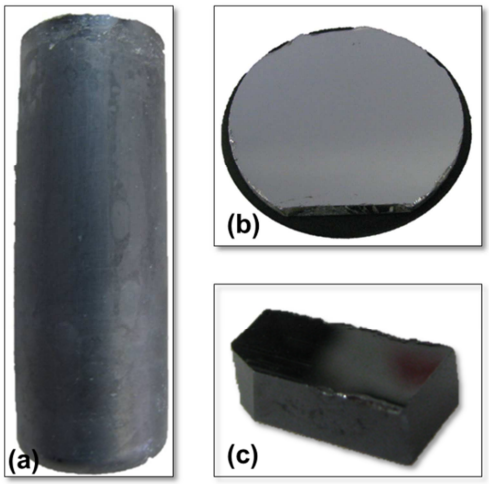

Figure 12: (a) As grown ingot, (b) Polished wafer and (c) Polished sample

The radiation source is a Ekspla NL301G series electro-optically Q-switched nanosecond Nd:YAG lasers with a basic frequency (1.06μm) or second harmonic (0.532μm). Semiconductor sample located on the micrometer table and is moved according to a program. Micrometric table has two coordinate controllers in the plane perpendicular to the laser beam, which is carried out by the control program installed in the computer. The block diagram of experimental laser system is shown in **Figure 13**.

The electro-optically Q-switched nanosecond Nd:YAG lasers produce high energy with pulse duration τ =10-15ns and power P=1.0MW. Irradiation of the crystals was carried out with intensity in the range of I=0.48–12MW/cm^2 and maximum number of the laser pulses 3.6×10^4. The diameter of the laser beam spot was 0.9mm. The experimental conditions used for the irradiation are summarized in **Table 4**.

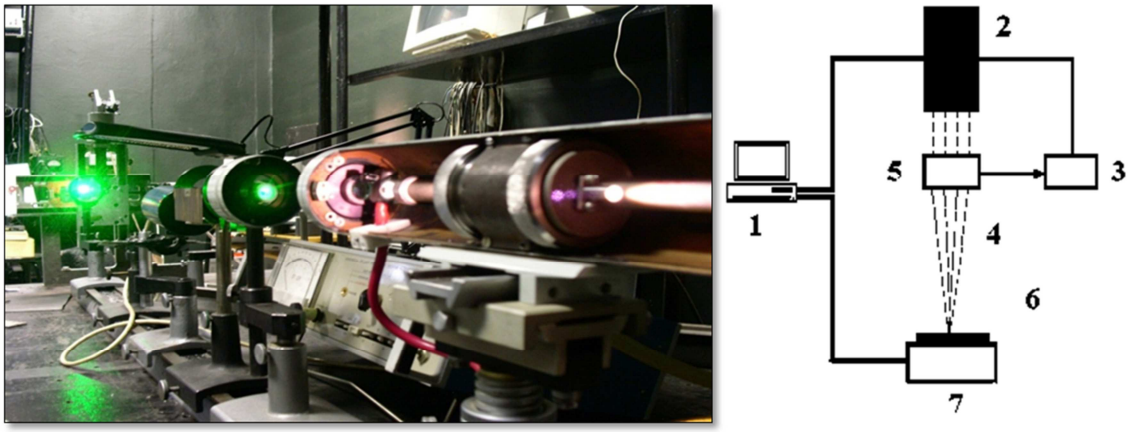

Figure 13: Laser equipment and its Block diagram: 1 – Software device, 2 – Laser 3 – Sensor radiation parameters, 4 – Laser radiation, 5 – Optical system 6 – Sample, 7 – Device for fixing and moving the sample (micrometer table)

Experiments were carried out at room temperature and atmospheric pressure. To prevent evaporation of Cd, the surface of CdZnTe crystals was coated with a thin (0.3μm) film of SiO_2, which is transparent for the wavelength of laser radiation Intensity of the laser radiation was below the threshold of thermal destruction of the SiO_2/CdZnTe structure. The irradiated surface was treated in aqueous solution of HF to remove the SiO_2 film before the characterization.

Table 4: Summary of experimental conditions used for laser irradiation

Experimental conditions	
Laser	Nd:YAG
pulse duration τ (ns)	10-15
Power P (MW)	1.0
Intensity I (MW/cm^2)	I=4–12
Beam spot (mm)	0.9
Laser pulses	3.6x10^4

V.3.3. Results and discussion

a) Surface morphology

In order to analyze the surface morphology of CZT samples before and after irradiation AFM measurements have been carried out. The 3D AFM images of CZT crystal surfaces before and after laser irradiation with intensity of 12MW/cm^2 are presented in **Figure 14**. As can be seen, a large density of small particulates in the form of cones grows on the CZT surface after irradiation. It has been demonstrated that irradiation of $Cd_{0.9}Zn_{0.1}Te$ crystals by Nd:YAG laser at intensities below the threshold intensity of 4.0MW/cm^2 does not change the surface morphology. The nano-cones are formed at intensities I ≥ 4.0MW/cm^2 (50).

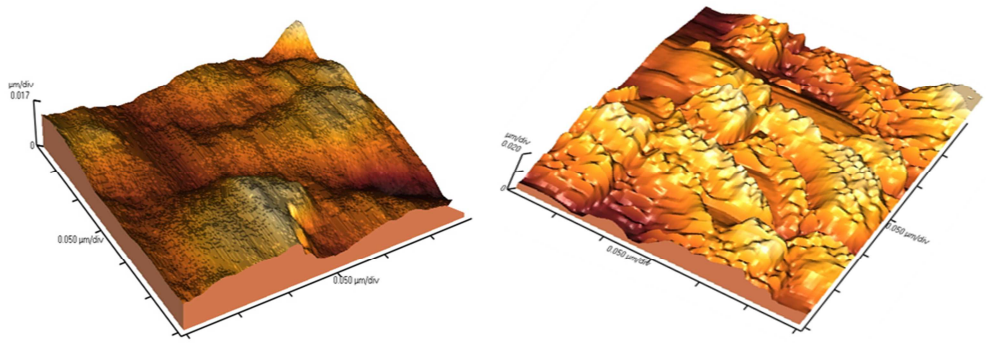

Figure 14: 3D AFM images of CZT samples before (left) and after (right) laser irradiation with intensity of 12 MW/cm^2

The formation of these nano-cones is shown in **Figure 15** and could be explained as follows: a) we assume a random distribution of Te, Cd and Zn atoms on the sample volume; (b) During the powerful laser irradiation process, a high absorption occurs and then a gradient temperature is created. This Thermo-Gradient Effect (TGE) causes the impurity atoms, interstitial and vacancies to drift toward the gradient of temperature. According to TGE theory, the atoms which have bigger effective diameter (Cd in our case) move to the irradiated surface where the temperature is higher, while atoms with smaller effective diameter (Zn) diffuse to the side of lower temperature which is the bulk of the CZT sample (51). (c) The concentration of Zn atoms at the irradiated surface decreases and new CdTe layer is formed at the top of the sample and ZnTe at the bottom. CdTe atoms are localized at the surface of CdZnTe like a thin film. (d) A mismatch value of the crystal lattice for CdTe and ZnTe crystals is equal to 6% (52) that is why the mechanical stress between the layers of CdTe and ZnTe takes place. The relaxation of this mechanical stress is reached by plastic deformation. This deformation leads to the creation of nano-structures of the irradiated surface according to Stranski–Krastanov growth. The mechanism of nano-cones formation on the irradiated surface of $Cd_{0.9}Zn_{0.1}Te$ solid solution is characterized by two stages: Laser redistribution of atoms and laser annealing.

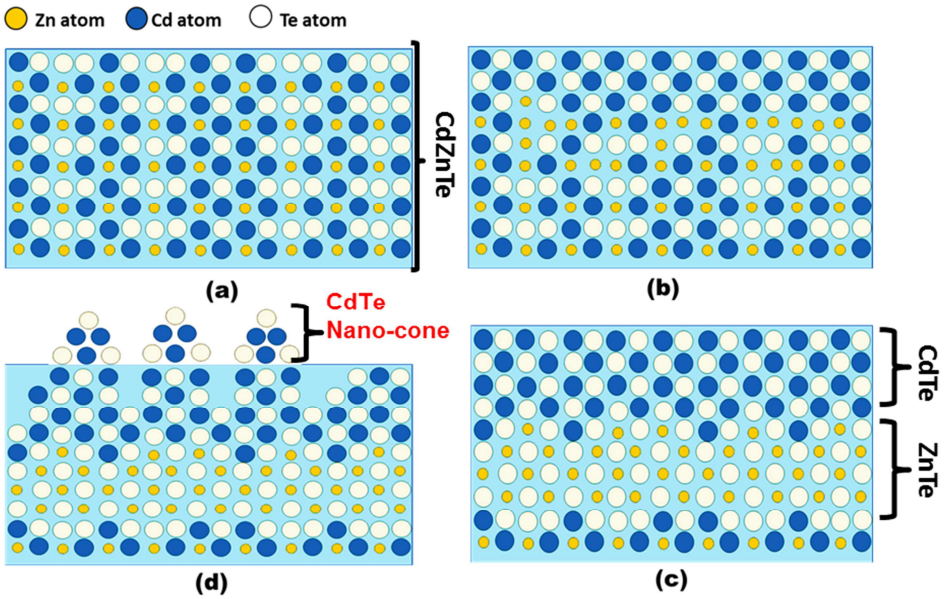

Figure 15: Schematic representation of the formation of nano-cones during laser irradiation

b) Effect of laser irradiation on Te inclusions

It has long been demonstrated that the presence of Te inclusions in CZT detectors, especially larger than 10µm and of relatively high densities, can degrade detector performance. The most effective method of detecting these crystal defects in CZT bulk materials is IR transmission microscopy (53). **Figure 16** shows IR images of a CZT crystal before and after laser irradiation. We observe that the number of the small Te inclusions (from 4 to 8.5µm) was reduced after laser irradiation, while the number of large Te inclusions (from 8.5 to 11µm) was increased. We can ascribe this reduction to the strong absorption of laser radiation by Te inclusions which create a temperature gradient and Te inclusions migrate in the direction of the higher temperature zone (54) (the surface). Thermo-migration of Te inclusions using an infrared (IR) CO_2 laser were also observed by M. Meier et.al. (55).

During laser irradiation, smaller Te inclusions migrate, some of them could interact and in consequence larger Te inclusions could be created, which could explain the increase of density of bigger Te inclusions (from 8.5 to 11µm).

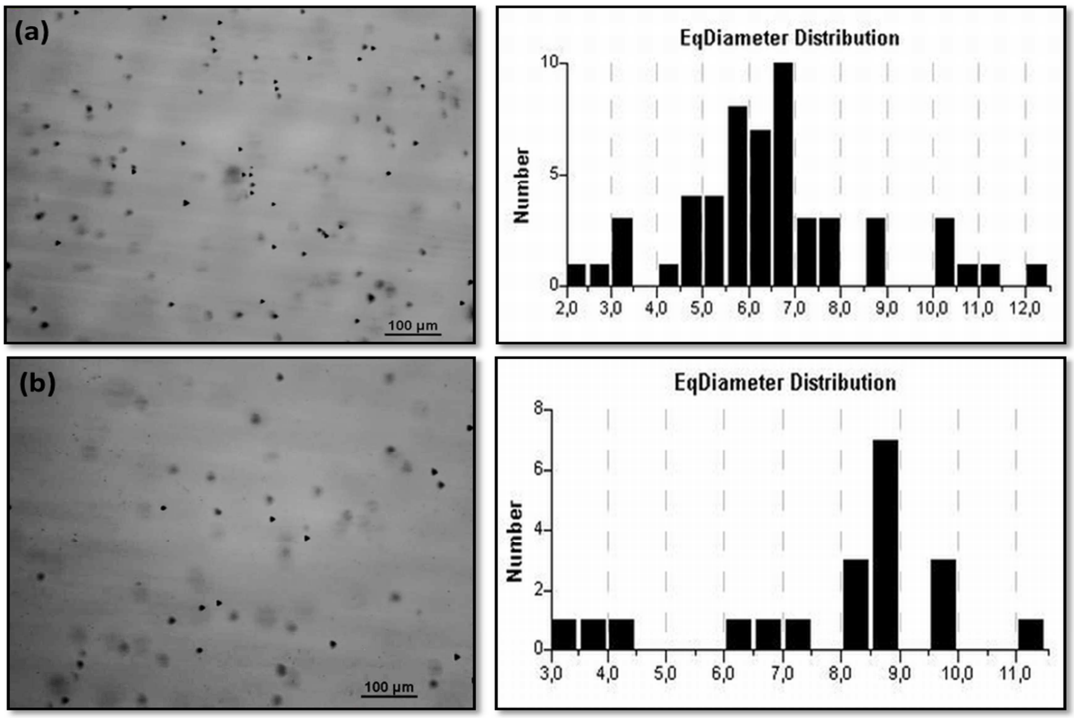

Figure 16: IR microscopy images and diameter distribution (µm) of the inclusions (a) before and (b) after irradiation with intensity of 5.4MW/cm^2

In this way, Fourier Transform Infrared Spectroscopy (FTIR) measurements were widely used to evaluate the presence of defects and dislocations inside CZT crystals. It is known that, for a high quality CZT crystal, the IR transmittance is usually constant

with a value near 63 %. However, the defects remaining in the CZT material, such as Te precipitates/inclusions, can decrease the IR transmission (56).

The IR transmission spectra were measured with the typical wavenumber from 7000 to 1000 cm^{-1} at room temperature. **Figure 17** shows the IR transmittance of CdZnTe crystal before and after laser irradiation. The IR transmittance of the as-grown CdZnTe crystal is about 63.7%, while the corresponding average transmittance of irradiated CdZnTe wafer is increased to about 64.2%. One could understand that this improvement is due to the reduction of crystal defects during irradiation. The lattice misfit existing in CdZnTe, such as dislocation and inclusions, changes the lattice parameter and destroys the uniformity as well as the periodicity of the lattice. Thus, the bigger the lattice misfits exist, the higher the IR lattice absorption (57).

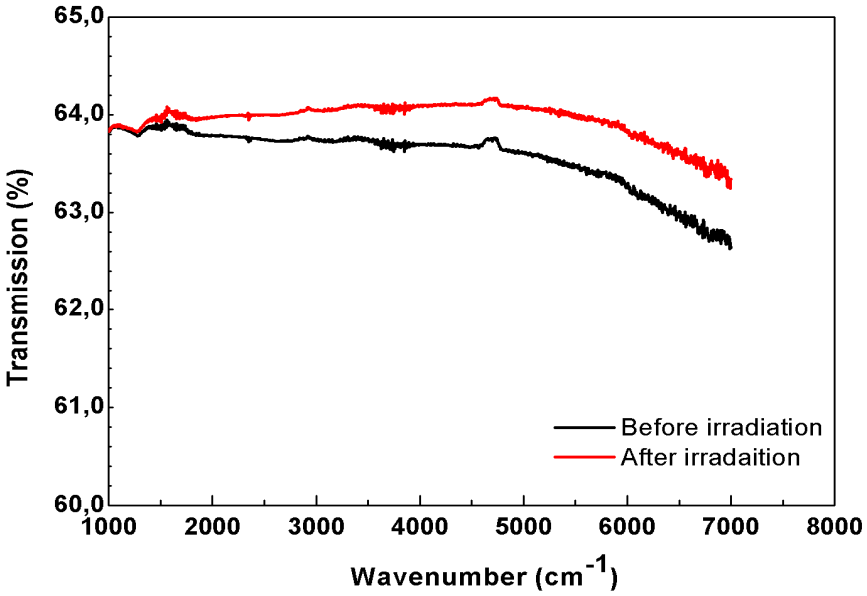

Figure 17: IR transmittance spectra for the CZT sample before and after laser irradiation

c) CZT detector performance

It has been demonstrated previously that laser irradiation leads to improved optical properties, a consequence of the reduction of Te inclusions. Therefore, in this section the electrical properties will be studied.

I-V measurements have been investigated in order to reveal how laser irradiation process and Te inclusions influence the leakage current. The contacts were prepared by electroless method using gold.

The I-V curves with the applied bias from –800V to +800Vof the CZT detectors before and after laser irradiation are exhibited in **Figure 18**. This figure shows clearly the influence of laser irradiation on the leakage current. We observe that the no irradiated

sample which contains high density of Te inclusions show a leakage current of 80nA, while the leakage current decreases to about 50nA after irradiation.

Considering that the contacts and bulk resistivity have not changed and therefore we can attribute this change to the Te inclusions which act as trapping centers and eventually enhance the leakage current.

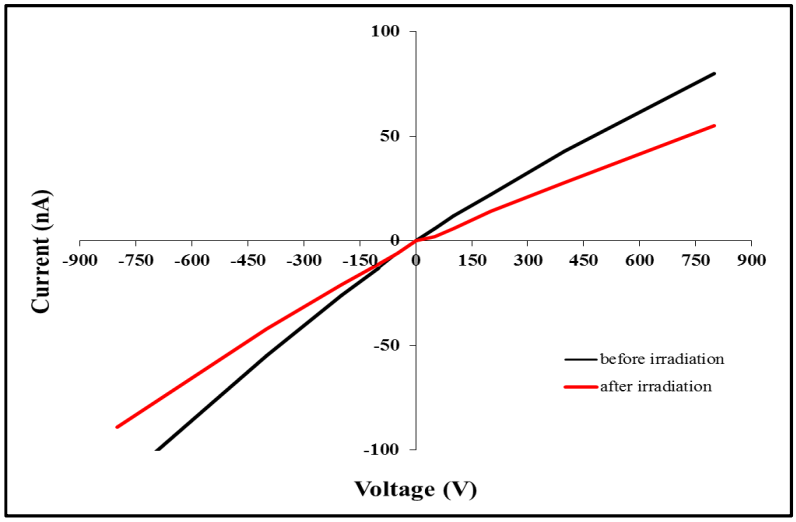

Figure 18: Comparison of I-V curves obtained from the same CZT detector before and after laser irradiation

In fact, the leakage current is always one dominant factor to influence the detector performance and acts as a source of noise during the spectroscopy measurements. In consequence the next step is to study the detectors performance and as well compare the detectors harvested from samples before and after irradiation. Gamma response was carried out using ^{241}Am source at the same voltage of 800V for the same sample before and after irradiation. **Figure** 19 shows the ^{241}Am spectra obtained. Even under the same operating conditions, there is substantial difference between the measured spectra.

As can be seen, small peak was observed for the sample before irradiation, indicating the incomplete charge collection due to the trapping of free carriers created during gamma radiation. However, after irradiation the photo peaks are clearly visible which could be attributed to the improvement of the sample.

It is important to mention that the results of the gamma spectroscopy measurements are consistent with the *I–V* curves. In fact, gamma response depends strongly to the leakage current. In consequence, the improvement of detector performance after laser irradiation could be explained by the redistribution of impurities and intrinsic defects in the crystal due to the presence of thermo-migration effect.

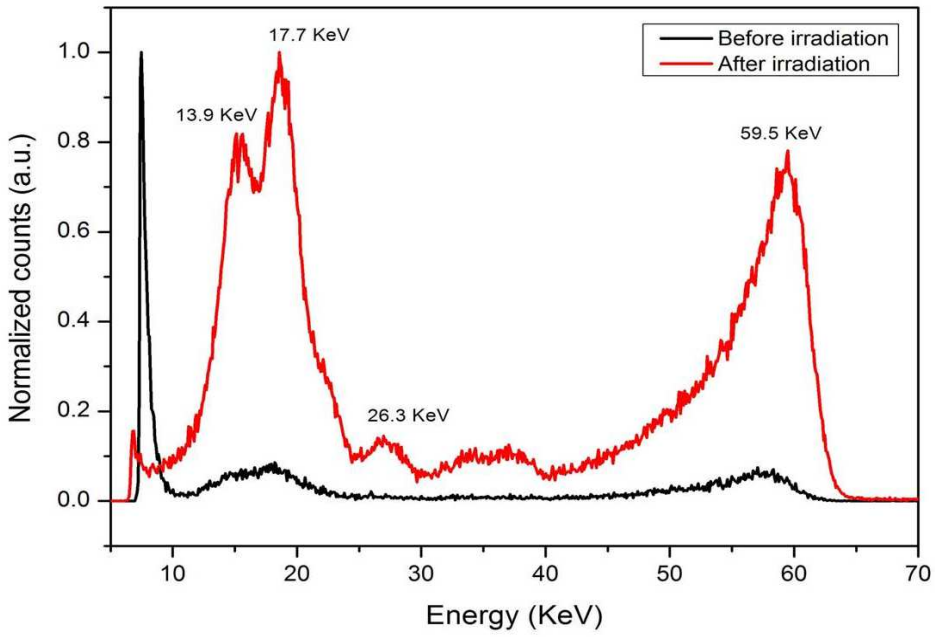

Figure 19: Room temperature ^{241}Am gamma spectra of CZT detector before and after irradiation at 800V

V.4. Conclusions

Despite the fact that argon irradiation differs from the laser irradiation in its principal mechanism. While the argon irradiation process remove material from the surface due to the bombardment, the principle of laser is to heat the samples which create a temperature gradient between opposing surfaces and then a thermo-migration effect occurs. The objective to reduce Te inclusions and improve the quality of CZT crystals using both processes of irradiation was achieved using different techniques of characterization.

The conclusions of this chapter could be summarized as follows:

- ✓ Improvement of the quality of the crystal by means of a reduction of surface defects, which is deduced from the increase of the luminescence intensity and the diminution of the peak intensity at 1.49eV related to extended surface defects.
- ✓ Ion bombardment seems to produce accumulation of Te inclusions, some of them visible on the surface of the samples. The used of elevated fluences lead to a higher diminution of the Te aggregates, as deduced from the Raman spectra of the surfaces.
- ✓ The reduction of Te inclusions and redistribution of impurities and intrinsic defects due to the thermo-migration effect created by Nd:YAG laser irradiation lead to reduce the leakage current and thereby improve the energy resolution.

V.5. Bibliography

1. **H. Bensalah, J.L. Plaza, J. Crocco, Q. Zheng, V. Carcelen, A. Bensouici, E. Diéguez.** The Effect of Etching Time on the CdZnTe Surface. 2011, Vol. 257, p. 4633.
2. **Rudolph, P.** Non-stoichiometry related defects at the melt growth of semiconductor compound crystals – a review. 2003, Vol. 38, pp. 542 – 554 .
3. **Siffert, R. Triboulet and P.** *CdTe and Related Compounds; Physics, Defects, Hetero- and Nano-structures, Crystal Growth, Surfaces and Applications.* 2009.
4. **T. Wang, W. Jie, D. Zeng.** Observation of nano-scale Te precipitates in cadmium zinc telluride with HRTEM. 2008, Vol. 472, pp. 227–230.
5. **Fang, H.Y. Pei and J.X.** Low-Temperature Fourier Transform Raman Scattering Characterization of Cd1-xZnxTe Surfaces by Different Treatments. 2001, Vol. 188, p. 1161.
6. **G. Panin, P. Fernandez, J. Piqueras.** Effect of ion beam milling on the defect structure of CdTe. 1996, Vol. 11, p. 1354.
7. **J. Olvera, O. Martínez, M. Avella, J.L. Plaza, S. de Dios, E. Diéguez.** Effect of low energy ion irradiation on CdTe crystals: Luminescence enhancement. 2010, Vol. 108.
8. **Ragnar, H.** *Ion Beams in Nanoscience and Technology.* 2009.
9. **G.N. Panin, P.S. Dutta, J. Piqueras, E. Dieguez.** p- to n-type conversion in GaSb by ion beam milling. 1995, 67, p. 3584.
10. **J. Olvera, O. Martínez, J.L. Plaza and E. Dieguez.** Luminescence effects of ion-beam bombardment of CdTe surfaces. 2009, Vol. 129, p. 941.
11. **L.F. Voss, P.R. Beck, A.M. Conway, R.T. Graff, R.J. Nikolic, A.J. Nelson, S.A. Payne.** Surface current reduction in (211) oriented Cd0.46Zn0.04Te.50 crystals by Ar bombardment. 2010, Vol. 108.
12. **J.L. Plaza, Bárbara Capote, E. Diéguez.** Nanodot hexagonal ordered arrays on GaSb substrates by LEIS under the presence of chromium diffused impurities. 2007, Vol. 201, pp. 8456–8462.
13. **D. Paramanik, S. N. Sahu, S. Varma.** Morphological evolution of InP nano-dots and surface modifications after keV irradiation. 2008, Vol. 41.
14. **G. Carter, B. Navinsek, and J. L. Whitton.** *In Sputtering by Particle Bombardment II.* 1983.
15. **T. Bekkay, E. Sacher, A. Yelon.** Surface reaction during the argon ion sputter cleaning of surface oxidized crystalline silicon (111). 1989, Vol. 217, pp. 377–381.
16. **Taglauer, E.** Surface cleaning using sputtering. 1990, Vol. 51, pp. 238-251.
17. **Smith, T.** Sputter cleaning and etching of crystal surfaces (Ti, W, Si) monitored by Auger spectroscopy, ellipsometry and work function change. 1971, Vol. 27, pp. 45–59.
18. **Sigmund, P.** Sputtering by ion bombardment theoretical concepts. 1981, Vol. 47, pp. 9-71.
19. **Smentkowski, V.S.** Trends in sputtering. 2000, Vol. 64, pp. 1-58.
20. **GmbH, SPECS.** *Useful Information and Facts about the Practice of Sputtering.*
21. **J L. Sullivan, S.O. Saied, T. Choudhury.** Effects of low-energy ion beam bombardment on metal oxides. 1993, Vol. 5, pp. A291-A292.
22. **S. S. Todorov, E. R. Fossum.** Sputtering of silicon dioxide near threshold. 1988, Vol. 52, pp. 365-367.
23. **T. Kumar, S.A. Khan, U.B. Singh, S. Verma, D. Kanjilal.** Formation of nanodots on GaAs by 50keV Ar+. 2012, Vol. 258, pp. 4148–4151.
24. **C. W. Rischau, C. S. Schnohr, E. Wendler, W. Wesch.** Ion-beam-induced damage formation in CdTe. 2011, Vol. 109.

25. **R Gago, L Vázquez, R Cuerno, M Varela, C Ballesteros, J M Albella.** Nanopatterning of silicon surfaces by low-energy ion-beam sputtering: dependence on the angle of ion incidence. 2002, Vol. 13, pp. 304–308.
26. **Egan, Christopher K.** *Morphology, structure and electronic properties of CdTe surfaces studied by scanning tunneling microscopy.* 2011.
27. **M. A. Makeev, A. L. Barabasi.** Effect of surface roughness on the secondary ion yield in ion sputtering. 1998, Vol. 73.
28. **M.A. Makeev, A.L. Barabasi.** Effect of surface morphology on the sputtering yields.I. Ion sputtering from self-affine surfaces. 2004, Vol. 222, pp. 316–334.
29. **G. Ozaydin, K. F. Ludwig, H. Zhou, Lan Zhou, R. Headrick.** Transition behavior of surface morphology evolution of Si(100) during low-energy normal incidence Ar+ ion bombardment. 2008, Vol. 103.
30. **F. Frost, B. Ziberi, T. Hoche, B. Rauschenbach.** The shape and ordering of self-organized nanostructures by ion sputtering. 2004, Vol. 216, pp. 9–19.
31. **S. Facsko, H. Kurz.** Energy dependence of quantum dot formation by ion sputtering. 2001, Vol. 63.
32. **P. Rudolph, M. Neubert, M. Miihlberg.** Defects in CdTe bridgman monocrystals caused by nonstoichiometric growth conditions. 1993, Vol. 128, p. 582.
33. **T. J.Yang, T.B. Wu.** Effect of Etching on Composition and Morphology of CdTe(111) Surfaces. 1995, Vol. 34, pp. 6184-6194 .
34. http://www.srim.org/. [Online]
35. **J.K. Radhakrishnan, G. Salviati.** Cathodoluminescence investigations on CdTe and Cd0.96Zn0.04Te crystals. 2005, Vol. 113, pp. 235-242.
36. **N.V. Sonchinskii, M.D. Serrano, E. Diéguez, F. Agulló-Rueda, U. Pal, J. Piqueras, P. Fernández.** Effect of thermal annealing on Te precipitates in CdTe wafers studied by Raman scattering and cathodoluminescence. 1995, Vol. 77, p. 2806.
37. **N.Q.Lam.** Segregation processes in alloys during ion bombardment. 1993.
38. **Y.W. Bao, W. Wang, Y.C. Zhou.** Investigation of the relationship between elastic modulus and hardness based on depth-sensing indentation measurements. 2004, Vol. 52, pp. 5397–5404.
39. **Pharr, G.M.** Measurement of mechanical properties by ultra-low load indentation. 1998, Vol. 253, pp. 151–159.
40. **Y. Hatanaka, M. Niraula, A. Nakamura, T. Aoki.** Excimer laser doping techniques for II–VI semiconductors. 2001, Vols. 175–176, pp. 462-467.
41. **L.V. Poperenko, D.V. Gnatyuk, V.A. Odarych.** Laser-Induced Modification of the Surface State and Optical Properties of CdTe Crystals. 2011, Vol. 222, pp. 28-31.
42. **D Mochizuki, M Niraula, T Aoki, Y Tomita, T Nihashi, Y Hatanaka.** Excimer laser doping technique for application in an integrated CdTe imaging device. 1999, Vol. 436, pp. 127-131.
43. **D. Mochizuki, M. Niraula, T. Aoki, T. Nagai, M. Kinoshita, Y. Hatanak.** Pattern doping on CdTe by excimer laser irradiation. 2000, Vols. 214–215, pp. 520–523.
44. **Y. Hatanak, M. Niraul, Y. Aoki, T. Aoki, Y. Nakanishi.** Surface processing of CdTe compound semiconductor by excimer laser doping. 1999, Vol. 142, pp. 227–232.
45. **F. de Moure-Flores, J.G. Quiñones-Galván, A. Guillén-Cervantes, J. Santoyo-Salazar, A. Hernández-Hernández, G. Contreras-Puente, M. de la L. Olvera, M. Meléndez-Lir.** Hexagonal CdTe films with Te excess grown at room temperature by laser ablation. 2013, Vol. 92, pp. 94–95.
46. **V.A. Gnatyuk, T. Aoki, O.I. Vlasenko, S.N. Levytskyi, B.K. Dauletmuratov, C.P. Lambropoulos.** Modification of the surface state and doping of CdTe and CdZnTe crystals by pulsed laser irradiation. 2009, Vol. 255, pp. 9813–9816.

47. **K.Sugioka.** *Laser Precision Microfabrication.* 2010.
48. **M.S. Brown, C.B. Arnold.** Fundamentals of Laser-Material Interaction and Application to Multiscale Surface Modification. 2010.
49. **L.A. Golovan, B.A. Markov, RK. Kashkarov, V.Yu. Timoshenko.** Evaporation effect on laser induced solid–liquid phase transitions in CdTe and HgCdTe. 1998, Vol. 108, pp. 707-712.
50. **A. Medvid, A. Mychko, V. Gnatyuk, S. Levytskyi, Yu. Naseka.** Mechanism of nano-cone formation on Cd0.9Zn0.1Te crystal by laser radiation. *Optical Materials.* 2010, Vol. 32, pp. 836–839.
51. **A. Medvid, L. Fedorenko.** Thermogradient mechanism of p–n junction formation by laser radiation in semiconductors. *Applied Surface Science.* 2002, Vols. 197–198, pp. 877-882.
52. **R. H. Miles, T. C. McGill, S. Sivananthan, X. Chu, J. P. Faurie.** Structure of CdTe/ZnTe superlattices. *J. Vac. Sci. Technol. B.* 1987, Vol. 5.
53. **H. Chen, S. A. Awadalla, K. Iniewski, P. H. Lu, F. Harris, J. Mackenzie, T. Hasanen, W. Chen, R. Redden, G. Bindley.** Characterization of large cadmium zinc telluride crystals grown by traveling heater method. *Journal of Applied Physics.* 2008, Vol. 103.
54. **H.R. Vydyanath, J.A. Ellsworth, J.B. Parkinson.** Thermomigration of Te Precipitates and Improvement of (Cd,Zn)Te Substrate Characteristics for the Fabrication of LWlR (Hg,Cd)Te Photodiodes. *Journal of Electronic Materials.* 1993, Vol. 22.
55. **M. Meier, M.J. Harrison, S. Spalsbury, D.S. McGregor.** Laser-induced thermomigration of Te precipitates in CdZnTe crystals. *Journal of Crystal Growth.* 2009, Vol. 311, pp. 4247–4250.
56. **Y. Li, Z. Gu, G. Li, W. Jie.** Infrared Transmission Spectra of Cd1-xZnxTe (x=0.04) Crystals. 2004, Vol. 33, pp. 861-866.
57. **L. Guoqiang, J. Wanqi, G. Zhi, H. Hui.** Correlation Between the IR Transmission Spectra and the CdZnTe Qualities. *Chin. Phys. Lett.* 2003, Vol. 20.

Conclusions

The effect of crystal growth conditions and surface treatment on CdZnTe bulk single crystal has been investigated. The general conclusions reached during the course of this study are summarized as follows:

The growth of bulk CdZnTe crystals doped with indium have been carried out by Vertical Gradient Freeze (VGF) technique. Different growth processes including superheating, cooling and annealing have been investigated in order to improve the properties of CZT crystals. This investigation was mainly focused on the influence of these parameters on Te inclusions, shallow and deep defects, the optical and electrical properties of CdZnTe detectors, resulting in improved performance.

- Superheating of the melt by 26ºC was successful at improving material homogeneity, eliminating conical shape and voids at the top of the ingots, and breaking down Te clusters.
- Ingots grown with fast cooling show the smallest Te inclusions due to the retrograde solubility of the phase diagram, where Te does not have time to agglomerate. However fast cooling can affect the shallow defects and can also influence the zinc uniformity of CZT samples.
- Bigger Te inclusions can degrade the detector performance by distorting the internal electric field. In addition, big inclusions can reduce the active volume of the detectors leading to a voltage breakdown and increasing the leakage current.
- Annealing for 24 hours at 950°C, creating a radial temperature gradient in the ingot, was successful at eliminating Te inclusions and improving the homogeneity of the samples.

After the crystal growth, the investigation was focused on the detector preparation. A complete description of lapping, mechanical polishing, chemical etching and lateral edges passivation has been discussed. The objective was to study the influence of these processes on the morphological, optical and electrical properties of CZT and then select the best process to be followed for the preparation of CZT detectors.

- Chemical etching is an important step after lapping and mechanical polishing in order to eliminate scrashes, decrease surface roughness and therefore reduce the leakage current.

- Etching process for 30s can be considered as the best etching time regarding Te concentration, surface roughness and leakage current.
- It has also been demonstrated that the lateral edges passivated immediately after etching has the best results because the enriched Te layer present on the surface is completely oxidized to TeO_2, and the surface leakage current is reduced by two orders of magnitude.

The influence of irradiation process on the properties of CdZnTe crystals has been studied. The investigation was essentially focused on the irradiation of the surface by argon ion beam and Nd:YAG laser in order to improve the properties of CdZnTe. Different techniques have been used to characterize the samples before and after irradiation including AFM, CL, I-V and gamma response.

- Improvement of the quality of the crystal by means of a reduction of surface defects, which is deduced from the increase of the luminescence intensity and the diminution of the peak intensity at 1.49eV related to extended surface defects.
- Ion bombardment seems to produce agglomeration of Te inclusions, some of them visible on the surface of the samples. Increasing fluences leads to a reduction of the Te aggregates, as deduced from the Raman spectra of the surfaces.
- The reduction of Te inclusions and redistribution of impurities and intrinsic defects due to the thermo-migration effect created by Nd:YAG laser irradiation lead to a reduction of the leakage current and therefore improved the energy resolution.

Conclusiones

El presente trabajo se ha centrado en el estudio de las condiciones de crecimiento y de tratamiento superficial y de cómo éstas afectan a los lingotes monocristalinos de CdZnTe. Las conclusiones generales se podrían resumir de la siguiente manera:

Se ha empleado la técnica de Vertical Gradient Freeze (VGF) para el crecimiento de cristales de CdZnTe dopados con indio. Varios procesos de crecimiento como el superheating, enfriamiento y recocido han sido sometidos a análisis con el fin de optimizar la calidad de los cristales así obtenidos. Esta tesis se ha centrado fundamentalmente en el estudio de estos parámetros y su efecto sobre las inclusiones de Te, defectos superficiales y profundos, las propiedades ópticas y eléctricas de los detectores fabricados a partir de los cristales de CdZnTe, lo que condujo a una mejora en el rendimiento de dichos detectores.

- El proceso de superheating del fundido a 26ºC por encima del punto de fusión resultó positivo a la hora de mejorar la homogeneidad del material, eliminando la terminación cónica del lingote así como los huecos. Además de favorecer la descomposición de agregados de Te
- El enfriamiento rápido muestra las más pequeñas inclusiones de Te debido a la solubilidad retrógrada del diagrama de fases, dado el poco tiempo del que dispone el Te para formar aglomerados y crecer antes de quedar en posiciones fijas. Sin embargo el enfriamiento rápido puede afectar los defectos superficiales y también puede influir la homogeneidad de zinc en muestras de CZT.
- Las inclusiones de Te de mayor tamaño son perjudiciales para el rendimiento del detector ya que distorsionan el campo eléctrico interno. Además, las inclusiones grandes reducen el volumen activo del detector incremento las corrientes de fuga y la ruptura del voltaje.
- El proceso de recocido a 950ºC durante 24 horas, que establece un gradiente de temperatura radial en el interior del lingote, se ha demostrado como una práctica efectiva para la reducción de inclusiones de Te y la homogeneización de la muestra.

Tras el crecimiento de los cristales, la investigación se centró en la preparación de los detectores. A lo largo del presente documento se ha dado una descripción exhaustiva de los procesos de lapping, pulido mecánico, ataque químico y

pasivación de los bordes del lingote. El objetivo de esta parte es el estudio de la influencia de estos pasos en las propiedades morfológicas, ópticas y eléctricas del CZT determinando de esta manera las condiciones óptimas de preparación de los detectores basados en CZT.

- El ataque químico es un paso fundamental tras el lapping y el pulido mecánico a la hora de eliminar daños superficiales y disminuir la rugosidad, reduciendo de esta manera las corrientes de fuga
- Un tiempo de 30 segundos ha demostrado ser óptimo para el ataque químico, en cuanto a la presencia de concentración de Te, rugosidad superficial y corrientes de fuga.
- Igualmente se ha demostrado que la pasivación de los bordes llevada a cabo inmediatamente después del ataque químico ha sido la mejor elección, ya que la capa superficial rica en Te se oxida casi completamente pasando a TeO_2, minimizando de esta manera las corrientes de fuga superficiales

Por último, se han estudiado los efectos de la irradiación en las propiedades de los cristales de CdZnTe, empleando para ello el bombardeo por haz de iones de argón y la irradiación con fuentes láser. Se emplearon diferentes técnicas de caracterización antes y después de la irradiación incluyendo entre otras: AFM, CL, I-V y gamma response.

- Se ha observado una mejora en las calidades cristalinas gracias a la reducción de defectos superficiales, patente en el incremento de la intensidad de luminiscencia y la disminución del pico relativo a 1.49eV asociado a defectos superficiales
- El bombardeo por haz de iones parece inducir la aglomeración de inclusiones de Te, algunas de ellas visibles en la superficie del lingote. Incrementar la fluencia supone la reducción de tales agregados como se infiere de los resultados de microscopía Ramman
- La reducción de inclusiones de Te y la redistribución de las impurezas y defectos debida a la termomigración inducida por la fuente láser de Nd:YAG conduce a la reducción de las corrientes de fuga mejorando así la resolución en energías del detector.

Scientific activity during PhD studies

Publications list:

1. **H. Bensalah**, J.L. Plaza, J. Crocco, Q. Zheng, V. Carcelen, A. Bensouici, E. Dieguez, "The Effect of Etching Time on the CdZnTe Surface", Applied Surface Science ,257, 4633–4636 (2011).
2. **H. Bensalah**, J. Crocco, V. Carcélen, J.L. Plaza, Q. Zheng, L. Marchini, M. Zanichelli, G. Domínguez, L. Soriano, E.Diéguez, "Study of ammonium fluoride passivation time on CdZnTe bulk crystal wafers", Cryst. Res. Technol., 46, No. 7, 659 – 663 (2011)
3. **H. Bensalah,** J. Crocco, V. Carcelén, A. Black, Q. Zheng, J.L. Plaza, E. Diéguez, "Effect of Superheating and fast cooling On Te inclusions of Cd0.9Zn0.1Te:In Crystals Grown by Vertical Gradient Freezing", Journal of Crystal growth, 361, 5–10 (2012)
4. **H. Bensalah,** V. Hortelano, J.L. Plaza, O. Martínez, J. Crocco, Q. Zheng, V. Carcelen, E.Dieguez, "Characterization of CdZnTe after Argon Ion Beam Bombardment", Journal of Alloys and Compounds, 543, 233–238 (2012)
5. **H. Bensalah**, M.L. Corro, A. Black, J.Medina, V.Carcelen, J.Crocco, Q. Zheng, E. Diéguez "Effect of Te inclusions on the structural properties of CdZnTe", submitted, (2013)
6. **H.Bensalah**, J.Crocco, J.Franc, A.Black, Q.Zheng, P.Hlidek, V.Dedic, E.Dieguez," PL characterization of CdZnTe samples grown using different growth conditions", submitted, (2013)
7. J. Crocco, **H. Bensalah**, Q Zheng, V. Carcelen, E. Dieguez, "Influence of SiC pedestal in the growth of 50 mm CZT by Vertical gradient freeze method " Journal of Crystal Growth, 360, (2012), 92–94
8. J. Crocco, **H. Bensalah**, Q. Zheng F. Dierre, P. Hidalgo, J.Carrascal, O. Vela, J. Piqueras, E. Diéguez, "Study of the Effects of Edge Morphology on Detector Performance by Leakage Current and Cathodoluminescence", IEEE TRANSACTIONS ON NUCLEAR SCIENCE, VOL. 58, NO. 4, AUGUST 2011
9. J. Crocco, **H. Bensalah**, Q. Zheng,A. Castaldini, B. Fraboni, D. Cavalcoli, A. Cavallini, E. Dieguez, "Influence of Dynamic Temperature Adjustments During Growth on the Material Properties of CZT Radiation Devices", J. Crystal. Growth, 361, (2012), 66–72
10. J. Crocco, **H. Bensalah**, Q. Zheng, V. Corregidor, E. Avles,A. Castaldini, B. Fraboni, D. Cavacoli,A. Cavallini,O. Vela, and E. Dieguez, Study of asymmetries of Cd(Zn)Te devices investigated using photo-induced current transient spectroscopy, Rutherford backscattering, surface photo-voltage spectroscopy, and gamma ray spectroscopies, Journal of Applied Physics 112, 074503 (2012)
11. J.Crocco, A. Black, **H.Bensalah**, Q.Zheng, V.Carcelen, E.Dieguez, "Influence of SiC pedestal in the growth of 50 mm CZT by Vertical gradient freeze method", Journal of Crystal Growth 355 (2012) 46–51
12. J. Crocco, Q. Zheng, **H. Bensalah**, E. Dieguez, "Detector surface preparation of Cd0.9Zn0.1Te for electrode patterning", Applied Surface Science 258 (2012) 2948–2952
13. J.L. Plaza, O. Martínez, V. Hortelano, **H. Bensalah** and E. Diéguez , "Nanodot and nanocrystal pattern formation and luminescent properties of BiB3O6 glasses after

moderate energy ion beam sputtering", Nuclear Instruments and Methods in Physics Research B 272 (2012) 466–470

14. Q Zheng, F Dierre, J Franc, J Crocco, **H Bensalah**, V Corregidor,E Alves, E Ruiz, O Vela, J M Perez and E Dieguez, "Investigation of generation of defects due to metallization on CdZnTe detectors", J. Phys. D: Appl. Phys. 45 (2012) 175102 (6pp)
15. Q.Zheng, F.Dierre, J. Crocco, V. Carcelen, **H. Bensalah**, J.L. Plaza, E. Dieguez, "Influence of surface preparation on CdZnTe nuclear radiation detectors", Appl. Surf. Sci., vol. 257, pp. 8742-8746, 2011.
16. Q. Zheng, F. Dierre, M. Ayoub, J. Crocco, **H. Bensalah**, V. Corregidor, E. Alves, R. Fernandez-Ruiz, J. M. Perez, and E. Dieguez, "Comparison of radiation detector performance for different metal contacts on CdZnTe deposited by electroless deposition method", Cryst. Res. Technol., vol. 46, no. 11, pp. 1131-1136, 2011.
17. Zheng, Q., Dierre, F., Corregidor, V.,Crocco, J., **Bensalah, H**., Plaza, J.L.,Alves, E., Dieguez, E. "Electroless plating of Au, Pt, or Ru thin film layer on CdZnTe", IEEE Nuclear Science Symposium Conference Record , art. no. 6154727, pp. 4848-4852
18. J. Crocco, V. Carcelen, B. Methven, I. Gallardo, **H. Bensalah**, Q. Zheng, I. Rivas, F. Moreno, O. Vela, E. Dieguez, "Influence of Carbon Coated pBN Crucible on Crystal Growth of Cd0.9Zn0.1Te for Radiation Detector Applications", Journal of Crystal Growth 349, (2012) 61–67
19. Q. Zheng, F. Dierre, V. Corregidor, J. Crocco, **H. Bensalah,** J.L. Plaza, E.Alves, E.Dieguez, " Electroless deposition of Au,Pt, or Ru Matallic Film Layer on CdZnTe", Thin Solid Films, 525, 15 (2012), 56–63
20. Q. Zheng, F. Dierre, V. Corregidor, R. Fernández-Ruiz, J. Crocco, **H. Bensalah**, E. Alves, E. Diéguez, "Deposition of nanometric double layers Ru/Au, Ru/Pd, and Pd/Au onto CdZnTe by the electroless method", J. Crystal. Growth, 543,(2012), 233–238
21. Bensouici, V. Carcelen, J. L. Plaza, S. De Dios, N. Vijayan, J. Crocco, **H. Bensalah**, E. Dieguez & M. Elaatmani, "Study of Effects of Polishing and Etching Processes on $Cd_{1-x}Zn_xTe$ Surface Quality", J. Crystal Growth 312 (2010) 2098–2102.
22. V. Carcelen , K.H.Kim , G.S.Camarda , A.E.Bolotnikov , A.Hossain, G.Yang , J.Crocco, **H.Bensalah**, F.Dierre,E.Dieguez,R.B.James, "Pt cold finger improves quality of Bridgman-grown Cd0.9Zn0.1Te:Bi crystals", Journal of Crystal Growth 338, (2012), 1–5
23. L A Kosyachenko, C P Lambropoulos, T Aoki, E Dieguez,M Fiederle, D Loukas, O V Sklyarchuk, O L Maslyanchuk,E V Grushko, V M Sklyarchuk, J Crocco and **H Bensalah**, "Concentration of uncompensated impurities as a key parameter of CdTe and CdZnTe crystals for Schottky diode x/γ-ray detectors" Semicond. Sci. Technol. 27 (2012) 015007 (11pp)
24. Medvid', A. Mychko, E. Dauksta, V. Ivanov, L. Alekseeva, E. Dieguzs, J.Crosso, **H. Bensalah**, "Improvement of CdZnTe Radiation Detectors Parameters by Laser Radiation", 2011 IEEE Nuclear Science Symposium Conference Record

Conference participation list:

1. *October 29 – 4 November, IEEE Nuclear Science Symposium, Medical Imaging Conference, Disneyland Hotel, Anaheim, California:* ***Getting the Best Poster Award***

- **H. Bensalah**, J. Crocco, A. Black, Q. Zheng, O. Vela, J.L. Plaza, E. Dieguez, "Reduction of Te Inclusions in CdZnTe Crystals by Growth Process to Improve the Detector Performance", **Oral presentation**
- **H. Bensalah**, A. Medvids, J. Crocco, A. Michko, E. Dauksta, V. Ivanov, Q. Zheng, J.L. Plaza, E. Dieguez, "Improvement of the Quality of CdZnTe Detectors after Laser Irradiation", **Poster presentation**
- J. Crocco, **H. Bensalah**, Q. Zheng, A. Black, B. Fraboni, D. Cavalcoli, A. Castaldini, A. Cavallini, E. Alves, V. Corregidor, P. Hidalgo, O. Vela, E. Dieguez, " Asymmetries of CZT Detectors Used for Gamma Ray Spectroscopy", **Oral presentation**
- Q. Zheng, J. Crocco, P. Wellmann, A. Osvet, U. Künecke, F. Dierre, **H. Bensalah**, A. Black, O. Vela, J.M. Perez, E. Dieguez, "Influence of Crystal Growth Process on CZT Radiation Detectors", **Poster presentation**,

2. *October 28 – 31, 7th International Workshop on Modeling in Crystal Growth Taipei, Taiwain*

- Black, A**.**, Crocco, J., **Bensalah, H**., Dieguez, E. "Experimental and modeling results of 50 mm diameter cadmium zinc telluride ingots in a VGF furnace", **Oral Presentation**

3. *June 17 – 20, European Conference on Crystal Growth, University of Strathclyde, Glasgow, Scotland:*

- J. Crocco, **H. Bensalah**, A. Black, Q. Zheng, E. Diéguez, Growth of CdZnTe by Vertical Gradient Freeze technique with melt superheating and a SiC cold finger: Experimental and Numerical Simulation Results, **Oral presentation**

4. *October 23-29, IEEE Nuclear Science Symposium, Medical Imaging Conference, Valence, Spain:*

- **H. Bensalah**, V. Hortelano, J.L. Plaza, O. Martínez, J. Crocco, Q. Zheng, V. Carcelen, E.Dieguez , Surface Characterization of CdZnTe after Argon Ion Beam Bombardment, **poster presentation**
- **H. Bensalah**, J. Crocco, J.L. Plaza, Q. Zheng, E.Dieguez **, "**Effect of different Growth Temperature On Te inclusions of Cd0.9Zn0.1Te:I", **poster presentation**
- Q. Zheng, F. Dierre, V. Corregidor, J. Crocco, **H. Bensalah**, J.L. Plaza, E. Alves, and E. Dieguez, "Electroless Plating of Au, Pt, or Ru Thin Film Layers on CdZnTe", Oral presentation
- Q. Zheng, F. Dierre, J. Franc, J. Crocco, **H. Bensalah**, V. Corregidor, E. Alves, E. Ruiz, O. Vela, J.M. Perez, E. Dieguez, "Investigation of Generated defects due to Processes of Metallisation on CdZnTe detectors", **Poster presentation**

5. *June 26-30,5th International Workshop on Crystal Growth Technology (IWCGT-5) , Berlin, Germany:*

- J. Crocco, **H. Bensalah**, Q. Zheng, I. Gallardo, E. Dieguez, "Challenges for improving the growth of bulk CZT crystals", **Poster presentation**

6. *May 9-13, the European Materials Research Society (E-MRS) Spring Meeting*

- J. L. Plaza, O. Martínez, D. González , J. P. Allain, O. El-Atwani, A. Cimaroli, **H. Bensalah** , V. Hortelano , T. Ben , R. Fath and E. Diéguez, "Ultralow Ebergy Iion Irradiation of ZnO Nanowires Grown on CdTe/CdZnTe and LiNbO3 Substrates" **Poster presentation**

7. *October 30 – November 6 , IEEE 17th Room Temperature Semiconductor Detector Workshop Knoxville,Tennessee (USA):*
   - **H. Bensalah**, J. Crocco, V. D. Carcelen, J. L. Plaza, Q. Zheng, G. Rodriguez, L. Soriano, E. Dieguez, "Study of Passivation Time on CdZnTe Bulk Crystal By X-Ray Photoemission Spectroscopy, Photoconductivity, and Intensity Voltage measurement", **Poster presentation**
   - J. Crocco, F. Dierre, **H. Bensalah**, Q. Zheng, P. Hidalgo, J. Piqueras, E. Dieguez, "Effects of Surface Morphology on CZT Detectors Studied by I-V and Cathode Luminescence", **Oral presentation**
   - Q. Zheng, F. Dierre, M. Ayoub, J. Crocco, **H. Bensalah**, V. Corregidor, E. Alves, R. Fernandez-Ruiz,J. M. Perez, and E. Dieguez, "Comparison of the Detector Performance for Different Metal Contacts on Cd(Zn)Te for Radiation Applications", **Poster presentation**
   - J. Crocco, **H. Bensalah**, Q. Zheng, E. Dieguez, "Crystal Growth of CZT using SiC Pedestal and pBN Crucible", **Oral presentation**,
   - J. Crocco, **H. Bensalah**, Q. Zheng, I. Gallardo, E. Dieguez, "Vaccum Carbon Coating of Quartz and pBN Crucibles Applied to VGF Growth of Cadimum Zinc Telluride", **Poster presentation**

8. *September 13-17, European Materials Research Society Fall Meeting, University of Technology , Warsaw, Poland* ***Getting the Best Poster Award***
   - **H. Bensalah**, J.L. Plaza, J. Crocco, Q. Zheng, V. Carcelen, A. Bensouici, E. Dieguez, " The effect of etching time on the CdZnTe surface", **Poster presentation**
   - Q. Zheng, F. Dierre, V. Corregidor, R. Fernández-Ruiz, J. Crocco, **H.Bensalah**, E. Alves, E. Diéguez, "Deposition of nanometric double layers Ru/Au, Ru/Pd, and Pd/Au onto CdZnTe by the electroless method", **Poster presentation**

9. *August 22-27, International Conference on Ion Beam Modification of Materials (IBMM), Montréal, Canada*
   - *J.L. Plaza, O. Martínez, V. Hortelano,* ***H. Bensalah*** *and E. Diéguez "Nananodot patterning and luminescent properties of BiB3O6 Glasses after Low Energy Ion Sputtering"* **Poster presentation**

Research stays:

- May – July 2012 Research Internship – Institute of Physics, Charles University in Prague, Czech Republic

- From 09 to 12 June - 2012 Research in European Synchrotron Radiation Facility (ESRF) Grenoble, France